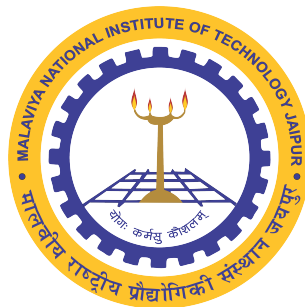


**SEARCH FOR RARE B TO CHARM DECAYS AT BELLE
AND SENSITIVITY STUDY FOR ϕ_3 AT BELLE II**

Ph.D. Thesis

MANISH KUMAR

ID No. 2016RPY9052



**DEPARTMENT OF PHYSICS
MALAVIYA NATIONAL INSTITUTE OF TECHNOLOGY JAIPUR
December 2022**

**Search for rare B to charm decays at Belle and
sensitivity study for ϕ_3 at Belle II**

*Submitted in
fulfillment of the requirements for the degree of*

Doctor of Philosophy

by

Manish Kumar

ID:2016RPY9052

Under the joint supervision of

Dr. Kavita Lalwani
(Supervisor)
(Assistant Professor)
MNIT Jaipur

Dr. Vishal Bhardwaj
(Co-Supervisor)
(Assistant Professor)
IISER Mohali



DEPARTMENT OF PHYSICS
MALAVIYA NATIONAL INSTITUTE OF TECHNOLOGY JAIPUR
December 2022

© Malaviya National Institute of Technology Jaipur - 2022.

All rights reserved.

*This thesis is dedicated to my family
for their unconditional love and motivation.*

DECLARATION

I, **Manish Kumar**, declare that this thesis titled, “**Search for rare B to charm decays at Belle and sensitivity study for ϕ_3 at Belle II** ” and the work presented in it, are my own. I confirm that:

- This work was done wholly or mainly while in candidature for a research degree at this university.
- Where any part of this thesis has previously been submitted for a degree or any other qualification at this university or any other institution, this has been clearly stated.
- Where I have consulted the published work of others, this is always clearly attributed.
- Where I have quoted from the work of others, the source is always given. With the exception of such quotations, this thesis is entirely my own work.
- I have acknowledged all main sources of help.
- Where the thesis is based on work done by myself, jointly with others, I have made clear exactly what was done by others and what I have contributed myself.

Date:

Manish Kumar
(2016RPY9052)

CERTIFICATE

This is to certify that the thesis entitled “**Search for rare B to charm decays at Belle and sensitivity study for ϕ_3 at Belle II**” being submitted by **Mr. Manish Kumar (2016RPY9052)** is a bonafide research work carried out under my supervision and guidance in fulfillment of the requirement for the award of the degree of **Doctor of Philosophy** in the Department of Physics, Malaviya National Institute of Technology, Jaipur, India. The matter embodied in this thesis is original and has not been submitted to any other University or Institute for the award of any other degree.

Dr. Kavita Lalwani
Supervisor
Assistant Professor
Department of Physics
MNIT Jaipur

Dr. Vishal Bhardwaj
Co-Supervisor
Assistant Professor
Department of Physical Science
IISER Mohali

Place: Jaipur

Date:

ACKNOWLEDGEMENT

First of all, I would like to express my thanks and gratitude to the Almighty, the most kind and merciful, who granted me health, ability, and strength for the successful completing of this venture, which helped me overcome the troubles and difficulties with vigor and vitality.

I feel great privilege and pleasure in expressing my sincere and deepest sense of gratitude to my supervisor and mentor Dr. Kavita Lalwani, Department of Physics, for her scholarly guidance and affection. Because of her helpful attitude, incessant directions, invaluable support, uninterrupted and expert supervision, I could accomplish the present manuscript.

I would always oblige to Dr. Vishal Bhardwaj (IISER Mohali) for whatever I have learned and for giving straightforward direction to my thesis work. I am thankful that he had given the chance to work with him. And I think without his suggestions and guidance, my work never get such a beautiful shape. He did impact not only professional but also personal life. He taught me how to always motivate myself and others in opposite situations. I hope that I will try to follow whatever I have learned from him in future.

I express my heartiest thanks to Dr. Karim Trabelsi (LAL, France) and Dr. Jim Libby (IIT Madras) for their suggestion and comments during each B2Charm meeting. I want to express my gratitude to the Belle and Belle II Collaborations

for providing me the opportunity to work at KEK.

I never forgot the help from Dr. Gagan Mohtany (TIFR, Mumbai), who always appreciated me working with him in the SVD sub-detector part of the Belle detector.

I acknowledge all the Belle India Group members who encouraged and supported me during my Ph.D., especially the faculty members of collaborating institutes who initiated the Belle analysis workshops (BAW), which allow the students to understand various aspects of theoretical and experimental particle physics. The BAW, held every year, helped me to understand the technical details of the analysis. It was an excellent opportunity to interact with other collaborators and learn about their research areas.

I am privileged to acknowledge all the faculty members of the Department of Physics, MNIT Jaipur, for their continuous support and encouragement. I sincerely thank to my DREC members Prof. Kanupriya Sachdev, Dr. Rahul Singhal, Dr. Kamendra Awasthi, Dr. K. Venkataratnam Kamma for their constant help and permitting me to carry out research activity within or outside the department. Their valuable and critical suggestions were a continuous source of encouragement throughout the entire course of this work.

I am also thankful to MNIT family: Assistant Professor Yogesh saini, Dr. Karam chand, Dr. Renu Dhayal, Dr. Meghna Rathore, Dr. Mamta Yadav, Dr. Shivani, Dr. Neeru, Dr. Radhe Shyam, Sanjeeda Bharati Das, Chanchal Sharma, Priyanka Boora, Anuj Malik (Pushpa), Deepak Negi, Pooja Pareek, Jyoti Lakhera, Saisandri Saini, Radhika Goswami, Dharmendra Kumar, Yogita, Vikesh, Hem Kanwar Rathore, Sapna, Shiv Dutta Lawaniya, Bhawna Rathi, Gaurav Pandey, Komal Shekhawat, Amena Salim, Deependra Jhankal, Devandar Chauhan, Himanshu Gupta, Monika Shrivastav, Nabarun Bera, Nishel Saini, Sanjay Kumar, Sachin Sharma, Deepika, Prakwan Dutta, Ankita Jangid who make this journey memorable.

I want to thank my Belle Colleagues: Dr. Renu, Dr. Sourav Patra, Dr. Niharika, Dr. Seema, Rajesh, Dr. Debashis, Soumen, Souvik, Lopa, Rashmi, Sushree Ipsita, Rahul, Sagar, Latika, Devender.

I am also thankful to staff members of the Department of Physics, Mr. Khem Singh, Mr. Firoz Khan, Mr. Ramkishor, Mr. Sunil Kumar, and Mr. Ritesh for their support in making the departmental activities easy and cheerful. I am also thankful to all office and technical staff for their valuable help and support.

Last but not least, I would like to thank my family; without their support, this thesis could not have come to successful completion. I owe a lot to my parents for their motivation and support throughout my life. Nothing can replace their unconditional love. I would like to thank all my family members and relatives for their support.

This thesis is the end of my journey toward obtaining my Ph.D. degree. I have not travelled in a vacuum on this journey. This thesis has been kept on track and been through to completion with the support and encouragement of numerous people, including my teachers, family, well-wishers, friends, and colleagues. At the end of my thesis, I would like to thank all those people who made this thesis possible and an unforgettable experience for me.

(Manish Kumar)

ABSTRACT

The objective of this work is to search for the rare decay modes like $B^+ \rightarrow D_s^{(*)+}\eta$, $D_s^{(*)+}\bar{K}^0$, $D^+\eta$, and D^+K^0 along with the branching fraction measurement of $\bar{B}^0 \rightarrow D^0\eta$ and $\bar{B}^0 \rightarrow D^0K^0$ decay modes. To perform these studies, we used the data sample corresponding to an integrated luminosity of 711 fb^{-1} collected with the Belle detector at KEKB an asymmetric energy of e^+e^- collider.

In the absence of any significant signal events, we provide upper limits at 90% confidence level on the branching fraction of $B^+ \rightarrow D_s^+h$, $D_s^{(*)+}h$, and D^+h modes, where h denotes the neutral mesons (η , K^0). Along with rare decay modes, we also report the improved measurement results of the color-suppressed decay modes: $\mathcal{B}(\bar{B}^0 \rightarrow D^0\eta) = (26.6 \pm 1.2 \pm 2.1) \times 10^{-5}$ and $\mathcal{B}(\bar{B}^0 \rightarrow D^0K^0) = (5.6 \pm 0.5 \pm 0.2) \times 10^{-5}$. The first and second uncertainties are statistical and systematic, respectively.

Along the study of rare decay modes, we also reconstructed $D_s^{*\pm} \rightarrow D_s^\pm\gamma(D_s^\pm\pi^0)$ and $D^{*\pm} \rightarrow D^0\pi^\pm$ decay modes using Phase III data. The D_s^+ is reconstructed from four sub-decay modes: $K_S^0K^+$, $K^+K^-\pi^+$, $\phi\pi^+$, and $\bar{K}^{*0}K^+$ while the D^0 is reconstructed from three sub-decay modes: $K^-\pi^+$, K^+K^- , and $\pi^+\pi^-$. We get the clear signature of D_s^+ and D^0 mesons with 3.14 fb^{-1} data sample.

In parallel to the analysis activities, I also contributed to the Belle II experiment, an upgrade of the Belle detector. I contributed mainly to the performance studies of Silicon Vertex Detector (SVD) from the Test Beam data and the visual

inspection of the SVD 4th layer.

Contents

List of Figures	xiii
List of Tables	xxxii
1 Introduction	1
1.1 Introduction	2
1.1.1 CP violation	5
1.2 Sources of CP violation	7
1.3 Rare B decays	10
1.4 Summary	13
2 Experimental Facility	14
2.1 KEKB accelerator	15
2.2 Belle detector	17
2.2.1 Beam pipe	19
2.2.2 Silicon Vertex Detector (SVD)	19
2.2.3 Central Drift Chamber (CDC)	22

2.2.4	Aerogel Cherenkov Counter (ACC)	23
2.2.5	Time of Flight counter	25
2.2.6	Electromagnetic Calorimeter (ECL)	27
2.3	The Belle Trigger system	29
2.4	Data Acquisition System (DAQ)	31
2.5	Belle II Experiment	32
2.6	Summary	36
3	Blind Analysis of Signal and Control modes	37
3.1	Blind Analysis	39
3.2	Analysis Procedure	39
3.3	Signal and Generic Monte Carlo Sample	40
3.4	Selection criteria	42
3.4.1	Final state particles selection	43
3.4.2	Reconstruction of ϕ , \bar{K}^{*0} , K_S^0 Mesons	44
3.4.3	Invariant mass spectra of ϕ , \bar{K}^{*0} and K_S^0	45
3.4.4	Reconstruction of D_s^+	45
3.4.5	Reconstruction of D^+	46
3.4.6	Reconstruction of $D_s^{(*)+}$	47
3.4.7	Reconstruction of B Meson	47
3.4.8	Optimization of photons energy	47
3.4.9	Best Candidate Selection (BCS)	49
3.5	Signal MC study	50
3.6	Generic MC Study	54

3.7	Continuum Suppression	56
3.8	Optimization Cut on FBDT Output	62
3.9	Rare Background Study	65
3.10	Fitted ΔE distribution with Signal MC	67
3.11	Control Mode Study	70
3.12	Event Selection	70
3.13	Generic MC study	72
3.14	Continuum Suppression	73
3.15	The Probability Density Functions (PDFs)	74
3.15.1	Signal PDF	74
3.15.2	Background PDF	76
3.16	Toy MC Study	80
3.17	Fitting Strategy for Signal decay modes	83
3.18	Toy study for signal modes	86
3.19	Data/MC (Side-band) Comparison	90
3.20	Summary	93
4	Extraction of branching fraction for signal and control mode from data	94
4.1	Crosscheck with Data	95
4.1.1	Individual D^0 sub decay mode study of control modes	98
4.2	Systematic study of Control modes	100
4.2.1	Kaon identification	101
4.2.2	Pion identification	101

4.2.3	Tracking	102
4.2.4	$N_{B\bar{B}}$	102
4.2.5	K_S^0 reconstruction	103
4.2.6	η , π^0 , and γ detection	103
4.2.7	Secondary Branching Fraction	103
4.2.8	Fit bias	103
4.2.9	ΔE Fit	104
4.2.10	Comparison of branching fraction	105
4.3	Systematics Study of Signal Decay Modes	106
4.3.1	Kaon- pion Identification	106
4.3.2	Tracking	106
4.4	Signal Decay Mode study with Data	108
4.5	Summary	112
5	Silicon Vertex Detector at Belle II	113
5.1	SVD	114
5.2	Performance Studies of the SVD	117
5.3	Visual Inspection of L4	120
5.4	Summary	124
6	Rediscovery of $D^{*\pm}$ and $D_s^{*\pm}$ and measurement of the CKM angle ϕ_3 using $B \rightarrow DK$ at Belle II	125
6.1	Introduction	126
6.2	Data sample and Selection criteria	127
6.3	Rediscovery of D^{*+} and D_s^{*+} with Phase III data sample	128

6.3.1	$D_s^{*+} \rightarrow D_s^+ \gamma, D_s^+ \rightarrow K^+ K^- \pi^+, K_S^0 K^+, \phi \pi^+, \bar{K}^{*0} K^+$	128
6.3.2	$D_s^{*+} \rightarrow D_s^+ \pi^0, D_s^+ \rightarrow K^+ K^- \pi^+, K_S^0 K^+, \phi \pi^+, \bar{K}^{*0} K^+$	130
6.3.3	$D^{*+} \rightarrow D^0 \pi^+, D^0 \rightarrow K^- \pi^+, K^+ K^-, \pi^+ \pi^-$	132
6.3.4	Reconstruct D_s^+ and D^+ from $K_S^0 K^+, K^+ K^- \pi^+, \phi \pi^+$, and $\bar{K}^{*0} K^+$ decay mode	133
6.4	Measurement of the CKM angle ϕ_3	135
6.4.1	Physics Analysis for $B^\pm \rightarrow D^0 K^\pm, D^0 \rightarrow K_S^0 \pi^+ \pi^-$	137
6.4.2	Physics Analysis for $B^\pm \rightarrow D_{CP} K^\pm, D_{CP} \rightarrow K^+ K^-$ and $\pi^+ \pi^-$ decay modes	138
6.5	Summary	139
7	Summary & Conclusions	141
7.1	Search for rare B to charm decays at Belle	142
7.1.1	Conclusions	144
7.2	Rediscovery of $D^{*\pm}$ and $D_s^{*\pm}$ at Belle II	144
7.2.1	Conclusions	144
7.3	Performance Studies of the SVD	145
7.3.1	Conclusions	145
7.4	Measurement of the CKM angle ϕ_3 using $B \rightarrow DK$ at Belle II	146
7.4.1	Conclusions	146
	BIBLIOGRAPHY	147
	List of Publications	154
	Bio-Data	164

List of Figures

1.1	Fundamental particles of the SM and their properties [1].	4
1.2	Unitarity triangle in ρ - η plane [5].	9
1.3	Possible quark level transition.	11
1.4	Feynman diagrams for the (a) $B^+ \rightarrow D_s^{(*)+}\eta$ (b) $B^+ \rightarrow D_s^{(*)+}\bar{K}^0$ (c) $B^+ \rightarrow D^+K^0$, and (d) $B^+ \rightarrow D^+\eta$ decay modes.	11
2.1	KEKB accelerator [36].	16
2.2	A pictorial view of crab crossing and cross angle [39].	16
2.3	Cross section versus energy of different Υ resonances [44].	18
2.4	A pictorial view of Belle detector [47].	18
2.5	Cross section and side view of Belle beam pipe.	20
2.6	View SVDI detector [48].	21
2.7	Configuration of SVDII detector [51].	22
2.8	View CDC detector [52].	23

LIST OF FIGURES

2.9	dE/dx measurements for different particle types (π, K, e, p) as a function of momentum in CDC [45].	24
2.10	ACC detector [45].	25
2.11	TOF detector [45].	26
2.12	π, K, p separation in TOF detector [57].	27
2.13	ECL detector [45].	28
2.14	Belle Trigger system [58].	30
2.15	Belle Data Acquisition System [45].	31
2.16	SuperKEKB accelerator with Belle II detector position [60].	33
2.17	The schematic view of beam crossing angle at KEKB (left) and SuperKEKB (right) [61].	34
2.18	The schematic view of the Belle II detector [62].	35
3.1	Flow chart of analysis procedure.	41
3.2	Flow chart of analysis procedure [66].	41
3.3	Invariant mass distribution of (a) $\phi \rightarrow K^+K^-$ (b) $\bar{K}^{*0} \rightarrow K^-\pi^+$ and (c) $K_S^0 \rightarrow \pi\pi$ sub-decay modes for signal MC. Blue curve shows the overall fit.	45
3.4	The fit to the reconstructed D_s^+ mass for (a) $D_s^+ \rightarrow \phi\pi^+$ (b) $D_s^+ \rightarrow \bar{K}^{*0}K^+$ and (c) $D_s^+ \rightarrow K_S^0K^+$ sub-decays for Signal MC. 1D UML fit is performed, Red (green) curve used for signal (background) and the overall fit is shown by the blue color.	46

LIST OF FIGURES

3.5	Distributions of (a) optimization of the 2D cut for E_{γ_1} and E_{γ_2} (GeV) for $B^+ \rightarrow D_s^+(\rightarrow \phi\pi)\eta(\rightarrow \gamma_1\gamma_2)$ decay mode (b) FOM curve for E_γ (GeV) from $D_s^{*+} \rightarrow D_s^+\gamma$ decay mode.	48
3.6	Multiple B candidates per event for the (a) $B^+ \rightarrow D_s^+(\rightarrow \phi\pi^+)\eta(\rightarrow \gamma\gamma)$ (b) $B^+ \rightarrow D_s^+(\rightarrow \bar{K}^{*0}K^+)\eta(\rightarrow \gamma\gamma)$ and (c) $B^+ \rightarrow D_s^+(\rightarrow K_S^0K^+)\eta(\rightarrow \gamma\gamma)$ decay mode for Signal MC.	49
3.7	Distributions of ΔE for (a) $D_s^+ \rightarrow \phi\pi^+$ (b) $D_s^+ \rightarrow \bar{K}^{*0}K^+$ and (c) $D_s^+ \rightarrow K_S^0K^+$ decay modes. The upper distribution for $\eta \rightarrow \gamma\gamma$ and lower for $\eta \rightarrow \pi^-\pi^+\pi^0$. Red color histogram shows the truth matched events and blue shows the self cross feed events.	51
3.8	Distributions of ΔE for (a) $D_s^+ \rightarrow \phi\pi^+$ (b) $D_s^+ \rightarrow \bar{K}^{*0}K^+$ and (c) $D_s^+ \rightarrow K_S^0K^+$ decay modes. The upper distribution for $\eta \rightarrow \gamma\gamma$ and lower for $\eta \rightarrow \pi^-\pi^+\pi^0$	51
3.9	Distributions of ΔE for (a) $D^+ \rightarrow K^-\pi^+\pi^+$ (b) $D^+ \rightarrow K_S^0\pi^+$ decay modes. The upper distribution for $\eta \rightarrow \gamma\gamma$ and lower for $\eta \rightarrow \pi^-\pi^+\pi^0$. Red color histogram shows the truth matched events and blue shows the self cross feed events.	52
3.10	Distributions of ΔE for (a) $D_s^+ \rightarrow \phi\pi^+$ (b) $D_s^+ \rightarrow \bar{K}^{*0}K^+$ and (c) $D_s^+ \rightarrow K_S^0K^+$ decay modes. Red color histogram shows the truth matched events and blue shows the self cross feed events.	53
3.11	Distributions of ΔE for (a) $D_s^+ \rightarrow \phi\pi^+$ (b) $D_s^+ \rightarrow \bar{K}^{*0}K^+$ and (c) $D_s^+ \rightarrow K_S^0K^+$ decay modes. Red color histogram shows the truth matched events and blue shows the self cross feed events.	53

3.12 Distributions of ΔE for (a) $D^+ \rightarrow K^-\pi^+\pi^+$ (b) $D^+ \rightarrow K_S^0\pi^+$ decay modes. Red color histogram shows the truth matched events and blue shows the self cross feed events.	53
3.13 Expected background in ΔE distributions for the (a) $B^+ \rightarrow D_s^+\eta$ (left) (b) $B^+ \rightarrow D_s^{(*)+}\eta$ (middle) and (c) $B^+ \rightarrow D^+\eta$ (right) decay mode using generic MC. The upper distribution for $\eta \rightarrow \gamma\gamma$ and lower for $\eta \rightarrow \pi^-\pi^+\pi^0$	55
3.14 Expected background in ΔE distributions for the (a) $B^+ \rightarrow D_s^+K_S^0$ (left) (b) $B^+ \rightarrow D_s^{(*)+}K_S^0$ (middle) and (c) $B^+ \rightarrow D^+K_S^0$ (right) decay mode using generic MC.	55
3.15 Distribution of continuum variables (a) ksfwhso12 (b) ksfwhso02 (c) cleo cone1 (d) $ \cos\theta_T $ (e) $ \cos\theta_B $ (f) $B_{ThrustB}$ and (g) FBBDT_qrCombined.	58
3.16 Distribution of (a) Neural Network output with train and test samples (b) Purity for $B^+ \rightarrow D_s^+(\rightarrow \phi\pi^+)\eta(\rightarrow \gamma\gamma)$ decay mode.	59
3.17 Distribution of ROC curve for (a) $B^+ \rightarrow D_s^+(\rightarrow \phi\pi^+)\eta(\rightarrow \gamma\gamma)$ (b) $B^+ \rightarrow D_s^+(\rightarrow \bar{K}^{*0}K^+)\eta(\rightarrow \gamma\gamma)$ (c) $B^+ \rightarrow D_s^+(\rightarrow K_S^0K^+)\eta(\rightarrow \gamma\gamma)$ decay mode.	59
3.18 Distribution of ROC curve for (a) $B^+ \rightarrow D_s^+(\rightarrow \phi\pi^+)K_S^0$ (b) $B^+ \rightarrow D_s^+(\rightarrow \bar{K}^{*0}K^+)K_S^0$ (c) $B^+ \rightarrow D_s^+(\rightarrow K_S^0K^+)K_S^0$ decay modes.	59
3.19 Correlation matrix of signal and background for $B^+ \rightarrow D_s^+(\rightarrow \phi\pi^+)\eta$ decay mode.	61
3.20 Correlation matrix of signal and background for $B^+ \rightarrow D_s^+(\rightarrow \bar{K}^{*0}K^+)\eta$ decay mode.	61

3.21	Correlation matrix of signal and background for $B^+ \rightarrow D_s^+(\rightarrow K_S^0 K^+) \eta$ decay mode.	61
3.22	NN Versus ΔE (a) Signal (b) Generic MC samples for $B^+ \rightarrow D_s^+ \eta$ decay mode.	63
3.23	NN Versus M_{bc} (a) Signal (b) Generic MC samples for $B^+ \rightarrow D_s^+ \eta$ decay mode.	63
3.24	NN Versus M_{D_s} (a) Signal (b) Generic MC samples for $B^+ \rightarrow D_s^+ \eta$ decay mode.	63
3.25	Distribution of FOM curve for (a) $B^+ \rightarrow D_s^+ \eta(\rightarrow \gamma\gamma)$ (b) $B^+ \rightarrow D_s^{(*)+} \eta(\rightarrow \gamma\gamma)$ (c) $B^+ \rightarrow D^+ \eta(\rightarrow \gamma\gamma)$ decay modes.	64
3.26	Distribution of FOM curve for (a) $B^+ \rightarrow D_s^+ K_S^0$ (b) $B^+ \rightarrow D_s^{(*)+} K_S^0$ (c) $B^+ \rightarrow D^+ K_S^0$ decay modes.	64
3.27	Distribution of ΔE (a) Without NN cut (b) $NN > 0.8$ and (c) $NN > 0.92$ for $B^+ \rightarrow D_s^+ \eta(\rightarrow \gamma\gamma)$ decay mode with $M_{bc} > 5.27 \text{ GeV}/c^2$	65
3.28	Expected background in ΔE distributions for the (a) $B^+ \rightarrow D_s^+ \eta(\rightarrow \gamma\gamma)$ (left) (b) $B^+ \rightarrow D_s^{(*)+} \eta(\rightarrow \gamma\gamma)$ (middle) and (c) $B^+ \rightarrow D^+ \eta(\rightarrow \gamma\gamma)$ (right) decay modes using rare MC. Red color histogram used for charged and blue color histogram for mixed sample.	66
3.29	Expected background in ΔE distributions for the (a) $B^+ \rightarrow D_s^+ K_S^0$ (left) (b) $B^+ \rightarrow D_s^{(*)+} K_S^0$ (middle) and (c) $B^+ \rightarrow D^+ K_S^0$ (right) decay modes using rare MC. Red color histogram used for charged and blue color histogram for mixed sample.	66

<p>3.30 1D UML fit of ΔE for the signal MC sample of $B^+ \rightarrow D_s^+ \eta(\rightarrow \gamma\gamma)$ (a) $D_s^+ \rightarrow \phi\pi^+$ (left) (b) $D_s^+ \rightarrow \bar{K}^{*0}K^+$ (middle) and (c) $D_s^+ \rightarrow K_S^0K^+$ (right) decay modes. Here, a2a = area of Gaussian 2/ area of Gaussian 1, slr = σ_L/σ_1, srr = σ_R/σ_1. Red (green) curve used for a sum of Gaussian (1st order polynomial) and blue curve show the overall fit.</p>	67
<p>3.31 1D UML fit of ΔE for the signal MC sample of $B^+ \rightarrow D_s^+ \eta(\rightarrow \pi^-\pi^+\pi^0)$ (a) $D_s^+ \rightarrow \phi\pi^+$ (left) (b) $D_s^+ \rightarrow \bar{K}^{*0}K^+$ (middle) and (c) $D_s^+ \rightarrow K_S^0K^+$ (right) decay modes.</p>	67
<p>3.32 1D UML fit of ΔE for the signal MC sample of $B^+ \rightarrow D_s^{*+} \eta(\rightarrow \gamma\gamma)$ (a) $D_s^+ \rightarrow \phi\pi^+$ (left) (b) $D_s^+ \rightarrow \bar{K}^{*0}K^+$ (middle) and (c) $D_s^+ \rightarrow K_S^0K^+$ (right) decay modes.</p>	67
<p>3.33 1D UML fit of ΔE for the signal MC sample of $B^+ \rightarrow D_s^{*+} \eta(\rightarrow \pi^-\pi^+\pi^0)$ (a) $D_s^+ \rightarrow \phi\pi^+$ (b) $D_s^+ \rightarrow \bar{K}^{*0}K^+$ and (c) $D_s^+ \rightarrow K_S^0K^+$ decay modes. Red (green) color used for a sum of Gaussian (1st order polynomial) PDF and blue curve shows the overall fit.</p>	68
<p>3.34 1D UML fit of ΔE for the signal MC sample of $B^+ \rightarrow D_s^+ K_S^0$ (a) $D_s^+ \rightarrow \phi\pi^+$ (b) $D_s^+ \rightarrow \bar{K}^{*0}K^+$ and (c) $D_s^+ \rightarrow K_S^0K^+$ decay modes. Here, a2a = area of Gaussian 2/ area of Gaussian 1, s2s1 = σ_2/σ_1. Red (green) color used for a sum of Gaussian (2nd order polynomial) PDF and blue curve shows the overall fit.</p>	68

- 3.35 1D UML of ΔE for the signal MC sample of $B^+ \rightarrow D_s^{(*)+} K_S^0$
(a) $D_s^+ \rightarrow \phi\pi^+$ (b) $D_s^+ \rightarrow \bar{K}^{*0}K^+$ and (c) $D_s^+ \rightarrow K_S^0 K^+$ decay
modes. Red (green) color used for a sum of Gaussian (2^{nd} order
polynomial) PDF and blue curve shows the overall fit. 68
- 3.36 1D UML fit of ΔE for the signal MC sample of $B^+ \rightarrow D^+ K_S^0$ (a)
 $D^+ \rightarrow K^- \pi^+ \pi^+$ (b) $D^+ \rightarrow K_S^0 \pi^+$ decay modes. Here, a2a = area
of Gaussian 2/ area of Gaussian 1, s2s1 = σ_2/σ_1 . Red (green) color
used for a sum of Gaussian (2^{nd} order polynomial) PDF and blue
curve shows the overall fit. 69
- 3.37 1D UML fit of ΔE for the signal MC sample of $B^+ \rightarrow D^+ \eta$ (a)
 $D^+ \rightarrow K^- \pi^+ \pi^+$ (b) $D^+ \rightarrow K_S^0 \pi^+$ decay modes. Here, a2a = area
of Gaussian 2/ area of Gaussian 1, slr = σ_L/σ_1 , srr = σ_R/σ_1 . Red
(green) color used for a sum of Gaussian (2^{nd} order polynomial)
PDF and blue curve shows the overall fit. 69
- 3.38 1D UML fit of ΔE for the signal MC sample of $B^+ \rightarrow D^+ \eta(\rightarrow$
 $\pi^- \pi^+ \pi^0)$ (a) $D^+ \rightarrow K^- \pi^+ \pi^+$ (b) $D^+ \rightarrow K_S^0 \pi^+$ decay modes. Here,
a2a = area of Gaussian 2/ area of Gaussian 1, slr = σ_L/σ_1 , srr =
 σ_R/σ_1 . Red (green) color used for a sum of Gaussian (2^{nd} order
polynomial) PDF and blue curve shows the overall fit. 69
- 3.39 Distributions of M_{D^0} for $\bar{B}^0 \rightarrow D^0 \eta(\rightarrow \gamma\gamma)$, (a) $D^0 \rightarrow K^- \pi^+$, (b)
 $D^0 \rightarrow K^- \pi^+ \pi^+ \pi^-$, (c) $D^0 \rightarrow K_S^0 \pi^+ \pi^-$ and (d) $D^0 \rightarrow K^- \pi^+ \pi^0$
decay mode for Signal MC. Red color histogram shows the truth
matched events and blue shows the self cross feed events. 71

3.40	Distributions of ΔE for $\bar{B}^0 \rightarrow D^0\eta(\rightarrow \gamma\gamma)$, (a) $D^0 \rightarrow K^-\pi^+$, (b) $D^0 \rightarrow K^-\pi^+\pi^+\pi^-$, (c) $D^0 \rightarrow K_S^0\pi^+\pi^-$ and (d) $D^0 \rightarrow K^-\pi^+\pi^0$ decay mode for Signal MC. Red color histogram shows the truth matched events and blue shows the self cross feed events.	71
3.41	Distributions of M_{D^0} for $\bar{B}^0 \rightarrow D^0K_S^0$, (a) $D^0 \rightarrow K^-\pi^+$, (b) $D^0 \rightarrow K^-\pi^+\pi^+\pi^-$, (c) $D^0 \rightarrow K_S^0\pi^+\pi^-$ and (d) $D^0 \rightarrow K^-\pi^+\pi^0$ decay mode for Signal MC. Red color histogram shows the truth matched events and blue shows the self cross feed events.	71
3.42	Distributions of ΔE for $\bar{B}^0 \rightarrow D^0K_S^0$, (a) $D^0 \rightarrow K^-\pi^+$, (b) $D^0 \rightarrow K^-\pi^+\pi^+\pi^-$, (c) $D^0 \rightarrow K_S^0\pi^+\pi^-$ and (d) $D^0 \rightarrow K^-\pi^+\pi^0$ decay mode for Signal MC. Red color histogram shows the truth matched events and blue shows the self cross feed events.	72
3.43	Distributions of ΔE for (a) $\bar{B}^0 \rightarrow D^0\eta(\rightarrow \gamma\gamma)$ (b) $\bar{B}^0 \rightarrow D^0K_S^0$ decay mode without NN cut and (c) $\bar{B}^0 \rightarrow D^0\eta(\rightarrow \gamma\gamma)$ (d) $\bar{B}^0 \rightarrow D^0K_S^0$ decay mode with NN cut using generic MC samples.	73

- 3.44 The 1D UML fitted distributions of ΔE variable for $\bar{B}^0 \rightarrow D^0 \eta(\rightarrow \gamma\gamma)$, (a) $D^0 \rightarrow K^- \pi^+$ (top left), (b) $D^0 \rightarrow K^- \pi^+ \pi^+ \pi^-$ (top middle left), (c) $D^0 \rightarrow K_S^0 \pi^+ \pi^-$ (top middle right) and (d) $D^0 \rightarrow K^- \pi^+ \pi^0$ (top right) decay mode with signal MC sample. Distributions of ΔE for $\bar{B}^0 \rightarrow D^0 \eta(\rightarrow \pi^- \pi^+ \pi^0)$, (e) $D^0 \rightarrow K^- \pi^+$ (lower left), (f) $D^0 \rightarrow K^- \pi^+ \pi^+ \pi^-$ (lower middle left), (g) $D^0 \rightarrow K_S^0 \pi^+ \pi^-$ (lower middle right) and (h) $D^0 \rightarrow K^- \pi^+ \pi^0$ (lower right) decay mode with signal MC sample. Here, a2a = fraction of area of Gaussian 2 and area of Gaussian 1, slr = fraction of σ_L and σ_1 and srr = fraction of σ_R and σ_1 . Red (green) color used for a sum of Gaussian (first order polynomial, 2nd order polynomial($\eta \rightarrow \pi\pi\pi$)) PDF and blue curve shows the overall fit. 75
- 3.45 The 1D UML fitted distributions of ΔE variable for $\bar{B}^0 \rightarrow D^0 K_S^0$, (a) $D^0 \rightarrow K^- \pi^+$, (b) $D^0 \rightarrow K^- \pi^+ \pi^+ \pi^-$, (c) $D^0 \rightarrow K_S^0 \pi^+ \pi^-$ and (d) $D^0 \rightarrow K^- \pi^+ \pi^0$ decay mode with signal MC sample. Here, a2a = fraction of area of Gaussian 2 and area of Gaussian 1, s2s1 = fraction of σ_2 and σ_1 . Red (green) color used for a sum of Gaussian (1st order polynomial) PDF and blue curve shows the overall fit. 75
- 3.46 The 1D UML fitted distributions of ΔE for (a) $\bar{B}^0 \rightarrow D^0 \eta(\rightarrow \gamma\gamma)$, (b) $\bar{B}^0 \rightarrow D^0 \eta(\rightarrow \pi^- \pi^+ \pi^0)$ (excluded $D^0 \rightarrow K \pi \pi^0$), (c) $\bar{B}^0 \rightarrow D^0 K_S^0$ decay mode with signal MC sample (combine D^0 sub decays). Here, a2a = area of Gaussian 2/ area of Gaussian 1, slr = σ_L/σ_1 , srr = σ_R/σ_1 and s2s1 = σ_2/σ_1 76

- 3.47 The fitted distributions of ΔE for $\bar{B}^0 \rightarrow D^0\eta(\rightarrow \gamma\gamma)$ decay mode, (a) continuum events (PDF: 1st order poly.) (b) continuum and $B\bar{B}$ (exclude $D^{*0}\eta$ and B^+ from 3 final states particles) (PDF: 1st order polynomial) (c) continuum and $B\bar{B}$ events (PDF: exponential and 1st order polynomial) with generic MC sample (combine D^0 sub decays). Distributions of ΔE for $\bar{B}^0 \rightarrow D^0\eta(\rightarrow \pi^-\pi^+\pi^0)$ decay mode (excluded $D^0 \rightarrow K\pi\pi^0$), (d) continuum events (PDF: 1st order poly.) (e) continuum and $B\bar{B}$ (exclude $D^{*0}\eta$ and B^+ from 3 final states particles) (PDF: 1st order polynomial)(f) $B\bar{B}$ peaking background events (PDF: exponential) with generic MC sample (combine D^0 sub decays). Red (green) color curve use for 1st order polynomial (exponential) PDF and blue curve shows the overall fit. 78
- 3.48 Distributions of ΔE for $\bar{B}^0 \rightarrow D^0K_S^0$ decay mode, continuum events (PDF: 1st order poly.) (b) continuum and $B\bar{B}$ (exclude $D^{*0}K_S^0$ and D^0K^{*+}) (PDF: 1st order polynomial) (c) $B^0 \rightarrow D^{*0}K_S^0$ and $B^+ \rightarrow D^0K^{*+}$ events (PDF: sum of two Gaussian with common mean) with generic MC sample (combine D^0 sub decays). Blue curve shows the overall fit. 78

<p>3.49 The fitted distributions of ΔE for $\bar{B}^0 \rightarrow D^0\eta(\rightarrow \gamma\gamma)$ decay mode, (a) stream 1 (b) stream 2 (c) stream 3 with generic MC sample (combine D^0 sub decays). Distributions of ΔE for $\bar{B}^0 \rightarrow D^0\eta(\pi^-\pi^+\pi^0)$ (exclude $D^0 \rightarrow K\pi\pi^0$) decay mode, (d) stream 1 (e) stream 2 (f) stream 3 with generic MC sample (combine D^0 sub decays). Red (green, magenta) color curve use for a sum of Gaussian(1^{st} order polynomial, peaking bkg.) PDF and blue curve shows the overall fit.</p>	79
<p>3.50 The fitted distributions of ΔE for $\bar{B}^0 \rightarrow D^0K_S^0$ decay mode, (a) stream 1 (b) stream 2 (c) stream 3 with generic MC sample (combine D^0 sub decays). Red (green, magenta) color curve use for a sum of Gaussian(1^{st} order polynomial, peaking bkg.) PDF and blue curve shows the overall fit.</p>	79
<p>3.51 A typical example for (a) $\bar{B}^0 \rightarrow D^0\eta(\rightarrow \gamma\gamma)$, (b) $\bar{B}^0 \rightarrow D^0\eta(\rightarrow \pi^-\pi^+\pi^0)$, (c) $\bar{B}^0 \rightarrow D^0K_S^0$ decay mode. Red color shows signal, green (magenta) shows for background (peaking background) and blue shows the overall fit.</p>	80
<p>3.52 (a) Pull distribution (b) yield distribution and (c) error distribution for $\bar{B}^0 \rightarrow D^0\eta$ decay mode. The upper distribution for $\eta \rightarrow \gamma\gamma$ and lower for $\eta \rightarrow \pi^-\pi^+\pi^0$ decay mode.</p>	81
<p>3.53 (a) Pull distribution (b) yield distribution and (c) error distribution for $\bar{B}^0 \rightarrow D^0K_S^0$ decay mode.</p>	81

3.54 Result of linearity test for $\bar{B}^0 \rightarrow D^0\eta$ decay mode: (a) reconstructed yield versus input signal yield (b) pull error versus input signal yield. The upper distribution for $\eta \rightarrow \gamma\gamma$ and lower for $\eta \rightarrow \pi^-\pi^+\pi^0$ decay mode.	82
3.55 Result of linearity test for $\bar{B}^0 \rightarrow D^0K_S^0$ decay mode: (a) reconstructed yield versus input signal yield (b) pull error versus input signal yield.	82
3.56 The fitted distribution of ΔE for (a) $B^+ \rightarrow D_s^+\eta(\rightarrow \gamma\gamma)$ (b) $B^+ \rightarrow D_s^{(*)+}(\rightarrow D_s^+\gamma)\eta(\rightarrow \gamma\gamma)$ (c) $B^+ \rightarrow D^+\eta(\rightarrow \gamma\gamma)$ (d) $B^+ \rightarrow D_s^+\eta(\rightarrow \pi\pi\pi)$ (e) $B^+ \rightarrow D_s^{(*)+}(\rightarrow D_s^+\gamma)\eta(\rightarrow \pi\pi\pi)$ (f) $B^+ \rightarrow D^+\eta(\rightarrow \pi\pi\pi)$ (g) $B^+ \rightarrow D_s^+K_S^0$ (h) $B^+ \rightarrow D_s^{(*)+}(\rightarrow D_s^+\gamma)K_S^0$ (i) $B^+ \rightarrow D^+K_S^0$ decay modes with signal MC sample (combine D_s^+ , D^+ sub decays). Red (green) color curve use for a sum of Gaussian (2^{nd} order polynomial) PDF and blue curve shows the overall fit. .	84
3.57 Distributions of ΔE for (a) $B^+ \rightarrow D_s^+\eta(\rightarrow \gamma\gamma)$ (b) $B^+ \rightarrow D_s^{(*)+}(\rightarrow D_s^+\gamma)\eta(\rightarrow \gamma\gamma)$ (c) $B^+ \rightarrow D^+\eta(\rightarrow \gamma\gamma)$ (d) peaking in $B^+ \rightarrow D^+\eta(\rightarrow \gamma\gamma)$ (e) $B^+ \rightarrow D_s^+\eta(\rightarrow \pi\pi\pi)$ (f) $B^+ \rightarrow D_s^{(*)+}(\rightarrow D_s^+\gamma)\eta(\rightarrow \pi\pi\pi)$ (g) $B^+ \rightarrow D^+\eta(\rightarrow \pi\pi\pi)$ (h) peaking in $B^+ \rightarrow D^+\eta(\rightarrow \pi\pi\pi)$ (i) $B^+ \rightarrow D_s^+K_S^0$ (j) $B^+ \rightarrow D_s^{(*)+}(\rightarrow D_s^+\gamma)K_S^0$ (k) $B^+ \rightarrow D^+K_S^0$ (l) peaking in $B^+ \rightarrow D^+K_S^0$ decay modes with generic MC sample (combine D_s^+ , D^+ sub decays). Red color shows 1^{st} order polynomial.	85
3.58 Pull distribution for (a) $B^+ \rightarrow D_s^+K_S^0$ (b) $B^+ \rightarrow D_s^{(*)+}K_S^0$ (c) $B^+ \rightarrow D^+K_S^0$ decay mode.	86

LIST OF FIGURES

3.59	Pull distribution for (a) $B^+ \rightarrow D_s^+ \eta$ (b) $B^+ \rightarrow D_s^{(*)+} \eta$ (c) $B^+ \rightarrow D^+ \eta$ decay mode. The upper distribution for $\eta \rightarrow \gamma\gamma$ and lower for $\eta \rightarrow \pi^- \pi^+ \pi^0$ decay modes.	86
3.60	Yield distribution for (a) $B^+ \rightarrow D_s^+ K_S^0$ (b) $B^+ \rightarrow D_s^{(*)+} K_S^0$ (c) $B^+ \rightarrow D^+ K_S^0$ decay mode.	87
3.61	Yield distribution for (a) $B^+ \rightarrow D_s^+ \eta$ (b) $B^+ \rightarrow D_s^{(*)+} \eta$ (c) $B^+ \rightarrow D^+ \eta$ decay mode. The upper distribution for $\eta \rightarrow \gamma\gamma$ and lower for $\eta \rightarrow \pi^- \pi^+ \pi^0$ decay modes.	87
3.62	Reconstructed vs generated yield distribution for (a) $B^+ \rightarrow D_s^+ K_S^0$ (b) $B^+ \rightarrow D_s^{(*)+} K_S^0$ (c) $B^+ \rightarrow D^+ K_S^0$ decay mode.	88
3.63	Reconstructed vs generated yield distribution for (a) $B^+ \rightarrow D_s^+ \eta$ (b) $B^+ \rightarrow D_s^{(*)+} \eta$ (c) $B^+ \rightarrow D^+ \eta$ decay mode. The upper distribution for $\eta \rightarrow \gamma\gamma$ and lower for $\eta \rightarrow \pi^- \pi^+ \pi^0$ decay modes.	88
3.64	Pull sigma vs generated yield distribution for (a) $B^+ \rightarrow D_s^+ K_S^0$ (b) $B^+ \rightarrow D_s^{(*)+} K_S^0$ (c) $B^+ \rightarrow D^+ K_S^0$ decay mode.	89
3.65	Pull sigma vs generated yield distribution for (a) $B^+ \rightarrow D_s^+ \eta$ (b) $B^+ \rightarrow D_s^{(*)+} \eta$ (c) $B^+ \rightarrow D^+ \eta$ decay mode. The upper distribution for $\eta \rightarrow \gamma\gamma$ and lower for $\eta \rightarrow \pi^- \pi^+ \pi^0$ decay modes.	89
3.66	ΔE distributions for the (a) $B^+ \rightarrow D_s^+ \eta$ (b) $B^+ \rightarrow D_s^{(*)+} \eta$ and (c) $B^+ \rightarrow D^+ \eta$ decay mode using data (blue) and generic (red) MC. The upper distribution for $\eta \rightarrow \gamma\gamma$ and lower for $\eta \rightarrow \pi^- \pi^+ \pi^0$ decay modes.	90

3.67 ΔE distributions for the (a) $B^+ \rightarrow D_s^+ K_S^0$ (b) $B^+ \rightarrow D_s^{(*)+} K_S^0$ and (c) $B^+ \rightarrow D^+ K_S^0$ decay mode using data (blue) and generic (red) MC.	90
3.68 M_{bc} distributions for the (a) $B^+ \rightarrow D_s^+ \eta$ (b) $B^+ \rightarrow D_s^{(*)+} \eta$ and (c) $B^+ \rightarrow D^+ \eta$ decay mode using data (blue) and generic (red) MC. The upper distribution for $\eta \rightarrow \gamma\gamma$ and lower for $\eta \rightarrow \pi^- \pi^+ \pi^0$ decay modes.	91
3.69 M_{bc} distributions for the (a) $B^+ \rightarrow D_s^+ K_S^0$ (b) $B^+ \rightarrow D_s^{(*)+} K_S^0$ and (c) $B^+ \rightarrow D^+ K_S^0$ decay mode using data (blue) and generic (red) MC.	91
3.70 M_{D_s} (M_D) distributions for the (a) $B^+ \rightarrow D_s^+ \eta$ (b) $B^+ \rightarrow D_s^{(*)+} \eta$ and (c) $B^+ \rightarrow D^+ \eta$ decay mode using data (blue) and generic (red) MC. The upper distribution for $\eta \rightarrow \gamma\gamma$ and lower for $\eta \rightarrow \pi^- \pi^+ \pi^0$ decay modes.	92
3.71 M_{D_s} (M_D) distributions for the (a) $B^+ \rightarrow D_s^+ K_S^0$ (left) (b) $B^+ \rightarrow D_s^{(*)+} K_S^0$ (middle) and (c) $B^+ \rightarrow D^+ K_S^0$ (right) decay mode using data (blue) and generic (red) MC.	92
4.1 Data/MC comparison of ΔE for (a) $\bar{B}^0 \rightarrow D^0 \eta (\rightarrow \gamma\gamma)$, (b) $\bar{B}^0 \rightarrow D^0 \eta (\rightarrow \pi^- \pi^+ \pi^0)$, (c) $\bar{B}^0 \rightarrow D^0 K_S^0$ (right) decay modes. Red color shows generic (data) MC.	96

4.2	The fitted distribution of ΔE for (a) $\bar{B}^0 \rightarrow D^0\eta(\rightarrow \gamma\gamma)$, (b) $\bar{B}^0 \rightarrow D^0\eta(\rightarrow \pi^-\pi^+\pi^0)$, (c) $\bar{B}^0 \rightarrow D^0K_S^0$ decay mode. Red curve shows the signal, green curve for: $q\bar{q} + B\bar{B}$ bkg (exclude peaking background), magenta shows the: peaking background and blue curve explain the overall fit.	97
4.3	Fitted Distributions of ΔE for $\bar{B}^0 \rightarrow D^0\eta(\rightarrow \gamma\gamma)$, (a) $D^0 \rightarrow K^-\pi^+$, (b) $D^0 \rightarrow K^-\pi^+\pi^+\pi^-$, (c) $D^0 \rightarrow K_S^0\pi^+\pi^-$ and (d) $D^0 \rightarrow K^-\pi^+\pi^0$ decay mode with data sample. Here, only the mean and sigma of core Gaussian floated and all other PDF parameters fixed from the separate fit of the MC samples. Red curve shows the sum of a Gaussian, green (magenta) shows the combinatorial (peaking) background and blue curve shows the overall fit.	99
4.4	Distributions of ΔE for $\bar{B}^0 \rightarrow D^0\eta(\rightarrow \pi\pi\pi^0)$, (a) $D^0 \rightarrow K^-\pi^+$, (b) $D^0 \rightarrow K^-\pi^+\pi^+\pi^-$, (c) $D^0 \rightarrow K_S^0\pi^+\pi^-$ and (d) $D^0 \rightarrow K^-\pi^+\pi^0$ decay mode with data sample. Here, only the mean and sigma of core a Gaussian floated and all other PDF parameters are fixed from the separate fit of the MC samples. Red curve shows the sum of a Gaussian, green (magenta) shows the combinatorial (peaking) background and blue curve shows the overall fit.	99

4.5	Distributions of the ΔE variable for $\bar{B}^0 \rightarrow D^0 K_S^0$, (a) $D^0 \rightarrow K^- \pi^+$, (b) $D^0 \rightarrow K^- \pi^+ \pi^+ \pi^-$, (c) $D^0 \rightarrow K_S^0 \pi^+ \pi^-$ and (d) $D^0 \rightarrow K^- \pi^+ \pi^0$ decay mode with data sample. Here, only the mean and sigma of core Gaussian floated and all other PDF parameters are fixed from the separate fit of MC samples. Red curve shows the sum of a Gaussian, green (magenta) shows the combinatorial (peaking) background and blue curve shows the overall fit.	100
4.6	Fits of ΔE distributions in data for decay modes (a) $B^+ \rightarrow D_s^+ \eta(\gamma\gamma)$, (b) $B^+ \rightarrow D_s^+ \eta(\pi^- \pi^+ \pi^0)$, (c) $B^+ \rightarrow D_s^{*+} \eta(\gamma\gamma)$, (d) $B^+ \rightarrow D_s^{*+} \eta(\pi^- \pi^+ \pi^0)$, (e) $B^+ \rightarrow D^+ \eta(\gamma\gamma)$, (f) $B^+ \rightarrow D^+ \eta(\pi^- \pi^+ \pi^0)$, (g) $B^+ \rightarrow D_s^+ K_S^0$, (h) $B^+ \rightarrow D_s^{*+} K_S^0$, (i) $B^+ \rightarrow D^+ K_S^0$. The data points with error bars show the measurement result. The different curves show the various PDF components: the solid (blue) line: total PDF, the dotted (red) line: signal PDF, the dotted (magenta) line: peak-ing background on the lower side of ΔE and the dotted (green) line:combinatorial background mainly from $q\bar{q}$ events.	110
4.7	Yield obtained at 90% CL for (a) $B^+ \rightarrow D_s^+ \eta$, (b) $B^+ \rightarrow D_s^{*+} \eta$, (c) $B^+ \rightarrow D^+ \eta$, (d) $B^+ \rightarrow D_s^+ K_S^0$, (e) $B^+ \rightarrow D_s^{*+} K_S^0$, (f) $B^+ \rightarrow D^+ K_S^0$. 111	111
5.1	SVD ladders.	115
5.2	Geometry of DSSD sensor.	116
5.3	Cluster charge for layer 3 (sensor 2): U side (left) and V side (right) with test beam data.	117

LIST OF FIGURES

5.4	Schematic layout of a detector making use of capacitive charge division (left) [80]; Measurement of C_{int} for layer 3 (sensor 2): U side (center) and V side (right).	118
5.5	S/N ratio (left), Signal Hit time (right) with first data (Phase-II).	119
5.6	(a) Microscope attached with camera (left) (b) Ladder container box (right).	120
5.7	(a) Backward side wall (b) Forward side wall (c) Back side (d) Front side (e) sliding the lid towards backward direction (f) removing the sliding part of the container of container.	121
5.8	(a) APV on FWD hybrid (b) APV on O-Z (c) APV on O-Z (d) n side bias on O-Z (e) APV on FWD hybrid (f) JAE connection to the FWD hybrid (g) APV chip numbering on the origami (h) standoff numbering.	122
5.9	L4 ladder.	123
5.10	Full SVD mounted to the final structure.	123
5.11	Group photo after successfully mounting the ladders.	123
6.1	Distribution of (a) ΔM (left) and (b) $M(K_S^0 K^+)$ (right) for D_s^+ candidates reconstructed from $D_s^{*\pm} \rightarrow D_s^+ \gamma$ and $D_s^+ \rightarrow K_S^0 K^+$ decay mode.	128
6.2	Distribution of (a) ΔM (left) and (b) $M(K^+ K^- \pi^+)$ (right) for D_s^+ candidates reconstructed from $D_s^{*+} \rightarrow D_s^+ \gamma$ and $D_s^+ \rightarrow K^+ K^- \pi^+$ decay mode.	128

6.3	Distribution of (a) ΔM and (b) $M(\phi\pi^+)$ for D_s^+ candidates reconstructed from $D_s^{*+} \rightarrow D_s^+\gamma$ and $D_s^+ \rightarrow \phi\pi^+$ decay mode.	129
6.4	Distribution of (a) ΔM and (b) $M(\bar{K}^{*0}K^+)$ for D_s^+ candidates reconstructed from $D_s^{*+} \rightarrow D_s^+\gamma$ and $D_s^+ \rightarrow \bar{K}^{*0}K^+$ decay mode.	129
6.5	Distribution of (a) ΔM and (b) $M(K_S^0K^+)$ for D_s^+ candidates reconstructed from $D_s^{*\pm} \rightarrow D_s^+\pi^0$ and $D_s^+ \rightarrow K_S^0K^+$ decay mode.	130
6.6	Distribution of (a) ΔM and (b) $M(K^+K^-\pi^+)$ for D_s^+ candidates reconstructed from $D_s^{*+} \rightarrow D_s^+\pi^0$ and $D_s^+ \rightarrow K^+K^-\pi^+$ decay mode.	130
6.7	Distribution of (a) ΔM and (b) $M(\phi\pi^+)$ for D_s^+ candidates reconstructed from $D_s^{*+} \rightarrow D_s^+\pi^0$ and $D_s^+ \rightarrow \phi\pi^+$ decay mode.	131
6.8	Distribution of (a) ΔM and (b) $M(\bar{K}^{*0}K^+)$ for D_s^+ candidates reconstructed from $D_s^{*+} \rightarrow D_s^+\pi^0$ and $D_s^+ \rightarrow \bar{K}^{*0}K^+$ decay mode.	131
6.9	Distribution of (a) ΔM and (b) $M(K^-\pi^+)$ for D^0 candidates reconstructed from $D^{*+} \rightarrow D^0\pi^+$ and $D^0 \rightarrow K^-\pi^+$ decay mode. . .	132
6.10	Distribution of (a) ΔM and (b) $M(K^+K^-)$ for D^0 candidates reconstructed from $D^{*+} \rightarrow D^0\pi^+$ and $D^0 \rightarrow K^+K^-$ decay mode. The peaking around $1.96 \text{ GeV}/c^2$ in M_{D^0} coming from $D^0 \rightarrow K^-\pi^+$ decay mode.	132
6.11	Distribution of (a) ΔM and (b) $M(\pi^+\pi^-)$ for D^0 candidates reconstructed from $D^{*+} \rightarrow D^0\pi^+$ and $D^0 \rightarrow \pi^+\pi^-$ decay mode. The peaking around $1.78 \text{ GeV}/c^2$ in M_{D^0} coming from $D^0 \rightarrow K^-\pi^+$ decay mode.	133

6.12	Distribution of $M(K_S^0 K^+)$ (a) without fit (b) fitted for D_s^+ candidates reconstructed from $D_s^+ \rightarrow K_S^0 K^+$ decay mode.	134
6.13	Distribution of $M(K^+ K^- \pi^+)$ (a) without fit (b) fitted for D_s^+ candidates reconstructed from $D_s^+ \rightarrow K^+ K^- \pi^+$ decay mode.	134
6.14	Distribution of $M(\phi \pi^+)$ (a) without fit (b) fitted for D_s^+ candidates reconstructed from $D_s^+ \rightarrow \phi \pi^+$ decay mode.	134
6.15	Distribution of $M(\bar{K}^{*0} K^+)$ (a) without fit (b) fitted for D_s^+ candidates reconstructed from $D_s^+ \rightarrow \bar{K}^{*0} K^+$ decay mode.	135
6.16	Feynman diagram for $B^- \rightarrow D^0 K^-$ (left) and $B^- \rightarrow \bar{D}^0 K^-$ (right) [83].	136
6.17	The distribution shows the expected uncertainty ($\langle \sigma_{\phi_3} \rangle$) versus luminosity on ϕ_3 [91]. The expected uncertainty on the measurement of ϕ_3 at integrated luminosity of 50 ab^{-1} is 3° . It may also improve by adding more modes, such as $B^\pm \rightarrow D^0(K_S^0 K^+ K^-) K^\pm$	137
6.18	Invariant mass of K_S^0 with MC (left) and data (right).	137
6.19	Invariant mass (left) and ΔM (right) for D^* tagged mode $D^0 \rightarrow K_S^0 \pi^+ \pi^-$ shown with Phase II data.	138
6.20	ΔM (left) and M_D (right) distribution in Phase II data for $D^0 \rightarrow K^- \pi^+$ final state.	139
6.21	ΔE (left) and M_{bc} (right) distribution from MC simulation.	139

List of Tables

1.1	Results from previous and obtained measurements of branching fraction (B.F.).	13
2.1	Data collected at various Υ resonances by the Belle experiment. .	17
2.2	Geometrical parameters of ECL.	29
2.3	Parameters of KEKB and SuperKEKB accelerator.	34
2.4	Sub-detector which measures each particle property.	36
3.1	Selection Criteria along with its relative (absolute) efficiency. . . .	48
3.2	BCS and reconstructed efficiency for the decay mode of interest. .	54
3.3	Signal efficiency and background rejection from ROC curve for $B^+ \rightarrow D_s^+ \eta$, $B^+ \rightarrow D_s^+ K_S^0$ and $B^+ \rightarrow D^+ K_S^0$ decay modes.	60
3.4	Number of continuum events before and after applied NN cut for all signal decay modes with five streams of generic MC samples. .	65
3.5	Signal efficiency for the control modes.	76

LIST OF TABLES

3.6	Comparison of the observed signal and TM (truth-matched) events for $\bar{B}^0 \rightarrow D^0 h$ ($h = \eta, K_S^0$) decay mode.	77
4.1	Corrected efficiency (%) for the control modes from the signal MC samples.	98
4.2	Signal yield, extracted branching fraction and previous measured branching fraction of the control modes. We observed discrepancy between measured and the previous measured branching fraction by Belle [31]. It might be due to the fluctuation or some systematics bias.	98
4.3	Branching fraction measurement of individual D^0 sub decay modes from the yield of ΔE distribution for control mode.	100
4.4	Systematic uncertainty due to kaon identification.	101
4.5	Systematics uncertainty due to pion identification.	102
4.6	Fit bias estimation for the decay modes from the study of ToyMC.	103
4.7	Summary of systematic uncertainties.	104
4.8	Compared the measured B.F with the previously measured B.F given by Belle and BABAR.	105
4.9	Systematics uncertainty due to Kaon identification.	107
4.10	Systematics uncertainty due to pion identification.	108
4.11	The summary of systematic uncertainties for the signal modes.	109
4.12	Signal yield, branching fraction (\mathcal{B}) @ 90% CL and signal significance for signal decay modes.	111

LIST OF TABLES

4.13	The upper limit at 90% C.L. for extraction the signal yield and branching fraction (\mathcal{B}) of signal and control decay modes.	112
5.1	Basic parameters of different sensors.	116
6.1	Summary of the available measurement of the branching fraction.	126
6.2	Summary of the mass and Lifetime/width of non final states particles.	127
6.3	Summary of selection criteria.	127
6.4	Comparison of ΔM between data and PDG live.	135
6.5	Previous measurement results of ϕ_3	136
7.1	Summary of the fitted results.	143
7.2	Comparison of ΔM between data and PDG live.	145

1

Introduction



Based on the most of probable and accepted results, our universe originated from a singularity around 13.7 billion years ago. Before the beginning of the universe, there was absolutely nothing but the universe's object is varying from the microscopic level, such as leptons and quarks, to the macroscopic level, such as galaxies. The basic building blocks of universe objects are the same as elementary particles. In Particle Physics, we deal with these elementary particles and their interactions. Until about 1932, fundamental constituents of matter were regarded as electron, proton, and neutron. Most of the matter around us is made up of fundamental particles such as leptons and quarks.

This chapter describes the elementary particles' Standard Model (SM) and the interaction of the particles' is explained in Sec. 1.1. The symmetries, conservation law, and their violation is defined in Sec. 1.1.1. We also explain Cabibbo-Kobayashi-Maskawa (CKM) matrix, which is the only source of CP violation in the quark sector in Sec. 1.2. Finally, we conclude the motivation behind this thesis work in Sec. 1.3.

1.1 Introduction

The SM gives information about the elementary particles and their interactions in nature. The SM describes all matter are consisting of fundamental, structureless units of spin $\frac{1}{2}$ particles (leptons and quarks) and their interactions via the exchange of bosons. The leptons and quarks come in three families (plus

corresponding anti-particles) as listed below:

$$\text{quarks} \quad \begin{pmatrix} u \\ d \end{pmatrix} \begin{pmatrix} c \\ s \end{pmatrix} \begin{pmatrix} t \\ b \end{pmatrix} \quad (1.1.1)$$

$$\text{leptons} \quad \begin{pmatrix} e \\ \nu_e \end{pmatrix} \begin{pmatrix} \mu \\ \nu_\mu \end{pmatrix} \begin{pmatrix} \tau \\ \nu_\tau \end{pmatrix} \quad (1.1.2)$$

The lepton family consists of the charged electron, muon, tau, and corresponding neutral neutrinos. The charged leptons interact via weak and electromagnetic forces, whereas neutrinos interact via the weak force. The 6 quarks have $\pm\frac{1}{3}e$ or $\pm\frac{2}{3}e$ charge and have broad range of masses as listed in Fig. 1.1. Quarks interact via the strong, electromagnetic, and weak forces. The quarks, however possess an extra quantum number called color. The existence of color leads to spectroscopies and interactions vastly different from the leptons. The colors are named red(r), green(g), and blue(b). The requirement that quark states must have net zero values of all three color charges (i.e. color singlets), e.g. $r\bar{r}$ or $r.b.g$, is expressed in the principle of color confinement as first developed by Greenberg in 1964 [2]. This principle provides for the fact that quarks are only found in $q\bar{q}$ states called mesons or in qqq or $\bar{q}\bar{q}\bar{q}$ states called baryons. The strong, weak, and electromagnetic force propagators are integer spin particles called bosons. Electric charge can be considered as the source of the electromagnetic force, the photon's propagator. Photon has zero mass, therefore infinite range. Its interactions are described by quantum electrodynamics (QED). The strong force's analogous source charge is the color charge, the propagator being the massless

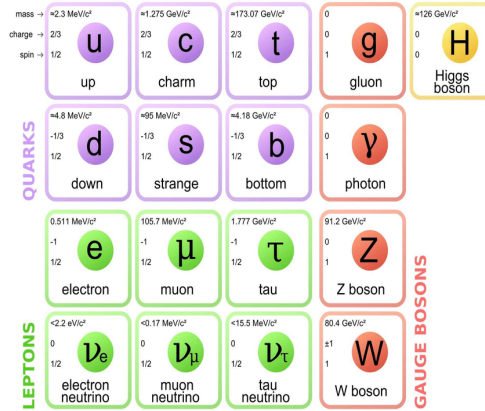


Figure 1.1: Fundamental particles of the SM and their properties [1].

gluon. Strong interactions are described by quantum chromodynamics (QCD). As the gluon is massless, the strong force is likewise infinite in range; however bound quark states are color-neutral. Therefore a much shorter range residual of the strong force is responsible for the forces between mesons and baryons. The force mediators for the weak force are the W^\pm and Z^0 bosons, which have the masses of $80.4 \text{ GeV}/c^2$ and $91.2 \text{ GeV}/c^2$, respectively and consequently have very short ranges even on the scale of nuclear sizes.

The SM is the most successful theory of the universe, but it is not a complete theory and has limitations. For example, it does not adequately explain: Neutrino oscillations, gravity, dark matter, dark energy, and anti-matter asymmetry. In this thesis, we focus on the matter-antimatter asymmetry. According to Andrei Sakharov, one of the reasons for matter-antimatter asymmetry is Charge Parity (CP) violation. It is explained in the section 1.1.1.

1.1.1 CP violation

The charge conjugation operator (C) transforms the particle into an antiparticle. This operation will invert the sign of all additive quantities, for example, electric charge, lepton number etc. While other properties such as position, momentum, and spin are unchanged. The antiparticle of a neutral particle will be the same particle, for example, neutral pion.

Parity operator (P) reflects the space coordinates(x, y, z) of a particle/particle system. Conservation of parity means that the laws of physics are the same for the original particle and its mirror image. Before 1950s, C and P were assumed to be exact symmetries of elementary processes involving weak, strong, and electromagnetic interactions. Time-reversal operator (T) transforms the time coordinate($t \rightarrow -t$). Since 1956, there has been no observation of the violation of discrete symmetries such as C , P , and T . Theoretical physicists Tsung-Dao Lee and Chen-Ning Yang suggested the idea of parity non-conservation and the experimental proof was given by Wu's experiment with beta decay of Co-60 [3, 4]. This experiment also proved that charge conjugation symmetry was also violated. Hence, CP was established as a symmetry of nature. The neutral kaons can decay into two different CP states: $CP = 1$ (two pions) and $CP = -1$ (three pions). The former is known as K_S^0 and the latter is K_L^0 ; with their different lifetimes [5] are:

$$\tau(K_S^0 \rightarrow 2\pi) \approx (8.954 \pm 0.004) \times 10^{-11} \text{ sec}$$

$$\tau(K_L^0 \rightarrow 3\pi) \approx (5.116 \pm 0.021) \times 10^{-8} \text{ sec}$$

Another feature of these neutral kaons are that, they are produced by the processes governed by the strong interaction e.g. $\pi^- p \rightarrow K^0 \lambda$ and $\pi^+ p \rightarrow \bar{K}^0 K^+ p$ but they decay via the weak interaction. Hence, another additive quantum number strangeness (S) is associated with neutral kaons, therefore K^0 having $S = 1$ is mixed with \bar{K}^0 having $S = -1$, a linear superposition of them is an eigenstate of the Hamiltonian.

In 1964 this theory has been violated, when the $K_L^0 \rightarrow \pi^+ \pi^-$ decay was observed with a small branching ratio of 10^{-3} level [6]. Initially, C and P violation was never included in electroweak theory [7, 8, 9]. This was later extended to the family of quarks (evidence of a charm quark [10]). However, no explanation was provided for the observed phenomenology of the neutral kaon sector. Finally, in 1973 M. Kobayashi and T. Maskawa [11] proposed that, CP violation in the SM with a single irreducible complex phase in the interactions of quarks if the existence of at least six generation of quark. In 1974 [12, 13] and in 1977 [14], respectively, the charm and the bottom quarks were established, while the top was discovered in 1995 [15, 16]. This proposal was also experimentally validated through $K^0 \rightarrow \pi^0 \pi^0$ [17, 18] decay which revealed the presence of direct CP violation in the K^0 - \bar{K}^0 system. More pronounced effect of CP violation was observed in the B oscillation (B^0 , B_s) [19, 20] and in two body charmless decay modes of the B^0 [21, 22] mesons. Kobayashi and Maskawa awarded the Nobel prize in 2008, for the experimental evidence of CP violation in electroweak interaction.

1.2 Sources of CP violation

CP violation in SM is explained by the Cabibbo-Kobayashi-Maskawa (CKM) matrix [11, 23]. CKM matrix is basically a quark mixing matrix and gives the relation between weak eigenstate and mass eigenstate of quark. This matrix was present for two generations of quarks and it was given by Cabibbo. This formalism was later extended by Makoto Kobayashi and Toshihide Maskawa. It is defined below:

$$\begin{bmatrix} d' \\ s' \\ b' \end{bmatrix} = \begin{bmatrix} V_{ud} & V_{us} & V_{ub} \\ V_{cd} & V_{cs} & V_{cb} \\ V_{td} & V_{ts} & V_{tb} \end{bmatrix} \begin{bmatrix} d \\ s \\ b \end{bmatrix} \quad (1.2.1)$$

where d' , s' , b' represent the weak eigenstate and d , s , b represent the quark mass eigenstate. The square of matrix element represents the probability of mixing one quark to the other quark. The probability of mixing of quark along the diagonal of CKM matrix is maximum due to the same generation of the family. For the definition of the CKM matrix, four independent parameters are required. Many parameterizations have been proposed, but a more convenient parametrization of the CKM matrix is the Wolfenstein parameterization [23], named after its proposer Lincoln Wolfenstein. The CKM matrix in this parameterization is written as:

$$\begin{bmatrix} 1 - \frac{1}{2}\lambda^2 & \lambda & A\lambda^3(\rho - i\eta) \\ -\lambda & 1 - \frac{1}{2}\lambda^2 & A\lambda^2 \\ A\lambda^3(1 - \rho - i\eta) & -A\lambda^2 & 1 \end{bmatrix} + \mathcal{O}(\lambda^4). \quad (1.2.2)$$

Where, λ , ρ , η , and A are real parameters. The transition probability is maximum

1.2 Sources of CP violation

along with the diagonal element. However, the source of CP violation in SM because of single irreducible complex phase due to η in V_{ub} and V_{td} element. It means the magnitude of CP violation is maximum in V_{ub} and V_{td} elements. CKM matrix is unitarity in nature and the relation between matrix elements is written as:

$$\sum_{j=d,s,b} V_{ij}V_{kj}^* = \delta_{ik}, \quad (1.2.3)$$

Where i and k are u, c, t . Out of 9 expressions, six expressions from the non-diagonal CKM matrix for which the righthand side of equation six is zero are given below:

$$V_{ud}^*V_{td} + V_{us}^*V_{ts} + V_{ub}^*V_{tb} = 0 \quad (1.2.4)$$

$$V_{us}V_{ub}^* + V_{cs}V_{cb}^* + V_{ts}V_{tb}^* = 0 \quad (1.2.5)$$

$$V_{ud}^*V_{cd} + V_{us}^*V_{cs} + V_{ub}^*V_{cb} = 0 \quad (1.2.6)$$

$$V_{ud}V_{ub}^* + V_{cd}V_{cb}^* + V_{td}V_{tb}^* = 0 \quad (1.2.7)$$

$$V_{ud}V_{us}^* + V_{cd}V_{cs}^* + V_{td}V_{ts}^* = 0 \quad (1.2.8)$$

$$V_{cd}^* V_{td} + V_{cs}^* V_{ts} + V_{cb}^* V_{tb} = 0 \quad (1.2.9)$$

The six equations can be pictured as six triangles in a complex plane with sides $V_{ij}V_{kj}^*$. Each triangle has the same area, which measure the amount of CP violation in the SM. The unitarity triangle from equation 1.2.7 is more critical because all sides are similar in length, $\mathcal{O}(\lambda^3)$ and B decays measure all the three angles of the triangle. Fig. 1.2 shows the unitarity triangle in ρ - η plane.

Each side of unitarity triangle is normalized by the factor of $V_{cd}V_{cb}^*$ and where,

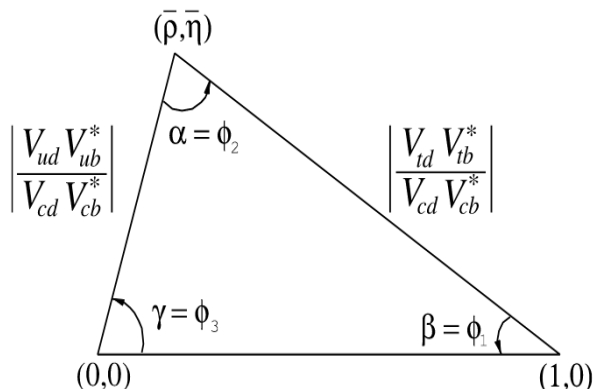


Figure 1.2: Unitarity triangle in ρ - η plane [5].

$\bar{\rho} = \rho(1 - \lambda^2/2 + \dots)$ and $\bar{\eta} = \eta(1 - \lambda^2/2 + \dots)$. ϕ_1 , ϕ_2 and ϕ_3 angle of unitarity triangle define as:

$$\alpha = \phi_2 = \arg \left(\frac{-V_{td}V_{tb}^*}{V_{ud}V_{ub}^*} \right); \quad (1.2.10)$$

$$\beta = \phi_1 = \arg \left(\frac{-V_{cd}V_{cb}^*}{V_{td}V_{tb}^*} \right); \quad (1.2.11)$$

$$\gamma = \phi_3 = \arg\left(\frac{-V_{ud}V_{ub}^*}{V_{cd}V_{cb}^*}\right); \quad (1.2.12)$$

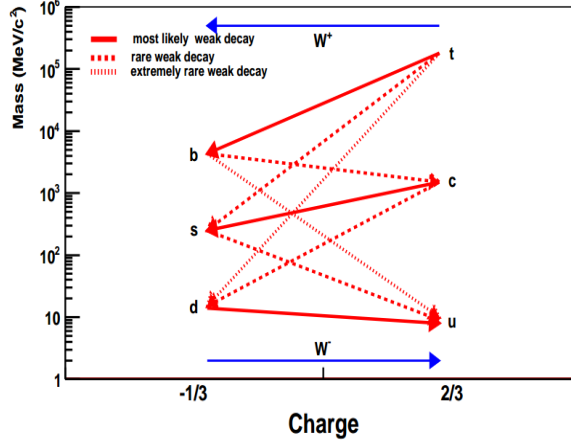
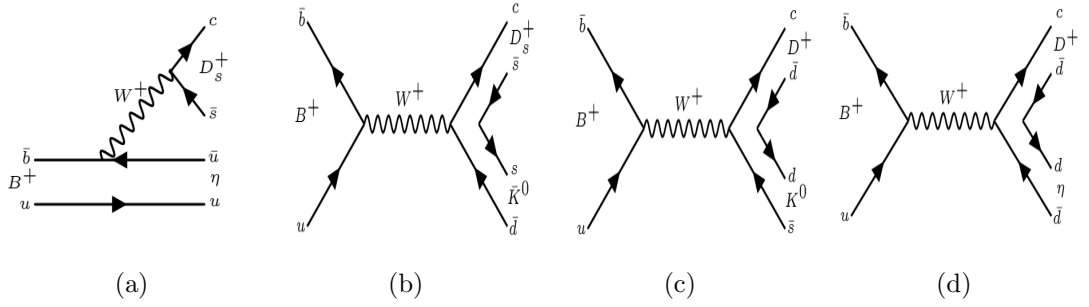
With $B^0 \rightarrow J/\psi K_S^0$ decay mode, measurement of $\sin(2\phi_1)$ is performed by two B factory: Belle and BABAR [24, 25]. This discovery validate the CP violation mechanism in SM in 2001, which led the Nobel prize in 2008 to Kobayashi and Maskawa.

Significant CP violation is described by a single irreducible complex phase [11, 23] is considered too small to produce the observed matter-antimatter asymmetry in the Universe. The study of rare B decays could also provide hints of the physics beyond the SM.

1.3 Rare B decays

Rare B decays are those decay modes whose probability of occurrence is very very less. As shown in Fig 1.3, the simplest schematic for a rare B decay, $b \rightarrow u$ transition suppressed by CKM factor.

Charged B meson decay such as $B^+ \rightarrow D_s^{(*)+} \eta$ dominated by the spectator diagram involving the $b \rightarrow u$ quark level transition as shown in the Fig. 1.4 (a). Here also one expects suppression of $|V_{ub}| \sim \lambda^3$. Searching for these decay modes are crucial in order to improve the theoretical understanding, as they provide insight into the internal dynamics of the B mesons.


Figure 1.3: Possible quark level transition.

Figure 1.4: Feynman diagrams for the (a) $B^+ \rightarrow D_s^{(*)+} \eta$ (b) $B^+ \rightarrow D_s^{(*)+} \bar{K}^0$ (c) $B^+ \rightarrow D^+ K^0$, and (d) $B^+ \rightarrow D^+ \eta$ decay modes.

Along with this, we also search for the $B^+ \rightarrow D_s^{(*)+} \bar{K}^0$, which is expected to be dominated by the weak-annihilation diagrams, where the $\bar{b}u$ pair annihilating into W^+ boson as shown in the Fig. 1.4 (b). We cannot evaluate the annihilation amplitudes with the factorization approach. The annihilation amplitude should be proportional to f_B/m_B , where m_B is the mass of the B meson and f_B for pseudoscalar B meson decay constant. The number of f_B is represented by overlapping of the probability amplitude for the two quark wave functions. In terms

of mathematics, f_B/m_B is roughly equal to λ^2 , where λ is the sine of the Cabibbo angle [26, 27]. In addition, these processes are suppressed by the CKM factor $|V_{ub}| \sim \lambda^3$. In most theoretical calculations of non-leptonic decays, assumptions are made to neglect these amplitudes. The rescattering effects from other modes might also increase the branching fraction of this decay mode.

$B^+ \rightarrow D^+K^0$ and $B^+ \rightarrow D^+\eta$ modes are of interest as these modes are also dominated by weak-annihilation diagram, where the $\bar{b}u$ pair annihilating into W^+ boson as shown in the Fig. 1.4 (c,d). This helps in understanding the complete picture. The upper limit of branching fraction of $B^+ \rightarrow D_s^{(*)+}(\rightarrow D_s^+\gamma)\eta$ and $B^+ \rightarrow D_s^{(*)+}(\rightarrow D_s^+\gamma)\bar{K}^0$ have been reported at 90% of confidence level by CLEO with 1.16×10^6 $B\bar{B}$ events [28] and $B^+ \rightarrow D^+K^0$ has been also measured at 90% of confidence level by BABAR with 226×10^6 $B\bar{B}$ events [29] and are listed in the Table 1.1. So far, $B^+ \rightarrow D^+\eta$ decay mode has not been searched by any other experiment. With a full Belle data sample, we might be able to measure these rare decays for the first time.

To validate the signal mode study, we use $\bar{B}^0 \rightarrow D^0\eta$ as a control mode for $B^+ \rightarrow D_s^+\eta$, $D_s^{(*)+}\eta$, $D^+\eta$ decay modes and $\bar{B}^0 \rightarrow D^0K^0$ as a control mode for the study of $B^+ \rightarrow D_s^+\bar{K}^0$, $D_s^{(*)+}\bar{K}^0$, D^+K^0 decay modes, where $D^0 \rightarrow K^-\pi^+$, $K^-\pi^+\pi^+\pi^-$, $K_S^0\pi^+\pi^-$, $K^-\pi^+\pi^0$, $\pi^0 \rightarrow \gamma\gamma$, and $\eta \rightarrow \gamma\gamma$ ($\pi^-\pi^+\pi^0$). Both control modes were already studied by Belle and BABAR with less data than we are using.

Table 1.1 summarized the previous measurement along with the outcome result of this thesis research. In the absence of a significant signal yield, an upper limit at

Decay mode	Previous ($\mathcal{B.F.} \times 10^{-4}$)	Obtained ($\mathcal{B.F.} \times 10^{-4}$)
$B^+ \rightarrow D_s^+ \eta$	< 4 [28]	< 0.14
$B^+ \rightarrow D_s^{(*)+} \eta$	< 6 [28]	< 0.17
$B^+ \rightarrow D_s^+ K^0$	< 8 [28]	< 0.03
$B^+ \rightarrow D_s^{(*)+} \bar{K}^0$	< 9 [28]	< 0.06
$B^+ \rightarrow D^+ K^0$	< 0.05 [29]	< 0.02
$B^+ \rightarrow D^+ \eta$	–	< 0.12
$B^0 \rightarrow D^0 \eta$	(2.53 ± 0.09) [30] (1.77 ± 0.16) [31]	2.7 ± 0.12
$\bar{B}^0 \rightarrow D^0 \bar{K}^0$	(0.53 ± 0.07) [32] $(0.50^{+0.13}_{-0.12})$ [33]	0.56 ± 0.05

Table 1.1: Results from previous and obtained measurements of branching fraction (B.F.).

the 90% confidence level is given for each signal decay mode. We present the first search result for the $B^+ \rightarrow D^+ \eta$ decay mode. The obtained upper limits are 20 times more stringent than the previous one. We report the most precise measurement to date of the branching fraction for the $\bar{B}^0 \rightarrow D^0 \bar{K}^0$ [32, 33] decay, which supersedes the previous Belle result [33]. The branching fraction measurement of $\bar{B}^0 \rightarrow D^0 \eta$ decay modes is consistent with the world average and supersedes the previous Belle [31] result.

1.4 Summary

We study the signal (rare) and control (color-suppressed) decay modes with data collected by the Belle experiment. With complete Belle data set, we might be able to provide a more stringent measurement of the branching fraction of the aforementioned modes as compared previously estimated branching fraction by different experiments.

2

Experimental Facility

In the thesis, the study of rare decays and rediscovery of B^\pm and D^\pm mesons are carried out using the data collected by two experiments, Belle and Belle II. An overview of both the Belle and Belle II detector and their associated accelerators, KEKB and SuperKEKB are described in the following subsections.

2.1 KEKB accelerator

The KEKB [34, 35] is consist of an asymmetric-energy (e^+e^-) collider with center-of-mass energy of $\Upsilon(4S)$ resonance. This is situated at High Energy Accelerator Research Organization (KEK), Japan and operated from the year 1999 to 2010. The schematic view of the KEKB accelerator is shown in Fig. 2.1, where electron beams are accelerated using LINAC. The beam of electrons bombarded on the target material (tungsten) placed in the path of beam, where few electrons of the beam hit the tungsten, which results the production of positrons. The path of the ejected positrons can be further deviated with the magnetic field. The both beams are then injected into two different rings, a high energy ring (HER) for the electron beam with 8 GeV energy and a low energy ring (LER) for a positron beam with 3.5 GeV energy. The asymmetric-energy collisions create the boost, which helps to measure of CP violation in B and D decay modes. The LER and HER are located 11 m below the ground in a tunnel, which was used by earlier experiment TRISTAN [37]. The current storage capacity in LER and HER are 2.6 A and 1.1 A, respectively. Both rings use the RF of 508.9 MHz [38] to accelerate the beams. Further, the beams are made to circulate in their precise paths

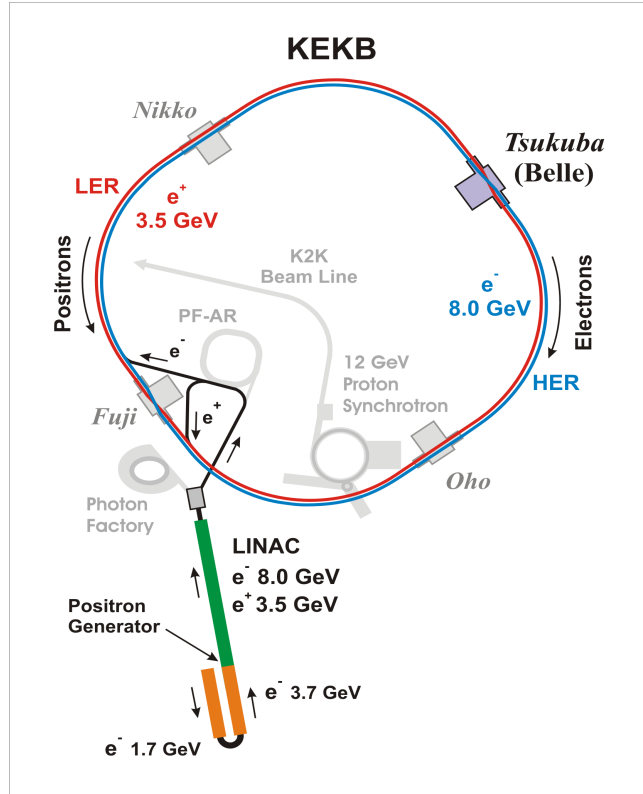


Figure 2.1: KEKB accelerator [36].

using dipole, quadrupole and sextupole magnets.

The electron and positron beams collide at the interaction point (IP) in Tsukuba

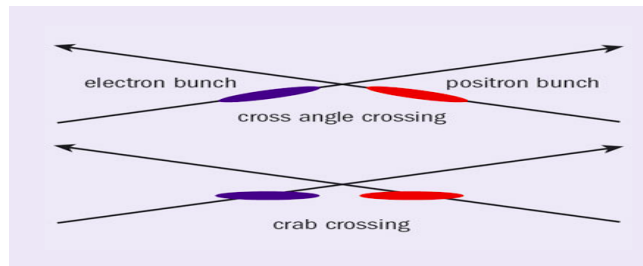


Figure 2.2: A pictorial view of crab crossing and cross angle [39].

hall with a cross angle value of ± 11 mrad [40], which makes the interaction region free from any parasitic collisions due to multiple bunches. The maximum

luminosity is obtained, when the beams perform head-on collision and two superconductivity crab cavities [41, 42] are used to kick the bunches into a horizontal plane. Further, a transverse RF in the crab cavities permits the bunches to rotate and collide with maximum overlap at the IP, which is shown in Fig. 2.2.

The e^+e^- collision at KEKB is carried out at different center-of-mass energies (\sqrt{s}) corresponding to various Υ resonances. The majority of data ($\sim 75\%$) recorded by the Belle experiment is collected at $\Upsilon(4S)$ resonance. The data collected at or near different Υ resonances are listed in Table 2.1. The production cross-section of different Υ resonances is manifested in Fig. 2.3. The $2.11 \times 10^{34} \text{ cm}^{-2}\text{sec}^{-1}$ was the maximum highest instantaneous luminosity achieved by KEKB [43]. The total integrated luminosity of 1 ab^{-1} is obtained at the end of the physics run in 2010.

Resonance	\sqrt{s} (GeV)	Luminosity (fb^{-1})
$\Upsilon(1S)$ resonance (off-resonance)	9.46 (9.43)	8
$\Upsilon(2S)$ resonance (off-resonance)	10.02 (9.99)	28
$\Upsilon(3S)$ resonance (off-resonance)	10.35 (10.32)	2
$\Upsilon(4S)$ resonance (off-resonance)	10.58 (10.52)	711 (89)
$\Upsilon(5S)$ resonance	10.86	121
$\Upsilon(5S)$ scan	$10.58 < E_{CM} < 11.02$	7
Total		966

Table 2.1: Data collected at various Υ resonances by the Belle experiment.

2.2 Belle detector

The Belle detector [45, 46] is situated at the interaction region of the KEKB accelerator. As shown in Fig. 2.4, it is a layered general purpose detector consisting

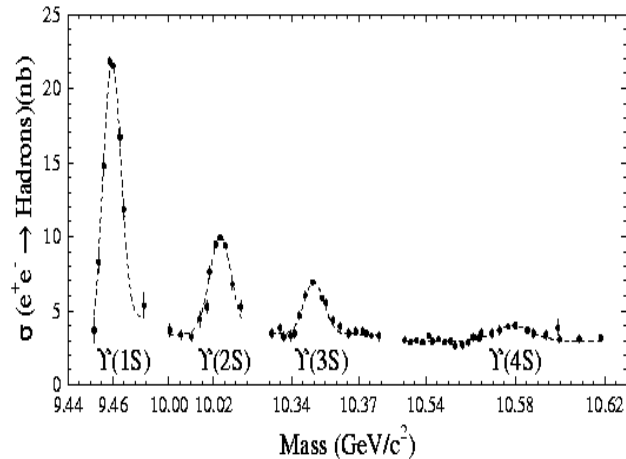


Figure 2.3: Cross section versus energy of different Υ resonances [44].

of different sub-detector systems, which are dedicated to various aspects of event reconstruction. The innermost sub-detector system is a Silicon Vertex Detector (SVD), which precisely measures the decay vertices of B -mesons. Outside the SVD, we have a Central Drift Chamber (CDC), the main tracking system along with SVD. It also helps to distinguish the various particles using dE/dx measure-

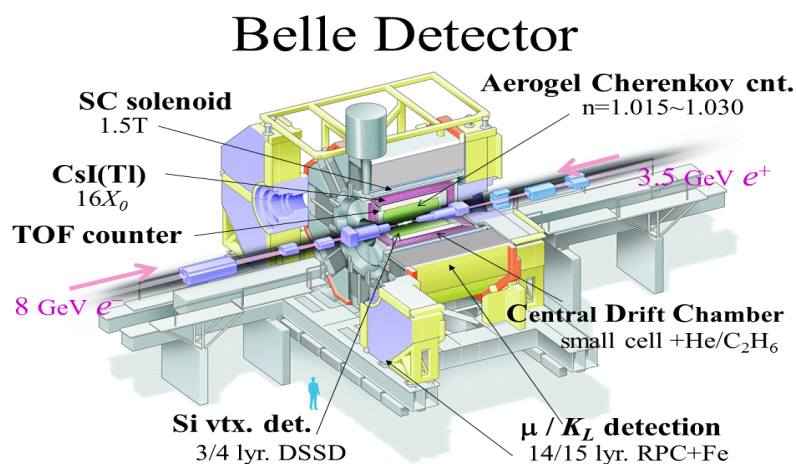


Figure 2.4: A pictorial view of Belle detector [47].

ments. Due to a large number of production of kaons and pions at Belle from the decay of primary particles, they behave identically at higher momentum. Therefore, we have a particle identification system consisting of CDC, Aerogel cherenko counter (ACC) and Time of Flight (TOF) counter. It aims to separate the particle species efficiently. Outside the PID, we have an electromagnetic calorimeter (ECL), used to detect electrons and photons produced in the electromagnetic interactions. The whole detector is placed in a magnetic field of 1.5 T produced by a superconducting solenoid. The outermost part is the K_L^0 and muons detection system (KLM). All sub-detector systems of the Belle experiment are discussed in detail in the following subsections.

2.2.1 Beam pipe

The beam pipe is the innermost part of the detector and closet to the IP region. The double-walled beryllium (Be) cylinder is used as the beam pipe to avoid coulomb scattering, which affects the resolution of the SVD. The beam pipe is 0.5 mm thick and the separation between both walls is 2.5 mm, through which helium gas is used as a coolant. To absorb X-rays from synchrotron radiation, the beam pipe enveloped with a gold foil with a thickness of 20 μm . At the interaction region, the cross-section of the beam pipe is shown in Fig. 2.5.

2.2.2 Silicon Vertex Detector (SVD)

The SVD helps in measuring the B , D mesons vertices, which plays an essential role in studying the time-dependent CP asymmetry. As the averaged separation

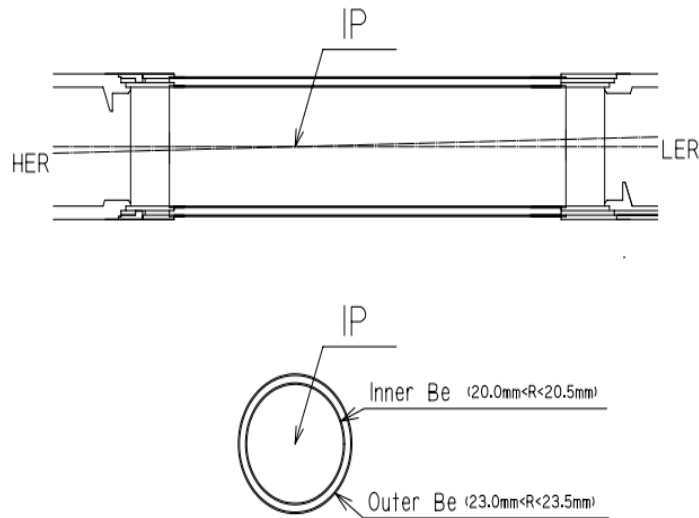


Figure 2.5: Cross section and side view of Belle beam pipe.

between the two B meson vertices is around $\sim 200 \mu\text{m}$. As we know, most of the particles produced in the Belle experiment have momenta less than or equal to 1 GeV/ c and multiple-coulomb scattering worsens vertex resolution. To minimize the effect of such scattering, the vertex detector should be placed close to the IP. Along with this, the electronics need to be kept outside the tracking volume and the supporting structure should be low in mass. The SVD is also used to measure the trajectory of charged particles. In the presence of a uniform magnetic field, the shape of the particle's path is helical. It is probable that some of charged particles are unable to reach the CDC and their path becomes curved in SVD detector. Belle has two types of SVD: a three-layer SVDI, which was operated till the summer of 2003 and four-layers SVDII, which was operated till 2010.

As displayed in Fig. 2.6, SVD includes the three concentric cylindrical layers having radii of 30.0, 45.5, and 60.5 mm. These layers are made up of differ-

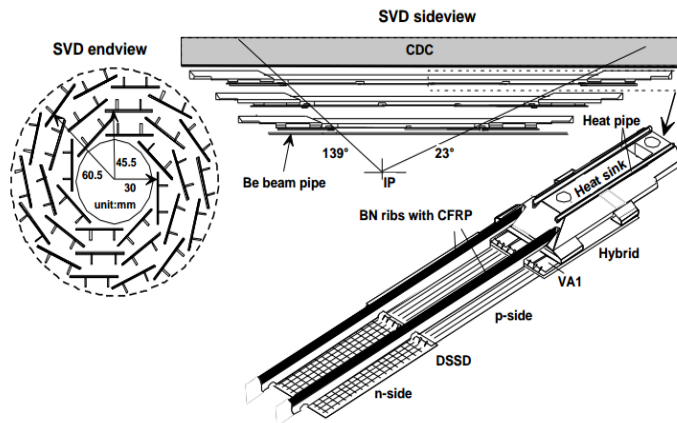


Figure 2.6: View SVDI detector [48].

ent ladders, where each one is comprised of a double-sided silicon-strip detector (DSSD). It is supported by boron-nitride ribs. Each DSSD has 1280 sense strips and 640 readout pads on either side. There are a total of 102 DSSDs used, where each sensor has the size of $57.5 \times 33.5 \text{ mm}^2$. The ϕ -strip pitch is 25 mm and the z -strip pitch is 42 mm. The readout system of SVD is based on the VA1 integrated circuit [49, 50].

SVDII was placed in 2003 due to the damage in SVDI by synchrotron radiation [51]. As shown in Fig. 2.7, SVDII covers 92% of the 4π solid angle and has four layers. As SVDII has an extra layer of DSSDs, which covers more area as compared to SVDI. Therefore, SVDII performance is obtained better than SVDI. As we know, K_S^0 is reconstructed from the two daughters' pions and the flight length of K_S^0 is less than 6 cm. Most of the K_S^0 particles decay within the SVD region into two oppositely charged pions. The K_S^0 are reconstructed using the hits of these pions on the SVD layers. The SVD helps in tracking the low momentum

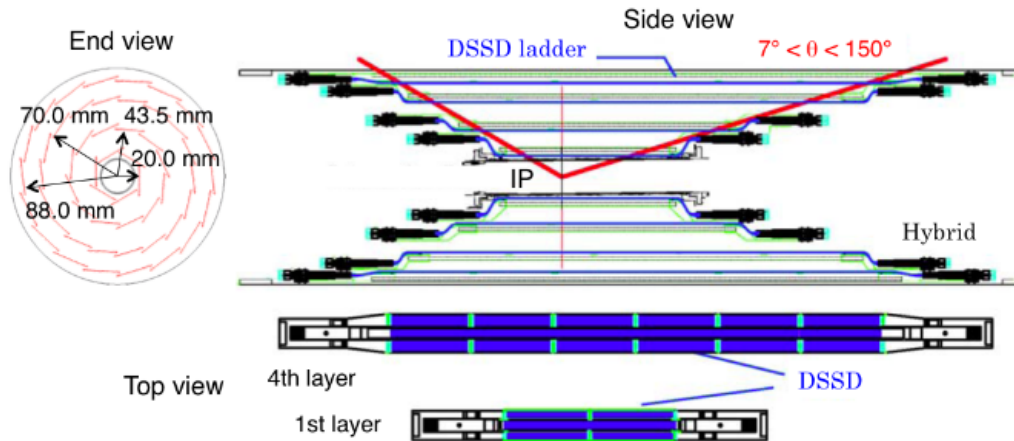


Figure 2.7: Configuration of SVDII detector [51].

particles and reduces the multiplicity.

2.2.3 Central Drift Chamber (CDC)

The CDC is a gaseous detector [52], which forms the tracking device, together with SVD in the Belle experiment. It covers the polar angle coverage of $[17^\circ - 150^\circ]$. The inner radius CDC is 103.5 mm, while the outer radius is 874.0 mm. In the CDC, an equal amount of He and C_2H_6 is filled to minimize the multiple scattering and to improve the momentum resolution. When charged particles travel through the gaseous medium, they interact with gas molecules and ionize them. Then a tracking algorithm is used to reconstruct the path of charged particles from their hits in CDC. A schematics view of CDC is shown in Fig. 2.8, where, there are 50 cylindrical layers and has a spatial resolution of about $130 \mu m$. There are 8400 drift cells in the CDC, where each cell consists of a sense

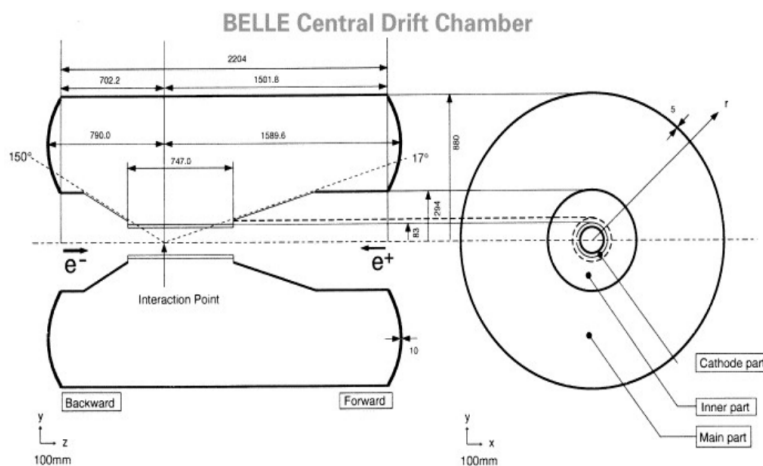


Figure 2.8: View CDC detector [52].

wire surrounded by eight parallel field wires. It is used to measure energy loss (dE/dx) of a charged particle using Bethe Bloch formula [53, 54, 55]. The dE/dx measurement for identification of various charged particle types versus particle's momentum in CDC is shown in Fig. 2.9. It provides a clear separation between charged particles like electron, pion, and proton.

2.2.4 Aerogel Cherenkov Counter (ACC)

ACC [40, 56] is implemented just after the CDC detector for the identification of particles such as kaons/pions within the momentum region of 1.2– 3.5 GeV/c. Particle identification plays a vital role in studying CP violation in B physics. ACC working is based on the principle of Cherenkov radiation. When a particle moves in a medium greater than the velocity of light c in that medium, it emits the Cherenkov radiation. The relation between the refractive index and β (velocity of the particle) is given as:

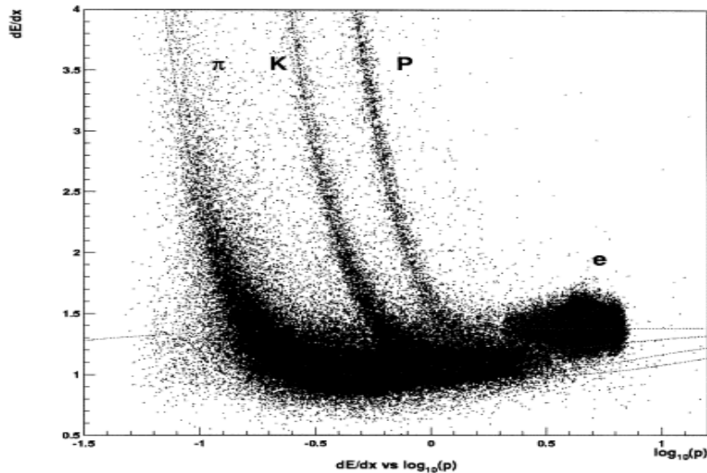


Figure 2.9: dE/dx measurements for different particle types (π , K , e , p) as a function of momentum in CDC [45].

$$n > \frac{1}{\beta} = \left(1 + \left(\frac{m}{p} \right)^2 \right)^{1/2} \quad (2.2.1)$$

where p represents the momentum and m is mass of the moving particle, and $\beta = v/c$. We understood from the above relation, that two different particles (kaon and pion) having the same momentum emit the Cherenkov light at different instances. Here n is selected so that only pions can emit the Cherenkov light not kaons. Fig. 2.10 [45] shows the configuration of ACC detector. The forward endcap part has 228 modules arranged in 5 concentric layers and the barrel part has 960 counter, which are differentiate into 60 different segmented cells. The single ACC cell is made up of silica aerogel tiles ($12 \times 12 \times 12 \text{ cm}^3$) boxed in a aluminium box of size around 0.2 mm. It equipped with photomultiplier tubes that are placed in the magnetic field of 1.5 T. n for aerogel is selected between 1.01–1.028 for better particle identification and the selection of n is related to

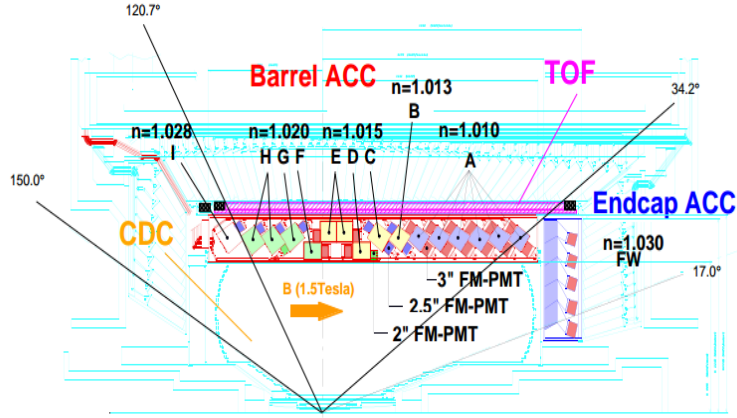


Figure 2.10: ACC detector [45].

the polar angle. The angular acceptance for ACC is 17° to 127° and is installed in the forward as well as in barrel endcap region.

2.2.5 Time of Flight counter

The TOF [56] is the third component of the particle identification system in the Belle experiment, which uses plastic scintillator counters. It has polar angle coverage of $34^\circ < \theta < 120^\circ$. It distinguishes different particles with momenta less than $1.2 \text{ GeV}/c$. Particles are having a minimum transverse momentum of $0.28 \text{ GeV}/c$ reach to TOF. It provides a fast signal with 100 ps of resolution. It involves 64 trigger scintillator counters (TSC) and 128 TOF counters. A TOF is manifested in Fig. 2.11. One TOF module consists of two TOF counters with trapezoidal-shaped and one TSC counter with a gap of 1.5 cm between them. The gap ensures that the TOF counters are protected from any electron-positron

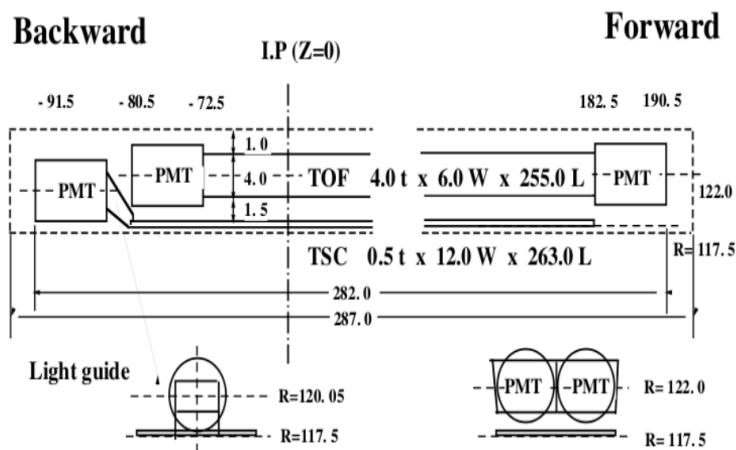


Figure 2.11: TOF detector [45].

created in the TSC layer. There are 64 such modules in the system. In the TOF, scintillator counters excite the molecule, radiating to generate the photon and photomultiplier tubes are used to detect them. The desired time resolution in TOF is achieved with the following design:

- A fast scintillator with an attenuation length greater than 2 m is used.
- The time dispersion of scintillation photos is minimized by eliminating the light guide.
- Photo tubes have a large area photo cathode to maximize the photon collection efficiency.

TOF detector counts the time of the particle from IP to TOF detector and the average time is measured around 3 ns. The measured time is expressed as

$$t = \frac{l}{c\beta} = \frac{l}{c} \left(1 + c^2 \left(\frac{m}{p} \right)^2 \right)^{1/2} \quad (2.2.2)$$

where t provides the information about the particle species. The mass distribution obtained for various particle types is displayed in Fig. 2.12. An overall likelihood is performed using the combined measurements of CDC, ACC, and TOF subsystem and this information is used to identify the particle type at the reconstruction level.

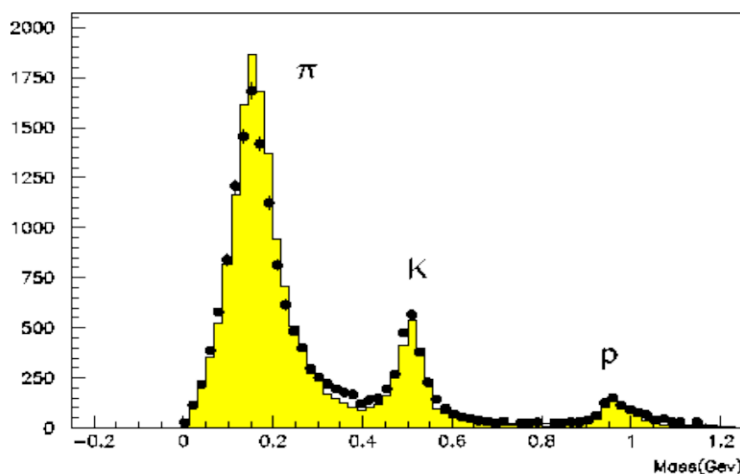


Figure 2.12: π , K , p separation in TOF detector [57].

2.2.6 Electromagnetic Calorimeter (ECL)

ECL was placed after following the tracking system. It plays an essential role in detecting photons with good resolution and high efficiency. And it is also helpful for the identification of electrons and positrons from the combined information of tracking detectors. When high energy photons and electrons are incident on

2.2 Belle detector

an absorber, then through the pair production and bremsstrahlung low energy photons and electrons are generated. The performance of ECL should be good for detecting the low energy photons with energy less than 500 MeV. In addition, to reduce the background from the high energy photons in the reaction, such as $B \rightarrow K^*\gamma$ and $D^0 \rightarrow \pi^0\pi^0$, excellent energy resolution is needed. In many B and D physics studies, π^0 is used as a final state particle. π^0 is reconstructed from the combination of two photons. To reduced the background from photons, it is vital to separate two photons with the help of energy deposits on the crystal of ECL and precisely determine their opening angle. Fig. 2.13 shows the overall configuration of ECL. It consists of an array of Thallium (Tl) doped CsI scintillat-

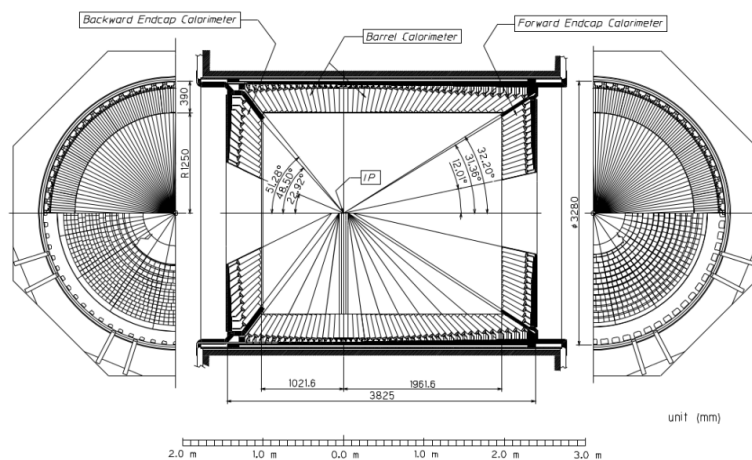


Figure 2.13: ECL detector [45].

ing crystals with silicon photodiode read-out installed inside a superconducting solenoid magnet having magnetic field of 1.5 T. CsI crystal use because of moderate price, mechanically stable and have large photon yield. We have divided ECL crystal into three parts: 3.0 m length of barrel region with 1.25 m of inner radius

2.3 The Belle Trigger system

and from the IP the annular forward section ($z = 2$ m) and backward section ($z = -1$ m). The number of crystals and angular region of each section is shown in Fig. 2.13. The angular acceptance of ECL is also in the range between $17^\circ < \theta < 150^\circ$. The geometrical parameters are mention in Table 2.2. The total number of 8736 crystals is used to make ECL detector with 43 ton weight.

Item	θ coverage	θ seg.	ϕ seg.	No. of crystals
Forward endcap	12.4° - 31.4°	13	48 - 144	1152
Barrel	32.2° - 128.7°	46	144	6624
Backward endcap	130.7° - 155.1°	10	64 - 144	960

Table 2.2: Geometrical parameters of ECL.

2.3 The Belle Trigger system

The trigger system plays an important role in selecting valuable events from the many unwanted events produced during the electron and positron collision at IP. At high luminosity, the large number of beam backgrounds is produced because of the high beam current. To avoid unwanted events, a triggering system of 500 Hz is used to select physics events.

The Belle trigger system has two-level states: Level-1 (L1) and Level-3 (L3) trigger. L1 is composed of a central trigger system and sub trigger system known as Global Decision Logic (GDL). The sub-trigger system working on the basis of an energy trigger and track detector. The CDC, TOF, and KLM trigger the signals from charged particles, while the ECL trigger system gives trigger signals based on cluster counting of crystal hits. Event signals process parallel in all sub

2.3 The Belle Trigger system

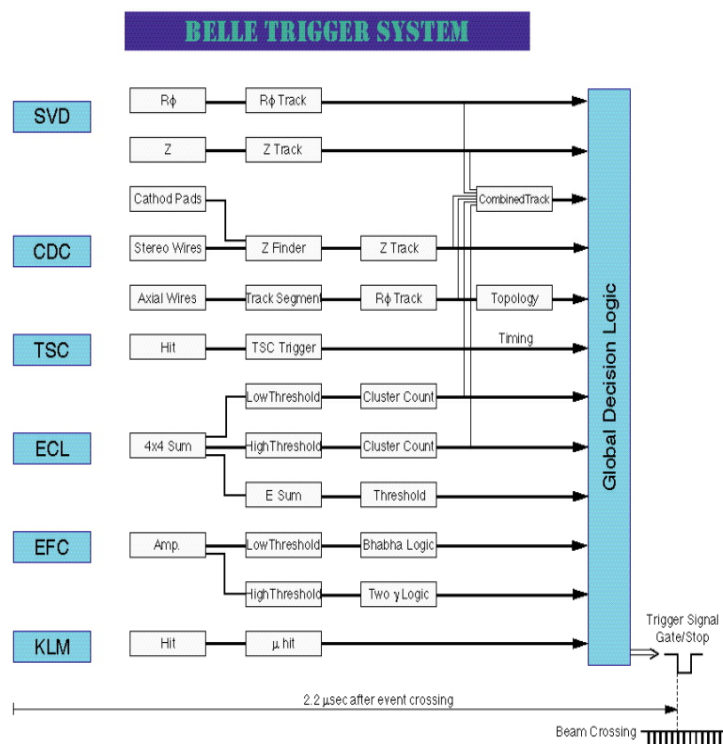


Figure 2.14: Belle Trigger system [58].

triggers and send the information of trigger to GDL, where all data is collected to separate physics and background events. Fig. 2.14 shows the Belle L1 trigger system. The efficiency of L1 trigger system is more than 98%. L3 level basically rejects those events with no tracks information with impact factor $|z| < 5$ cm and the events having energy less than 3 MeV deposit in ECL. After this procedure, most of the background from the beam will reduce. L3 trigger system gives 99% efficiency of physics events and 50-60% data reject.

2.4 Data Acquisition System (DAQ)

The DAQ system is configured to keep data up to a limit of 500 Hz. The hadronic event data size is a measure around 30 kB and the maximum data transfer rate is 15 MB/s. Fig. 2.15 manifest the overview of the Data Acquisition system. It reads the data from all subdetectors. In most of the subdetectors, signals are

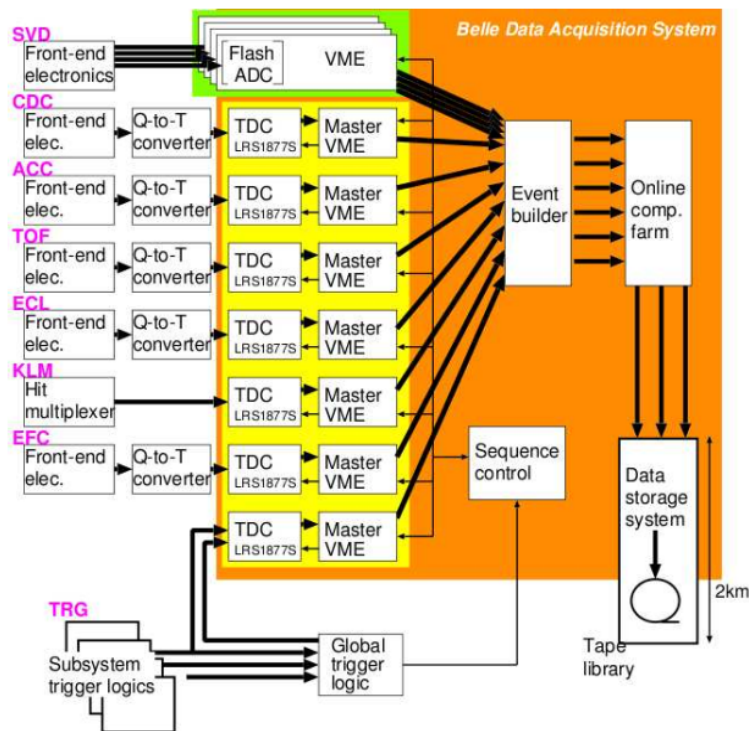


Figure 2.15: Belle Data Acquisition System [45].

directly related to the energy deposited in the individual detector. With the help of a time-to-digital converter (TDC), the analogue pulse converts into the digital expect SVD, because it uses a flash analogue-to-digital converter (FADCs). When the GDL get a trigger signal, then with the help of the event builder, the data

from each subdetector are combined into a single event, which converts “detector-by-detector” parallel data streams into “event-by-event” data. The output data is recorded in the online computer farm, which comes from the L3 trigger system. Finally, the information is transferred to the mass storage system at the KEK computing facility.

2.5 Belle II Experiment

The Belle II [59] detector is an upgrade of the Belle detector. The aim of upgrading the Belle II detector is to collect 50 times more data than the Belle detector. The SuperKEKB [60] is an upgrade of the KEKB collider, which provide 30 times higher instantaneous luminosity. To increase the instantaneous luminosity, optimized the beam parameter and the same accelerator ring is used for the upgrade version. Fig. 2.16 shows the schematics of the SuperKEKB collider. To achieve the world’s highest instantaneous luminosity, which is 30 times as compared to KEKB, accepts the Nano-Beam Scheme in which vertical beta function β_y^* is reduced by a factor of 20 and beam current (I) is doubled to the value that of KEKB. The instantaneous luminosity is defined as:

$$L = \frac{\gamma_{\pm}}{2er_e} \left(1 + \frac{\sigma_{y^*}}{\sigma_{x^*}}\right) \left(\frac{I_{\pm}\xi_y^{\pm}}{\beta_y^*}\right) \left(\frac{R_L}{R_{\xi_y}}\right) \quad (2.5.1)$$

where \pm specifies the positron (+) and electron (-). γ_{\pm} , e , and r_e represent the Lorentz factor, elementary charge, and classical radius, respectively. The parameters I_{\pm} , ξ_y , and β_y^* are used for the total beam current, vertical beam-beam

parameter, and vertical beta function at the IP, respectively. R_L and R_{ξ_y} are the reduction factors for luminosity and vertical beam-beam parameter, respectively. σ_x^* (σ_y^*) is the horizontal (vertical) beam size.

Fig. 2.17 shows the schematic view of beam crossing at KEKB and SuperKEKB.

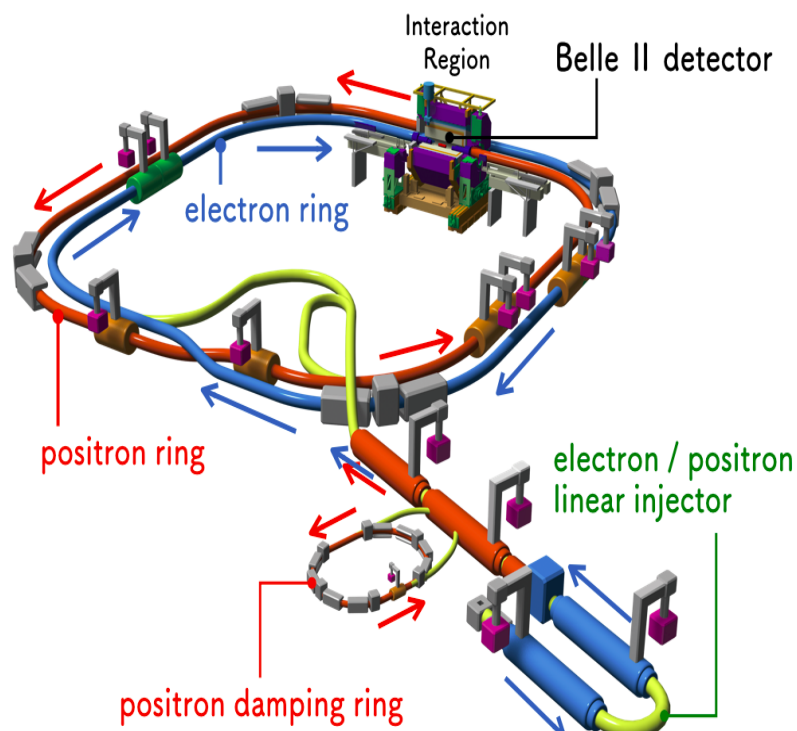


Figure 2.16: SuperKEKB accelerator with Belle II detector position [60].

The beam energy of the electron (positron) changed from 8(3.5) GeV to 7(4) GeV in the SuperKEKB accelerator. As the beam energies are less asymmetric in the SuperKEKB than the KEKB that leads to a reduction in the Lorentz boost in the CM system.

The most important parameters in SuperKEKB and KEKB are updated in the

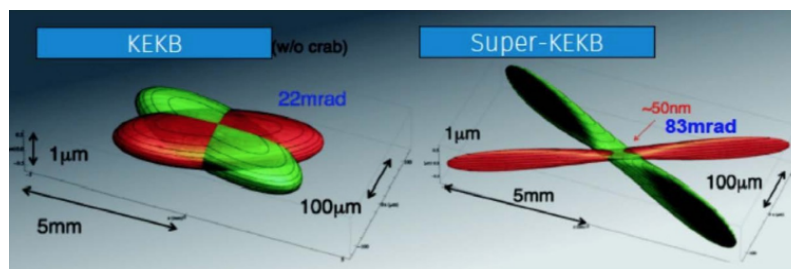


Figure 2.17: The schematic view of beam crossing angle at KEKB (left) and SuperKEKB (right) [61].

Table 2.3.

Parameters	KEKB	SuperKEKB
Energy (LER/HER) [GeV]	3.5/8.0	4.0/7.0
Instantaneous Luminosity [$10^{34} \text{ cm}^{-2}\text{sec}^{-1}$]	2.11	60
Beam current (LER/HER) [A]	1.64/1.19	3.60/2.62
Beam crossing angle (mrad)	22	83
Vertical beta function at IP [mm]	5.9/5.9	0.27/0.41
Horizontal beam size at IP [μm]	90	9
Vertical beam size at IP [nm]	1900	60
Boost	0.425	0.287
Number of bunches	1584	2500

Table 2.3: Parameters of KEKB and SuperKEKB accelerator.

To deal with reduced boost factor and higher background environment, there is a need of upgradation of the Belle detector. Fig. 2.18 shows schematic diagram of the Belle II detector.

Near the beam pipe, the Belle's SVD is changed by two layers of pixel detector (PXD) and four layers of silicon vertex detector (SVD). Increasing the layers of the vertex detector provides better vertex resolution and covers more coverage. At 2 GeV/c, the impact parameter resolution is 20 μm [59], and the value is

2.5 Belle II Experiment

half of Belle. The re-construction efficiency of K_S^0 is improved because of the six layers of vertex detector.

The CDC is designed with different cells of smaller size. To avoid higher back-

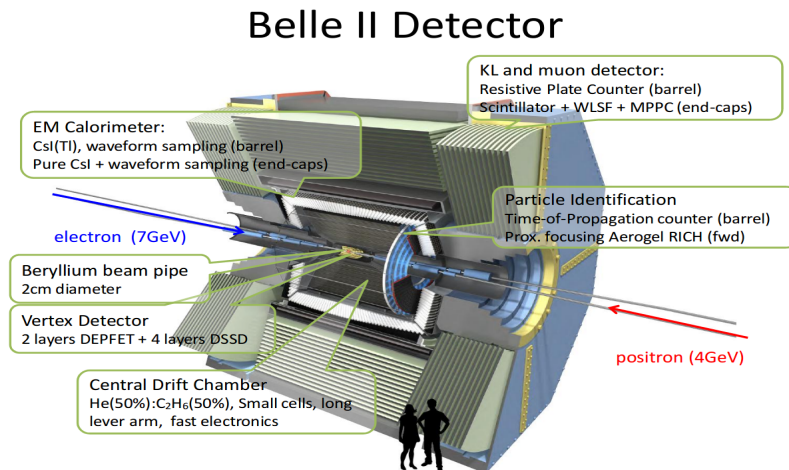


Figure 2.18: The schematic view of the Belle II detector [62].

ground near IP, the inner radius of CDC is 160 mm, while the outer radius of the CDC is 1130 mm.

For particle identification, two systems are installed and both are entirely new. TOP counter in the barrel region, consists of total internal reflected Cherenkov photons and ARICH in the forward end-cap region.

For the detection of electrons and photons, the original CsI(Tl) electromagnetic calorimeter has been re-used. The calorimetric readout system is upgraded.

For the detection of μ and K_L^0 the RPCs of Belle KLM in the end-caps and two inner layers of the barrel are changed with the scintillator's plastic modules.

2.6 Summary

This chapter gives the detailed introduction of the Belle and upgrade version i.e. Belle II experiment. In the KEKB collider, electron and positron collide at the CM energy of $\Upsilon(4S)$ resonance, which further decays into daughter particles. These primary and secondary decay particles are detected by the Belle detector, which consist of SVD, CDC, ACC, TOF, ECL, KLM, and EFC sub-detectors. In June 2020, the Belle experiment stopped for the major upgrade to the Belle II experiment. To increase the instantaneous luminosity by 30 times, a nano beam scheme is adopted in Belle II. The new Belle II detector consists of PXD, SVD, CDC, TOP, ARICH, ECL, and KLM sub-detectors. The detection of various particles in the Belle detector is summarized in Table 2.4.

Particle	Energy	Momentum	Position	Particle Identification
e	ECL	CDC	VXD, CDC	ECL, ARICH, TOP, CDC
μ		CDC	VXD, CDC	KLM, ARICH, TOP, CDC
π		CDC	VXD, CDC	ARICH, TOP, CDC
K		CDC	VXD, CDC	ARICH, TOP, CDC
p		CDC	VXD, CDC	ARICH, TOP, CDC
γ	ECL		ECL	ECL, CDC
K_L			KLM	KLM

Table 2.4: Sub-detector which measures each particle property.

3

Blind Analysis of Signal and Control modes

This chapter describes the analysis strategy for the decay modes of interest. We define the procedure adopted for the unbiased study. To avoid potential bias, we have used blind analysis strategy, which is explained in Sec. 3.1. The analysis procedure is further explained in Sec. 3.2. After introducing the signal and generic MC sample information, the event reconstruction process is defined in Sec. 3.3 and the selection criteria used to extract the signal events are described in Sec. 3.4. Sec. 3.5 and Sec. 3.6 show the study of signal modes with signal and generic MC sample, respectively. The main combinatorial background suppression comes from continuum events and the optimization of the neural network is defined in Sec. 3.7 and Sec 3.8, respectively. We show the background contribution from the rare sample for the signal decay modes in Sec. 3.9. We explain the fitting strategy used for signal modes with the signal MC sample in Sec. 3.10. In Sec. 3.11, we describe the control modes used to validate the study of signal modes. Sec. 3.12 and Sec. 3.13 used to show the study of control modes with signal and generic MC samples, respectively. The continuum suppression used for reducing the continuum event for control modes are explained in Sec. 3.14. We explain the strategy of modelling the signal and background components of ΔE variables with PDFs used in Sec. 3.15 and also compare the observed events with truth matched events with the generic MC sample for control modes. We perform the toy study and linearity test to check the stability of the fitter for the control modes in Sec. 3.16. In Sec. 3.17, we describe the modelling of signal and background components of ΔE variable with appropriate PDFs of combined sub decay modes with the signal and generic MC sample. In Sec. 3.18, we also perform

toy study and linearity test for the signal decay modes. Finally, data/MC side-band comparison of the energy difference (ΔE), beam constrained mass (M_{bc}) and mass of D meson (M_D) for all signal decay modes is given in Sec. 3.19.

3.1 Blind Analysis

Blind analysis is a procedure, where one optimizes the selection and fitting criteria on the Monte Carlo (MC) sample. Further, one uses a control mode to validate the MC and data. Only after many checks, once look for the answer in the data. Blind analysis procedures are intended to avoid or reduce the possibility of (subconscious) bias in favor of the experimenter [63] (unexpected influence on a measurement toward prior results or theoretical expectations).

The analyses performed in this thesis are blind analysis, implying that the signal region in the data was not accessed until all of the selection criteria were optimized. We have cross-checked our results in many methods and the signal region is unblinded at the appropriate moment.

3.2 Analysis Procedure

Analysis starts with the generation of signal Monte Carlo (MC) events using an event generation. The generated events are passed through the detector simulation software. According to our signal decay modes, we reconstruct the B mesons from the well-reconstructed particles that are selected by applying various requirements for photon candidates and charged tracks. For discrimination

3.3 Signal and Generic Monte Carlo Sample

of signal events from the background events, the selection criteria are optimized to maximize the expected significance $\frac{S}{\sqrt{S+B}}$, where S and B are signal yield and background events in the signal region, respectively. After optimization of all cuts, we estimate the efficiency from signal MC samples. During the event selection, the data signal region is hidden to avoid possible bias (blind analysis). The signal yield is extracted from the un-binned maximum likelihood fit in MC samples. We also validate our measurements by checking the results in several ways. Finally, we get permission to open the data box for interested decay modes and calculate the branching fractions, upper limits from obtained efficiencies and signal yield. Fig. 3.1 shows the flow chart of the analysis procedure for interested decay modes.

3.3 Signal and Generic Monte Carlo Sample

EvtGen [64] is used to generate the Signal Monte Carlo (MC) samples and generated events are simulated using GSIM (detector response GEANT3 simulation) [64]. We have generated 0.4 Million signal events for the signal MC study for each mode. While the background study, we have used the generic MC samples available at the Belle (5 streams of $udsc$, mixed, charged for all decay modes). One stream is equivalent to the 711 fb^{-1} of available data.

Signal events are generated using the Belle Analysis Software Framework (BASF) [64], while the reconstruction is done using the BASF2 [65] by using the B2BII framework with light-2012-minos release. The B2BII converter reads and converts

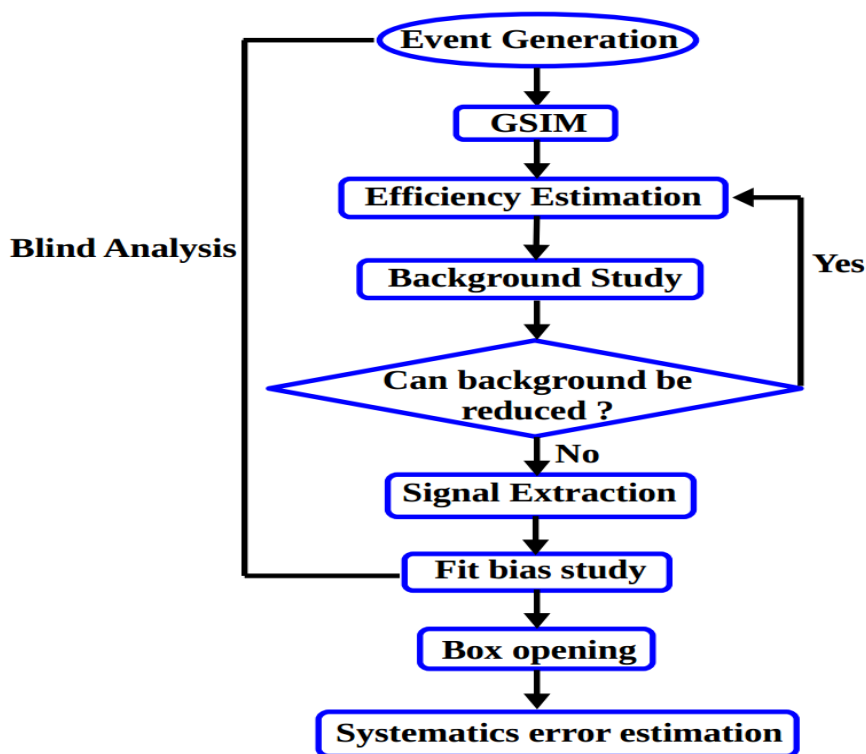


Figure 3.1: Flow chart of analysis procedure.

Belle MDST within BASF2. Fig. 3.2 shows the work flow of the B2BII framework [67].

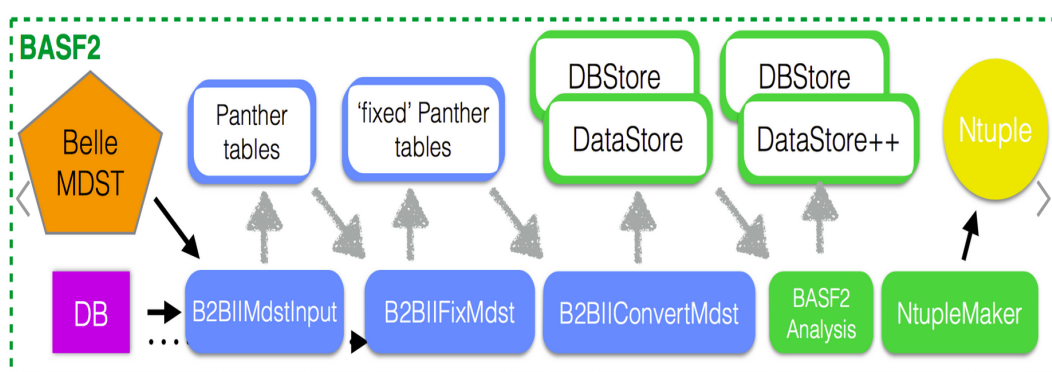


Figure 3.2: Flow chart of analysis procedure [66].

We have analyzed the following six decay modes:

- $B^+ \rightarrow D_s^{(*)+} (\rightarrow D_s^+ \gamma) \eta$

- $B^+ \rightarrow D_s^{(*)+} (\rightarrow D_s^+ \gamma) K_S^0$
- $B^+ \rightarrow D_s^+ \eta$
- $B^+ \rightarrow D_s^+ K_S^0$
- $B^+ \rightarrow D^+ K_S^0$
- $B^+ \rightarrow D^+ \eta$

The sub-decay modes are reconstructed as:

- $D_s^+ \rightarrow \phi \pi^+, \bar{K}^{*0} K^+, K_S^0 K^+$
- $D^+ \rightarrow K^- \pi^+ \pi^+, K_S^0 \pi^+$
- $\phi \rightarrow K^+ K^-$
- $\bar{K}^{*0} \rightarrow K^- \pi^+$
- $K_S^0 \rightarrow \pi^+ \pi^-$
- $\eta \rightarrow \gamma \gamma, \pi^- \pi^+ \pi^0$.

3.4 Selection criteria

The selection criteria used for reconstructing the particles of interest are mentioned in this section.

3.4.1 Final state particles selection

- $|dr| < 0.5$ cm and $|dz| < 4.0$ cm: All track candidates are required to have a point of closest approach (POCA) within ± 0.5 cm of the interaction point (IP) in the direction perpendicular to the beam axis (dr) and ± 4.0 cm in the direction parallel to the beam axis (dz).
- Binary particle identification (PID) criteria is applied on all kaons and pions, with $\text{kaonID} > 0.2$ for kaons and $\text{pionID} > 0.2$ for pions. kaonID and pionID are defined as $\mathcal{L}_K / (\mathcal{L}_K + \mathcal{L}_\pi)$ and $\mathcal{L}_\pi / (\mathcal{L}_K + \mathcal{L}_\pi)$, respectively. Here, \mathcal{L}_K (\mathcal{L}_π) are the likelihood of kaons (pions) estimated from the particular track based on the particle identification sub-detectors.
- η is reconstructed from $\eta \rightarrow \gamma\gamma$ with invariant mass lies between $[0.50 - 0.58]$ GeV/ c^2 . The mass constraint is also applied. For photons, we use `goodBelleGamma` list. Reconstruction of calorimeter showers starts with the formation of the cluster with individual crystal hits greater than 0.5 MeV. One then searches for the most energetic crystal (local maximum seed crystal) above the seed crystal energy threshold. Crystal should have energy greater than 10 MeV. Recorded hits inside the 5×5 matrix surrounding the seed crystal are clustered. There should be no hits which have an energy greater than the seed crystal in near-neighbour crystals. Energy is estimated by summing each hit, while the position is estimated using an energy-weighted center of gravity. Further, leakage and angle corrections are applied [68]. Gammas having energy greater than 50/100/150 MeV

in the barrel/forward/backward region, respectively, are kept for further processing.

- η is also reconstructed from $\eta \rightarrow \pi^- \pi^+ \pi^0$ with invariant mass lies between $[0.535 - 0.560]$ GeV/c^2 . The π^0 from η is reconstructed from two photons with invariant mass lies between $[0.115 - 0.155]$ GeV/c^2 and having momentum greater than $0.4 \text{ GeV}/c$. The mass constraint and vertex fit is also applied on both η and π^0 .

3.4.2 Reconstruction of ϕ , \bar{K}^{*0} , K_S^0 Mesons

- ϕ is reconstructed from $K^+ K^-$. In order to reduce the contribution from the combinatorial background, we kept the candidates, whose reconstructed mass lies between $[1.006, 1.034]$ GeV/c^2 .
- The \bar{K}^{*0} is reconstructed by combining $K^- \pi^+$. For further processing, we keep candidates satisfying the criteria $0.792 \text{ GeV}/c^2 < M(K^- \pi^+) < 0.992 \text{ GeV}/c^2$. This helps in keeping better multiplicity.
- We reconstruct K_S^0 candidates by combining pairs of oppositely charged particles compatible with originating from a common vertex (both assumed to be pions). Further, a multivariate algorithm is used to improve the purity of the sample [69]. The K_S^0 candidates are selected within mass window: $[0.487, 0.508]$ GeV/c^2 .
- Mass constrained and vertex fit are also performed on the ϕ , K_S^0 and only vertex fit is applied on \bar{K}^{*0} .

3.4.3 Invariant mass spectra of ϕ , \bar{K}^{*0} and K_S^0

Fig. 3.3 shows an invariant mass distributions of ϕ , \bar{K}^{*0} and K_S^0 sub-decays, where $M_{\phi \rightarrow K^+ K^-}$ is fitted with Breit-Wigner convolution with Gaussian, $M_{\bar{K}^{*0} \rightarrow K^- \pi^+}$ is fitted with Breit-Wigner function and $M_{K_S^0 \rightarrow \pi \pi}$ is fitted with sum of two Gaussians. The invariant mass cut for ϕ , \bar{K}^{*0} and K_S^0 are $14 \text{ MeV}/c^2$, $100 \text{ MeV}/c^2$ and $10 \text{ MeV}/c^2$, respectively around their respective nominal masses.

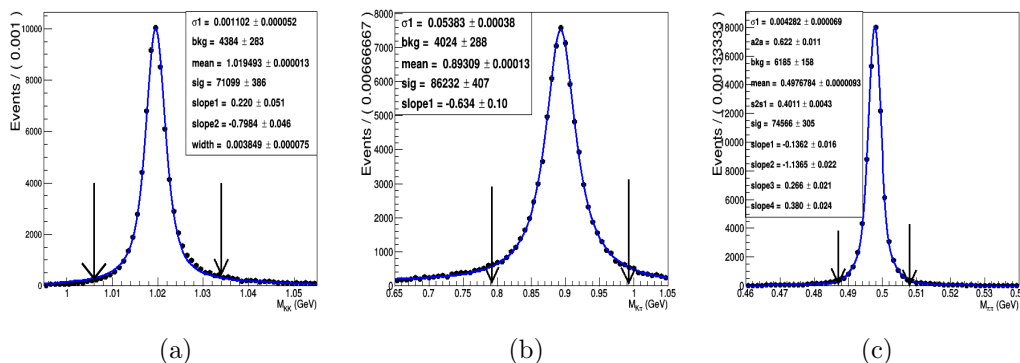


Figure 3.3: Invariant mass distribution of (a) $\phi \rightarrow K^+ K^-$ (b) $\bar{K}^{*0} \rightarrow K^- \pi^+$ and (c) $K_S^0 \rightarrow \pi \pi$ sub-decay modes for signal MC. Blue curve shows the overall fit.

3.4.4 Reconstruction of D_s^+

D_s^+ is reconstructed from $D_s^+ \rightarrow \phi \pi^+, \bar{K}^{*0} K^+, K_S^0 K^+$ decay modes. The reconstructed mass window are defined as:

- $1.955 \text{ GeV}/c^2 < M(\phi \pi^+) < 1.981 \text{ GeV}/c^2$ ($\sim \pm 3\sigma$ signal window)
- $1.953 \text{ GeV}/c^2 < M(\bar{K}^{*0} K^+) < 1.983 \text{ GeV}/c^2$ ($\sim \pm 3\sigma$ signal window)
- $1.951 \text{ GeV}/c^2 < M(K_S^0 K^+) < 1.985 \text{ GeV}/c^2$ ($\sim \pm 3\sigma$ signal window).

- Mass constrained and vertex fit is applied on the D_s^+ .

The signal window is selected from the fit of reconstructed distributions as shown in Fig. 3.4.

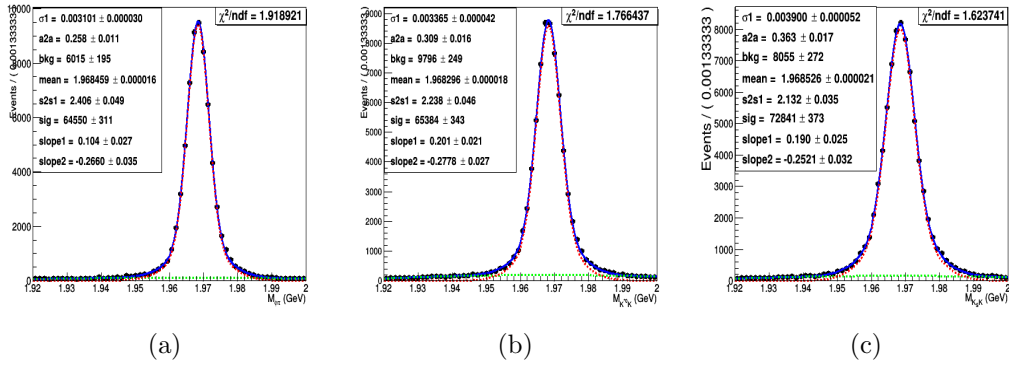


Figure 3.4: The fit to the reconstructed D_s^+ mass for (a) $D_s^+ \rightarrow \phi\pi^+$ (b) $D_s^+ \rightarrow \bar{K}^{*0}K^+$ and (c) $D_s^+ \rightarrow K_S^0K^+$ sub-decays for Signal MC. 1D UML fit is performed, Red (green) curve used for signal (background) and the overall fit is shown by the blue color.

3.4.5 Reconstruction of D^+

D^+ is reconstructed from the $D^+ \rightarrow K^-\pi^+\pi^+$, $K_S^0\pi^+$ decay modes with the same reconstructed mass window:

- $1.855 \text{ GeV}/c^2 < M(K^-\pi^+\pi^+, K_S^0\pi^+) < 1.885 \text{ GeV}/c^2$ ($\sim \pm 3\sigma$ signal window).
- Mass constrained and vertex fit is applied on the D^+ .

3.4.6 Reconstruction of $D_s^{(*)+}$

$D_s^{(*)+}$ is reconstructed from $D_s^+\gamma$. To reduce the combinatorial background, we keep only those candidates which satisfy the criteria: $0.13 \text{ GeV}/c^2 < \Delta M < 0.16 \text{ GeV}/c^2$, where ΔM is the difference between the reconstructed mass of $D_s^{(*)+}$ and D_s^+ ($\Delta M = M(D_s^{(*)+}) - M(D_s^+)$).

3.4.7 Reconstruction of B Meson

B^\pm mesons are reconstructed from: $D_s^{(*)+}\eta$, $D_s^{(*)+}K_S^0$, $D^+K_S^0$ and $D^+\eta$ decay modes. For signal candidates, we use the following selection criteria:

- $-0.18 \text{ GeV} < \Delta E < 0.18 \text{ GeV}$, where $\Delta E = E_B - E_{beam}$, where E_{beam} is the center-of-mass beam energy and E_B are energy of B meson candidates.
- $M_{bc} > 5.20 \text{ GeV}/c^2$, where beam-constrained mass (M_{bc}), $M_{bc} = \sqrt{E_{beam}^2 - |\vec{p}|^2}$.
- Vertex fit has been applied on the reconstructed B .

3.4.8 Optimization of photons energy

η is reconstructed from two photons. We did 2D optimization to optimize energy cut of both photons from eta and the optimized energy of both photons are coming to be greater than 0.3 GeV as shown in Fig. 3.5 (left). Fig. 3.5 (right) shows the FOM curve of energy of photon candidates from $D_s^{*+} \rightarrow D_s^+\gamma$ between the signal events from signal MC and background events are those photons candidates, which are not coming from D_s^{*+} . We have selected only those photons candidates from D_s^{*+} , whose energy in CMS frame is greater than 0.11 GeV.

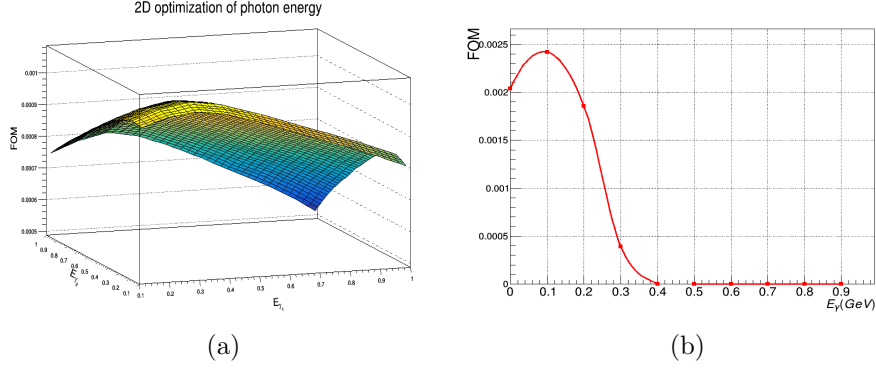


Figure 3.5: Distributions of (a) optimization of the 2D cut for E_{γ_1} and E_{γ_2} (GeV) for $B^+ \rightarrow D_s^+(\rightarrow \phi\pi)\eta(\rightarrow \gamma_1\gamma_2)$ decay mode (b) FOM curve for E_{γ} (GeV) from $D_s^{*+} \rightarrow D_s^+\gamma$ decay mode.

Table 3.1 summarizes the selection criteria and their relative (absolute) efficiency. Relative efficiency is the fraction of truth matched events after applied corresponding cut to truth matched events without cut and absolute efficiency is the fraction of truth matched events after applied corresponding cut to input events.

Selection criteria	Relative (absolute) efficiency (%)					
	$B^+ \rightarrow D_s^+\eta$			$B^+ \rightarrow D_s^+K_S^0$		
	$D_s^+ \rightarrow \phi\pi$	$D_s^+ \rightarrow \bar{K}^{*0}K$	$D_s^+ \rightarrow K_S^0K$	$D_s^+ \rightarrow \phi\pi$	$D_s^+ \rightarrow \bar{K}^{*0}K$	$D_s^+ \rightarrow K_S^0K$
$\pi\text{ID} > 0.2$	97.3(15.6)	98.6(17.4)	–	97.3 (27.4)	98.6(32.8)	–
$K\text{ID} > 0.2$	91.4(14.6)	90.9(16.1)	95.5(17.5)	91.4(25.8)	91.1(30.3)	95.5(32.0)
$0.50 < M_{\eta} \text{ (GeV}/c^2) < 0.58$	87.1(13.9)	86.7(15.3)	91.1(16.7)	–	–	–
$1.006 < M_{\phi} \text{ (GeV}/c^2) < 1.034$ $0.792 < M_{\bar{K}^{*0}} \text{ (GeV}/c^2) < 0.992$ $0.487 < M_{K_S^0} \text{ (GeV}/c^2) < 0.508$ (niskFinder)	83.1(13.3)	81.4(14.4)	79.6(14.6)	78.1(22.0)	76.4(25.4)	74.7(25.1)
$1.955 < M_{D_s(\phi\pi)} \text{ (GeV}/c^2) < 1.981$ $1.953 < M_{D_s(\bar{K}^{*0}K)} \text{ (GeV}/c^2) < 1.983$ $1.951 < M_{D_s(K_S^0K)} \text{ (GeV}/c^2) < 1.985$	75.1(12.0)	77.0(13.6)	76.6(14.0)	70.3(19.8)	72.4(24.1)	72.0(24.1)
$E_{\gamma} > 0.3 \text{ GeV}$	60.2(9.6)	61.7(10.9)	61.5(11.2)	–	–	–
$M_{bc} > 5.27 \text{ GeV}/c^2$	59.8(9.6)	61.4(10.8)	61.2(11.2)	70.2(19.8)	72.2(24.0)	71.9(24.1)

Table 3.1: Selection Criteria along with its relative (absolute) efficiency.

3.4.9 Best Candidate Selection (BCS)

After applying all selection criteria, multiple B candidates per event was manifested in Fig. 3.6 for the $B^+ \rightarrow D_s^+ \eta(\rightarrow \gamma\gamma)$ mode. To reduce the multiplicity,

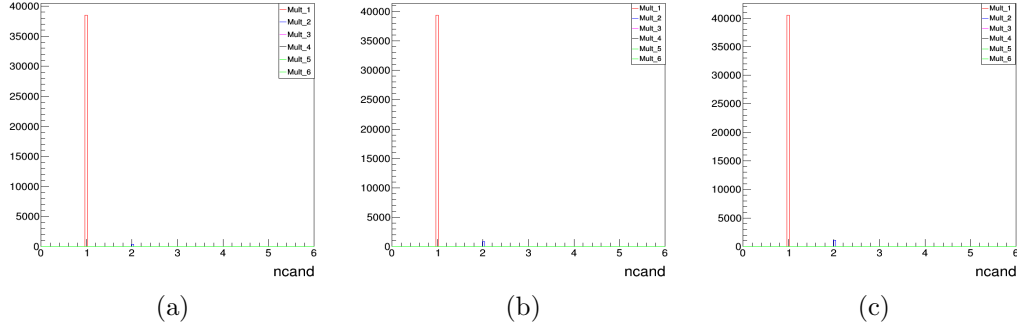


Figure 3.6: Multiple B candidates per event for the (a) $B^+ \rightarrow D_s^+(\rightarrow \phi\pi^+)\eta(\rightarrow \gamma\gamma)$ (b) $B^+ \rightarrow D_s^+(\rightarrow \bar{K}^{*0}K^+)\eta(\rightarrow \gamma\gamma)$ and (c) $B^+ \rightarrow D_s^+(\rightarrow K_S^0K^+)\eta(\rightarrow \gamma\gamma)$ decay mode for Signal MC.

we select B mesons having the least χ^2 , which is defined as:

$$\chi^2 = \left(\frac{M_{D_s} - m_{D_s}^{PDG}}{\sigma_{D_s}} \right)^2 + \left(\frac{M_{bc} - m_B^{PDG}}{\sigma_{M_{bc}}} \right)^2 \quad (3.4.1)$$

We define multiplicity as:

$$\text{Multiplicity (\%)} = \frac{\text{Number of events having candidates more than one} \times 100}{\text{Number of total events}} \quad (3.4.2)$$

BCS efficiency is defined as :

$$\text{BCS efficiency (\%)} = \frac{\text{Truth matched events after BCS (ncand > 1)} \times 100}{\text{Truth matched events before BCS (ncand > 1)}} \quad (3.4.3)$$

Reconstructed efficiency is defined as:

$$\text{Reconstructed efficiency (\%)} = \frac{\text{signal events} \times 100}{\text{Input event}} \quad (3.4.4)$$

Table 3.2 summarizes the multiple candidate in each decay modes. Multiplicity, BCS efficiency and signal efficiency for the mentioned signal modes are estimated in the signal window : $-50 \text{ MeV} < \Delta E < 50 \text{ MeV}$ and $M_{bc} > 5.27 \text{ GeV}/c^2$. For the study of $B^+ \rightarrow D^+ K_S^0$ and $B^+ \rightarrow D^+ \eta$ decay modes, we define χ^2 using the mass of D^+ mesons and M_{bc} . The fitted distribution of ΔE for signal modes are shown in Sec. 3.10 (signal events for reconstructed efficiency is taken from the fitted distribution).

3.5 Signal MC study

The reconstructed distribution of the ΔE variable for $B^+ \rightarrow D_s^+ \eta$, $B^+ \rightarrow D_s^{(*)+} \eta$, $B^+ \rightarrow D^+ \eta$ decay modes with signal MC are shown in Fig. 3.7, 3.8 and 3.9, respectively. The resolution of ΔE distribution for $\eta \rightarrow \pi^- \pi^+ \pi^0$ is coming better as compared to $\eta \rightarrow \gamma \gamma$ because of charge tracks. As expected, we observed self cross feed events for η decay modes, which are mainly coming from fake γ combination. In order to reduced the events from fake gamma combination, we selected only photons with energy in center-of-mass (CM) frame is greater than 0.3 GeV.

In $B^+ \rightarrow D_s^{(*)+} \eta$ decay mode, to reduced the contribution of fake photons from $D_s^{(*)+} \rightarrow D_s^+ \gamma$, we select only photons with energy in CM frame is greater than 0.11 GeV.

3.5 Signal MC study

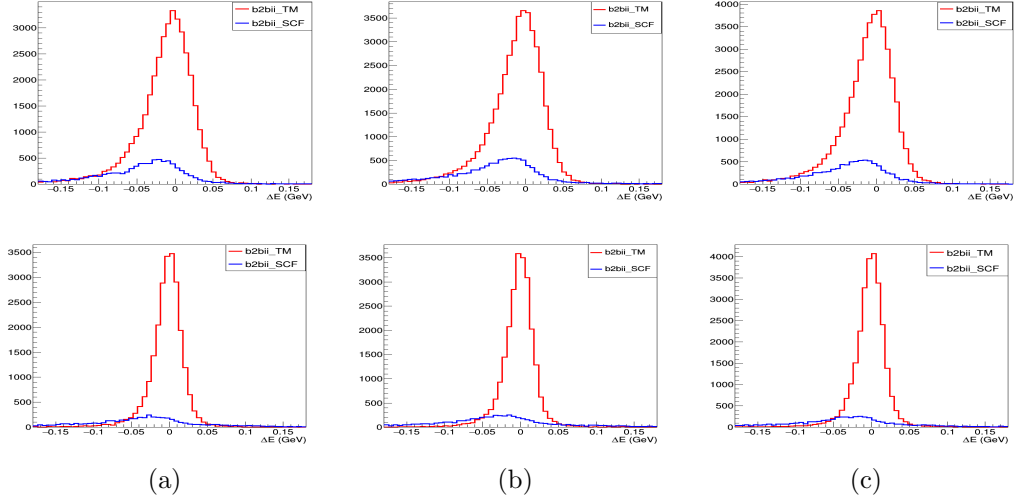


Figure 3.7: Distributions of ΔE for (a) $D_s^+ \rightarrow \phi\pi^+$ (b) $D_s^+ \rightarrow \bar{K}^{*0}K^+$ and (c) $D_s^+ \rightarrow K_S^0K^+$ decay modes. The upper distribution for $\eta \rightarrow \gamma\gamma$ and lower for $\eta \rightarrow \pi^-\pi^+\pi^0$. Red color histogram shows the truth matched events and blue shows the self cross feed events.

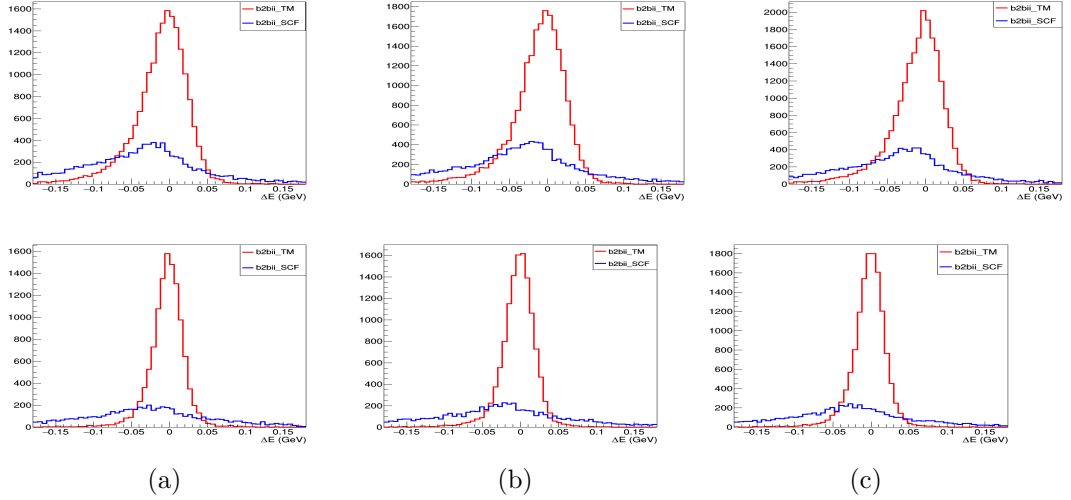


Figure 3.8: Distributions of ΔE for (a) $D_s^+ \rightarrow \phi\pi^+$ (b) $D_s^+ \rightarrow \bar{K}^{*0}K^+$ and (c) $D_s^+ \rightarrow K_S^0K^+$ decay modes. The upper distribution for $\eta \rightarrow \gamma\gamma$ and lower for $\eta \rightarrow \pi^-\pi^+\pi^0$.

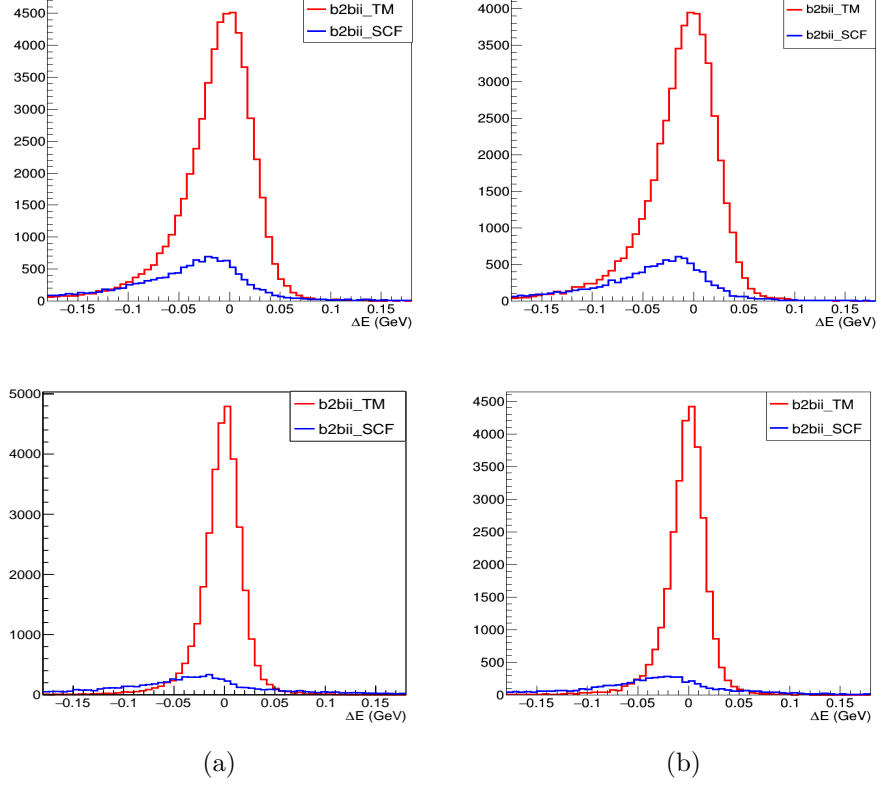


Figure 3.9: Distributions of ΔE for (a) $D^+ \rightarrow K^-\pi^+\pi^+$ (b) $D^+ \rightarrow K_S^0\pi^+$ decay modes. The upper distribution for $\eta \rightarrow \gamma\gamma$ and lower for $\eta \rightarrow \pi^-\pi^+\pi^0$. Red color histogram shows the truth matched events and blue shows the self cross feed events.

The reconstructed distribution of ΔE for $B^+ \rightarrow D_s^+K_S^0$, $B^+ \rightarrow D_s^{(*)+}K_S^0$, $B^+ \rightarrow D^+K_S^0$ decay modes are shown in Fig 3.10, 3.11 and 3.12, respectively.

In $B^+ \rightarrow D_s^{(*)+}K_S^0$ decay mode, to reduced the contribution of fake photons, we select only photons with energy in CM frame is greater than 0.11 GeV.

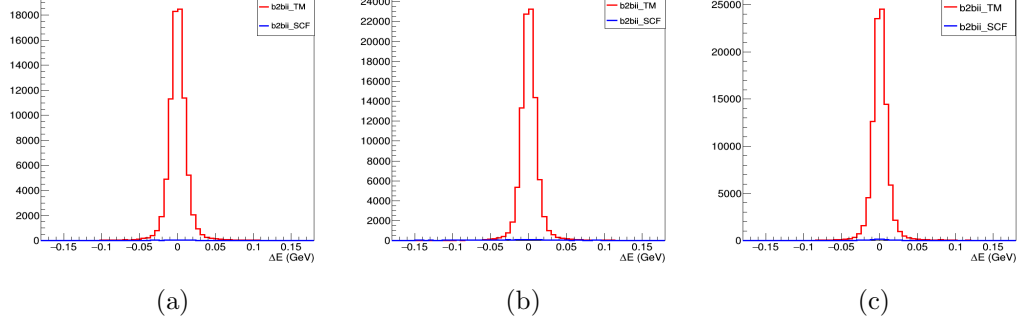


Figure 3.10: Distributions of ΔE for (a) $D_s^+ \rightarrow \phi\pi^+$ (b) $D_s^+ \rightarrow \bar{K}^{*0}K^+$ and (c) $D_s^+ \rightarrow K_S^0K^+$ decay modes. Red color histogram shows the truth matched events and blue shows the self cross feed events.

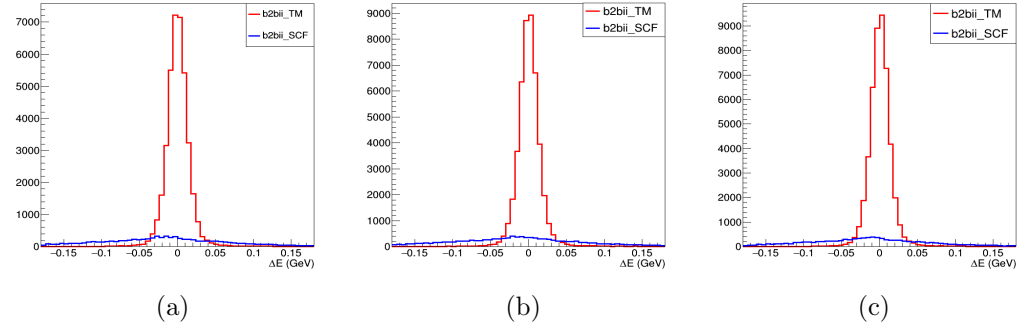


Figure 3.11: Distributions of ΔE for (a) $D_s^+ \rightarrow \phi\pi^+$ (b) $D_s^+ \rightarrow \bar{K}^{*0}K^+$ and (c) $D_s^+ \rightarrow K_S^0K^+$ decay modes. Red color histogram shows the truth matched events and blue shows the self cross feed events.

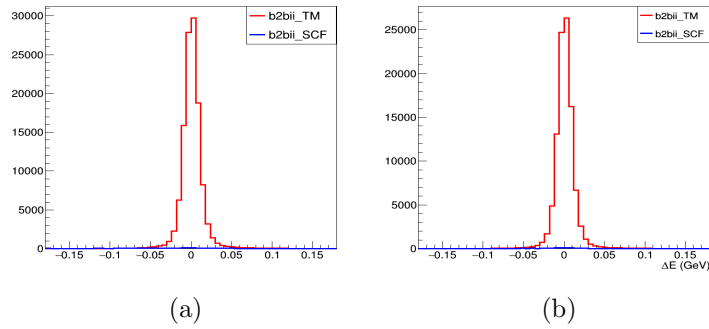


Figure 3.12: Distributions of ΔE for (a) $D^+ \rightarrow K^-\pi^+\pi^+$ (b) $D^+ \rightarrow K_S^0\pi^+$ decay modes. Red color histogram shows the truth matched events and blue shows the self cross feed events.

3.6 Generic MC Study

Decay mode	Multiplicity (%)	BCS efficiency (%)	reconstructed efficiency (%)
$B^+ \rightarrow D_s^+ \eta, \eta \rightarrow \gamma\gamma(\pi^- \pi^+ \pi^0)$			
$D_s^+ \rightarrow \phi\pi^+$	$0.53 \pm 0.04 (2.57 \pm 0.10)$	$61.96 \pm 6.27 (56.89 \pm 3.58)$	$6.0 \pm 0.05 (3.24 \pm 0.03)$
$D_s^+ \rightarrow \bar{K}^{*0} K^+$	$1.13 \pm 0.05 (3.34 \pm 0.11)$	$58.38 \pm 4.0 (60.40 \pm 3.2)$	$6.4 \pm 0.05 (3.26 \pm 0.03)$
$D_s^+ \rightarrow K_S^0 K^+$	$1.77 \pm 0.06 (4.0 \pm 0.11)$	$57.18 \pm 2.79 (55.94 \pm 2.29)$	$6.7 \pm 0.05 (3.95 \pm 0.03)$
$B^+ \rightarrow D_s^{(*)+} \eta, \eta \rightarrow \gamma\gamma(\pi^- \pi^+ \pi^0)$			
$D_s^+ \rightarrow \phi\pi^+$	$8.92 \pm 0.21 (12.80 \pm 0.30)$	$70.28 \pm 2.61 (68.50 \pm 2.55)$	$1.8 \pm 0.03 (0.97 \pm 0.02)$
$D_s^+ \rightarrow \bar{K}^{*0} K^+$	$9.13 \pm 0.21 (13.13 \pm 0.29)$	$69.37 \pm 2.54 (65.17 \pm 2.32)$	$1.4 \pm 0.03 (0.74 \pm 0.02)$
$D_s^+ \rightarrow K_S^0 K^+$	$9.57 \pm 0.20 (13.87 \pm 0.27)$	$66.69 \pm 2.17 (65.09 \pm 2.0)$	$1.2 \pm 0.04 (0.74 \pm 0.02)$
$B^+ \rightarrow D_s^+ K_S^0$			
$D_s^+ \rightarrow \phi\pi^+$	1.35 ± 0.04	54.99 ± 2.08	7.8 ± 0.05
$D_s^+ \rightarrow \bar{K}^{*0} K^+$	1.83 ± 0.04	57.87 ± 1.85	9.4 ± 0.05
$D_s^+ \rightarrow K_S^0 K^+$	3.32 ± 0.06	57.40 ± 1.30	9.7 ± 0.05
$B^+ \rightarrow D_s^{(*)+} K_S^0$			
$D_s^+ \rightarrow \phi\pi^+$	9.73 ± 0.15	66.65 ± 1.50	2.3 ± 0.03
$D_s^+ \rightarrow \bar{K}^{*0} K^+$	10.27 ± 0.15	66.17 ± 1.40	2.0 ± 0.03
$D_s^+ \rightarrow K_S^0 K^+$	11.12 ± 0.15	65.35 ± 1.21	1.6 ± 0.02
$B^+ \rightarrow D^+ K_S^0$			
$D^+ \rightarrow K^- \pi^+ \pi^+$	1.66 ± 0.04	57.87 ± 1.72	12.7 ± 0.06
$D^+ \rightarrow K_S^0 \pi^+$	3.04 ± 0.06	57.23 ± 1.36	13.4 ± 0.06
$B^+ \rightarrow D^+ \eta, \eta \rightarrow \gamma\gamma(\pi^- \pi^+ \pi^0)$			
$D^+ \rightarrow K^- \pi^+ \pi^+$	$0.89 \pm 0.04 (2.86 \pm 0.09)$	$66.22 \pm 4.58 (58.26 \pm 2.59)$	$8.4 \pm 0.05 (4.45 \pm 0.04)$
$D^+ \rightarrow K_S^0 \pi^+$	$1.68 \pm 0.06 (3.85 \pm 0.11)$	$56.61 \pm 2.83 (56.20 \pm 2.28)$	$8.1 \pm 0.05 (4.80 \pm 0.04)$

Table 3.2: BCS and reconstructed efficiency for the decay mode of interest.

From the table 3.2, we clearly observe that the multiplicity for $B^+ \rightarrow D_s^+ \eta$ and $B^+ \rightarrow D_s^+ K_S^0$ is around 2% but for $B^+ \rightarrow D_s^{(*)+} \eta$ and $B^+ \rightarrow D_s^{(*)+} K_S^0$ multiplicity is around 12% (the increase in multiplicity is due to the fake γ).

3.6 Generic MC Study

For generic MC study, we are using MC which contains all the possible decays and the size of sample is five times of Belle data. The expected background in ΔE distribution for the $B^+ \rightarrow D_s^+ \eta$, $B^+ \rightarrow D_s^{(*)+} \eta$ and $B^+ \rightarrow D^+ \eta$ decay modes are shown in the Fig. 3.13 with combined D_s^+ , D^+ sub decay modes. Few background events in $B^+ \rightarrow D^+ \eta$ decay mode are coming from $\bar{B}^0 \rightarrow D^+ \rho^-$, which are peaking around -0.17 GeV. On the other side, ΔE distribution for the

$B^+ \rightarrow D_s^+ K_S^0$, $B^+ \rightarrow D_s^{(*)+} K_S^0$ and $B^+ \rightarrow D^+ K_S^0$ decay modes are shown in Fig. 3.14 with combined D_s^+ , D^+ sub decay modes. Some background events in $B^+ \rightarrow D^+ K_S^0$ decay mode are coming from $\bar{B}^0 \rightarrow D^+ K^{*-}$, which are peaking around -0.17 GeV. The plots are scaled to the Belle luminosity. For the extraction of signal events use $M_{bc} > 5.27 \text{ GeV}/c^2$ and also using M_{D_s} signal window to plot ΔE distribution. As expected, large fraction of the combinatorial background is coming from the continuum samples.

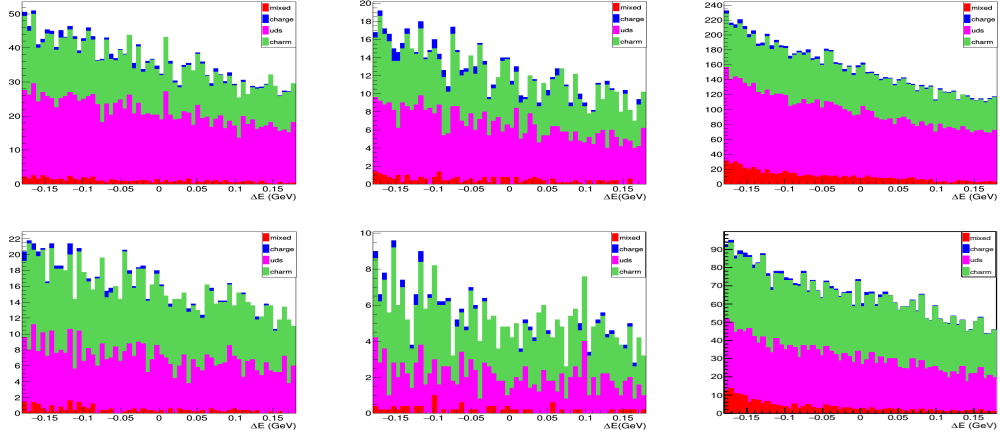


Figure 3.13: Expected background in ΔE distributions for the (a) $B^+ \rightarrow D_s^+ \eta$ (left) (b) $B^+ \rightarrow D_s^{(*)+} \eta$ (middle) and (c) $B^+ \rightarrow D^+ \eta$ (right) decay mode using generic MC. The upper distribution for $\eta \rightarrow \gamma\gamma$ and lower for $\eta \rightarrow \pi^- \pi^+ \pi^0$.

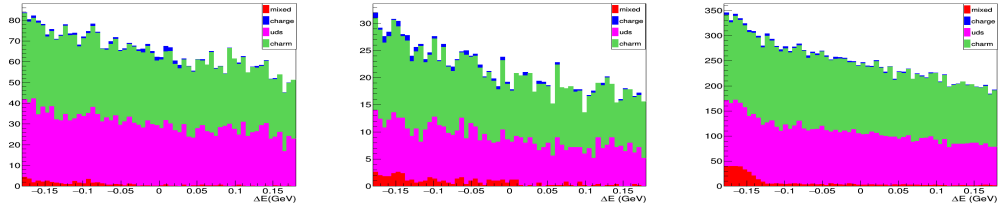


Figure 3.14: Expected background in ΔE distributions for the (a) $B^+ \rightarrow D_s^+ K_S^0$ (left) (b) $B^+ \rightarrow D_s^{(*)+} K_S^0$ (middle) and (c) $B^+ \rightarrow D^+ K_S^0$ (right) decay mode using generic MC.

3.7 Continuum Suppression

The dominant background comes from $e^+e^- \rightarrow q\bar{q}$ ($q = u, d, s, c$) continuum events. In the $\Upsilon(4S)$ rest frame, $B\bar{B}$ events are spherical for signal and jet-like shapes for continuum events. To distinguish between the signal and the background we use seven variables that are described below:

- KSW moments: two modified Fox-Wolfram moments according to their importance [70].
- $|\cos\theta_T|$: the absolute value of cosine of the angle between the thrust axis of the B candidate and that of the rest of the event in center of mass frame. This variable is uniform for the signal and peaks at 1 for continuum events.
- $B_{ThrustB}$: Magnitude of the signal B thrust axis.
- Cleo cone: The CLEO cones are a set of concentric cones with different opening angle having the thrust axis as symmetry axis. It has 9 cones, of opening angle between 10 and 90 degrees, 10 degrees apart one from the other. Out of 9 cleo cones, we have used only cleo cone with opening angle of 10° .
- Flavor tagger: The Flavor Tagger is a module based on multivariate methods. It can be used also in addition to continuum suppression in events with a charged B meson pair. We used **FBDT_qrcombined** variable [71].

3.7 Continuum Suppression

- $|\cos\theta_B|$: the absolute value of cosine of the angle between the B candidate and the beam axis in the e^+e^- center-of-mass frame. The B meson direction is almost perpendicular to the beam axis and hence for signal distribution peaks at zero, whereas the distribution for $q\bar{q}$ is flat due to its random direction.

Fig. 3.15 shows the 7 continuum variables, which are used for continuum suppression. The continuum suppression is done with the FastBDT default method of BASF2. It gives a good out-of-the-box performance, is robust against over-fitting and fast in training and application. It is trained with independent samples of truth-matched signal MC and $q\bar{q}$ generic MC samples. For training, we are using 80% and for the test, using 20% of signal and continuum events. We implement the loose selection window for ΔE : [-0.20 - 0.20] GeV and $M_{bc} > 5.20$ GeV/ c^2 to increase the number of continuum events. The Neural Network (NN) output from training and test sample and purity are shown in Fig. 3.16. It was verified with an independent sample of signal and $udsc$ MC that NN is not overtrained is shown in Fig. 3.16 (left) with train and test NN output for $B^+ \rightarrow D_s^+ \eta$ decay mode.

The signal efficiency vs background rejection performance of these variables is illustrated in the ROC curve given in Fig. 3.17. The area of the ROC curve determines the amount of improvement in terms of rejecting more background while retaining most of the signal. For $B^+ \rightarrow D_s^+(\rightarrow \bar{K}^{*0}K^+)\eta$ and $B^+ \rightarrow D_s^+(\rightarrow K_S^0K^+)\eta$ decay mode, we have used same continuum variables and the ROC curve as shown in Fig. 3.17. We have used the same seven input continuum variables

3.7 Continuum Suppression

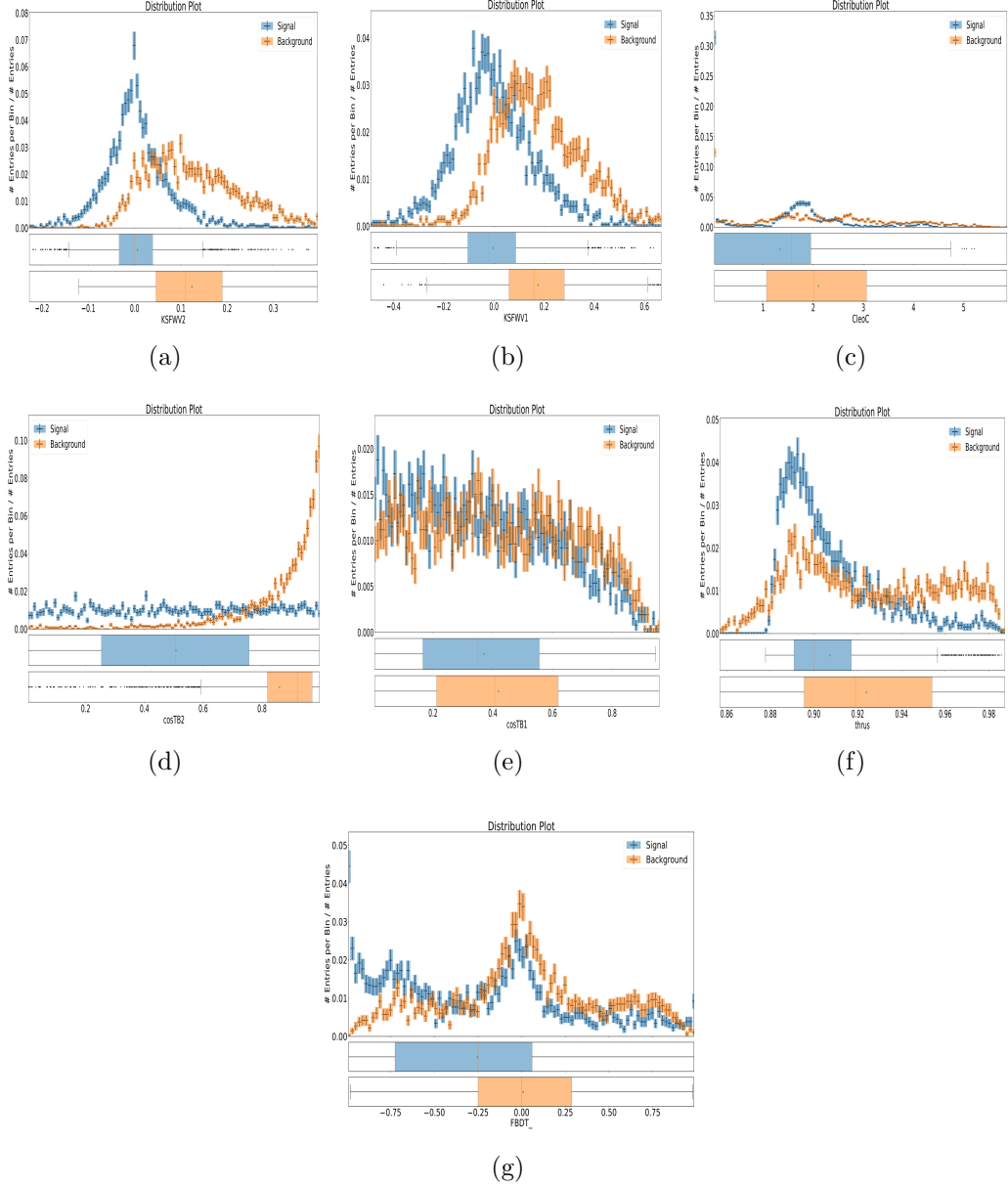


Figure 3.15: Distribution of continuum variables (a) ksfwhso12 (b) ksfwhso02 (c) cleo cone1 (d) $|\cos\theta_T|$ (e) $|\cos\theta_B|$ (f) $B_{ThrustB}$ and (g) FBDT_qrCombined.

for $B^+ \rightarrow D_s^+ K_S^0$ decay modes and the ROC curve is shown in the Fig. 3.18. For the reduction of continuum events from $B^+ \rightarrow D_s^{(*)+} \eta$ and $B^+ \rightarrow D_s^{(*)+} K_S^0$ decay modes, we have used the same seven input continuum variables with same

3.7 Continuum Suppression

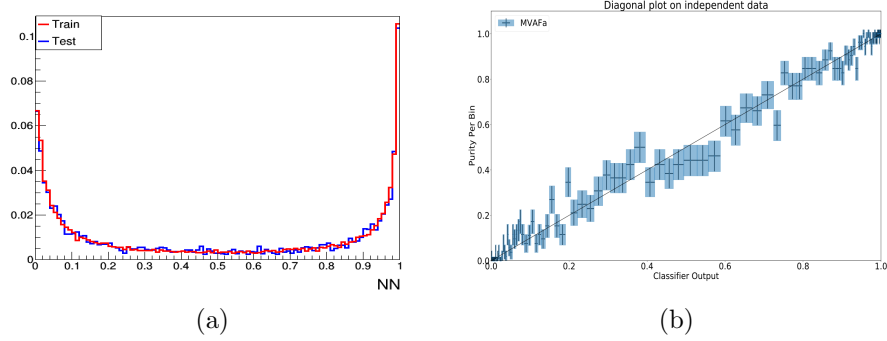


Figure 3.16: Distribution of (a) Neural Network output with train and test samples (b) Purity for $B^+ \rightarrow D_s^+(\rightarrow \phi\pi^+)\eta(\rightarrow \gamma\gamma)$ decay mode.

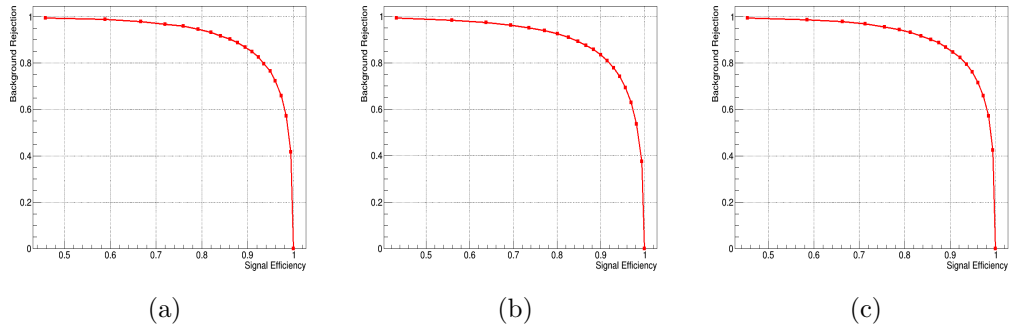


Figure 3.17: Distribution of ROC curve for (a) $B^+ \rightarrow D_s^+(\rightarrow \phi\pi)\eta(\rightarrow \gamma\gamma)$ (b) $B^+ \rightarrow D_s^+(\rightarrow \bar{K}^{*0}K^+)\eta(\rightarrow \gamma\gamma)$ (c) $B^+ \rightarrow D_s^+(\rightarrow K_S^0K^+)\eta(\rightarrow \gamma\gamma)$ decay mode.

trained sample of $B^+ \rightarrow D_s^+\eta$ and $B^+ \rightarrow D_s^+K_S^0$ decay mode, respectively.

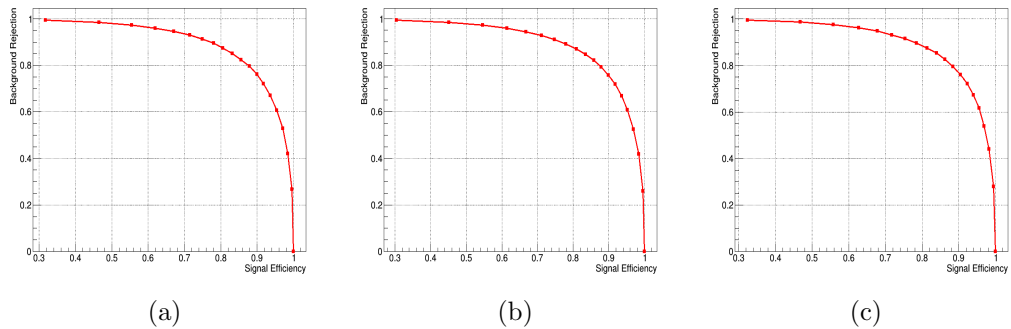


Figure 3.18: Distribution of ROC curve for (a) $B^+ \rightarrow D_s^+(\rightarrow \phi\pi^+)K_S^0$ (b) $B^+ \rightarrow D_s^+(\rightarrow \bar{K}^{*0}K^+)K_S^0$ (c) $B^+ \rightarrow D_s^+(\rightarrow K_S^0K^+)K_S^0$ decay modes.

3.7 Continuum Suppression

$B^+ \rightarrow D_s^+ \eta (\rightarrow \gamma\gamma)$			$B^+ \rightarrow D_s^+ K_S^0$			
	$D_s^+ \rightarrow \phi\pi^+$	$D_s^+ \rightarrow K^{*0}K^+$	$D_s^+ \rightarrow K_S^0 K^+$	$D_s^+ \rightarrow \phi\pi^+$	$D_s^+ \rightarrow K^{*0}K^+$	$D_s^+ \rightarrow K_S^0 K^+$
Signal eff.(%)	90	90	90	90	90	90
Bkg. reject.(%)	87	83	87	76	76	76
$B^+ \rightarrow D^+ K_S^0 (\rightarrow D^+ \eta (\rightarrow \gamma\gamma))$						
$D^+ \rightarrow K^- \pi^+ \pi^+$			$D^+ \rightarrow K_S^0 \pi^+$			
Signal eff.(%)	90 (90)		90 (90)			
Bkg. reject.(%)	77 (84)		84 (88)			

Table 3.3: Signal efficiency and background rejection from ROC curve for $B^+ \rightarrow D_s^+ \eta$, $B^+ \rightarrow D_s^+ K_S^0$ and $B^+ \rightarrow D^+ K_S^0$ decay modes.

We also perform the continuum suppression with same seven continuum variables as mentioned above for $B^+ \rightarrow D^+ K_S^0$ and $B^+ \rightarrow D^+ \eta$ decay modes. Table 3.3 is updated with the signal efficiency and background rejection obtained from ROC curve of signal decay modes.

When we look at correlation matrix between continuum variables with signal and background for $B^+ \rightarrow D_s^+ \eta$ decay modes, we did not find any high correlation between these variables. Fig. 3.19, 3.20 and 3.21 show the correlation matrix of signal and background, which show that no variable is correlated for $B^+ \rightarrow D_s^+ \eta$ decay mode.

3.7 Continuum Suppression

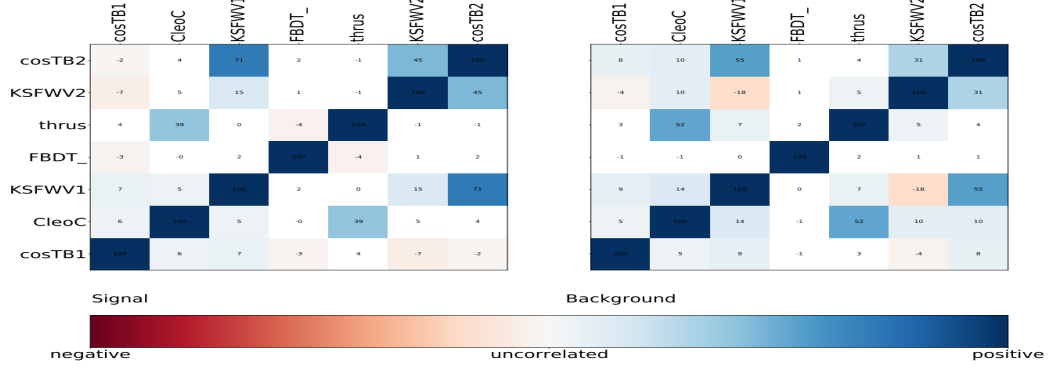


Figure 3.19: Correlation matrix of signal and background for $B^+ \rightarrow D_s^+(\rightarrow \phi\pi^+)\eta$ decay mode.

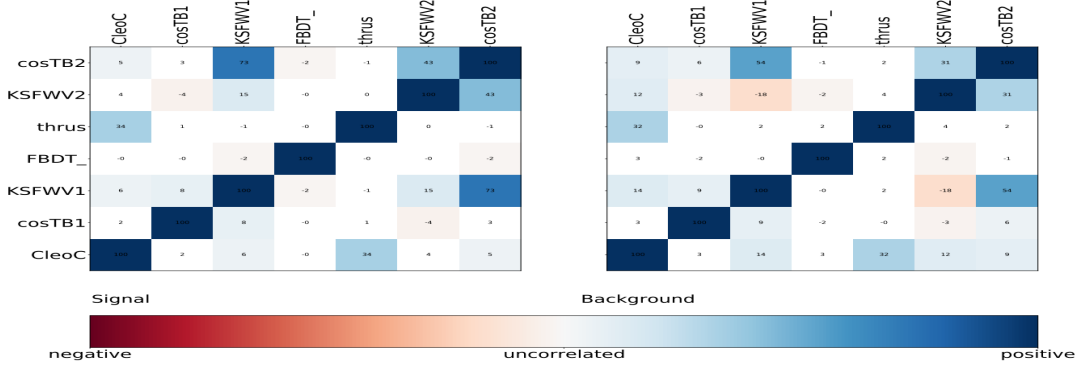


Figure 3.20: Correlation matrix of signal and background for $B^+ \rightarrow D_s^+(\rightarrow \bar{K}^{*0}K^+)\eta$ decay mode.

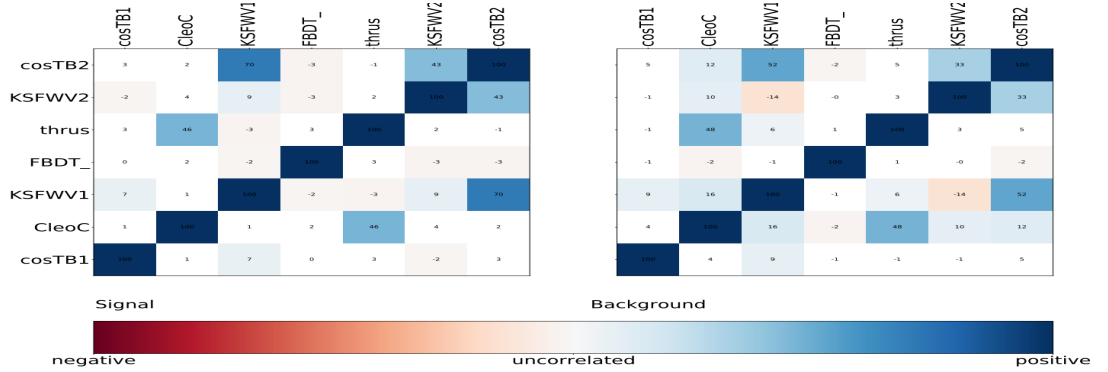


Figure 3.21: Correlation matrix of signal and background for $B^+ \rightarrow D_s^+(\rightarrow K_s^0 K^+)\eta$ decay mode.

3.8 Optimization Cut on FBDT Output

Fig. 3.22, 3.23 and 3.24 show the correlation between the ΔE , M_{bc} and M_{D_s} with NN variable for $B^+ \rightarrow D_s^+ \eta$ decay mode, respectively. We did not observe any correlation between these variables.

3.8 Optimization Cut on FBDT Output

The selection of FBDT cut should include as many signal events as possible while suppressing many background events. In this analysis, FBDT cut that makes the highest Figure of Merit (FoM) [72] is chosen.

$$FOM = \frac{\sum_{i=1}^{i=3} [\varepsilon_{signal(i)} \times \text{weight factor}_i]}{a/2 + \sqrt{bkg}} \quad (3.8.1)$$

Where, ε_{signal} = signal efficiency from signal MC, bkg is the expected number of background events within signal region from generic MC, $a = 3$, normalized the FOM by the weight factor of branching fraction of D_s^+ sub decay modes due to combine study.

$$\text{weight factor}_{\phi\pi^+} = \frac{B.F(D_s^+ \rightarrow \phi\pi^+)}{B.F(D_s^+ \rightarrow \phi\pi^+) + B.F(D_s^+ \rightarrow \bar{K}^{*0}K^+) + B.F(D_s^+ \rightarrow K_S^0 K^+)} \quad (3.8.2)$$

$$\text{weight factor}_{K^{*0}K^+} = \frac{B.F(D_s^+ \rightarrow K^{*0}K^+)}{B.F(D_s^+ \rightarrow \phi\pi^+) + B.F(D_s^+ \rightarrow \bar{K}^{*0}K^+) + B.F(D_s^+ \rightarrow K_S^0 K^+)} \quad (3.8.3)$$

3.8 Optimization Cut on FBDT Output

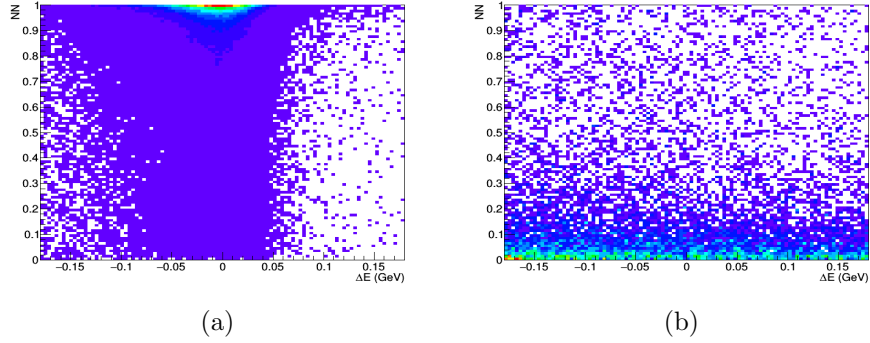


Figure 3.22: NN Versus ΔE (a) Signal (b) Generic MC samples for $B^+ \rightarrow D_s^+ \eta$ decay mode.

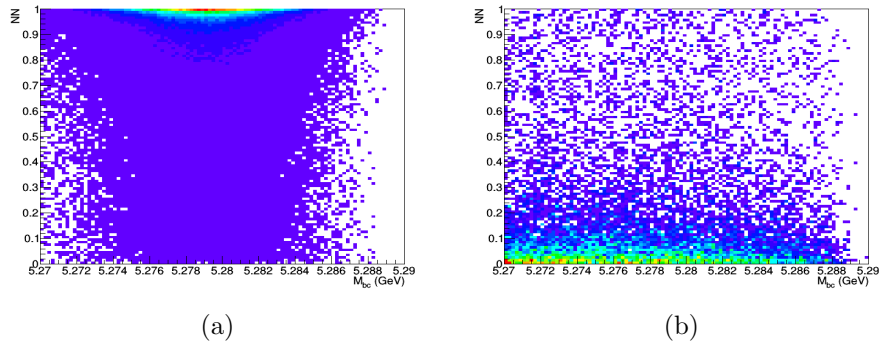


Figure 3.23: NN Versus M_{bc} (a) Signal (b) Generic MC samples for $B^+ \rightarrow D_s^+ \eta$ decay mode.

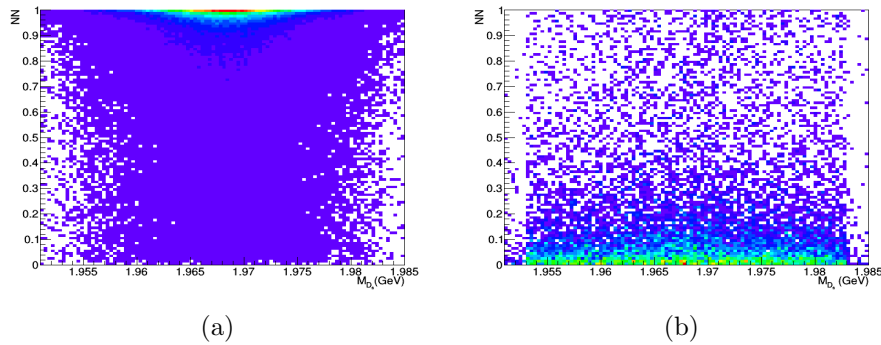


Figure 3.24: NN Versus M_{D_s} (a) Signal (b) Generic MC samples for $B^+ \rightarrow D_s^+ \eta$ decay mode.

3.8 Optimization Cut on FBDT Output

$$\text{weight factor}_{K_S^0 K^+} = \frac{B.F(D_s^+ \rightarrow K_S^0 K^+)}{B.F(D_s^+ \rightarrow \phi\pi^+) + B.F(D_s^+ \rightarrow \bar{K}^{*0} K^+) + B.F(D_s^+ \rightarrow K_S^0 K^+)} \quad (3.8.4)$$

For optimization of FOM, we used ΔE : [-100-100] MeV and $M_{bc} > 5.27 \text{ GeV}/c^2$. FOM distribution is shown in Fig. 3.25 for $B^+ \rightarrow D_s^+ \eta$, $B^+ \rightarrow D_s^{(*)+} \eta$ and $B^+ \rightarrow D^+ \eta$ decay modes. Fig. 3.26 shows the FOM distribution of $B^+ \rightarrow D_s^+ K_S^0$, $B^+ \rightarrow D_s^{(*)+} K_S^0$ and $B^+ \rightarrow D^+ K_S^0$ decay modes. Table 3.4 is updated with the number of continuum events before and after applied NN cut with five streams of generic MC samples. From Fig 3.25 and 3.26, are optimized with FOM cut,

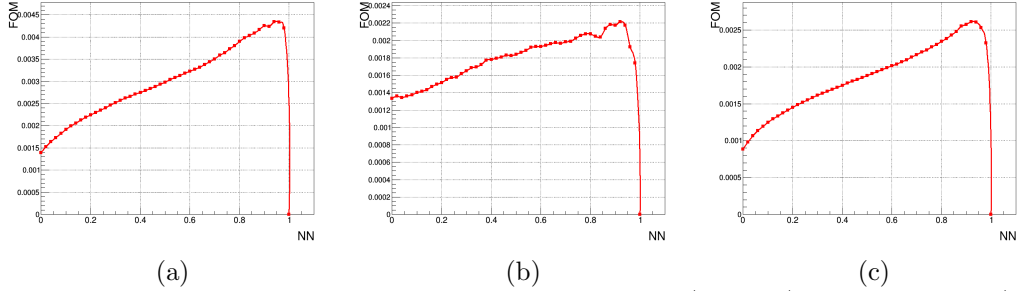


Figure 3.25: Distribution of FOM curve for (a) $B^+ \rightarrow D_s^+ \eta(\rightarrow \gamma\gamma)$ (b) $B^+ \rightarrow D_s^{(*)+} \eta(\rightarrow \gamma\gamma)$ (c) $B^+ \rightarrow D^+ \eta(\rightarrow \gamma\gamma)$ decay modes.

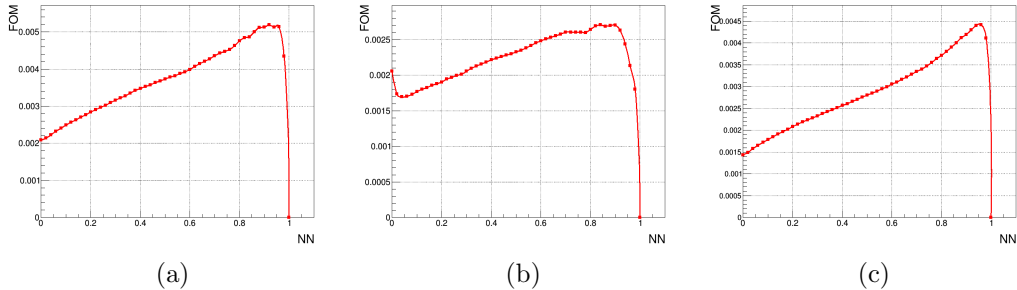


Figure 3.26: Distribution of FOM curve for (a) $B^+ \rightarrow D_s^+ K_S^0$ (b) $B^+ \rightarrow D_s^{(*)+} K_S^0$ (c) $B^+ \rightarrow D^+ K_S^0$ decay modes.

3.9 Rare Background Study

$B^+ \rightarrow D_s^+ \eta(\rightarrow \gamma\gamma)/B^+ \rightarrow D_s^{*+} \eta(\rightarrow \gamma\gamma)$			$B^+ \rightarrow D_s^+ K_S^0/B^+ \rightarrow D_s^{*+} K_S^0$			
	$D_s^+ \rightarrow \phi\pi^+$	$D_s^+ \rightarrow K^{*0}K^+$	$D_s^+ \rightarrow K_S^0K^+$	$D_s^+ \rightarrow \phi\pi^+$	$D_s^+ \rightarrow K^{*0}K^+$	$D_s^+ \rightarrow K_S^0K^+$
Without NN	13306/5454	59477/23354	11802/4854	28539/11474	95745/37501	24047/9798
With NN cut	152/97	1129/342	200/66	348/147	1392/403	324/95
$B^+ \rightarrow D^+ K_S^0/B^+ \rightarrow D^+ \eta(\rightarrow \gamma\gamma)$						
	$D^+ \rightarrow K^- \pi^+ \pi^+$			$D^+ \rightarrow K_S^0 \pi^+$		
Without NN	516460/314541			47130/22938		
With NN cut	8081/6505			752/513		

Table 3.4: Number of continuum events before and after applied NN cut for all signal decay modes with five streams of generic MC samples.

which comes out to be greater than 0.92 for η and K_S^0 decay modes. Fig. 3.27 shows the distribution of ΔE with combine sub decay modes of D_s^+ including five streams of generic MC after varying the NN cut. We clearly observed NN effect on ΔE distribution.

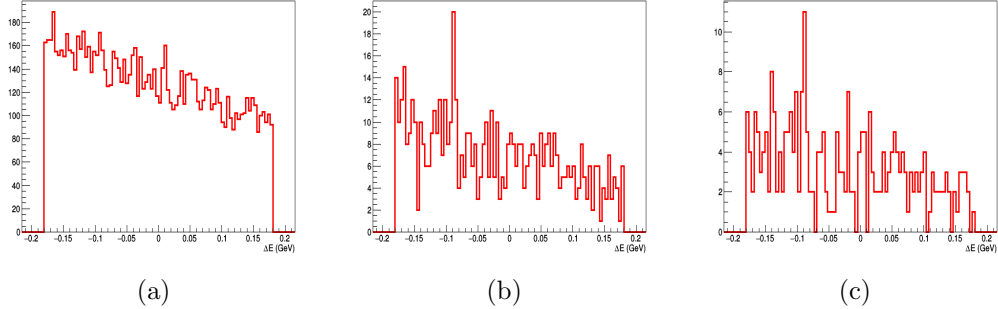


Figure 3.27: Distribution of ΔE (a) Without NN cut (b) NN > 0.8 and (c) NN > 0.92 for $B^+ \rightarrow D_s^+ \eta(\rightarrow \gamma\gamma)$ decay mode with $M_{bc} > 5.27 \text{ GeV}/c^2$.

3.9 Rare Background Study

For the rare background study, we use the rare MC sample counting possible rare B decays, which is 50 times as compared to the Belle data.

We do not observe any peaking background for $B^+ \rightarrow D_s^+ \eta(\rightarrow \gamma\gamma)$, $B^+ \rightarrow D_s^{(*)+}(\rightarrow D_s^+ \gamma) \eta(\rightarrow \gamma\gamma)$ and $B^+ \rightarrow D^+ \eta(\rightarrow \gamma\gamma)$ decay modes as shown in Fig. 3.28. Few background events are coming from $B^+ \rightarrow D_s^+ \pi^0, \bar{D}^{*0} \rho^+$ due to same final state as $B^+ \rightarrow D_s^+ \eta$ decay mode. And few events are coming

3.9 Rare Background Study

from $\bar{D}^{*0} e^+ \nu_e$ and $\bar{D}^{*0} \mu^+ \nu_\mu$ decay modes. In $B^+ \rightarrow D^+ \eta$ decay mode, few background events are coming from $B^+ \rightarrow \pi^+ K^0 \eta, \eta K_0^{*+}$. The plots are scaled to the Belle luminosity. Fig. 3.29 shows the ΔE distribution for the $B^+ \rightarrow D_s^+ K_S^0$,

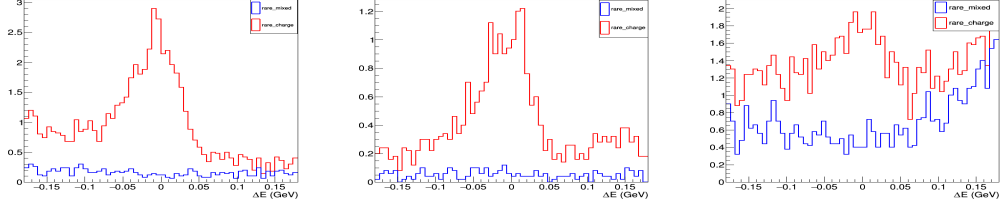


Figure 3.28: Expected background in ΔE distributions for the (a) $B^+ \rightarrow D_s^+ \eta(\rightarrow \gamma\gamma)$ (left) (b) $B^+ \rightarrow D_s^{(*)+} \eta(\rightarrow \gamma\gamma)$ (middle) and (c) $B^+ \rightarrow D^+ \eta(\rightarrow \gamma\gamma)$ (right) decay modes using rare MC. Red color histogram used for charged and blue color histogram for mixed sample.

$B^+ \rightarrow D_s^{(*)+}(\rightarrow D_s^+ \gamma) K_S^0$ and $B^+ \rightarrow D^+ K_S^0$ decay modes and all plots are scaled to the Belle luminosity. In $B^+ \rightarrow D_s^+ K_S^0$ decay mode, background around 0 GeV is coming from the $B^+ \rightarrow K^+ K^0 \bar{K}^{*0}, \phi \bar{K}^{*+}, a_1^+ K^0$ decay modes and peaking around -0.15 GeV due to $B^0 \rightarrow K^{*+} D_s^-$. We do not observe any significant peaking background for $B^+ \rightarrow D_s^{(*)+}(\rightarrow D_s^+ \gamma) K_S^0$ decay mode. For $B^+ \rightarrow D^+ K_S^0$ decay modes, background events are mainly coming from $B^+ \rightarrow \bar{K}^{*0} K^{*+}, a_1^+ K^0, \bar{D}^{*0} \rho^+$ decay modes.

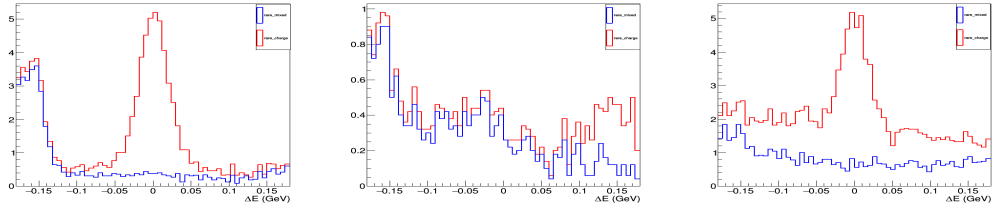


Figure 3.29: Expected background in ΔE distributions for the (a) $B^+ \rightarrow D_s^+ K_S^0$ (left) (b) $B^+ \rightarrow D_s^{(*)+} K_S^0$ (middle) and (c) $B^+ \rightarrow D^+ K_S^0$ (right) decay modes using rare MC. Red color histogram used for charged and blue color histogram for mixed sample.

3.10 Fitted ΔE distribution with Signal MC

Fig. 3.30, 3.31, 3.32, 3.33, 3.34, 3.35, 3.36, 3.37, and 3.38 show the fitted distribution of $B^+ \rightarrow D_s^+ \eta(\rightarrow \gamma\gamma)$, $B^+ \rightarrow D_s^+ \eta(\rightarrow \pi\pi\pi^0)$, $B^+ \rightarrow D_s^{(*)+} \eta(\rightarrow \gamma\gamma)$, $B^+ \rightarrow D_s^{(*)+} \eta(\rightarrow \pi\pi\pi^0)$, $B^+ \rightarrow D_s^+ K_S^0$, $B^+ \rightarrow D_s^{(*)+} K_S^0$, $B^+ \rightarrow D^+ K_S^0$ and $B^+ \rightarrow D^+ \eta(\rightarrow \gamma\gamma)$, $B^+ \rightarrow D^+ \eta(\rightarrow \pi\pi\pi^0)$ decay modes with signal MC, respectively. The events from the fitted distributions are used for calculating the reconstructed efficiency.

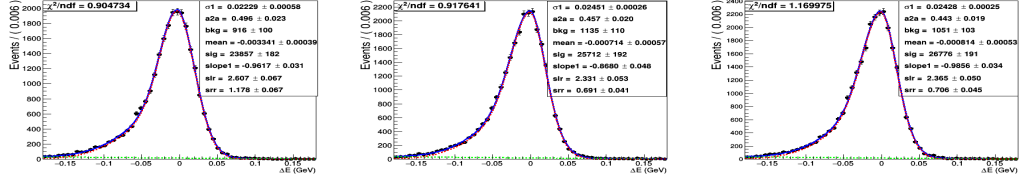


Figure 3.30: 1D UML fit of ΔE for the signal MC sample of $B^+ \rightarrow D_s^+ \eta(\rightarrow \gamma\gamma)$ (a) $D_s^+ \rightarrow \phi\pi^+$ (left) (b) $D_s^+ \rightarrow \bar{K}^{*0}K^+$ (middle) and (c) $D_s^+ \rightarrow K_S^0 K^+$ (right) decay modes. Here, $a2a = \text{area of Gaussian 2} / \text{area of Gaussian 1}$, $slr = \sigma_L / \sigma_1$, $srr = \sigma_R / \sigma_1$. Red (green) curve used for a sum of Gaussian (1^{st} order polynomial) and blue curve show the overall fit.

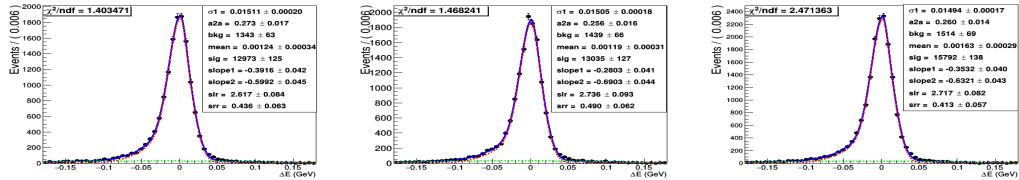


Figure 3.31: 1D UML fit of ΔE for the signal MC sample of $B^+ \rightarrow D_s^+ \eta(\rightarrow \pi^- \pi^+ \pi^0)$ (a) $D_s^+ \rightarrow \phi\pi^+$ (left) (b) $D_s^+ \rightarrow \bar{K}^{*0}K^+$ (middle) and (c) $D_s^+ \rightarrow K_S^0 K^+$ (right) decay modes.

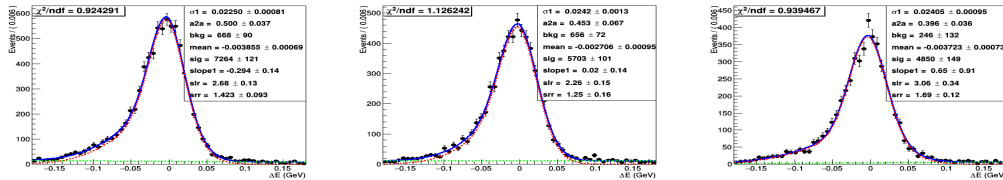


Figure 3.32: 1D UML fit of ΔE for the signal MC sample of $B^+ \rightarrow D_s^{*+} \eta(\rightarrow \gamma\gamma)$ (a) $D_s^{*+} \rightarrow \phi\pi^+$ (left) (b) $D_s^{*+} \rightarrow \bar{K}^{*0}K^+$ (middle) and (c) $D_s^{*+} \rightarrow K_S^0 K^+$ (right) decay modes.

3.10 Fitted ΔE distribution with Signal MC

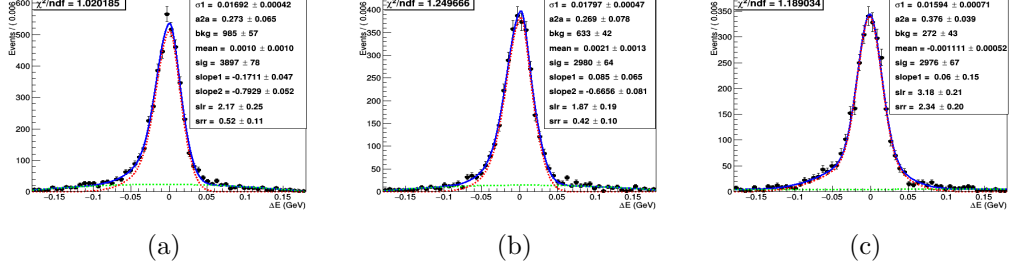


Figure 3.33: 1D UML fit of ΔE for the signal MC sample of $B^+ \rightarrow D_s^{*+} \eta (\rightarrow \pi^- \pi^+ \pi^0)$ (a) $D_s^+ \rightarrow \phi \pi^+$ (b) $D_s^+ \rightarrow \bar{K}^{*0} K^+$ and (c) $D_s^+ \rightarrow K_S^0 K^+$ decay modes. Red (green) color used for a sum of Gaussian (1^{st} order polynomial) PDF and blue curve shows the overall fit.

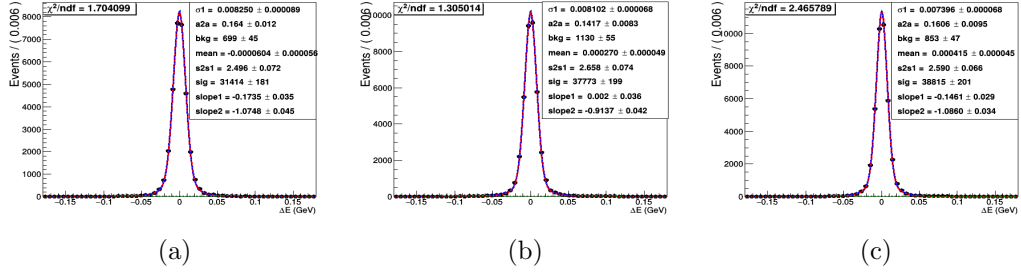


Figure 3.34: 1D UML fit of ΔE for the signal MC sample of $B^+ \rightarrow D_s^+ K_S^0$ (a) $D_s^+ \rightarrow \phi \pi^+$ (b) $D_s^+ \rightarrow \bar{K}^{*0} K^+$ and (c) $D_s^+ \rightarrow K_S^0 K^+$ decay modes. Here, $a_2a = \text{area of Gaussian 2/ area of Gaussian 1}$, $s_2s_1 = \sigma_2/\sigma_1$. Red (green) color used for a sum of Gaussian (2^{nd} order polynomial) PDF and blue curve shows the overall fit.

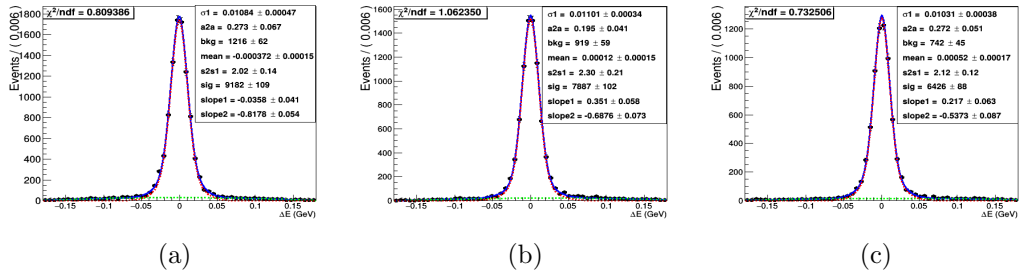


Figure 3.35: 1D UML of ΔE for the signal MC sample of $B^+ \rightarrow D_s^{(*)+} K_S^0$ (a) $D_s^+ \rightarrow \phi \pi^+$ (b) $D_s^+ \rightarrow \bar{K}^{*0} K^+$ and (c) $D_s^+ \rightarrow K_S^0 K^+$ decay modes. Red (green) color used for a sum of Gaussian (2^{nd} order polynomial) PDF and blue curve shows the overall fit.

3.10 Fitted ΔE distribution with Signal MC

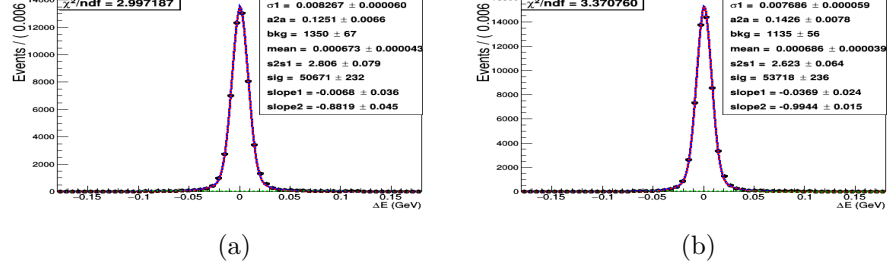


Figure 3.36: 1D UML fit of ΔE for the signal MC sample of $B^+ \rightarrow D^+ K_S^0$ (a) $D^+ \rightarrow K^- \pi^+ \pi^+$ (b) $D^+ \rightarrow K_S^0 \pi^+$ decay modes. Here, $a2a$ = area of Gaussian 2/ area of Gaussian 1, $s2s1 = \sigma_2/\sigma_1$. Red (green) color used for a sum of Gaussian (2^{nd} order polynomial) PDF and blue curve shows the overall fit.

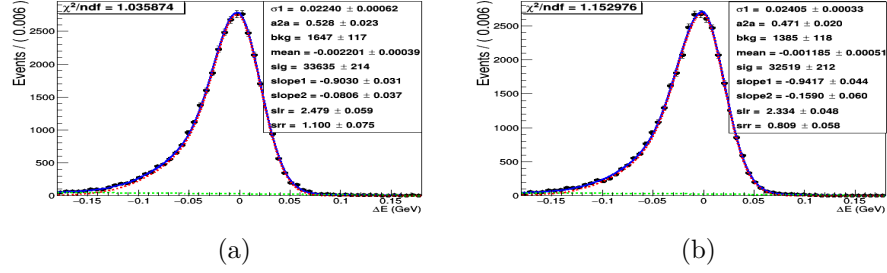


Figure 3.37: 1D UML fit of ΔE for the signal MC sample of $B^+ \rightarrow D^+ \eta$ (a) $D^+ \rightarrow K^- \pi^+ \pi^+$ (b) $D^+ \rightarrow K_S^0 \pi^+$ decay modes. Here, $a2a$ = area of Gaussian 2/ area of Gaussian 1, $slr = \sigma_L/\sigma_1$, $srr = \sigma_R/\sigma_1$. Red (green) color used for a sum of Gaussian (2^{nd} order polynomial) PDF and blue curve shows the overall fit.

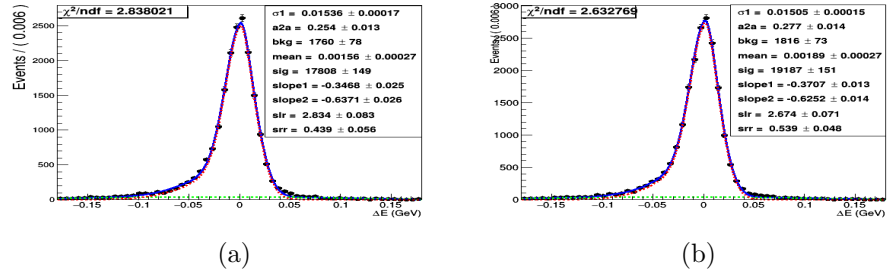


Figure 3.38: 1D UML fit of ΔE for the signal MC sample of $B^+ \rightarrow D^+ \eta(\rightarrow \pi^- \pi^+ \pi^0)$ (a) $D^+ \rightarrow K^- \pi^+ \pi^+$ (b) $D^+ \rightarrow K_S^0 \pi^+$ decay modes. Here, $a2a$ = area of Gaussian 2/ area of Gaussian 1, $slr = \sigma_L/\sigma_1$, $srr = \sigma_R/\sigma_1$. Red (green) color used for a sum of Gaussian (2^{nd} order polynomial) PDF and blue curve shows the overall fit.

3.11 Control Mode Study

We use $\bar{B}^0 \rightarrow D^0\eta$ as a control mode for $B^+ \rightarrow D_s^+\eta$, $D_s^{(*)+}\eta$, $D^+\eta$ decay modes and $\bar{B}^0 \rightarrow D^0K_S^0$ as a control mode for the study of $B^+ \rightarrow D_s^+K_S^0$, $D_s^{(*)+}K_S^0$, $D^+K_S^0$ decay modes, where $D^0 \rightarrow K^-\pi^+$, $K^-\pi^+\pi^+\pi^-$, $K_S^0\pi^+\pi^-$, $K^-\pi^+\pi^0$, $\pi^0 \rightarrow \gamma\gamma$ and $\eta \rightarrow \gamma\gamma$ ($\pi^-\pi^+\pi^0$). Both control modes are already studied by Belle and BABAR [30, 31, 32, 33].

3.12 Event Selection

We have used the same selection criteria for the final states particles as mentioned in section 3. We reconstruct D^0 mesons from the following decay modes: $K^-\pi^+$, $K^-\pi^+\pi^+\pi^-$, $K_S^0\pi^+\pi^-$, $K^-\pi^+\pi^0$ using the invariant mass cut around nominal mass within 20 MeV/ c^2 , 15 MeV/ c^2 , 20 MeV/ c^2 and 35 MeV/ c^2 , respectively. We have also applied mass constraint and vertex fit on D^0 meson. To reduce the combinatorial background coming due to π^0 in $D^0 \rightarrow K^-\pi^+\pi^0$ decay mode, we select π^0 having center of mass momentum greater than 0.4 GeV/ c and having invariant mass between [0.12 - 0.145] GeV/ c^2 . In addition, we also apply mass constraint on the selected π^0 .

For BCS, we use χ^2 based on the M_{bc} and M_{D^0} . Fig. 3.39, 3.40, 3.41 and 3.42 show the distributions of M_{D^0} and ΔE variables with signal MC samples for $\bar{B}^0 \rightarrow D^0\eta$ and $\bar{B}^0 \rightarrow D^0K_S^0$ decay modes, respectively.

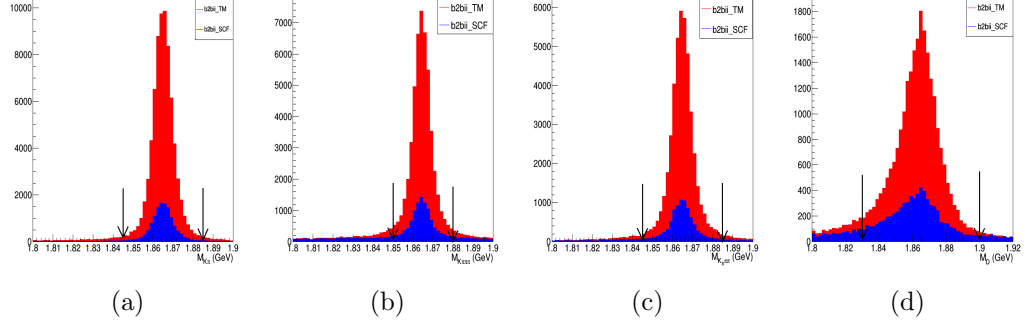


Figure 3.39: Distributions of M_{D^0} for $\bar{B}^0 \rightarrow D^0 \eta(\rightarrow \gamma\gamma)$, (a) $D^0 \rightarrow K^- \pi^+$, (b) $D^0 \rightarrow K^- \pi^+ \pi^+ \pi^-$, (c) $D^0 \rightarrow K_S^0 \pi^+ \pi^-$ and (d) $D^0 \rightarrow K^- \pi^+ \pi^0$ decay mode for Signal MC. Red color histogram shows the truth matched events and blue shows the self cross feed events.

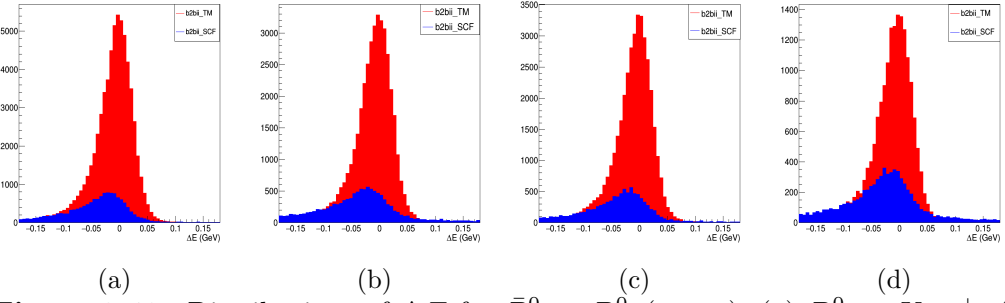


Figure 3.40: Distributions of ΔE for $\bar{B}^0 \rightarrow D^0 \eta(\rightarrow \gamma\gamma)$, (a) $D^0 \rightarrow K^- \pi^+$, (b) $D^0 \rightarrow K^- \pi^+ \pi^+ \pi^-$, (c) $D^0 \rightarrow K_S^0 \pi^+ \pi^-$ and (d) $D^0 \rightarrow K^- \pi^+ \pi^0$ decay mode for Signal MC. Red color histogram shows the truth matched events and blue shows the self cross feed events.

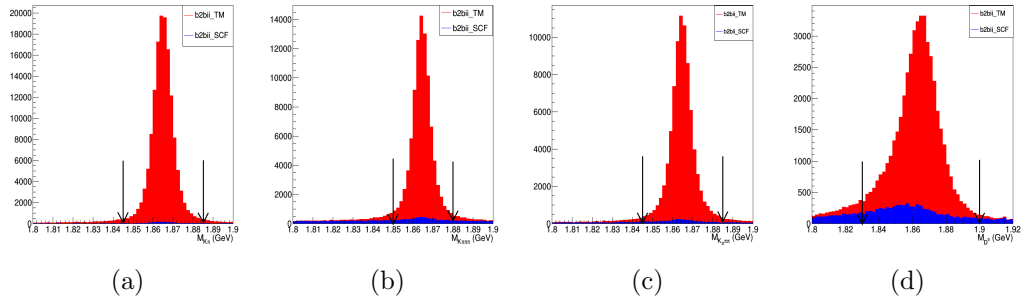


Figure 3.41: Distributions of M_{D^0} for $\bar{B}^0 \rightarrow D^0 K_S^0$, (a) $D^0 \rightarrow K^- \pi^+$, (b) $D^0 \rightarrow K^- \pi^+ \pi^+ \pi^-$, (c) $D^0 \rightarrow K_S^0 \pi^+ \pi^-$ and (d) $D^0 \rightarrow K^- \pi^+ \pi^0$ decay mode for Signal MC. Red color histogram shows the truth matched events and blue shows the self cross feed events.

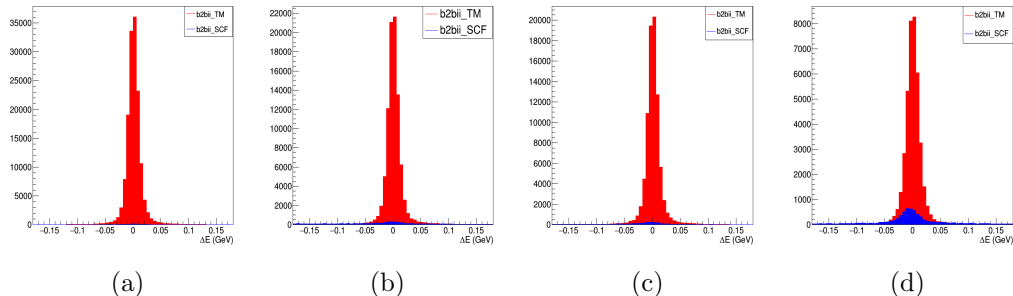


Figure 3.42: Distributions of ΔE for $\bar{B}^0 \rightarrow D^0 K_S^0$, (a) $D^0 \rightarrow K^- \pi^+$, (b) $D^0 \rightarrow K^- \pi^+ \pi^+ \pi^-$, (c) $D^0 \rightarrow K_S^0 \pi^+ \pi^-$ and (d) $D^0 \rightarrow K^- \pi^+ \pi^0$ decay mode for Signal MC. Red color histogram shows the truth matched events and blue shows the self cross feed events.

3.13 Generic MC study

To distinguish the peaking background in $\bar{B}^0 \rightarrow D^0 \eta$ and $\bar{B}^0 \rightarrow D^0 K_S^0$ decay modes, we use three streams of generic MC samples. In $\bar{B}^0 \rightarrow D^0 \eta$ mode, we have observed peaking background around -0.16 GeV in ΔE from the reconstruction of $\bar{B}^0 \rightarrow D^{*0} \eta$ due to extra gamma and few background events are coming from $B^+ \rightarrow \bar{D}^0 \rho^+$ and $B^+ \rightarrow \bar{D}^{*0} \rho^+$ decay modes. As expected, large number of combinatorial background is coming from the continuum events.

In the $\bar{B}^0 \rightarrow D^0 K_S^0$ decay mode, we observe peaking background around -0.16 GeV due to $\bar{B}^0 \rightarrow D^{*0} K_S^0$ and $B^+ \rightarrow D^0 K^{*+}$. Most of the combinatorial background is coming from the continuum events. Fig. 3.43 shows the distribution of ΔE with generic MC for $\bar{B}^0 \rightarrow D^0 \eta$ and $\bar{B}^0 \rightarrow D^0 K_S^0$ decay modes, respectively.

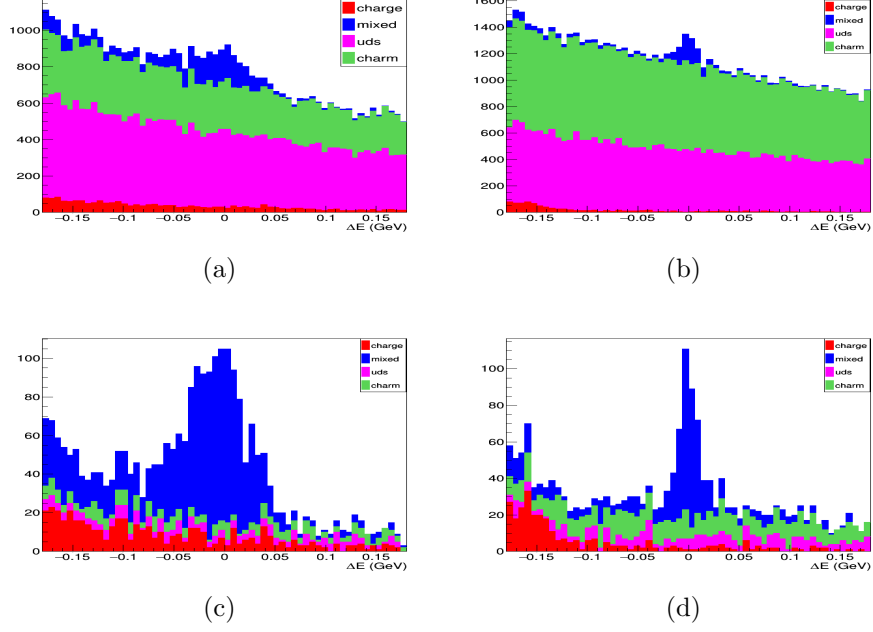


Figure 3.43: Distributions of ΔE for (a) $\bar{B}^0 \rightarrow D^0\eta(\rightarrow \gamma\gamma)$ (b) $\bar{B}^0 \rightarrow D^0K_S^0$ decay mode without NN cut and (c) $\bar{B}^0 \rightarrow D^0\eta(\rightarrow \gamma\gamma)$ (d) $\bar{B}^0 \rightarrow D^0K_S^0$ decay mode with NN cut using generic MC samples.

3.14 Continuum Suppression

In control mode, one expects the dominant background comes from the continuum events. We have used similar continuum variables (as mentioned in Sec. 3.7 for the signal decay modes). Having a similar set of continuum suppression variables further helps us to validate our continuum suppression and in Fig. 3.43, we clearly see the effect of NN by comparing the ΔE distribution without (upper) and with (lower) applied NN cut.

3.15 The Probability Density Functions (PDFs)

3.15.1 Signal PDF

In this subsection, we discuss the PDF used for signal extraction of the model for control modes. The fitted distributions of ΔE are shown in Fig. 3.44, 3.45 with signal MC samples for $\bar{B}^0 \rightarrow D^0\eta$ and $\bar{B}^0 \rightarrow D^0K_S^0$ decay modes, respectively. For $\bar{B}^0 \rightarrow D^0\eta$ decay mode, signal is fitted with a sum of Gaussian and a bifurcated Gaussian with a common mean. Signal is fitted with a sum of two Gaussians with a common mean for $\bar{B}^0 \rightarrow D^0K_S^0$ decay mode. The PDF used for background is first order polynomial for $\bar{B}^0 \rightarrow D^0\eta$ and $\bar{B}^0 \rightarrow D^0K_S^0$ decay modes.

We planned to proceed the study with the combine D^0 sub decays. We have analyzed both $\bar{B}^0 \rightarrow D^0\eta$ and $\bar{B}^0 \rightarrow D^0K_S^0$ decay mode individually with each stream, but in $D^0 \rightarrow K^-\pi^+\pi^+\pi^-$ decay mode, we have observed extra signal events from the following modes ($D^0 \rightarrow K^-a_1^+(\rho\pi^+, f_0\pi^+)/K^{*0}\rho^0/K^{*0}\pi^+\pi^-, K^-\pi^+\rho^0$) due to the same final state. One can see the distribution of ΔE with signal MC for $\bar{B}^0 \rightarrow D^0\eta$ and $\bar{B}^0 \rightarrow D^0K_S^0$ decay mode with combined D^0 sub decays mode in Fig. 3.46. The PDF used for signal is sum of Gaussian and a bifurcated Gaussian with a common mean (sum of two Gaussians with a common mean) and for background is 2nd (3rd) order polynomial for $\bar{B}^0 \rightarrow D^0\eta(\rightarrow \gamma\gamma)$ ($\bar{B}^0 \rightarrow D^0\eta(\pi\pi\pi), \bar{B}^0 \rightarrow D^0K_S^0$) decay mode.

Table 3.5 is updated with the signal efficiency for $\bar{B}^0 \rightarrow D^0\eta$ and $\bar{B}^0 \rightarrow D^0K_S^0$ decay modes.

3.15 The Probability Density Functions (PDFs)

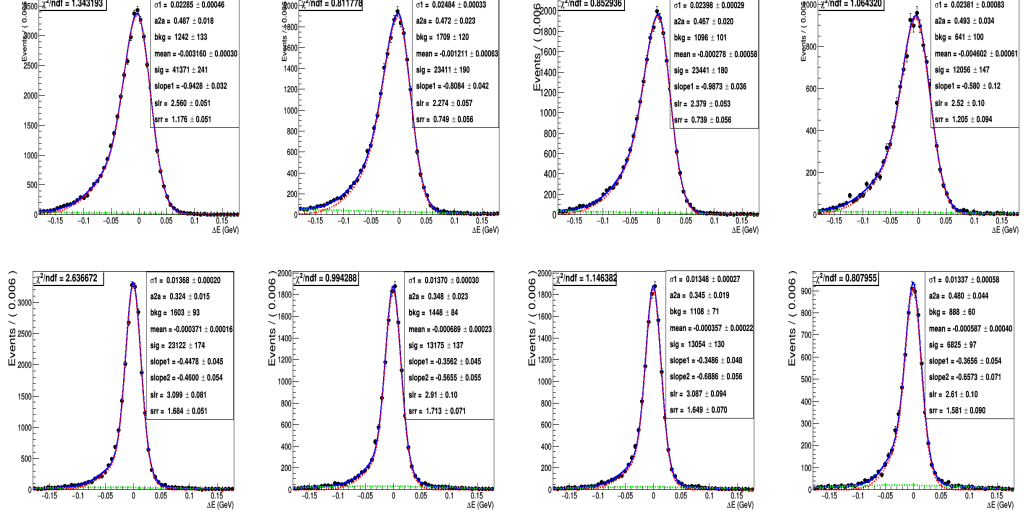


Figure 3.44: The 1D UML fitted distributions of ΔE variable for $\bar{B}^0 \rightarrow D^0 \eta (\rightarrow \gamma\gamma)$, (a) $D^0 \rightarrow K^- \pi^+ \pi^+$ (top left), (b) $D^0 \rightarrow K^- \pi^+ \pi^+ \pi^-$ (top middle left), (c) $D^0 \rightarrow K_S^0 \pi^+ \pi^-$ (top middle right) and (d) $D^0 \rightarrow K^- \pi^+ \pi^0$ (top right) decay mode with signal MC sample. Distributions of ΔE for $\bar{B}^0 \rightarrow D^0 \eta (\rightarrow \pi^- \pi^+ \pi^0)$, (e) $D^0 \rightarrow K^- \pi^+$ (lower left), (f) $D^0 \rightarrow K^- \pi^+ \pi^+ \pi^-$ (lower middle left), (g) $D^0 \rightarrow K_S^0 \pi^+ \pi^-$ (lower middle right) and (h) $D^0 \rightarrow K^- \pi^+ \pi^0$ (lower right) decay mode with signal MC sample. Here, a2a = fraction of area of Gaussian 2 and area of Gaussian 1, slr = fraction of σ_L and σ_1 and srr = fraction of σ_R and σ_1 . Red (green) color used for a sum of Gaussian (first order polynomial, 2^{nd} order polynomial ($\eta \rightarrow \pi\pi\pi$)) PDF and blue curve shows the overall fit.

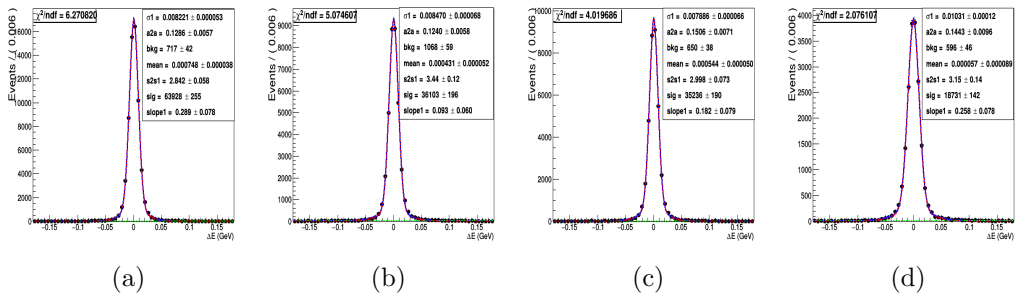


Figure 3.45: The 1D UML fitted distributions of ΔE variable for $\bar{B}^0 \rightarrow D^0 K_S^0$, (a) $D^0 \rightarrow K^- \pi^+$, (b) $D^0 \rightarrow K^- \pi^+ \pi^+ \pi^-$, (c) $D^0 \rightarrow K_S^0 \pi^+ \pi^-$ and (d) $D^0 \rightarrow K^- \pi^+ \pi^0$ decay mode with signal MC sample. Here, a2a = fraction of area of Gaussian 2 and area of Gaussian 1, s2s1 = fraction of σ_2 and σ_1 . Red (green) color used for a sum of Gaussian (1st order polynomial) PDF and blue curve shows the overall fit.

3.15 The Probability Density Functions (PDFs)

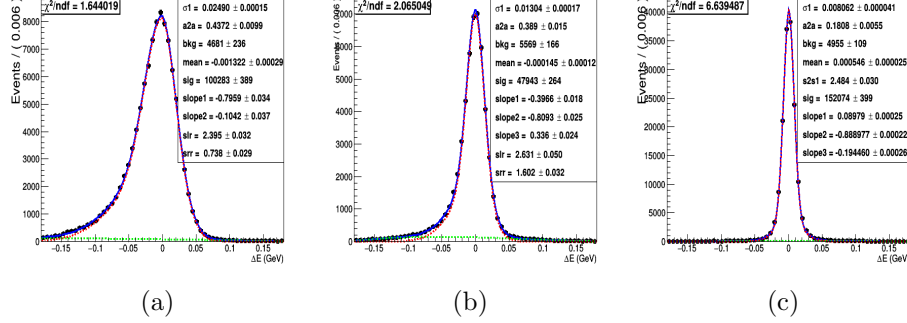


Figure 3.46: The 1D UML fitted distributions of ΔE for (a) $\bar{B}^0 \rightarrow D^0 \eta (\rightarrow \gamma \gamma)$, (b) $\bar{B}^0 \rightarrow D^0 \eta (\rightarrow \pi^- \pi^+ \pi^0)$ (excluded $D^0 \rightarrow K \pi \pi^0$), (c) $\bar{B}^0 \rightarrow D^0 K_S^0$ decay mode with signal MC sample (combine D^0 sub decays). Here, $a2a$ = area of Gaussian 2/ area of Gaussian 1, $slr = \sigma_L/\sigma_1$, $srr = \sigma_R/\sigma_1$ and $s2s1 = \sigma_2/\sigma_1$.

Decay mode	$D^0 \rightarrow K \pi$	$D^0 \rightarrow K \pi \pi \pi$	$D^0 \rightarrow K_S \pi \pi$	$D^0 \rightarrow K \pi \pi^0$
$\bar{B}^0 \rightarrow D^0 \eta, \eta \rightarrow \gamma \gamma (\pi^- \pi^+ \pi^0)$	10.3(5.8)	5.8(3.3)	5.9(3.3)	3.0(1.7)
$\bar{B}^0 \rightarrow D^0 K_S^0$	16.0	9.0	8.8	4.7

Table 3.5: Signal efficiency for the control modes.

3.15.2 Background PDF

Fig. 3.47, 3.48 show the distribution of ΔE with generic MC samples for $\bar{B}^0 \rightarrow D^0 \eta$ and $\bar{B}^0 \rightarrow D^0 K_S^0$ decay mode with combined D^0 sub decay modes, respectively. In $\bar{B}^0 \rightarrow D^0 \eta$ decay mode, we observed few peaking background events around -0.18 GeV in ΔE distribution, which are coming from $\bar{B}^0 \rightarrow D^{*0} \eta$ and B^+ decays into three final state particles. These peaking background events are fitted with exponential function, continuum and remaining $B\bar{B}$ background events are fitted with first order polynomial as shown in Fig 3.47 (right).

In $\bar{B}^0 \rightarrow D^0 K_S^0$ decay mode peaking background around -0.17 GeV is coming from $\bar{B}^0 \rightarrow D^{*0} K_S^0$ and $B^+ \rightarrow D^0 K^{*+}$ decay mode and fitted these peaking events with a sum two Gaussians with a common mean and the remaining back-

3.15 The Probability Density Functions (PDFs)

ground events from $B\bar{B}$ and $q\bar{q}$ is fitted with 1st order polynomial as shown in Fig 3.48. Fig. 3.49, 3.50 show the distribution of ΔE with generic MC samples for individual stream. We have used the same PDF and have also fixed the tail parameters (a2a, slr ,srr, s2s1) as mentioned in Fig. 3.46 (signal MC). The PDF used for $q\bar{q}$ and remaining $B\bar{B}$ background is first order polynomial while have fixed the PDF parameter of peaking background coming from $B\bar{B}$ as shown in Fig. 3.47, 3.48 (right).

Generic MC sample	A	B	C
$\bar{B}^0 \rightarrow D^0 \eta (\rightarrow \gamma\gamma)$			
Signal (TM) events	1131 \pm 60 (1153)	1148 \pm 58 (1199)	1141 \pm 59 (1221)
$q\bar{q}$ (TM) events	1160 \pm 75 (1047)	951 \pm 76 (1052)	1200 \pm 74 (1011)
Peaking (TM) events	267 \pm 35 (358)	508 \pm 59 (356)	252 \pm 33 (362)
$\bar{B}^0 \rightarrow D^0 \eta (\rightarrow \pi^- \pi^+ \pi^0)$			
Signal (TM) events	271 \pm 23 (315)	294 \pm 24 (323)	271 \pm 23 (295)
$q\bar{q}$ (TM) events	349 \pm 35 (296)	354 \pm 35 (336)	329 \pm 32 (308)
Peaking (TM) events	85 \pm 21 (94)	120 \pm 22 (109)	102 \pm 19 (99)
$\bar{B}^0 \rightarrow D^0 K_S^0$			
Signal (TM) events	324 \pm 26 (352)	400 \pm 29 (406)	323 \pm 25 (306)
$q\bar{q}$ (TM) events	1407 \pm 49 (1356)	1509 \pm 51 (1503)	1312 \pm 47 (1328)
Peaking (TM) events	188 \pm 25 (211)	207 \pm 26 (207)	203 \pm 26 (205)

Table 3.6: Comparison of the observed signal and TM (truth-matched) events for $\bar{B}^0 \rightarrow D^0 h$ ($h = \eta, K_S^0$) decay mode.

The discrepancy between observed yield and TM (truth-matched) events is coming within 1σ , as shown in Table 3.6 but it is around 1.5σ for $\bar{B}^0 \rightarrow D^0 \eta (\rightarrow \pi^- \pi^+ \pi^0)$ decay mode.

3.15 The Probability Density Functions (PDFs)

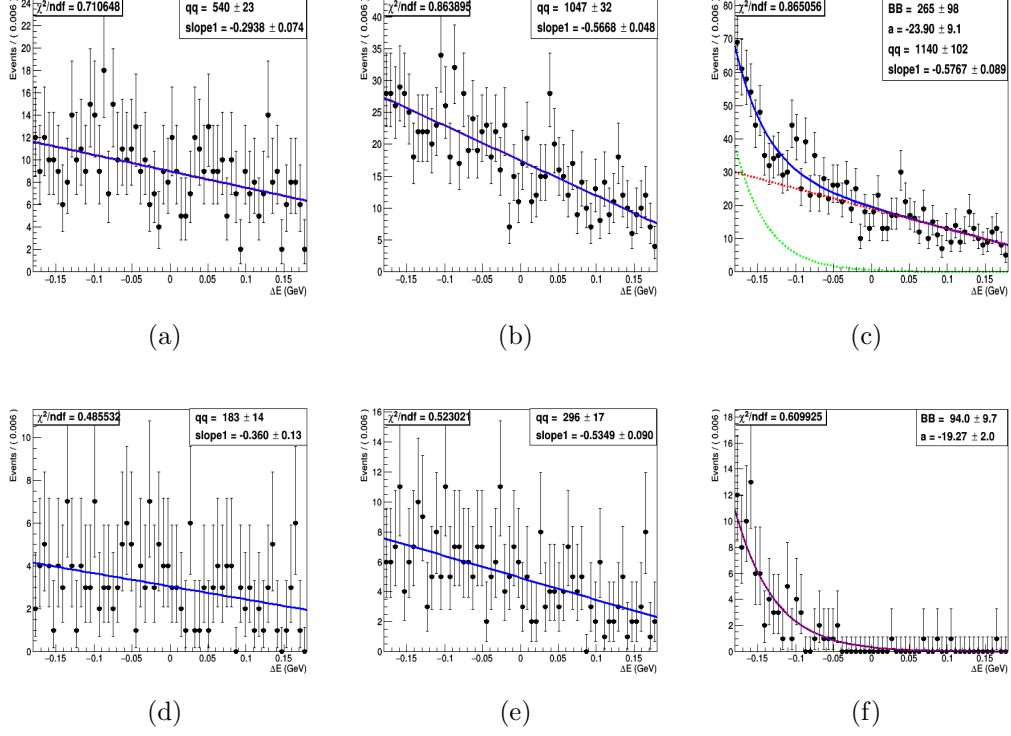


Figure 3.47: The fitted distributions of ΔE for $\bar{B}^0 \rightarrow D^0 \eta(\rightarrow \gamma\gamma)$ decay mode, (a) continuum events (PDF: 1st order poly.) (b) continuum and $B\bar{B}$ (exclude $D^{*0}\eta$ and B^+ from 3 final states particles) (PDF: 1st order polynomial) (c) continuum and $B\bar{B}$ events (PDF: exponential and 1st order polynomial) with generic MC sample (combine D^0 sub decays). Distributions of ΔE for $\bar{B}^0 \rightarrow D^0 \eta(\rightarrow \pi^- \pi^+ \pi^0)$ decay mode (excluded $D^0 \rightarrow K\pi\pi^0$), (d) continuum events (PDF: 1st order poly.) (e) continuum and $B\bar{B}$ (exclude $D^{*0}\eta$ and B^+ from 3 final states particles) (PDF: 1st order polynomial)(f) $B\bar{B}$ peaking background events (PDF: exponential) with generic MC sample (combine D^0 sub decays). Red (green) color curve use for 1st order polynomial (exponential) PDF and blue curve shows the overall fit.

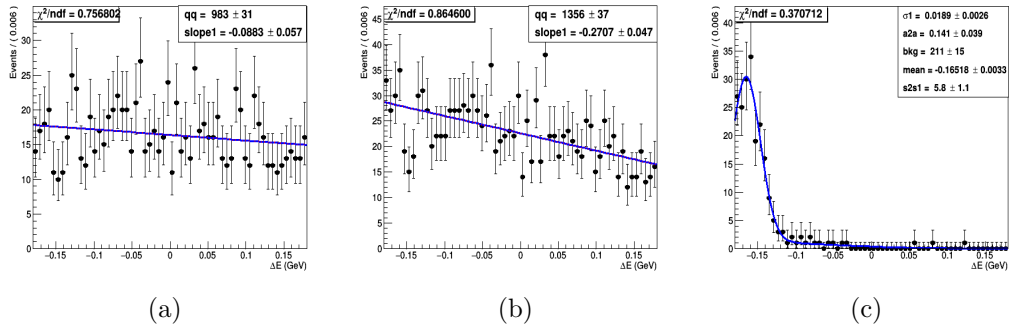


Figure 3.48: Distributions of ΔE for $\bar{B}^0 \rightarrow D^0 K_S^0$ decay mode, continuum events (PDF: 1st order poly.) (b) continuum and $B\bar{B}$ (exclude $D^{*0}K_S^0$ and $D^0 K^{*+}$) (PDF: 1st order polynomial) (c) $B^0 \rightarrow D^{*0} K_S^0$ and $B^+ \rightarrow D^0 K^{*+}$ events (PDF: sum of two Gaussian with common mean) with generic MC sample (combine D^0 sub decays). Blue curve shows the overall fit.

3.15 The Probability Density Functions (PDFs)

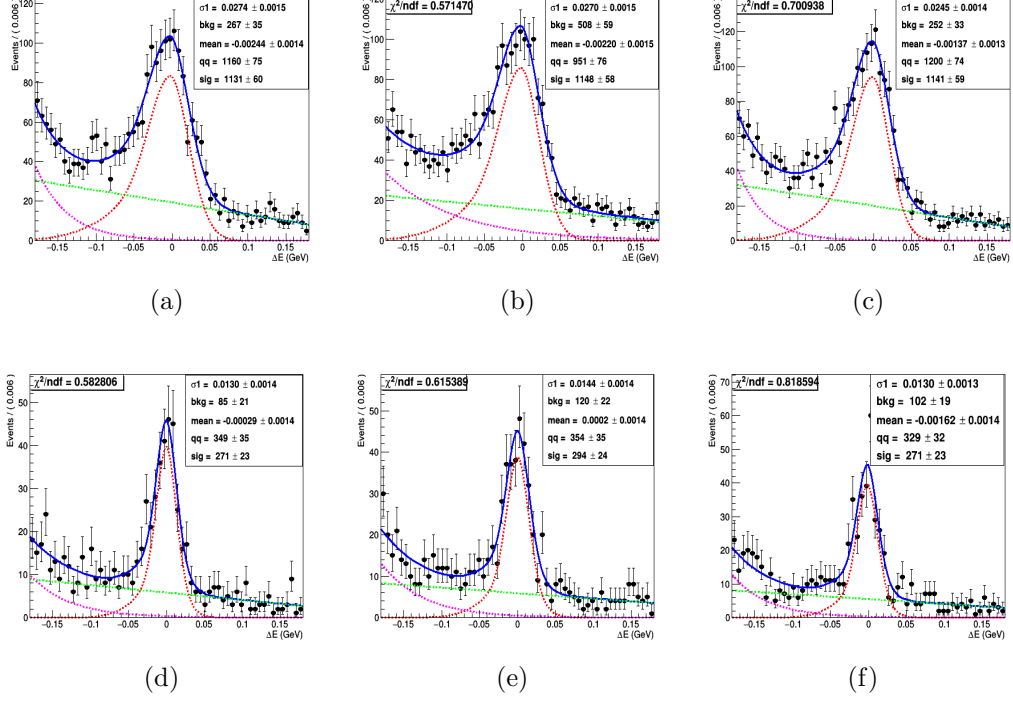


Figure 3.49: The fitted distributions of ΔE for $\bar{B}^0 \rightarrow D^0 \eta (\rightarrow \gamma \gamma)$ decay mode, (a) stream 1 (b) stream 2 (c) stream 3 with generic MC sample (combine D^0 sub decays). Distributions of ΔE for $\bar{B}^0 \rightarrow D^0 \eta (\pi^- \pi^+ \pi^0)$ (exclude $D^0 \rightarrow K \pi \pi^0$) decay mode, (d) stream 1 (e) stream 2 (f) stream 3 with generic MC sample (combine D^0 sub decays). Red (green, magenta) color curve use for a sum of Gaussian(1st order polynomial, peaking bkg.) PDF and blue curve shows the overall fit.

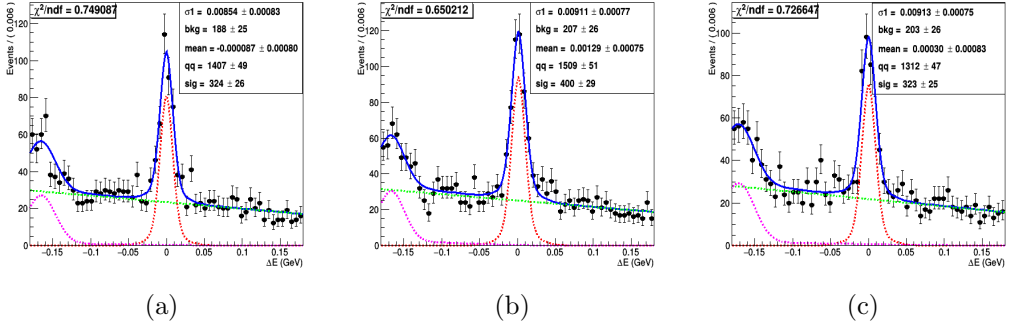


Figure 3.50: The fitted distributions of ΔE for $\bar{B}^0 \rightarrow D^0 K_S^0$ decay mode, (a) stream 1 (b) stream 2 (c) stream 3 with generic MC sample (combine D^0 sub decays). Red (green, magenta) color curve use for a sum of Gaussian(1st order polynomial, peaking bkg.) PDF and blue curve shows the overall fit.

3.16 Toy MC Study

Toy MC study is carried out to check the stability of the fitter. Here, we have generated 2000 toy MC samples according to the expected number of signal and backgrounds events. The typical distribution can be seen in Fig. 3.51 (a,b,c) for $\bar{B}^0 \rightarrow D^0\eta(\rightarrow \gamma\gamma)$, $\bar{B}^0 \rightarrow D^0\eta(\rightarrow \pi\pi\pi^0)$ and $\bar{B}^0 \rightarrow D^0K_S^0$ decay modes, respectively. In $\bar{B}^0 \rightarrow D^0\eta$ decay mode, signal is fitted with the sum of a Gaussian and a bifurcated Gaussian, while the background is fitted with first order polynomial and peaking background fitted with exponential function. Similarly, in $\bar{B}^0 \rightarrow D^0K_S^0$, background is fitted with first order polynomial while peaking background fitted with a sum of two Gaussians with common mean and PDF used for signal is sum of two Gaussians. The pull, signal yield and error distributions of $\bar{B}^0 \rightarrow D^0\eta$, $\bar{B}^0 \rightarrow D^0K_S^0$ decay modes are shown in Fig. 3.52, 3.53, respectively. The sigma and mean of the pull distributions are found to be consistent with 1 and 0, respectively. This suggest that the fit is not biased and error is accurate. Fig. 3.54, 3.55, show the linearity test for for $\bar{B}^0 \rightarrow D^0\eta$ and $\bar{B}^0 \rightarrow D^0K_S^0$ decay modes, respectively.

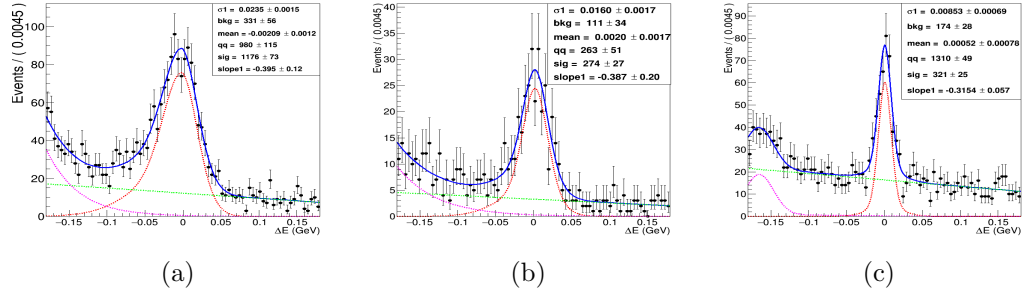


Figure 3.51: A typical example for (a) $\bar{B}^0 \rightarrow D^0\eta(\rightarrow \gamma\gamma)$, (b) $\bar{B}^0 \rightarrow D^0\eta(\rightarrow \pi^-\pi^+\pi^0)$, (c) $\bar{B}^0 \rightarrow D^0K_S^0$ decay mode. Red color shows signal, green (magenta) shows for background (peaking background) and blue shows the overall fit.

3.16 Toy MC Study

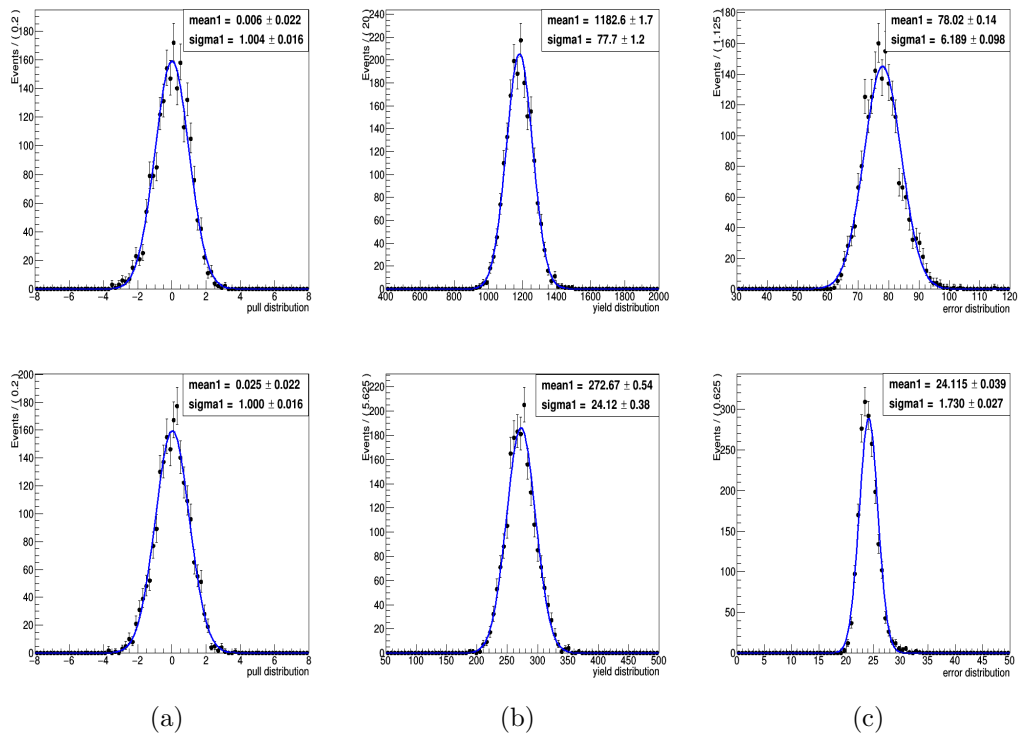


Figure 3.52: (a) Pull distribution (b) yield distribution and (c) error distribution for $\bar{B}^0 \rightarrow D^0\eta$ decay mode. The upper distribution for $\eta \rightarrow \gamma\gamma$ and lower for $\eta \rightarrow \pi^-\pi^+\pi^0$ decay mode.

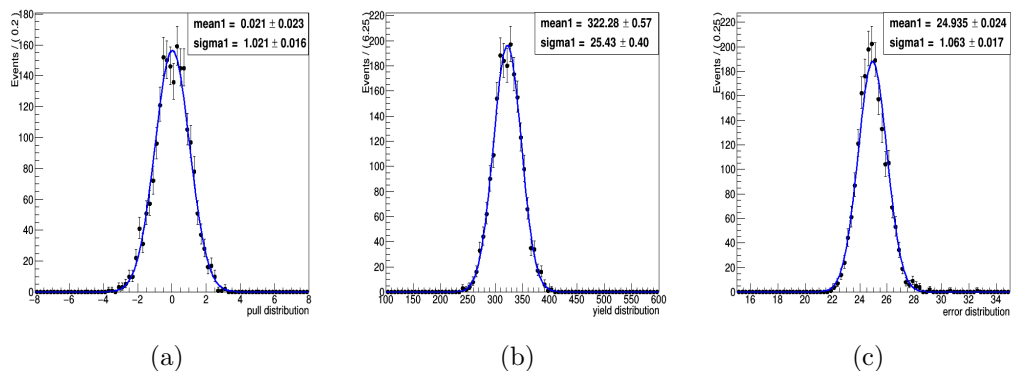


Figure 3.53: (a) Pull distribution (b) yield distribution and (c) error distribution for $\bar{B}^0 \rightarrow D^0K_S^0$ decay mode.

3.16 Toy MC Study

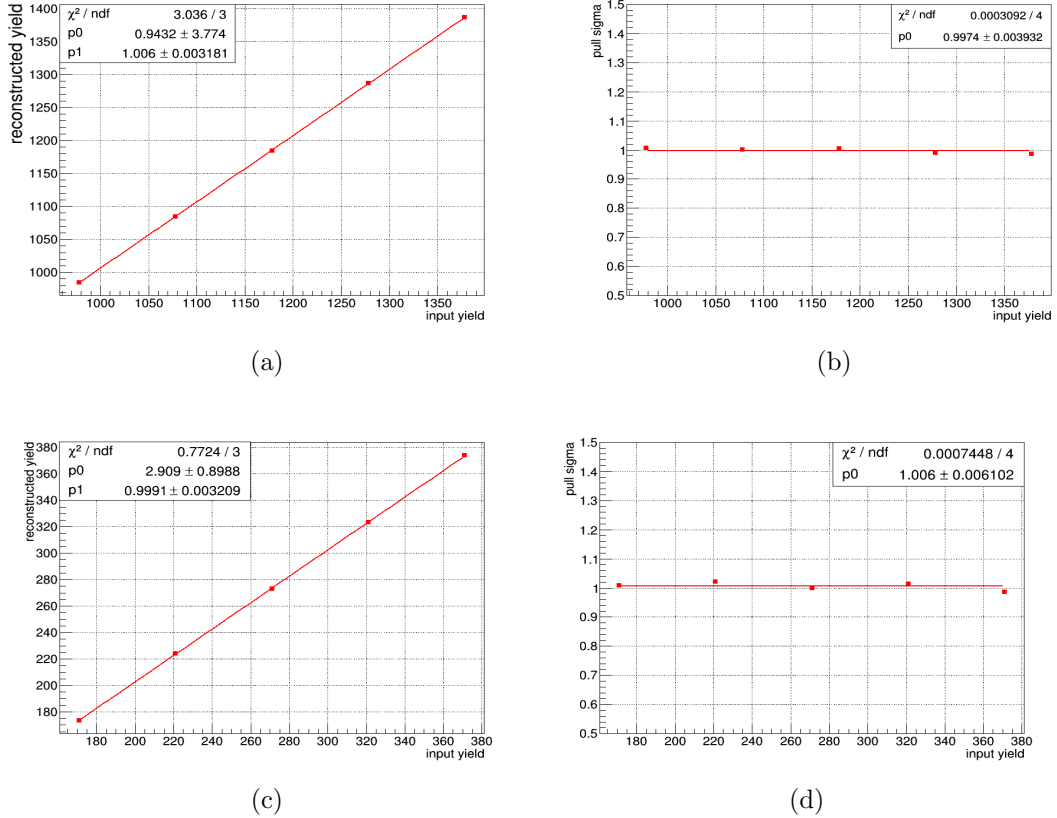


Figure 3.54: Result of linearity test for $\bar{B}^0 \rightarrow D^0 \eta$ decay mode: (a) reconstructed yield versus input signal yield (b) pull error versus input signal yield. The upper distribution for $\eta \rightarrow \gamma\gamma$ and lower for $\eta \rightarrow \pi^- \pi^+ \pi^0$ decay mode.

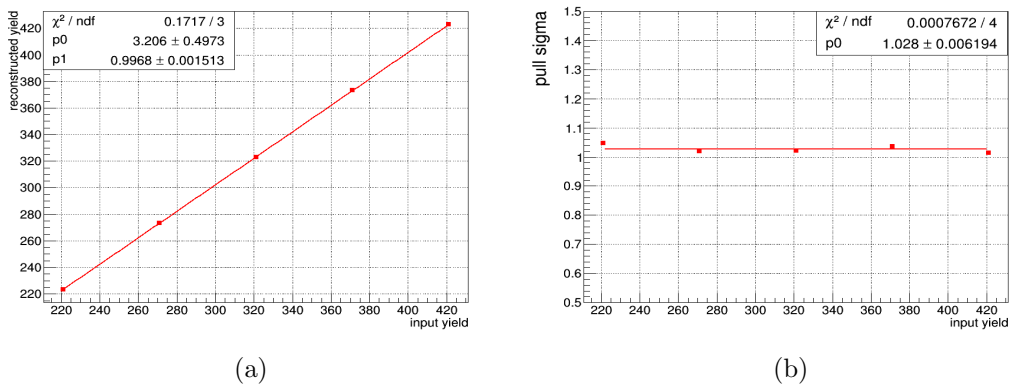


Figure 3.55: Result of linearity test for $\bar{B}^0 \rightarrow D^0 K_S^0$ decay mode: (a) reconstructed yield versus input signal yield (b) pull error versus input signal yield.

3.17 Fitting Strategy for Signal decay modes

In this section, fitted distribution of ΔE with combine D_s^+ ($D_s^+ \rightarrow \phi\pi^+, \bar{K}^{*0}K^+$ and $K_S^0K^+$) and D^+ ($D^+ \rightarrow K^-\pi^+\pi^+, K_S^0\pi^+$) sub-decay modes are shown in Fig. 3.56, 3.57 with signal MC and generic MC samples for signal decay modes, respectively. For $B^+ \rightarrow D_s^+\eta$, $B^+ \rightarrow D_s^{(*)+}(\rightarrow D_s^+\gamma)\eta$ and $B^+ \rightarrow D^+\eta$ decay mode, signal is fitted with a sum of Gaussian and a bifurcated Gaussian with a common mean as shown in Fig. 3.56 (upper row). Signal is fitted with a sum of two Gaussians with a common mean for $B^+ \rightarrow D_s^+K_S^0$, $B^+ \rightarrow D_s^{(*)+}(\rightarrow D_s^+\gamma)K_S^0$ and $B^+ \rightarrow D^+K_S^0$ decay mode as shown in Fig. 3.56 (lower row). Here, a2a = fraction of area of Gaussian 2 and area of Gaussian 1, slr = fraction of σ_L and σ_1 , srr = fraction of σ_R and σ_1 and s2s1 = fraction of σ_2 and σ_1 . The PDF used for background with signal MC is 2nd (1st) order polynomial for signal decay modes ($B^+ \rightarrow D_s^+\eta$, $B^+ \rightarrow D_s^{(*)+}\eta$). Fig. 3.57 shows the fitted distribution of ΔE with five streams of generic MC samples for all signal decay modes. The PDF used for the background is 1st order polynomial and peaking background in $B^+ \rightarrow D^+\eta$ and $B^+ \rightarrow D^+K_S^0$ decay mode fitted with a sum of two Gaussian with common mean coming from B^0 decay into three body and $B^0 \rightarrow D^+K^{*-}$, respectively. To perform the toy study, signal is fitted with a sum of Gaussian and a bifurcated Gaussian with a common mean for $B^+ \rightarrow D_s^+\eta$, $B^+ \rightarrow D_s^{(*)+}(\rightarrow D_s^+\gamma)\eta$ and $B^+ \rightarrow D^+\eta$ decay modes and for $B^+ \rightarrow D_s^+K_S^0$, $B^+ \rightarrow D_s^{(*)+}(\rightarrow D_s^+\gamma)K_S^0$ and $B^+ \rightarrow D^+K_S^0$ decay modes signal is fitted with a sum of two Gaussians with a common mean, while the background is fitted as 1st order polynomial and peaking

3.17 Fitting Strategy for Signal decay modes

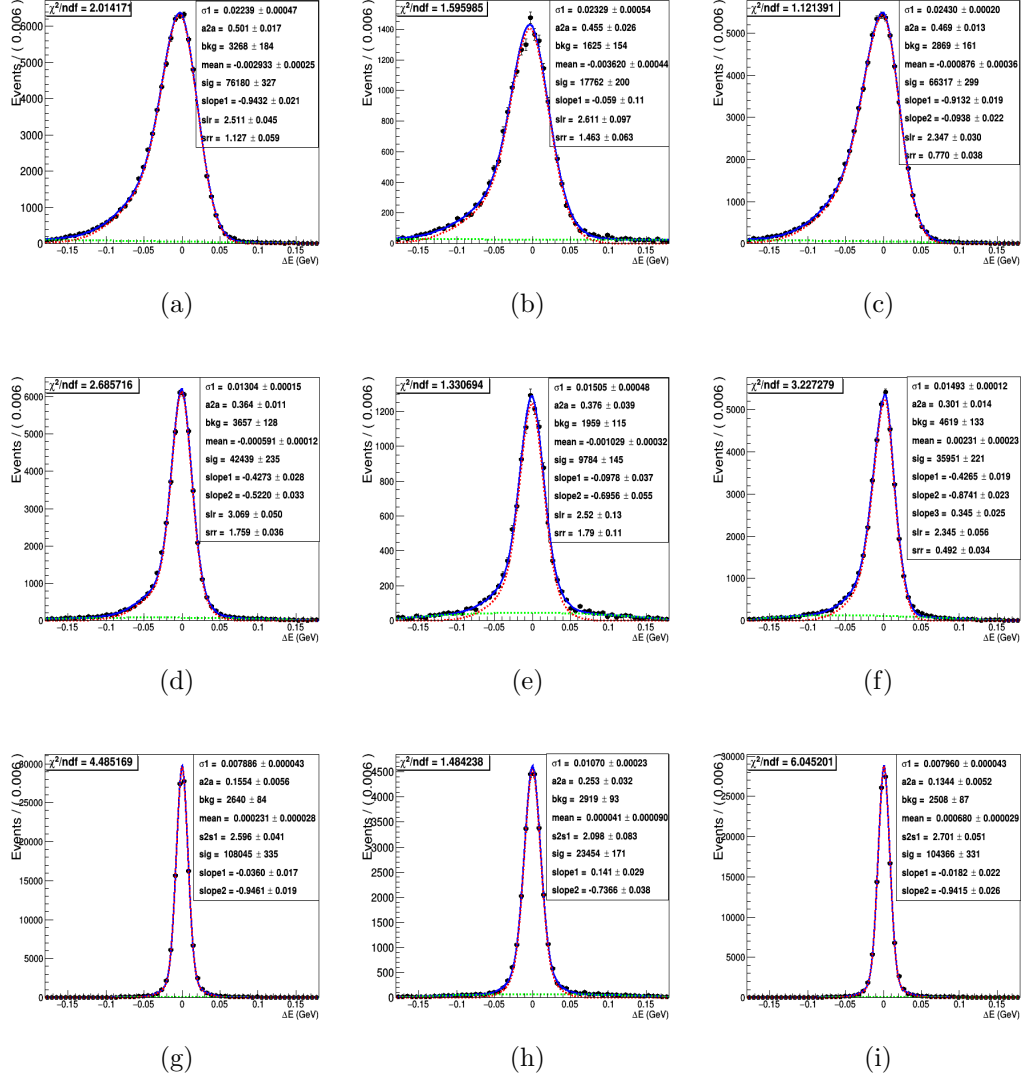


Figure 3.56: The fitted distribution of ΔE for (a) $B^+ \rightarrow D_s^+ \eta (\rightarrow \gamma\gamma)$ (b) $B^+ \rightarrow D_s^{(*)+} (\rightarrow D_s^+ \gamma) \eta (\rightarrow \gamma\gamma)$ (c) $B^+ \rightarrow D^+ \eta (\rightarrow \gamma\gamma)$ (d) $B^+ \rightarrow D_s^+ \eta (\rightarrow \pi\pi\pi)$ (e) $B^+ \rightarrow D_s^{(*)+} (\rightarrow D_s^+ \gamma) \eta (\rightarrow \pi\pi\pi)$ (f) $B^+ \rightarrow D^+ \eta (\rightarrow \pi\pi\pi)$ (g) $B^+ \rightarrow D_s^+ K_S^0$ (h) $B^+ \rightarrow D_s^{(*)+} (\rightarrow D_s^+ \gamma) K_S^0$ (i) $B^+ \rightarrow D^+ K_S^0$ decay modes with signal MC sample (combine D_s^+ , D^+ sub decays). Red (green) color curve use for a sum of Gaussian (2^{nd} order polynomial) PDF and blue curve shows the overall fit.

background fitted with a sum of two Gaussians with common mean. In signal we have fixed the mean, sigma and tail parameters as shown in Fig. 3.56 and we

3.17 Fitting Strategy for Signal decay modes

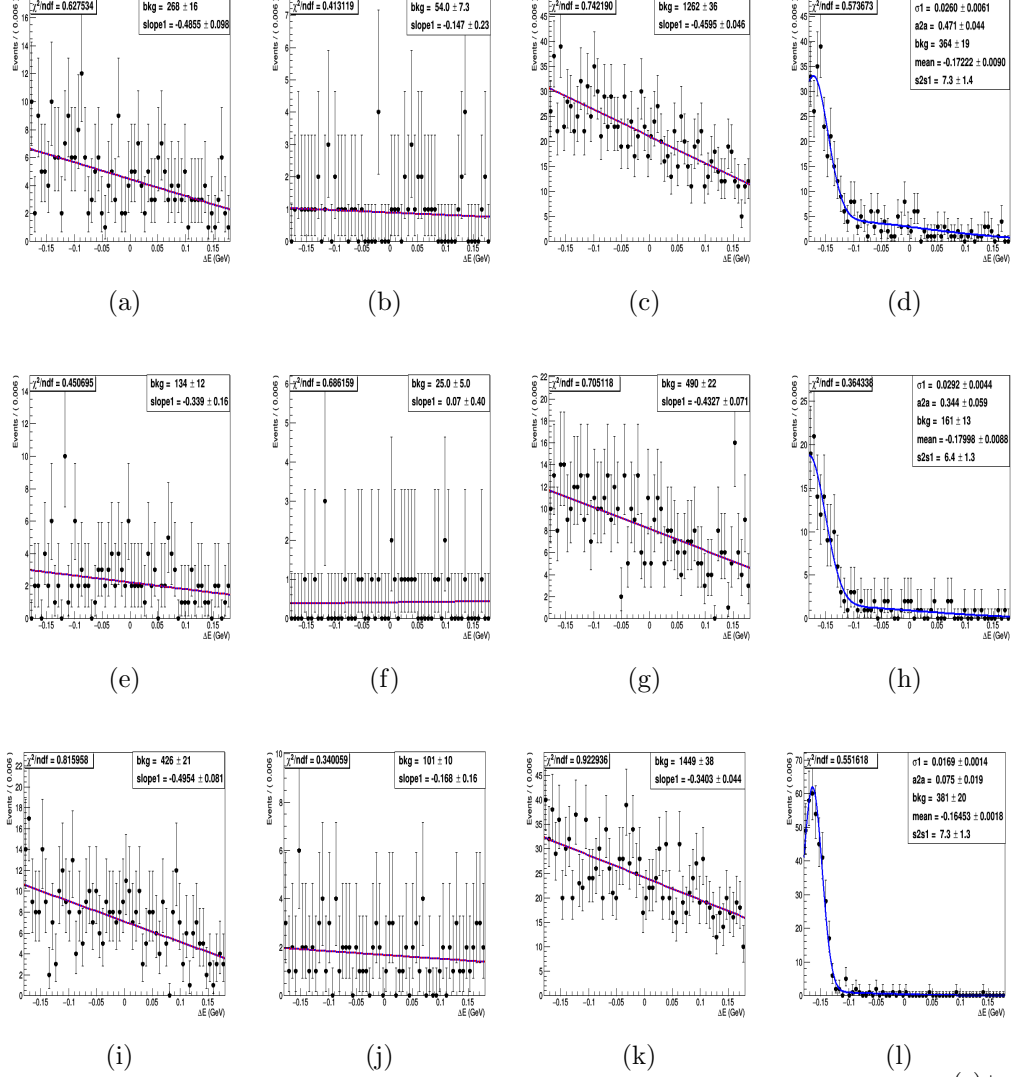


Figure 3.57: Distributions of ΔE for (a) $B^+ \rightarrow D_s^+ \eta(\rightarrow \gamma\gamma)$ (b) $B^+ \rightarrow D_s^{(*)+}(\rightarrow D_s^+ \gamma) \eta(\rightarrow \gamma\gamma)$ (c) $B^+ \rightarrow D^+ \eta(\rightarrow \gamma\gamma)$ (d) peaking in $B^+ \rightarrow D^+ \eta(\rightarrow \gamma\gamma)$ (e) $B^+ \rightarrow D_s^+ \eta(\rightarrow \pi\pi\pi)$ (f) $B^+ \rightarrow D_s^{(*)+}(\rightarrow D_s^+ \gamma) \eta(\rightarrow \pi\pi\pi)$ (g) $B^+ \rightarrow D^+ \eta(\rightarrow \pi\pi\pi)$ (h) peaking in $B^+ \rightarrow D^+ \eta(\rightarrow \pi\pi\pi)$ (i) $B^+ \rightarrow D_s^+ K_S^0$ (j) $B^+ \rightarrow D_s^{(*)+}(\rightarrow D_s^+ \gamma) K_S^0$ (k) $B^+ \rightarrow D^+ K_S^0$ (l) peaking in $B^+ \rightarrow D^+ K_S^0$ decay modes with generic MC sample (combine D_s^+ , D^+ sub decays). Red color shows 1^{st} order polynomial.

have also fixed the 1^{st} order polynomial and peaking background parameters for background as shown in Fig. 3.57.

3.18 Toy study for signal modes

In this section, we will perform the toy study for the signal modes. But for calculating the expected yield of the signal, we use $\mathcal{B}(B^+ \rightarrow D_s^+ \pi^0)$ decay mode. Fig. 3.58 and 3.59 show the pull distribution of signal decay modes. And also for the signal decay modes, we did not observe any significant bias. Fig. 3.60 and 3.61 show the yield distribution of signal decay modes. We also performed the linearity test for signal decay modes. Fig. 3.62 and 3.63 show the linearity test between reconstructed yield and input yield. Fig. 3.64 and 3.65 show the linearity test between pull sigma and input yield.

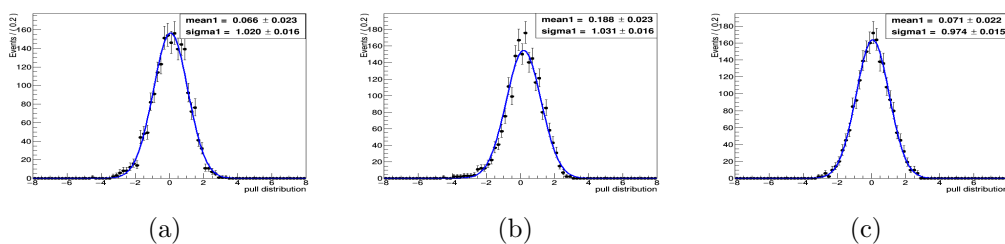


Figure 3.58: Pull distribution for (a) $B^+ \rightarrow D_s^+ K_S^0$ (b) $B^+ \rightarrow D_s^{(*)+} K_S^0$ (c) $B^+ \rightarrow D^+ K_S^0$ decay mode.

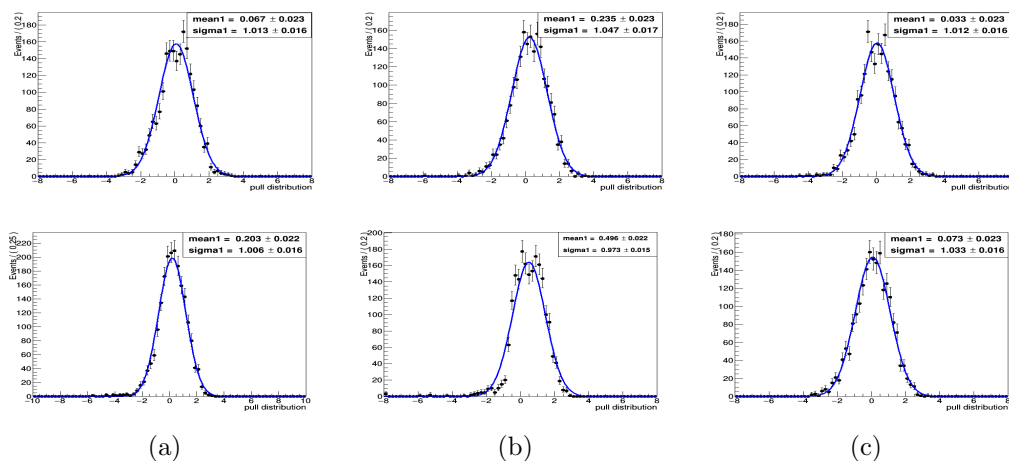


Figure 3.59: Pull distribution for (a) $B^+ \rightarrow D_s^+ \eta$ (b) $B^+ \rightarrow D_s^{(*)+} \eta$ (c) $B^+ \rightarrow D^+ \eta$ decay mode. The upper distribution for $\eta \rightarrow \gamma\gamma$ and lower for $\eta \rightarrow \pi^- \pi^+ \pi^0$ decay modes.

3.18 Toy study for signal modes

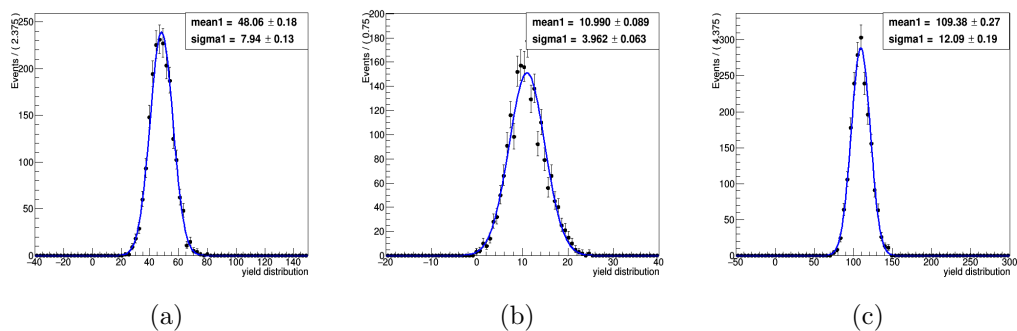


Figure 3.60: Yield distribution for (a) $B^+ \rightarrow D_s^+ K_S^0$ (b) $B^+ \rightarrow D_s^{(*)+} K_S^0$ (c) $B^+ \rightarrow D^+ K_S^0$ decay mode.

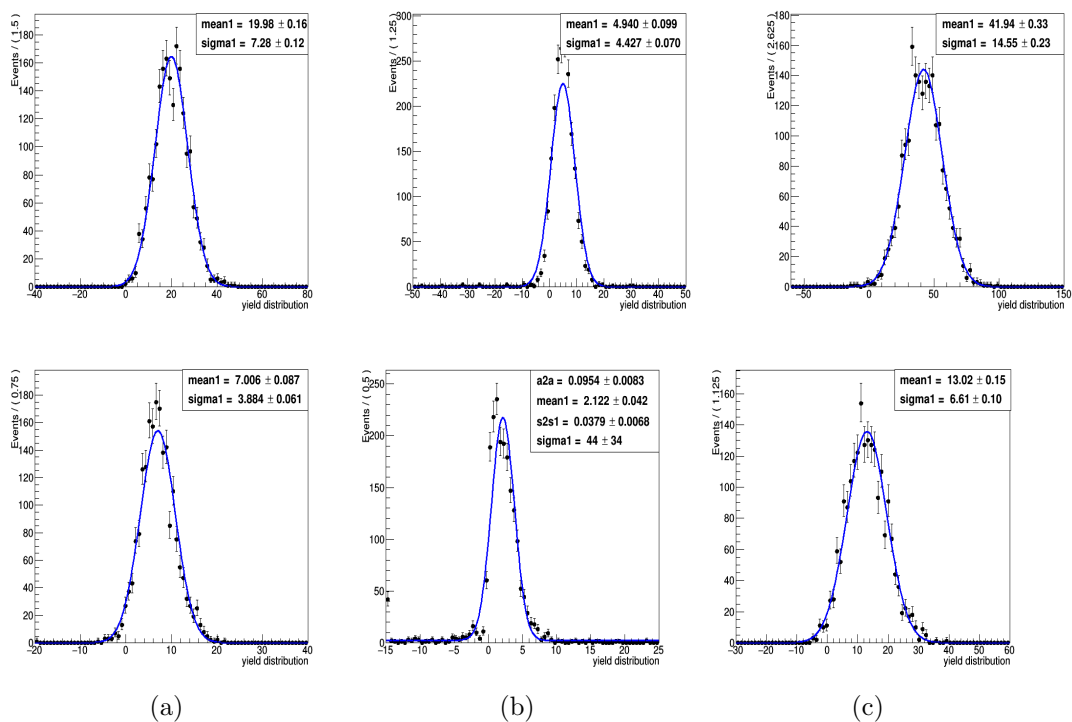


Figure 3.61: Yield distribution for (a) $B^+ \rightarrow D_s^+ \eta$ (b) $B^+ \rightarrow D_s^{(*)+} \eta$ (c) $B^+ \rightarrow D^+ \eta$ decay mode. The upper distribution for $\eta \rightarrow \gamma\gamma$ and lower for $\eta \rightarrow \pi^- \pi^+ \pi^0$ decay modes.

3.18 Toy study for signal modes

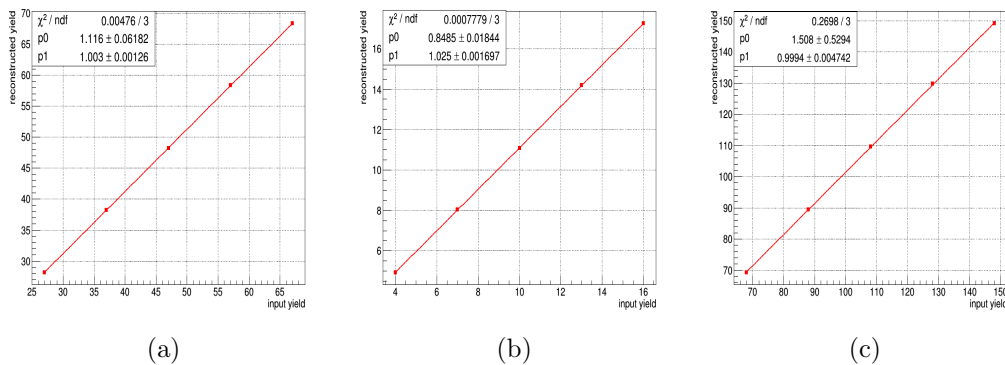


Figure 3.62: Reconstructed vs generated yield distribution for (a) $B^+ \rightarrow D_s^+ K_S^0$ (b) $B^+ \rightarrow D_s^{(*)+} K_S^0$ (c) $B^+ \rightarrow D^+ K_S^0$ decay mode.

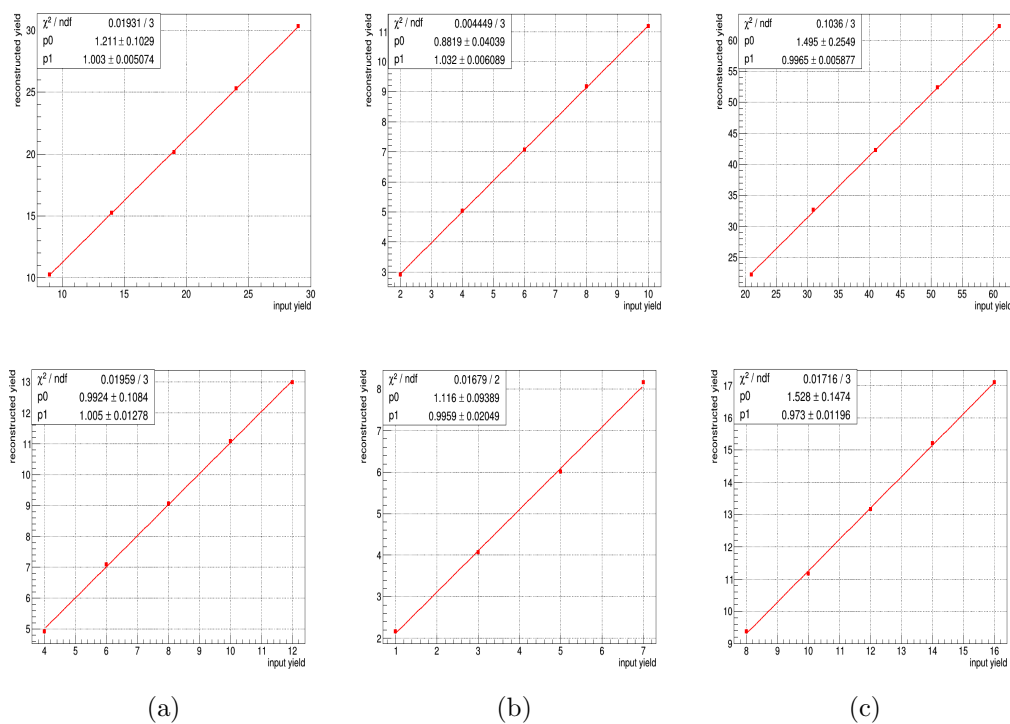


Figure 3.63: Reconstructed vs generated yield distribution for (a) $B^+ \rightarrow D_s^+ \eta$ (b) $B^+ \rightarrow D_s^{(*)+} \eta$ (c) $B^+ \rightarrow D^+ \eta$ decay mode. The upper distribution for $\eta \rightarrow \gamma\gamma$ and lower for $\eta \rightarrow \pi^- \pi^+ \pi^0$ decay modes.

3.18 Toy study for signal modes

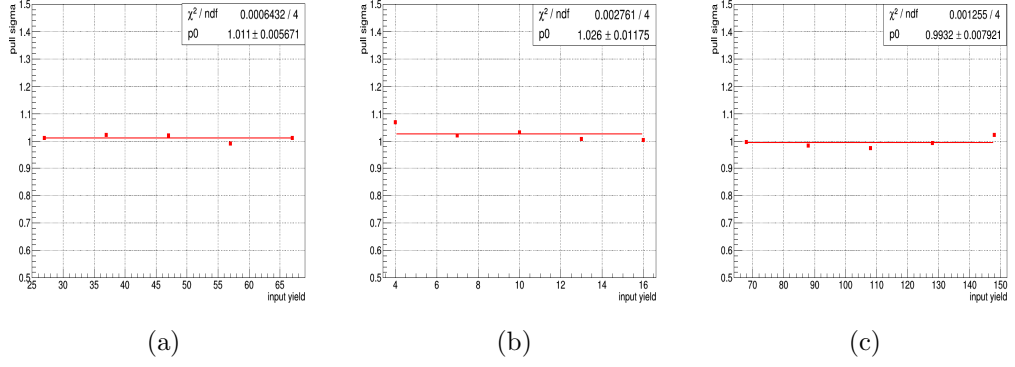


Figure 3.64: Pull sigma vs generated yield distribution for (a) $B^+ \rightarrow D_s^+ K_S^0$ (b) $B^+ \rightarrow D_s^{(*)+} K_S^0$ (c) $B^+ \rightarrow D^+ K_S^0$ decay mode.

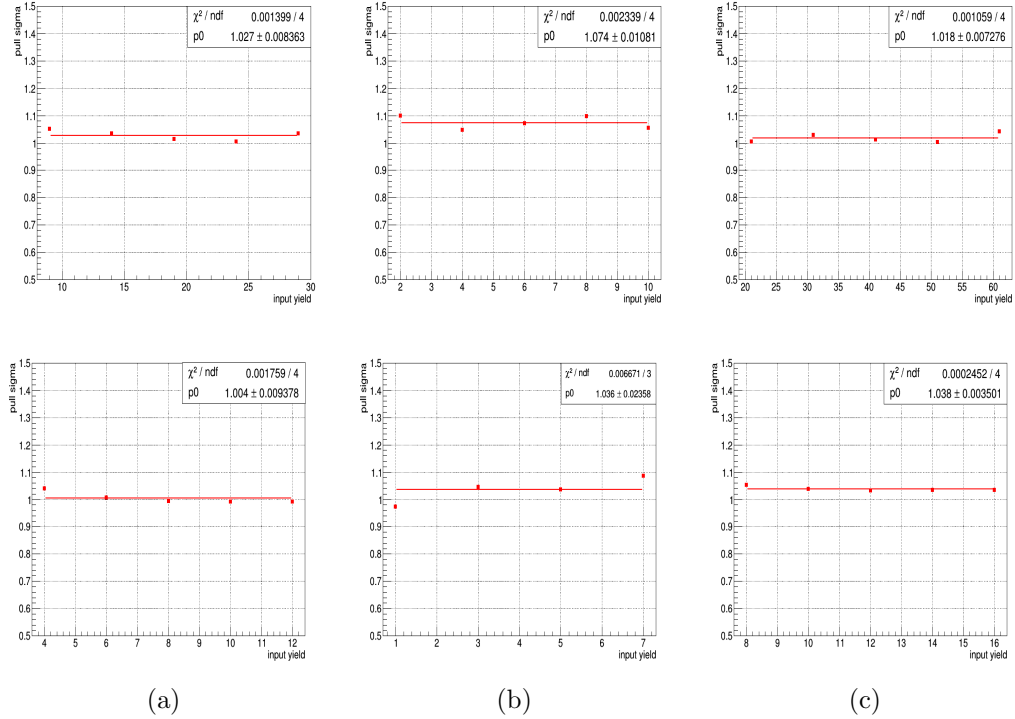


Figure 3.65: Pull sigma vs generated yield distribution for (a) $B^+ \rightarrow D_s^+ \eta$ (b) $B^+ \rightarrow D_s^{(*)+} \eta$ (c) $B^+ \rightarrow D^+ \eta$ decay mode. The upper distribution for $\eta \rightarrow \gamma\gamma$ and lower for $\eta \rightarrow \pi^- \pi^+ \pi^0$ decay modes.

3.19 Data/MC (Side-band) Comparison

In this section, we have compared the sideband of ΔE variable for the data and generic MC (lower sideband: $[-0.18 - -0.05]$ GeV, upper sideband: $[0.05 - 0.18]$ GeV) and they are found to be in good agreement as shown in Fig. 3.66, 3.67.

The distributions are scaled to the Belle luminosity.

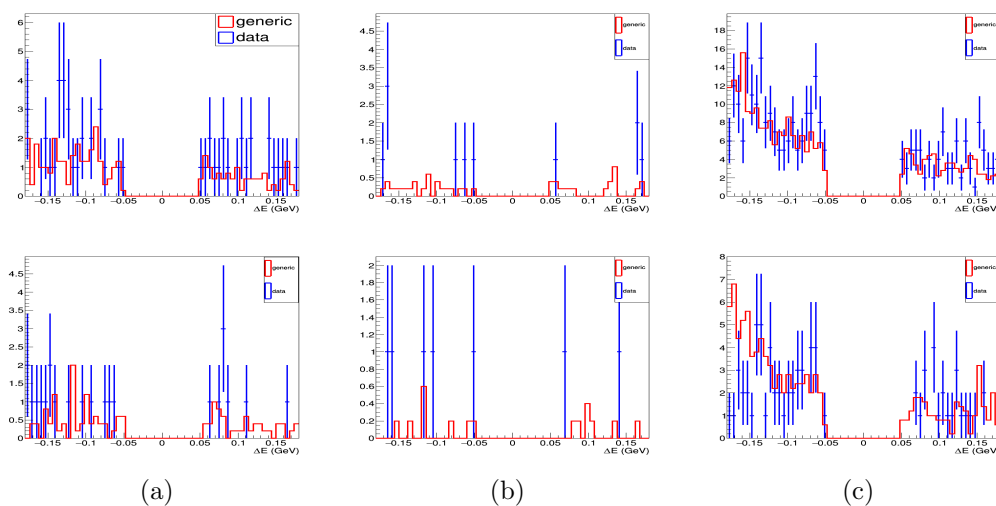


Figure 3.66: ΔE distributions for the (a) $B^+ \rightarrow D_s^+ \eta$ (b) $B^+ \rightarrow D_s^{(*)+} \eta$ and (c) $B^+ \rightarrow D^+ \eta$ decay mode using data (blue) and generic (red) MC. The upper distribution for $\eta \rightarrow \gamma\gamma$ and lower for $\eta \rightarrow \pi^- \pi^+ \pi^0$ decay modes.

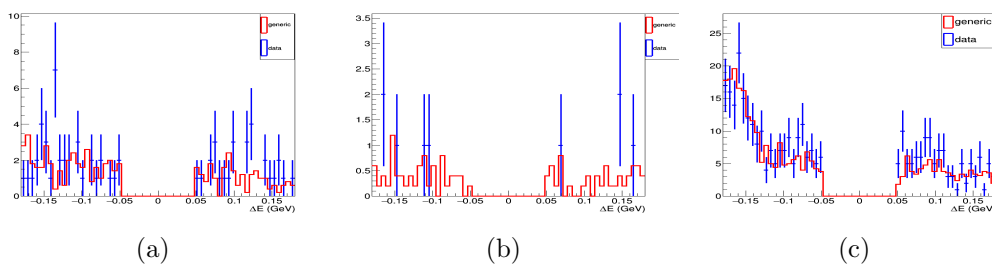


Figure 3.67: ΔE distributions for the (a) $B^+ \rightarrow D_s^+ K_S^0$ (b) $B^+ \rightarrow D_s^{(*)+} K_S^0$ and (c) $B^+ \rightarrow D^+ K_S^0$ decay mode using data (blue) and generic (red) MC.

3.19 Data/MC (Side-band) Comparison

We have compared the sideband of M_{bc} , M_{D_s} and M_{D^+} variables for the data and generic MC (lower sideband (M_{bc} : [5.27 – 5.276] GeV, M_{D_s} : [1.951 – 1.963] GeV/ c^2 , M_{D^+} : [1.855 – 1.865] GeV/ c^2) and upper sideband: (M_{bc} : [5.283 – 5.29] GeV, M_{D_s} : [1.974 – 1.985] GeV/ c^2 , M_{D^+} : [1.875 – 1.885] GeV/ c^2) and they are found to be in good agreement as shown in Fig. 3.68, 3.69, 3.70, 3.71. The distributions are scaled to the Belle luminosity.

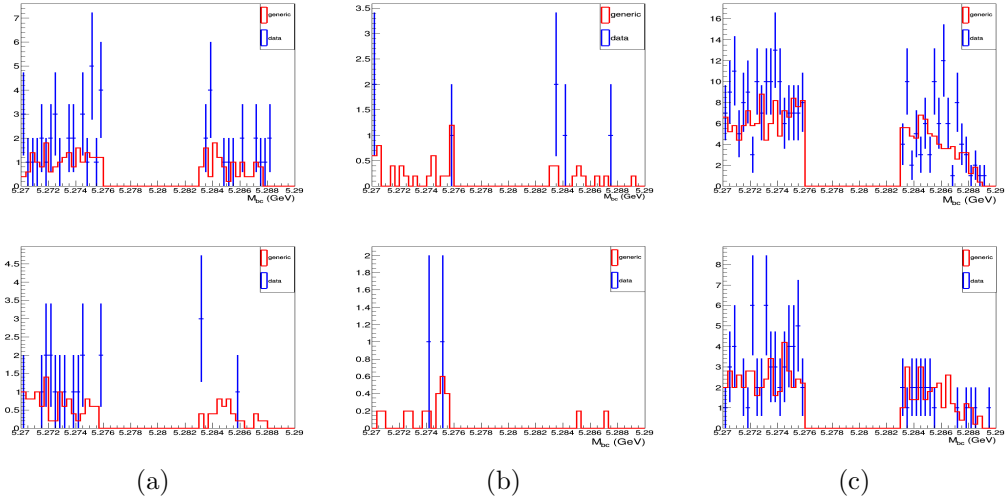


Figure 3.68: M_{bc} distributions for the (a) $B^+ \rightarrow D_s^+ \eta$ (b) $B^+ \rightarrow D_s^{(*)+} \eta$ and (c) $B^+ \rightarrow D^+ \eta$ decay mode using data (blue) and generic (red) MC. The upper distribution for $\eta \rightarrow \gamma\gamma$ and lower for $\eta \rightarrow \pi^- \pi^+ \pi^0$ decay modes.

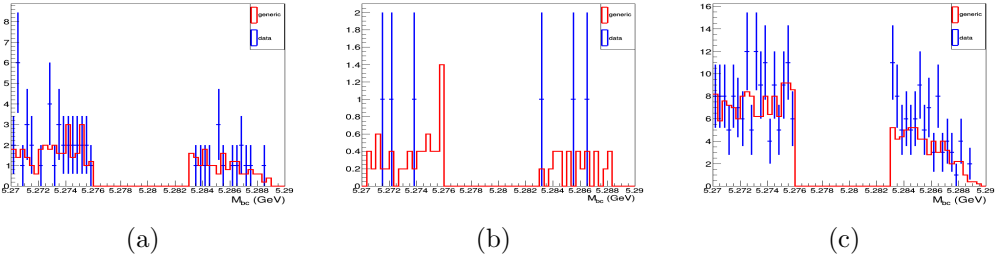


Figure 3.69: M_{bc} distributions for the (a) $B^+ \rightarrow D_s^+ K_S^0$ (b) $B^+ \rightarrow D_s^{(*)+} K_S^0$ and (c) $B^+ \rightarrow D^+ K_S^0$ decay mode using data (blue) and generic (red) MC.

3.19 Data/MC (Side-band) Comparison

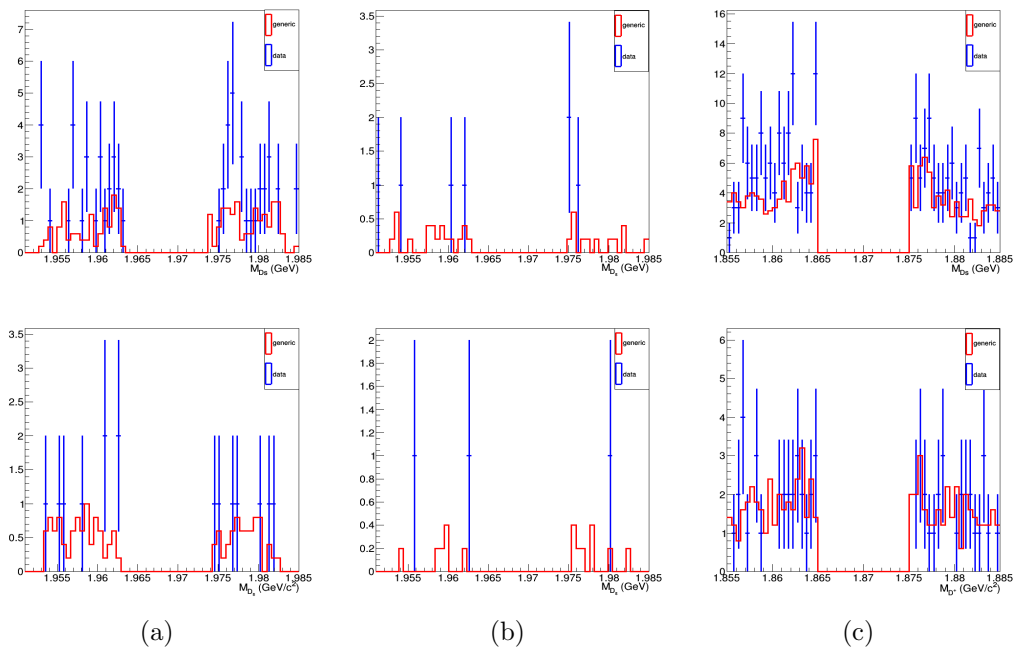


Figure 3.70: M_{D_s} (M_D) distributions for the (a) $B^+ \rightarrow D_s^+ \eta$ (b) $B^+ \rightarrow D_s^{(*)+} \eta$ and (c) $B^+ \rightarrow D^+ \eta$ decay mode using data (blue) and generic (red) MC. The upper distribution for $\eta \rightarrow \gamma\gamma$ and lower for $\eta \rightarrow \pi^-\pi^+\pi^0$ decay modes.

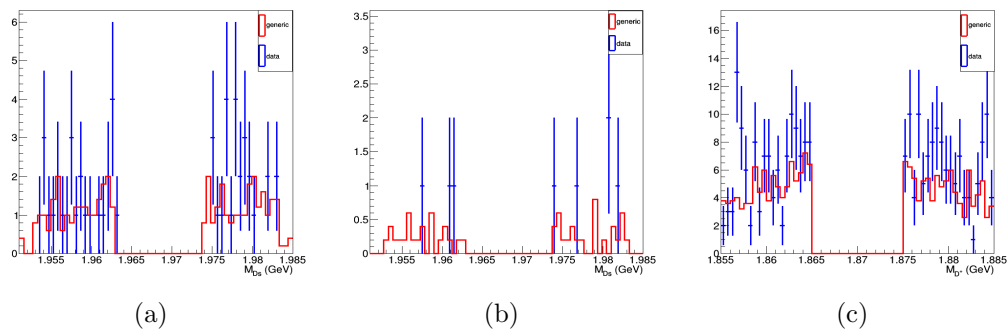


Figure 3.71: M_{D_s} (M_D) distributions for the (a) $B^+ \rightarrow D_s^+ K_S^0$ (left) (b) $B^+ \rightarrow D_s^{(*)+} K_S^0$ (middle) and (c) $B^+ \rightarrow D^+ K_S^0$ (right) decay mode using data (blue) and generic (red) MC.

3.20 Summary

We have discussed the Monte Carlo (MC) studies for rare decays, $B^+ \rightarrow D_s^{(*)+}(\rightarrow D_s^+\gamma)\eta$, $D_s^{(*)+}(\rightarrow D_s^+\gamma)\bar{K}^0$, $D_s^+\eta$, $D_s^+K_S^0$ decay modes. Major sources of the background have been studied using generic and rare MC samples. The neural network is used to reduce the continuum background with 7 continuum variables. $\bar{B}^0 \rightarrow D^0\eta$ and $\bar{B}^0 \rightarrow D^0K_S^0$ decay modes used as control sample for signal modes. We have also compared the observed yield with TM events from generic MC. The Data/MC agreement is checked in the side-band region and they are found to be in good agreement.

4

Extraction of branching fraction for signal and control mode from data

This chapter summarizes the result from the analysis of both signal and control modes with the complete Belle data taken at an integrated luminosity of 711 fb^{-1} . First, we show the data-MC comparison study with ΔE variable for the control modes in Sec.4.1. In the same section, we extract the yield with the same fitting strategy for signal and background events explained in chapter 3 and compare the measured branching fraction with the previously measured branching fraction for the control modes. In Sec. 4.2, we present the systematics study from the various sources for the control decay modes. Similarly, we also conclude the systematic uncertainty and extraction of signal yield at 90% confidence level for the signal decay modes in Sec. 4.3 and Sec. 4.4.

In Chapter 3, we already described the fitting strategy of the ΔE variables with appropriate PDFs from the complete generic MC sample for control modes and with five streams of generic MC for signal decay modes. After performing the toy study, we conclude that no bias in the fitting, hence can be used to analyse the real data.

4.1 Crosscheck with Data

Before fitting the ΔE variable for control modes, we compare data with MC as shown in Fig. 4.1. We see a good agreement in the ΔE distribution of data and generic MC samples for the control modes.

The one-dimensional unbinned maximum likelihood fitted distribution of ΔE for the control modes, $\bar{B}^0 \rightarrow D^0 \eta(\rightarrow \gamma\gamma)$, $\bar{B}^0 \rightarrow D^0 \eta(\rightarrow \pi^- \pi^+ \pi^0)$ and $\bar{B}^0 \rightarrow D^0 K_S^0$ for data are shown in Fig. 4.2. We perform a simultaneous fit on $\eta \rightarrow \gamma\gamma$ and

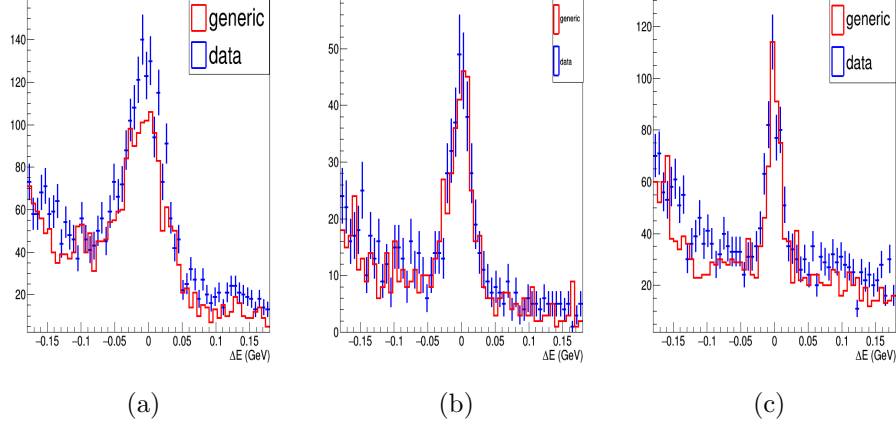


Figure 4.1: Data/MC comparison of ΔE for (a) $\bar{B}^0 \rightarrow D^0 \eta(\rightarrow \gamma\gamma)$, (b) $\bar{B}^0 \rightarrow D^0 \eta(\rightarrow \pi^- \pi^+ \pi^0)$, (c) $\bar{B}^0 \rightarrow D^0 K_S^0$ (right) decay modes. Red color shows generic (data) MC.

$\eta \rightarrow \pi^- \pi^+ \pi^0$ decay modes. For the signal, parameters of core PDF (mean, sigma) are floated and the tail parameters are fixed from the signal MC. The background is parameterized from the fit to the generic MC. The result of extracted branching fractions of the combined and the individual D^0 sub decay modes are given in the Table 4.2 and 4.3. But in Table 4.3, we observed that the branching fraction for $\bar{B}^0 \rightarrow D^0(\rightarrow K \pi \pi^0) \eta(\rightarrow \pi^- \pi^+ \pi^0)$ sub decay mode is higher because of extra yield coming from the different resonance states having the same final state. Therefore, we have excluded $D^0 \rightarrow K \pi \pi^0$ sub decay mode and proceed the study with three D^0 sub decay modes for $\bar{B}^0 \rightarrow D^0 \eta(\rightarrow \pi^- \pi^+ \pi^0)$ decay mode. Calculation of branching fraction is carried out using the expression as given in equation 4.1.1:

$$\mathcal{B} = \frac{N_s}{N_{B\bar{B}} \times \mathcal{B}(\eta/K_S^0) \times \sum_{i=1}^{i=4} [\varepsilon_{corr(i)} \times \mathcal{B}(D^0 \text{ sub decays})]} \quad (4.1.1)$$

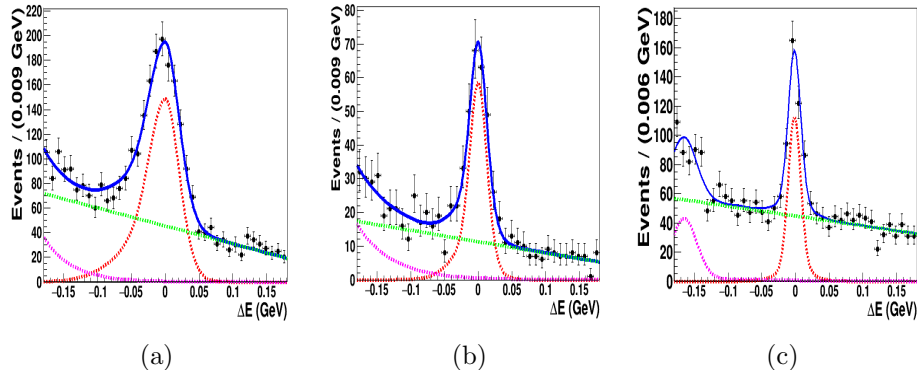


Figure 4.2: The fitted distribution of ΔE for (a) $\bar{B}^0 \rightarrow D^0 \eta(\rightarrow \gamma\gamma)$, (b) $\bar{B}^0 \rightarrow D^0 \eta(\rightarrow \pi^- \pi^+ \pi^0)$, (c) $\bar{B}^0 \rightarrow D^0 K_S^0$ decay mode. Red curve shows the signal, green curve for: $q\bar{q} + B\bar{B}$ bkg (exclude peaking background), magenta shows the peaking background and blue curve explain the overall fit.

Where, N_s is the number of signal yield, $N_{B\bar{B}}$ is the number for $B\bar{B}$ events from the data sample, \mathcal{B} is the branching fraction of the secondary decays and is taken from PDG [5] and ϵ_{corr} is the corrected signal efficiency from the signal MC. The corrected signal efficiency of the control modes are given in Table 4.1. Further, the results are also compared with a previous study carried out by the Belle [31]. We observe the significant improvement in the measured branching fraction as compared to the previously estimated branching fraction for $\bar{B}^0 \rightarrow D^0 K_S^0$ decay mode. In the case of eta mode, the measured branching fraction is also improved as compared to the previous Belle [31] measurement but consistent with BABAR [30] result. The discrepancy in the estimated branching fraction of eta mode with Belle result might be due to fluctuation and systematics bias.

4.1 Crosscheck with Data

Decay mode	$D^0 \rightarrow K\pi$	$D^0 \rightarrow K\pi\pi\pi$	$D^0 \rightarrow K_S\pi\pi$	$D^0 \rightarrow K\pi\pi^0$
$\bar{B}^0 \rightarrow D^0\eta(\rightarrow \gamma\gamma)$ ([31])	10.0(14.0)	5.6(6.6)	5.8(--)	3.0(3.6)
$\bar{B}^0 \rightarrow D^0\eta(\rightarrow \pi^-\pi^+\pi^0)$ ([31])	5.4(9.2)	3.0(4.6)	3.0(--)	1.6(2.6)
$\bar{B}^0 \rightarrow D^0K_S^0$	15.5	8.7	8.4	4.6

Table 4.1: Corrected efficiency (%) for the control modes from the signal MC samples.

Channel	Signal yield	Branching Fraction (10^{-4})	
		Measured	Previous Measurement
$\bar{B}^0 \rightarrow D^0\eta(\text{comb.})$	1373 ± 63	2.66 ± 0.12	2.53 ± 0.09 [30], 1.77 ± 0.16 [31]
$\bar{B}^0 \rightarrow D^0K_S^0$	323 ± 27	0.56 ± 0.05	0.53 ± 0.07 [32], $0.50^{+0.13}_{-0.12}$ [33]

Table 4.2: Signal yield, extracted branching fraction and previous measured branching fraction of the control modes. We observed discrepancy between measured and the previous measured branching fraction by Belle [31]. It might be due to the fluctuation or some systematics bias.

4.1.1 Individual D^0 sub decay mode study of control modes

Fig. 4.3 shows the fitted distribution of ΔE with individual D^0 sub decay modes for $\bar{B}^0 \rightarrow D^0\eta(\rightarrow \gamma\gamma)$ with data samples. In individual decay mode, the PDF used for the signal is the sum of a Gaussian with a bifurcated Gaussian (red color), combinatorial (peaking) background fitted with the 1st order polynomial (exponential function). Fig. 4.4 shows the fitted distribution of ΔE with the individual D^0 sub decay modes for $\bar{B}^0 \rightarrow D^0\eta(\rightarrow \pi\pi\pi^0)$ with the data samples. In individual decay mode, PDF used for the signal is the sum of a Gaussian with a bifurcated Gaussian (red color), combinatorial (peaking) background fitted with the 1st order polynomial (exponential function) (except peaking background in $D^0 \rightarrow K\pi$ mode fitted with sum of two Gaussian with common mean). Fig. 4.5 shows the distribution of ΔE with individual sub decay modes for $\bar{B}^0 \rightarrow D^0K_S^0$

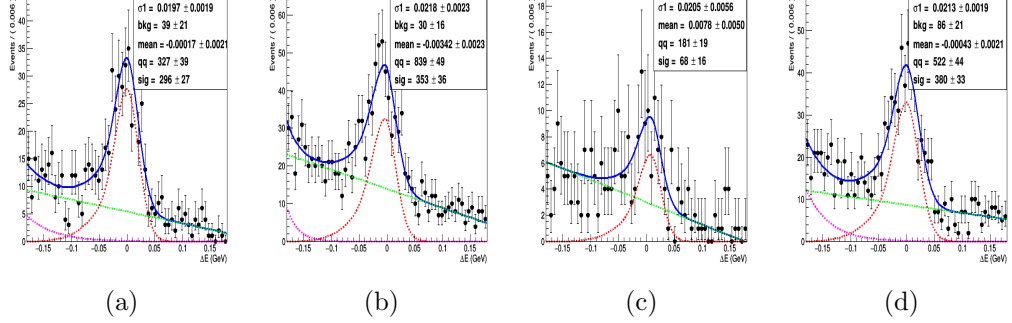


Figure 4.3: Fitted Distributions of ΔE for $\bar{B}^0 \rightarrow D^0 \eta (\rightarrow \gamma \gamma)$, (a) $D^0 \rightarrow K^- \pi^+$, (b) $D^0 \rightarrow K^- \pi^+ \pi^+ \pi^-$, (c) $D^0 \rightarrow K_S^0 \pi^+ \pi^-$ and (d) $D^0 \rightarrow K^- \pi^+ \pi^0$ decay mode with data sample. Here, only the mean and sigma of core Gaussian floated and all other PDF parameters fixed from the separate fit of the MC samples. Red curve shows the sum of a Gaussian, green (magenta) shows the combinatorial (peaking) background and blue curve shows the overall fit.

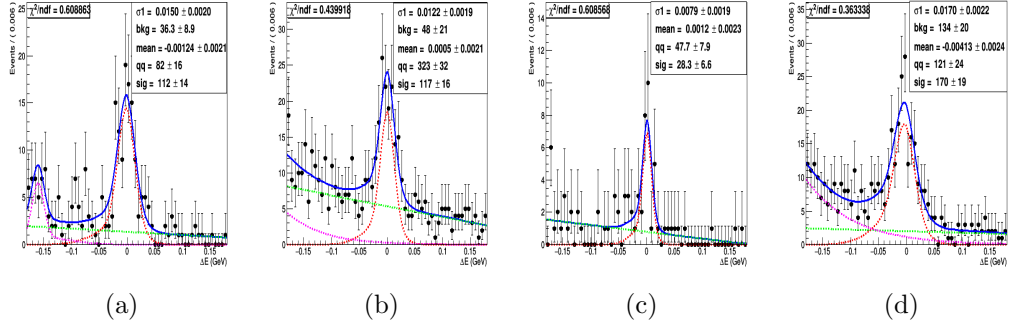


Figure 4.4: Distributions of ΔE for $\bar{B}^0 \rightarrow D^0 \eta (\rightarrow \pi \pi \pi^0)$, (a) $D^0 \rightarrow K^- \pi^+$, (b) $D^0 \rightarrow K^- \pi^+ \pi^+ \pi^-$, (c) $D^0 \rightarrow K_S^0 \pi^+ \pi^-$ and (d) $D^0 \rightarrow K^- \pi^+ \pi^0$ decay mode with data sample. Here, only the mean and sigma of core a Gaussian floated and all other PDF parameters are fixed from the separate fit of the MC samples. Red curve shows the sum of a Gaussian, green (magenta) shows the combinatorial (peaking) background and blue curve shows the overall fit.

decay mode with data samples. In individual decay mode, PDF used for the signal is sum of two Gaussian with common mean (red color), combinatorial (peaking) background fitted with the 1st order polynomial (sum of two Gaussian).

4.2 Systematic study of Control modes

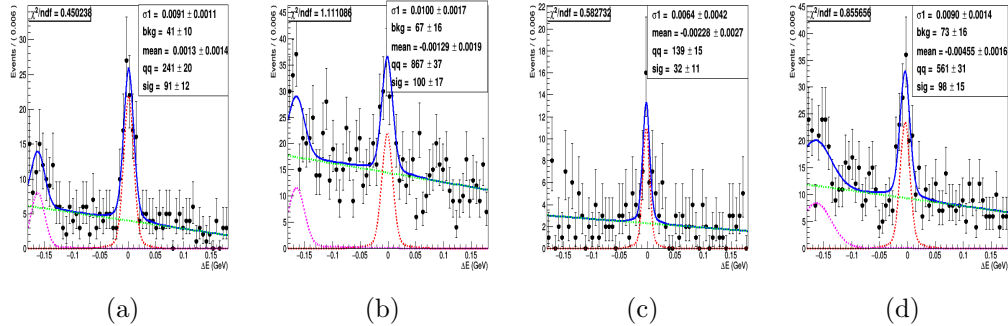


Figure 4.5: Distributions of the ΔE variable for $\bar{B}^0 \rightarrow D^0 K_S^0$, (a) $D^0 \rightarrow K^- \pi^+$, (b) $D^0 \rightarrow K^- \pi^+ \pi^+ \pi^-$, (c) $D^0 \rightarrow K_S^0 \pi^+ \pi^-$ and (d) $D^0 \rightarrow K^- \pi^+ \pi^0$ decay mode with data sample. Here, only the mean and sigma of core Gaussian floated and all other PDF parameters are fixed from the separate fit of MC samples. Red curve shows the sum of a Gaussian, green (magenta) shows the combinatorial (peaking) background and blue curve shows the overall fit.

Decay mode	$D^0 \rightarrow K\pi$	$D^0 \rightarrow K\pi\pi\pi$	$D^0 \rightarrow K_S\pi\pi$	$D^0 \rightarrow K\pi\pi^0$
$\bar{B}^0 \rightarrow D^0 \eta (\rightarrow \gamma\gamma) (10^{-4})$	2.46 ± 0.22	2.52 ± 0.26	2.0 ± 0.47	2.96 ± 0.26
$B^0 \rightarrow D^0 \eta (\rightarrow \pi^- \pi^+ \pi^0) (10^{-4})$	3.0 ± 0.37	2.70 ± 0.37	2.73 ± 0.64	4.24 ± 0.47
$B^0 \rightarrow D^0 K_S^0 (10^{-5})$	5.6 ± 0.74	5.2 ± 0.88	7.3 ± 2.52	5.6 ± 0.86

Table 4.3: Branching fraction measurement of individual D^0 sub decay modes from the yield of ΔE distribution for control mode.

4.2 Systematic study of Control modes

Table 4.7 shows the systematic uncertainties on the branching fraction measurements are calculated due to uncertainty coming from different sources such as pion/kaon identification, track finding efficiency, $N_{B\bar{B}}$, secondary branching fraction, K_S^0 reconstruction, and ΔE fit.

4.2 Systematic study of Control modes

4.2.1 Kaon identification

In $\bar{B}^0 \rightarrow D^0\eta(\rightarrow \gamma\gamma)$, $\bar{B}^0 \rightarrow D^0\eta(\rightarrow \pi^-\pi^+\pi^0)$ and $\bar{B}^0 \rightarrow D^0K_S^0$ decay modes, where the D^0 is reconstructed from: $D^0 \rightarrow K\pi$, $K\pi\pi\pi$, $K_S^0\pi\pi$, $K\pi\pi^0$ and kaons have an uncertainty on their identification. In order to estimate the kaon efficiency correction, we use PID group estimation based on the decay $D^{*+} \rightarrow D^0(K\pi)\pi^+$ [73]. This correction is used to correct the efficiency and error and is added as systematic error coming from kaon identification. Table 4.4 summarizes the kaon identification systematic study.

Decay	Correction with error		Correction factor	Systematic error(%)
	SVD1	SVD2		
$B^0 \rightarrow D^0\eta(\rightarrow \gamma\gamma)$				
$D^0 \rightarrow K\pi$	1.002 ± 0.0092	1.001 ± 0.0042	1.00	0.52
$D^0 \rightarrow K\pi\pi\pi$	1.001 ± 0.0108	1.009 ± 0.0050	1.01	0.61
$D^0 \rightarrow K\pi\pi^0$	1.001 ± 0.0173	1.005 ± 0.0081	1.00	0.99
$B^0 \rightarrow D^0\eta(\rightarrow \pi^-\pi^+\pi^0)$				
$D^0 \rightarrow K\pi$	1.002 ± 0.0114	1.000 ± 0.0050	1.00	0.63
$D^0 \rightarrow K\pi\pi\pi$	1.000 ± 0.0143	1.010 ± 0.0062	1.01	0.78
$D^0 \rightarrow K\pi\pi^0$	1.002 ± 0.0208	1.006 ± 0.0096	1.00	1.18
$B^0 \rightarrow D^0K_S^0$				
$D^0 \rightarrow K\pi$	1.002 ± 0.0062	1.001 ± 0.0027	1.00	0.34
$D^0 \rightarrow K\pi\pi\pi$	1.000 ± 0.0074	1.009 ± 0.0033	1.01	0.41
$D^0 \rightarrow K\pi\pi^0$	1.002 ± 0.0109	1.006 ± 0.0050	1.00	0.62

Table 4.4: Systematic uncertainty due to kaon identification.

4.2.2 Pion identification

A similar procedure is applied for pion to find systematic uncertainty and PID correction as used for kaon. Table 4.5 summarizes the uncertainty due to pion identification.

4.2 Systematic study of Control modes

Decay	Correction factor	Systematic error(%)
$B^0 \rightarrow D^0 \eta (\rightarrow \gamma \gamma)$		
$D^0 \rightarrow K \pi$	0.97	0.50
$D^0 \rightarrow K \pi \pi \pi$	0.96	1.02
$D^0 \rightarrow K_S^0 \pi \pi$	0.98	0.86
$D^0 \rightarrow K \pi \pi^0$	0.99	0.87
$B^0 \rightarrow D^0 \eta (\rightarrow \pi^- \pi^+ \pi^0)$		
$D^0 \rightarrow K \pi$	0.93	1.03
$D^0 \rightarrow K \pi \pi \pi$	0.91	1.64
$D^0 \rightarrow K_S^0 \pi \pi$	0.92	1.50
$D^0 \rightarrow K \pi \pi^0$	0.95	1.86
$B^0 \rightarrow D^0 K_S^0$		
$D^0 \rightarrow K \pi$	0.97	0.32
$D^0 \rightarrow K \pi \pi \pi$	0.97	0.72
$D^0 \rightarrow K_S^0 \pi \pi$	0.96	0.62
$D^0 \rightarrow K \pi \pi^0$	0.98	0.57

Table 4.5: Systematics uncertainty due to pion identification.

4.2.3 Tracking

The detection efficiency for the charged particle track has an uncertainty of about 0.35% per track and reconstruction of charged particle tracks are studied using partially reconstructed $D^{*+} \rightarrow D^0(K_S^0(\pi^- \pi^+) \pi^+ \pi^-) \pi^+$ decay mode with $p_T > 200 \text{ MeV}/c$ [74].

4.2.4 $N_{B\bar{B}}$

In the analysis, we use the Belle data, which contains $(771.581 \pm 10.6) \times 10^6$ ($N_{B\bar{B}}$), which is used for the calculation. 1.4% error is used as a systematic uncertainty on the branching fraction measurement.

4.2.5 K_S^0 reconstruction

To calculate the systematics uncertainty in K_S^0 , multiply the correction factor ([75]) with the weight factor and the quadrature sum of the multiplication factor.

4.2.6 η , π^0 , and γ detection

The uncertainties in reconstruction efficiencies of photon and η (π^0) are 3.0% [76] and 4.1% [77] per particle, respectively.

4.2.7 Secondary Branching Fraction

We used the secondary branching fraction to calculate the primary branching fraction. These secondary fractions have some uncertainty, which is taken from the PDG [5].

4.2.8 Fit bias

To calculate uncertainty from the fit bias, 2000 toys samples are generated using the PDF for each decay mode and yield is obtained from the fit. Fit is performed on each sample and we obtain the average yield from these fits. The difference between the generated and obtained yield is taken as fit bias. Table 4.6 summarizes the expected fit bias in each decay mode.

Mode	Fit bias(%)
$B^0 \rightarrow D^0 \eta (\rightarrow \gamma \gamma)$	0.4
$\bar{B}^0 \rightarrow D^0 \eta (\rightarrow \pi^- \pi^+ \pi^0)$	0.6
$B^0 \rightarrow D^0 \eta$ (combine)	0.6
$\bar{B}^0 \rightarrow D^0 K_S^0$	0.4

Table 4.6: Fit bias estimation for the decay modes from the study of ToyMC.

4.2.9 ΔE Fit

Signal yield is extracted by fitting the experimental data. To fit the data, we fix some signal and background PDF parameters from the signal and generic MC, respectively. Those parameters have some uncertainty which may affect the signal yield. We have estimated those systematics by varying all the fixed parameters $\pm 1\sigma$ from the central values and finally their quadrature addition results in the systematic uncertainty from the ΔE fit.

Total systematics uncertainty is calculated as a quadrature sum of systematic uncertainty from the individual sources of systematic error and is summarized in Table 4.7.

Source	$B^0 \rightarrow D^0\eta$ (combine)	$B^0 \rightarrow D^0K_S^0$
π ID (%)	1.4	0.8
K ID(%)	0.7	0.5
Tracking (%)	1.2	1.7
$N_{B\bar{B}}$ (%)	1.4	1.4
K_S^0 reconstruction (%)	0.1	1.5
η detection (%)	5.7	2.0
Secondary $\mathcal{B.F}$ (%)	2.0	1.9
Fit bias (%)	0.6	0.4
$\Delta E(+\sigma, -\sigma)$ fit (%)	+4.4, -4.0	+1.2, -1.2
Total	+7.9, -7.7	4.1

Table 4.7: Summary of systematic uncertainties.

4.2.10 Comparison of branching fraction

In Table 4.8, we have compared the measured branching fraction with previously measured branching fraction by the Belle [31, 33] and BABAR [30, 32]. We observed expected improvement in $\bar{B}^0 \rightarrow D^0 K_S^0$ decay mode, but we did not see significant improvement for $\bar{B}^0 \rightarrow D^0 \eta$ decay mode.

Mode	Measured B.F (10^{-4})	Previous B.F (10^{-4})	
		BABAR	Belle
$\bar{B}^0 \rightarrow D^0 \eta$ (combine)	$2.66 \pm 0.12(\text{stat}) \pm 0.21(\text{syst})$	$2.53 \pm 0.09 \pm 0.11$ [30]	$1.77 \pm 0.16 \pm 0.21$ [31]
$\bar{B}^0 \rightarrow D^0 K_S^0$	$0.56 \pm 0.05(\text{stat}) \pm {}^{+0.02}_{-0.02}(\text{syst})$	$0.53 \pm 0.07 \pm 0.03$ [32]	$0.50^{+0.13}_{-0.12} \pm 0.06$ [33]

Table 4.8: Compared the measured B.F with the previously measured B.F given by Belle and BABAR.

4.3 Systematics Study of Signal Decay Modes

In the previous section, we already mentioned the procedure for estimation of systematics uncertainty from different sources such as pion/kaon identification, track finding efficiency, $N_{B\bar{B}}$, K_S^0 reconstruction and ΔE fit. The same method is adopted to calculate the uncertainty from these sources for the signal decay modes. Table 4.11 summarizes possible sources of systematics uncertainty for signal decay modes.

4.3.1 Kaon- pion Identification

Table 4.9 and 4.10 updated with the systematic uncertainty from Kaon and pion identification, respectively.

4.3.2 Tracking

The detection efficiency for the charged particle track has an uncertainty of about 0.35% per track as discussed in previous section.

- $B^+ \rightarrow D_s^+ \eta$, $D_s^{(*)+} \eta$ the uncertainty comes out to be 1.05% (3 tracks from $D_s^+ \rightarrow \phi(KK)\pi^+$, $D_s^+ \rightarrow \bar{K}^{*0}(K\pi)K^+$, $D_s^+ \rightarrow K_S^0(\pi\pi)K^+$).
- For $B^+ \rightarrow D_s^+ K_S^0$, $D_s^{(*)+} K_S^0$ the uncertainty comes out to be 1.75% (2 additional tracks from $K_S^0(\pi\pi)$).
- For $B^+ \rightarrow D^+ K_S^0$, $D^+ \eta$ the uncertainty comes out to be 1.75% (5 tracks: 2 from $K_S^0(\pi\pi)$, $K\pi\pi$, $K_S^0(\pi\pi)\pi$) and 1.05% (3 tracks), respectively.

4.3 Systematics Study of Signal Decay Modes

Decay	Correction factor	Systematic error(%)
$B^+ \rightarrow D_s^+ \eta (\rightarrow \gamma\gamma)$		
$D_s^+ \rightarrow \phi (\rightarrow KK) \pi^+$	1.02	0.89
$D_s^+ \rightarrow \bar{K}^{*0} (\rightarrow K\pi) K^+$	1.02	0.85
$D_s^+ \rightarrow K_S^0 K^+$	1.00	0.62
$B^+ \rightarrow D_s^+ \eta (\rightarrow \pi\pi\pi)$		
$D_s^+ \rightarrow \phi (\rightarrow KK) \pi^+$	1.02	1.09
$D_s^+ \rightarrow \bar{K}^{*0} (\rightarrow K\pi) K^+$	1.01	1.09
$D_s^+ \rightarrow K_S^0 K^+$	1.00	0.76
$B^+ \rightarrow D_s^{*+} \eta (\rightarrow \gamma\gamma)$		
$D_s^+ \rightarrow \phi (\rightarrow KK) \pi^+$	1.02	1.22
$D_s^+ \rightarrow \bar{K}^{*0} (\rightarrow K\pi) K^+$	1.02	1.14
$D_s^+ \rightarrow K_S^0 K^+$	1.00	0.83
$B^+ \rightarrow D_s^{*+} \eta (\rightarrow \pi\pi\pi)$		
$D_s^+ \rightarrow \phi (\rightarrow KK) \pi^+$	1.02	1.47
$D_s^+ \rightarrow \bar{K}^{*0} (\rightarrow K\pi) K^+$	1.02	1.46
$D_s^+ \rightarrow K_S^0 K^+$	1.00	1.03
$B^+ \rightarrow D_s^+ K_S^0$		
$D_s^+ \rightarrow \phi (\rightarrow KK) \pi^+$	1.02	0.64
$D_s^+ \rightarrow \bar{K}^{*0} (\rightarrow K\pi) K^+$	1.02	0.57
$D_s^+ \rightarrow K_S^0 K^+$	1.00	0.43
$B^+ \rightarrow D_s^{*+} K_S^0$		
$D_s^+ \rightarrow \phi (\rightarrow KK) \pi^+$	1.02	0.85
$D_s^+ \rightarrow \bar{K}^{*0} (\rightarrow K\pi) K^+$	1.02	0.78
$D_s^+ \rightarrow K_S^0 K^+$	1.00	0.57
$B^+ \rightarrow D^+ K_S^0$		
$D^+ \rightarrow K\pi\pi$	1.01	0.37
$B^+ \rightarrow D^+ \eta (\gamma\gamma)$		
$D^+ \rightarrow K\pi\pi$	1.01	0.54
$B^+ \rightarrow D^+ \eta (\pi\pi\pi)$		
$D^+ \rightarrow K\pi\pi$	1.01	0.68

Table 4.9: Systematics uncertainty due to Kaon identification.

4.4 Signal Decay Mode study with Data

Decay	Correction factor	Systematic error(%)
$B^+ \rightarrow D_s^+ \eta (\rightarrow \gamma\gamma)$		
$D_s^+ \rightarrow \phi (\rightarrow KK) \pi^+$	0.97	0.62
$D_s^+ \rightarrow \bar{K}^{*0} (\rightarrow K\pi) K^+$	0.98	0.54
$B^+ \rightarrow D_s^+ \eta (\rightarrow \pi\pi\pi)$		
$D_s^+ \rightarrow \phi (\rightarrow KK) \pi^+$	0.93	1.29
$D_s^+ \rightarrow \bar{K}^{*0} (\rightarrow K\pi) K^+$	0.94	1.24
$D_s^+ \rightarrow K_S^0 K^+$	0.96	1.02
$B^+ \rightarrow D_s^{*+} \eta (\rightarrow \gamma\gamma)$		
$D_s^+ \rightarrow \phi (\rightarrow KK) \pi^+$	0.97	0.86
$D_s^+ \rightarrow \bar{K}^{*0} (\rightarrow K\pi) K^+$	0.98	0.71
$B^+ \rightarrow D_s^{*+} \eta (\rightarrow \pi\pi\pi)$		
$D_s^+ \rightarrow \phi (\rightarrow KK) \pi^+$	0.93	1.76
$D_s^+ \rightarrow \bar{K}^{*0} (\rightarrow K\pi) K^+$	0.94	1.65
$D_s^+ \rightarrow K_S^0 K^+$	0.96	1.36
$B^+ \rightarrow D_s^+ K_S^0$		
$D_s^+ \rightarrow \phi (\rightarrow KK) \pi^+$	0.97	0.44
$D_s^+ \rightarrow \bar{K}^{*0} (\rightarrow K\pi) K^+$	0.98	0.40
$B^+ \rightarrow D_s^{*+} K_S^0$		
$D_s^+ \rightarrow \phi (\rightarrow KK) \pi^+$	0.97	0.60
$D_s^+ \rightarrow \bar{K}^{*0} (\rightarrow K\pi) K^+$	0.98	0.52
$B^+ \rightarrow D^+ K_S^0$		
$D^+ \rightarrow K \pi \pi$	0.96	0.52
$D^+ \rightarrow K_S^0 \pi$	0.97	0.40
$B^+ \rightarrow D^+ \eta (\gamma\gamma)$		
$D^+ \rightarrow K \pi \pi$	0.96	0.74
$D^+ \rightarrow K_S^0 \pi$	0.97	0.59
$B^+ \rightarrow D^+ \eta (\pi\pi\pi)$		
$D^+ \rightarrow K \pi \pi$	0.91	1.30
$D^+ \rightarrow K_S^0 \pi$	0.93	1.21

Table 4.10: Systematics uncertainty due to pion identification.

4.4 Signal Decay Mode study with Data

We perform the 1D UML fit to the $\Upsilon(4S)$ (on resonance) data for each signal decay mode. Fig. 4.6 shows the fitted distribution of ΔE with data samples for

4.4 Signal Decay Mode study with Data

Source	$B^+ \rightarrow D_s^+ \eta$ (combine)	$B^+ \rightarrow D_s^{(*)+} \eta$ (combine)	$B^+ \rightarrow D_s^+ K_S^0$	$B^+ \rightarrow D_s^{(*)+} K_S^0$	$B^+ \rightarrow D^+ K_S^0$	$B^+ \rightarrow D^+ \eta$ (combine)
π ID	0.8	1.1	0.3	0.4	0.6	1.4
K ID	1.1	1.6	0.7	0.9	0.3	0.5
Tracking (%)	1.2	1.2	1.8	1.8	1.8	1.2
$N_{B\bar{B}}$ (%)	1.4	1.4	1.4	1.4	1.4	1.4
K_S^0 reconstruction	0.2	0.2	1.6	1.6	1.5	0.1
$\eta(\pi^0)$ detection	4.1	4.1	–	–	–	4.1
γ detection	–	3.0	–	3.0	–	–
Secondary $\mathcal{B.F}$ (%)	2.0	2.2	1.9	2.1	1.5	1.6
ΔE fit	+0.5, -0.5	+4.4, -4.0	1.2	1.2	1.2	+9.7, -12.1
Fit bias	8.4	23.2	2.2	9.9	1.3	4.1
Total sys.	9.8	+24.4, -24.3	4.3	11.0	3.6	+11.6, -13.7

Table 4.11: The summary of systematic uncertainties for the signal modes.

all signal decay modes. For eta modes, we perform a simultaneous fit on $\eta \rightarrow \gamma\gamma$ and $\eta \rightarrow \pi\pi\pi$ decay modes as shown in Fig. 4.6. Here, we fixed all the PDF parameters from the MC simulation and floated yield of signal and background events. The 1st order polynomial parameter is used for background events.

For all signal decay modes, the effective yield of signal events N_s (eq. 4.1.1) is expected to be 0, except $B^+ \rightarrow D_s^+ \eta$, $B^+ \rightarrow D^+ \eta$ decay modes. In the absence of a significant signal, we calculate the U.L. of branching fraction with the frequentist method [78] using an ensemble of 2000 pseudo experiments. We calculate the C.L. as a percentage of the pseudo experiments with a fitted yield greater than the expected signal yield in data. Systematic of decay modes have been included by smearing the yield of the pseudo experiments within the fluctuations. Fig. 4.7 shows the C.L. distribution as a function of input signal yield for different signal decay modes. The upper limit of signal yield and branching fraction @ 90% C.L. of all interested signal decay modes are updated in Table 4.12.

4.4 Signal Decay Mode study with Data

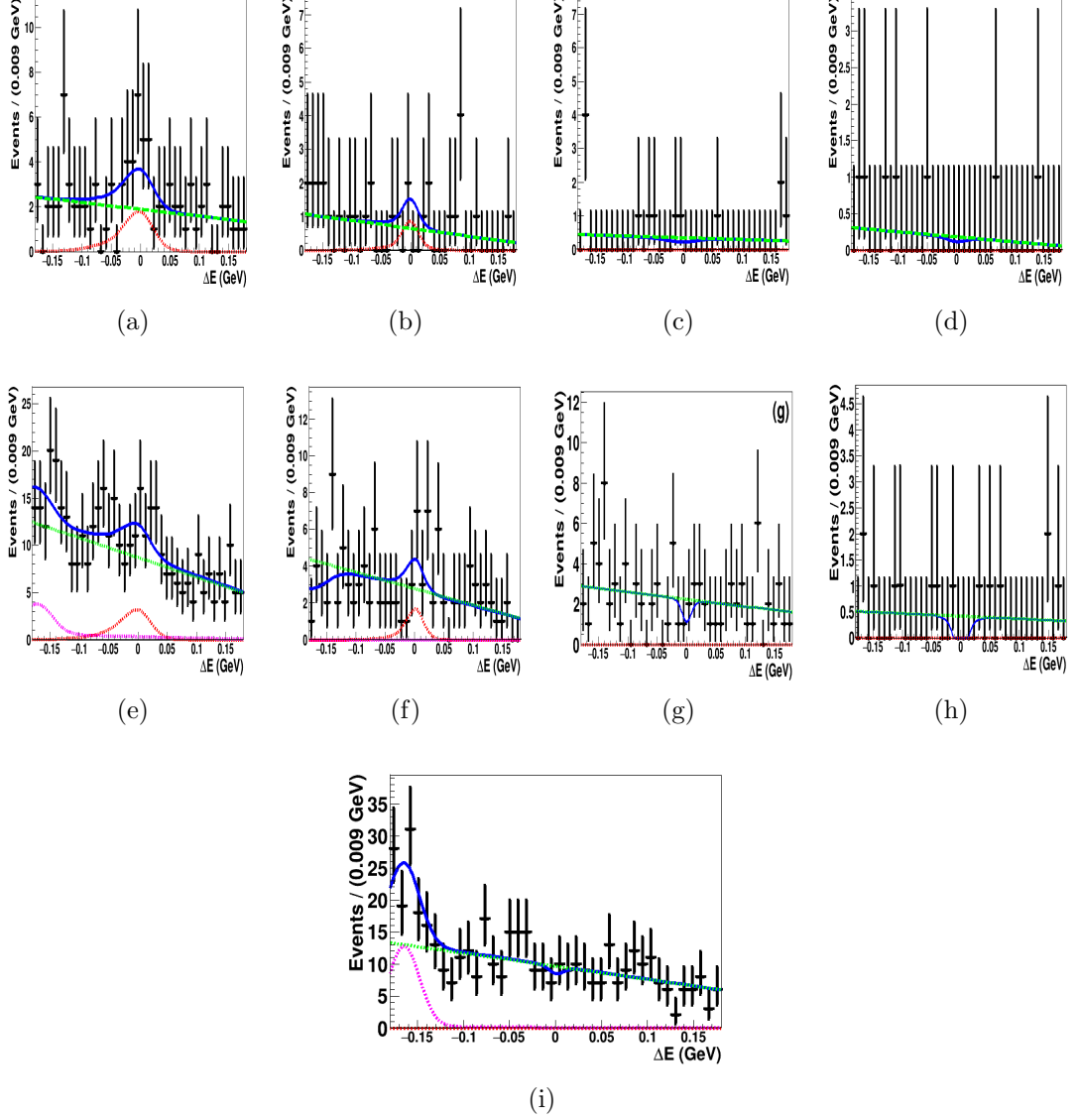


Figure 4.6: Fits of ΔE distributions in data for decay modes (a) $B^+ \rightarrow D_s^+ \eta(\gamma\gamma)$, (b) $B^+ \rightarrow D_s^+ \eta(\pi^- \pi^+ \pi^0)$, (c) $B^+ \rightarrow D_s^{*+} \eta(\gamma\gamma)$, (d) $B^+ \rightarrow D_s^{*+} \eta(\pi^- \pi^+ \pi^0)$, (e) $B^+ \rightarrow D^+ \eta(\gamma\gamma)$, (f) $B^+ \rightarrow D^+ \eta(\pi^- \pi^+ \pi^0)$, (g) $B^+ \rightarrow D_s^+ K_S^0$, (h) $B^+ \rightarrow D_s^{*+} K_S^0$, (i) $B^+ \rightarrow D^+ K_S^0$. The data points with error bars show the measurement result. The different curves show the various PDF components: the solid (blue) line: total PDF, the dotted (red) line: signal PDF, the dotted (magenta) line: peaking background on the lower side of ΔE and the dotted (green) line: combinatorial background mainly from $q\bar{q}$ events.

4.4 Signal Decay Mode study with Data

Decay Mode	Yield	$\mathcal{B} \times 10^{-5}$ @ 90% CL	Signal significance (\mathcal{S})
$B^+ \rightarrow D_s^+ \eta$ (combine)	< 21	< 1.4	1.2
$B^+ \rightarrow D_s^{*+} \eta$ (combine)	< 5.5	< 1.7	–
$B^+ \rightarrow D^+ \eta$ (combine)	< 41	< 1.2	1.4
$B^+ \rightarrow D_s^+ K^0$	< 4	< 0.3	–
$B^+ \rightarrow D_s^{*+} K^0$	< 1.8	0.6	–
$B^+ \rightarrow D^+ K^0$	< 8	< 0.2	–

Table 4.12: Signal yield, branching fraction (\mathcal{B}) @ 90% CL and signal significance for signal decay modes.

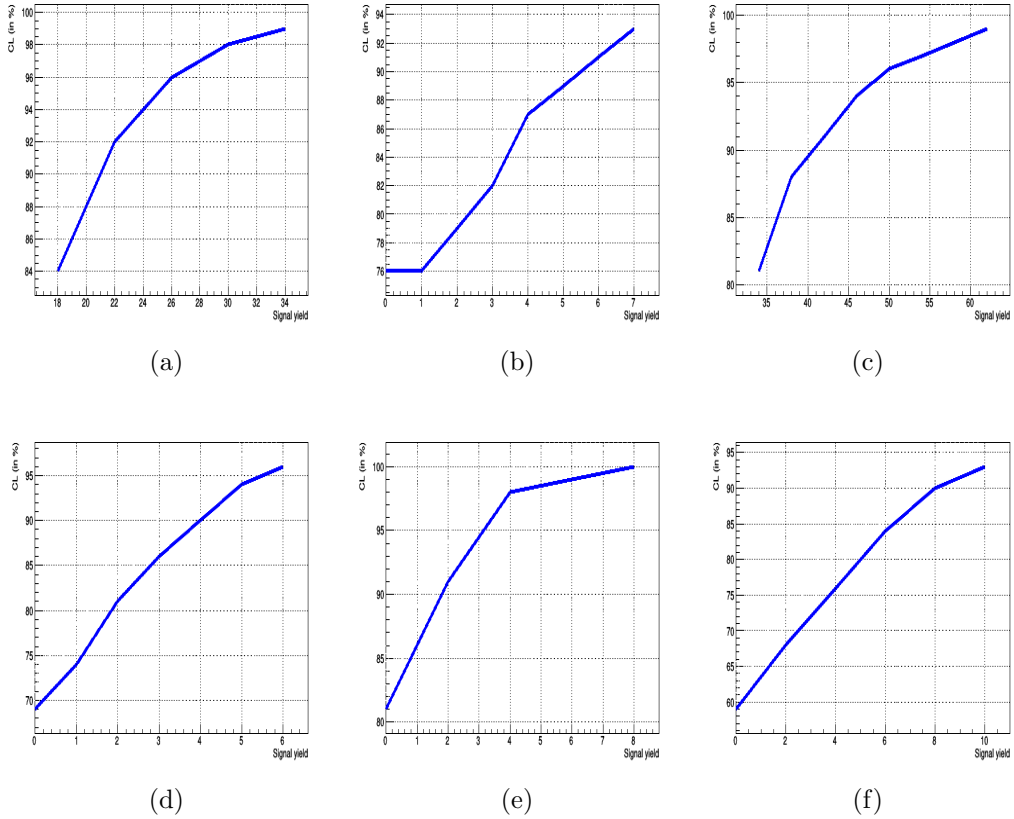


Figure 4.7: Yield obtained at 90% CL for (a) $B^+ \rightarrow D_s^+ \eta$, (b) $B^+ \rightarrow D_s^{*+} \eta$, (c) $B^+ \rightarrow D^+ \eta$, (d) $B^+ \rightarrow D_s^+ K_S^0$, (e) $B^+ \rightarrow D_s^{*+} K_S^0$, (f) $B^+ \rightarrow D^+ K_S^0$.

4.5 Summary

To summarize, we do not observe any significant signal yield for the signal decay modes, so the upper limit at 90% C.L. is given Table 4.13. With the full Belle data, we also provide the most precise branching fraction as compared to the previous measured branching fraction for $\bar{B}^0 \rightarrow D^0 K^0$ decay modes. On the other side, the measured branching fraction of $\bar{B}^0 \rightarrow D^0 \eta$ decay mode is also consistent with the previous measured branching fraction by the BABAR but it is not in agreement with the Belle last result might be due to fit bias or fluctuation.

Decay Mode	Yield	$\mathcal{B} \times 10^{-5}$
$B^+ \rightarrow D_s^+ \eta$ (combine)	< 21	< 1.4
$B^+ \rightarrow D_s^{*+} \eta$ (combine)	< 5.5	< 1.7
$B^+ \rightarrow D^+ \eta(\gamma\gamma)$	< 41	< 1.2
$B^+ \rightarrow D_s^+ K^0$	< 4	< 0.3
$B^+ \rightarrow D_s^{*+} K^0$	< 1.8	< 0.6
$B^+ \rightarrow D^+ K^0$	< 8	< 0.2
$B^0 \rightarrow D^0 \eta$ (combine)	1373 ± 63	$26.6 \pm 1.2 \pm 2.1$
$\bar{B}^0 \rightarrow D^0 K^0$	323 ± 27	$5.6 \pm 0.5 \pm 0.2$

Table 4.13: The upper limit at 90% C.L. for extraction the signal yield and branching fraction (\mathcal{B}) of signal and control decay modes.

Silicon Vertex Detector at Belle II

Chapter 2, explains the Belle II detector and its sub-detector in detail. This chapter, discuss my contributions in the upgrading of the silicon vertex detector (SVD). Section 5.1, gives a brief overview of the SVD detector. In section 5.2, simulation study along with the test beam data is described. Section 5.3 , discuss about the visual inspection of the SVD 4th layer.

5.1 SVD

The Belle II VXD consists of two sub-detector. One is the Pixel detector (PXD), having two layers of the DEPFET (Depleted Field Effect Transistor) based pixel sensor and the second one is the silicon vertex detector (SVD) having four layers of double sided silicon strip sensors (DSSDs). SVD is the outer part of the vertex detector, which is placed cylindrically around the beam pipe. SVD has four layers and is represented by L3 (innermost), L4, L5, and L6 (moving from inside to outside of the detector). The L3, L4, L5, and L6 have radius of 39 mm, 80 mm, 104 mm, and 135 mm, respectively. Layer 3 (L3) is assembled by the University of Melbourne, Australia. L3 consist 7 ladders and each ladder has 2 sensors (one is forward and the other is backward). Layer 4 (L4) is assembled by the Tata Institute of Fundamental Research, India. L4 has 10 ladders and each ladder has 3 sensors (one forward, one origami, and one backward). Layer 5 (L5) is assembled by the Institute of High Energy Physics, Vienna. L5 has 12 ladders and each ladder having 4 sensors (one forward, two origami, and one backward). Layer 6 (L6) is assembled by the Kavli Institute for The Physics

and Mathematics of The Universe, Japan. L6 has 16 ladders and each ladder has 5 (one forward, three origami, and one is backward) sensors. The backward and forward sensors for L4, L5, and L6 are assembled by Istituto Nazionale di Fisica Nucleare, Pisa. Fig. 5.1 shows the structure of each ladder with different layers [79]. Fig. 5.2 shows the different geometry of each sensor with their pitches on the p-side (below) and n-side (top), respectively.

We have three types of DSSD sensors. The trapezoidal are used for the forward's

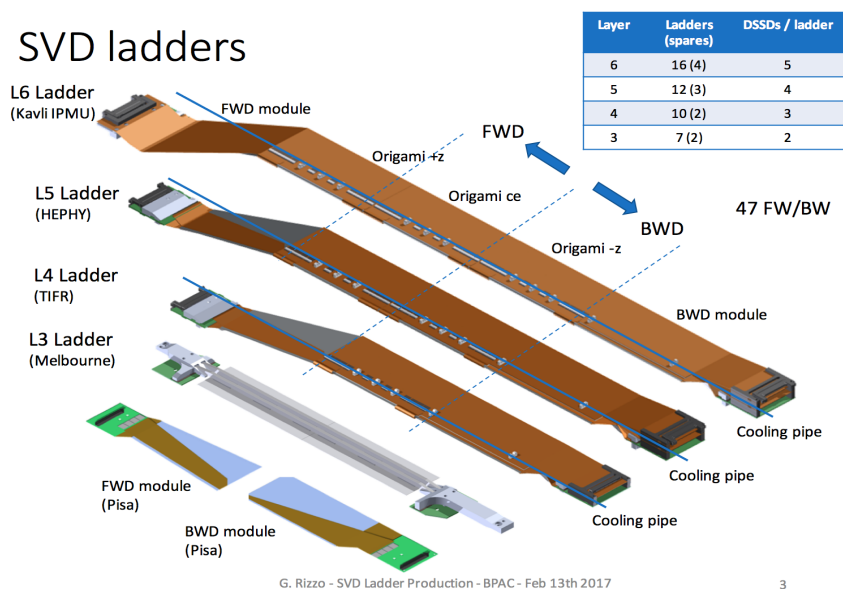


Figure 5.1: SVD ladders.

sensor of L4, L5, and L6 and the small sensors are used for L3. The rest of the modules is built with large sensors. The main characteristics of the three types of sensors are given in Table 5.1. The upgrade version SVD in Belle II improves reconstruction quality of the charge tracks and improves the vertex position of decay particles. With the combination of PXD, it also reconstructs low- p_T tracks,

	Small	Large	Trapezoidal
Readout strips (p/R- ϕ /U)	768	768	768
Readout strips (n/Z/V)	768	512	512
Readout pitch (p/R- ϕ /U)	50 μm	75 μm	75-50 μm
Readout pitch (n/Z/V)	160 μm	240 μm	240 μm
Chip size (mm ²)	5048.90	7442.85	6382.6
Active area (mm ²)	4737.80	7029.88	5890.0
Wafer Thickness	320 μm	320 μm	280 μm (to be checked)

Table 5.1: Basic parameters of different sensors.

which is important for the efficient reconstruction of the D^* daughters from B meson. It is also able to reconstruct K_S^0 mesons that decay outside the PXD

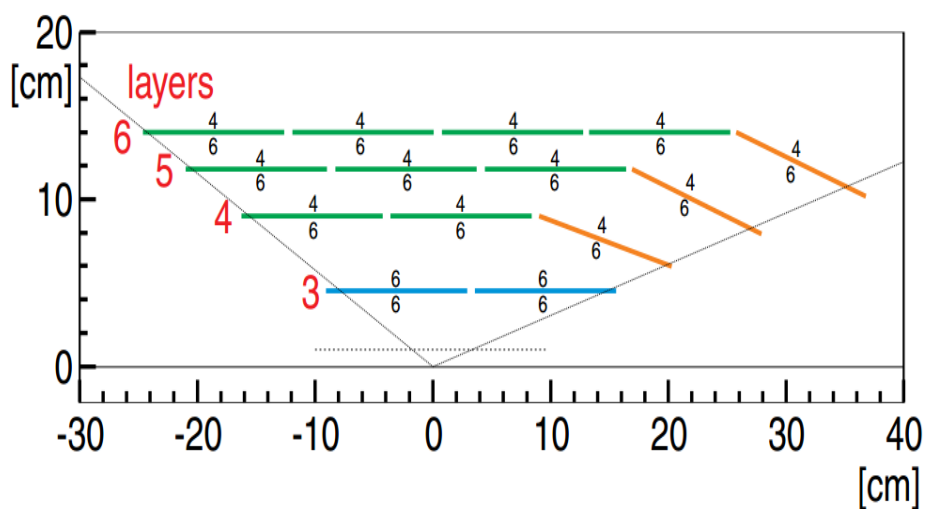


Figure 5.2: Geometry of DSSD sensor.

detector and it is also mechanically stable, has low mass, and operates reliably.

5.2 Performance Studies of the SVD

The performance of SVD is studied using the test beam data, taken at DESY, Hamburg on February 2017. The corresponding set-up relies on 4 GeV electron beam being incident on a detector system comprising of 2 PXD layers and 4 SVD layers in the presence of 1 T magnetic field. In the SVD sensors, with an intermediate floating strips between two readout strips, the charge seen on the floating electrode is coupled to the readout strip through capacitive charge division, via a network shown schematically in Fig. 5.4 (left). The charge loss due

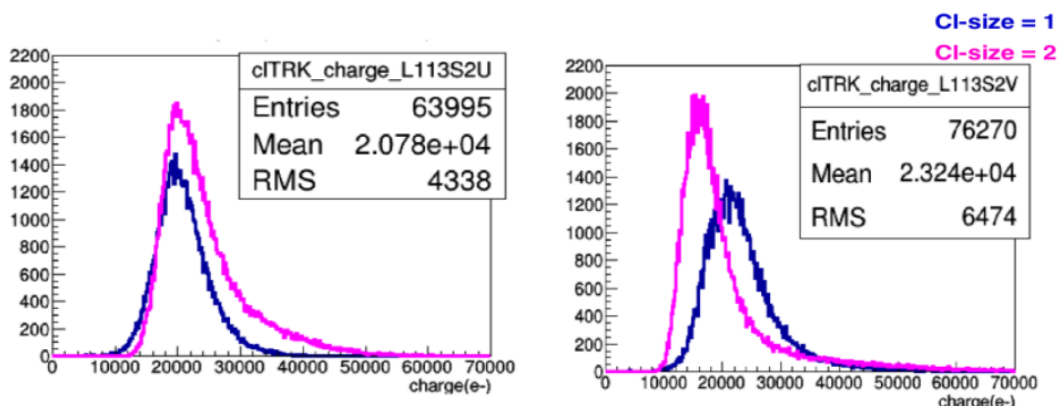


Figure 5.3: Cluster charge for layer 3 (sensor 2): U side (left) and V side (right) with test beam data.

to the presence of additional capacitive coupling between the floating strip and the backside of the sensor is significant in the sensors with large pitch, as the backside capacitance increases linearly with the implant pitch and becomes comparable to the interstrip capacitance (C_{int}). This effect is modeled in simulations and the resulting sensitivity of the cluster charge to C_{int} can be exploited in following two ways: (a) measure the actual C_{int} of SVD sensors; (b) tune this important

5.2 Performance Studies of the SVD

parameter for the full SVD simulation. Therefore, this measurement is carried out by comparing the test beam data and full SVD simulation. Fig. 5.3 shows the cluster charge for layer 3 (sensor 2) for both U (left) and V side (right). It can be seen that the V side, with large pitch, has lower cluster charge for cluster size 2, due to the above mentioned charge loss effect. For the U side, with small pitch, this effect is not present and charge for cluster size 2 is comparable or even a bit higher. Since complete charge reconstruction is instead possible for cluster size 1, if the second strip of cluster is below threshold. Further, the effect of C_{int} on the

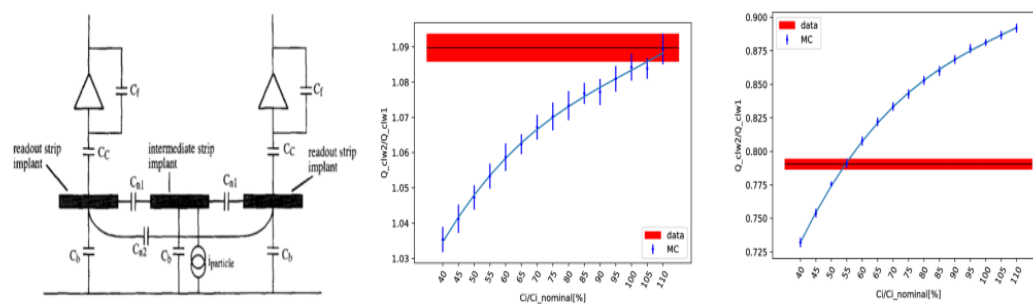


Figure 5.4: Schematic layout of a detector making use of capacitive charge division (left) [80]; Measurement of C_{int} for layer 3 (sensor 2): U side (center) and V side (right).

cluster charge is studied with the simulated data as a function of C_{int} , used to model charge division among the floating and readout strip, and compared with the result of test beam analysis to measure C_{int} for each sensor/side of the SVD. Fig. 5.4 shows results from the measurement of C_{int} , where cluster charge ratio $R = \frac{Q_{clw2}}{Q_{clw1}}$ is plotted as a function of C_{int} for layer 3, U (center) and V side (right). Here Q_{clw1} and Q_{clw2} are the cluster charge measured for strip with cluster size 1 and 2, respectively. In addition, the performance of the SVD is also studied using

5.2 Performance Studies of the SVD

the first collision data with Phase-II operation of Belle II. The set-up for data collection under Phase-II operation consists of a subset of the VXD comprising six layers with a single ladder per layer, installed in spring 2018. The cluster signal-to-noise ratio (S/N) with tracks of different momentum and inclination is calculated for both U and V side as shown in Fig. 5.5 (left). The S/N ratio is measured to be greater than 20 for N-side, which performs better than the P-side especially for 1-strip cluster. This is expected due to the longer P side

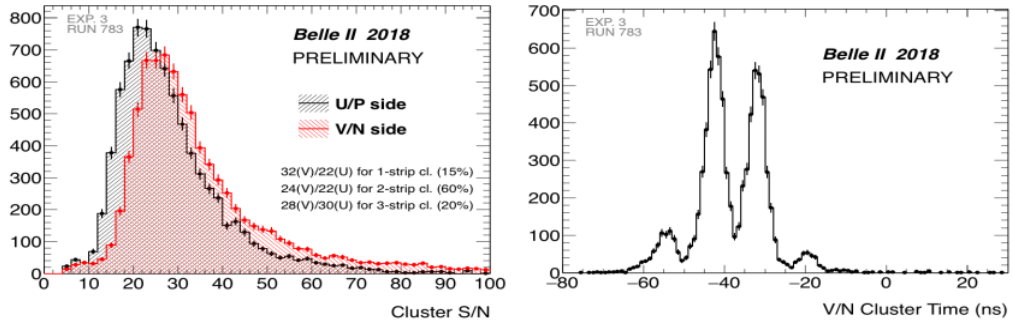


Figure 5.5: S/N ratio (left), Signal Hit time (right) with first data (Phase-II).

strips resulting in a larger capacitive load to the charge preamplifier used for the readout and hence higher noise on P-side. Further, signal hit time is also measured with first data as shown in Fig. 5.5 (right), where the RMS of signal hit time corresponding to a bunch crossing is found to be in the order of 3 ns, which is nicely matching with the design expectation. This study will be useful to remove the off-time hits as well as to improve the tracking performance of the SVD.

5.3 Visual Inspection of L4

Before mounting the SVD ladder to the final structure, we checked the wire bond of each strip, the mechanical and electrical strength of each ladder. In visual inspection, if we observed something strange then updated it to the expert. I personally participated in the visual inspection and mounted the L4 ladders during the visit at KEK, Japan, from 11 September - 11 November 2017. In the next section, we will discuss the visual inspection of L4 and the detail study finds in the Belle II Technical Design Report [59].

L4 ladder brought in its transport container and put into the small clean room. For visualization, microscope is used as shown in Fig. 5.6 (a) and the ladder container box in Fig 5.6 (b). We take out each ladder after wearing ESD safe

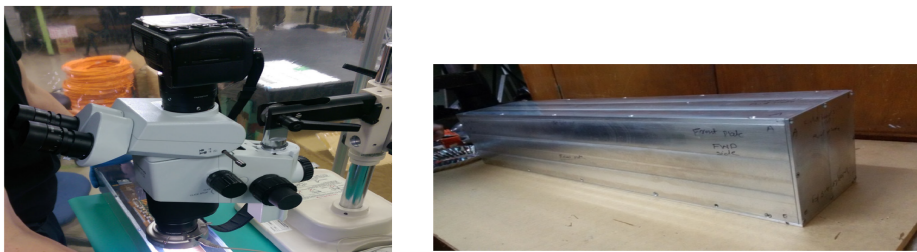


Figure 5.6: (a) Microscope attached with camera (left) (b) Ladder container box (right).

gloves with the screwdriver. Fig. 5.7 (a), (b), (c), (d) show the backward, forward, back, front side of container box, respectively. We loose the screws shown by the arrow from all sides of the container and always avoid touching any part of the container. Fig. 5.7 (e) and (f) also show the ladder after sliding the lid towards the back direction and after removal the sliding part of container box, respectively.

5.3 Visual Inspection of L4

Fig. 5.8 shows the visual inspection from the top side of each ladder. After visual

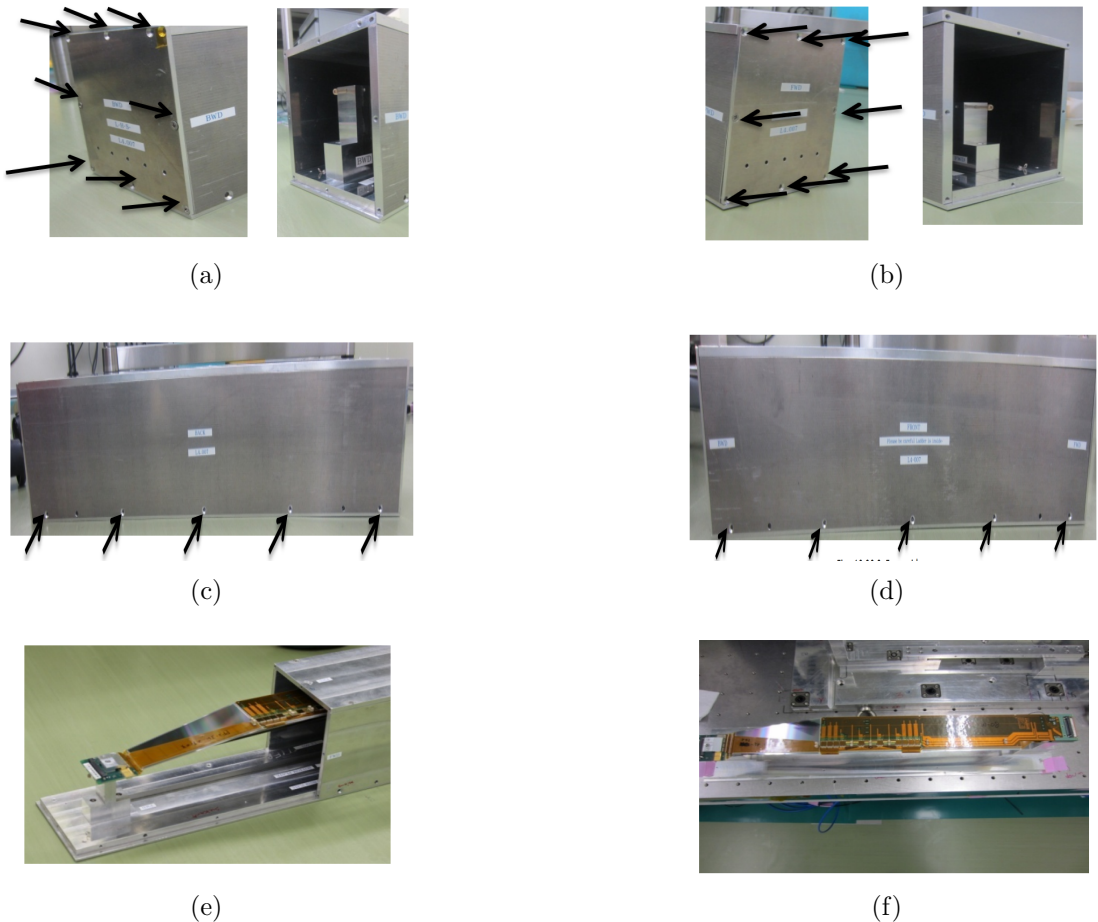


Figure 5.7: (a) Backward side wall (b) Forward side wall (c) Back side (d) Front side (e) sliding the lid towards backward direction (f) removing the sliding part of the container of container.

inspection, if everything is befitting we perform to an electrical test and finally put it back into its original position. Fig. 5.9 and 5.10 show the layer 4 ladder and SVD mounted to the final structure, respectively. Fig. 5.11 shows a few clicks after mounting the SVD L4.

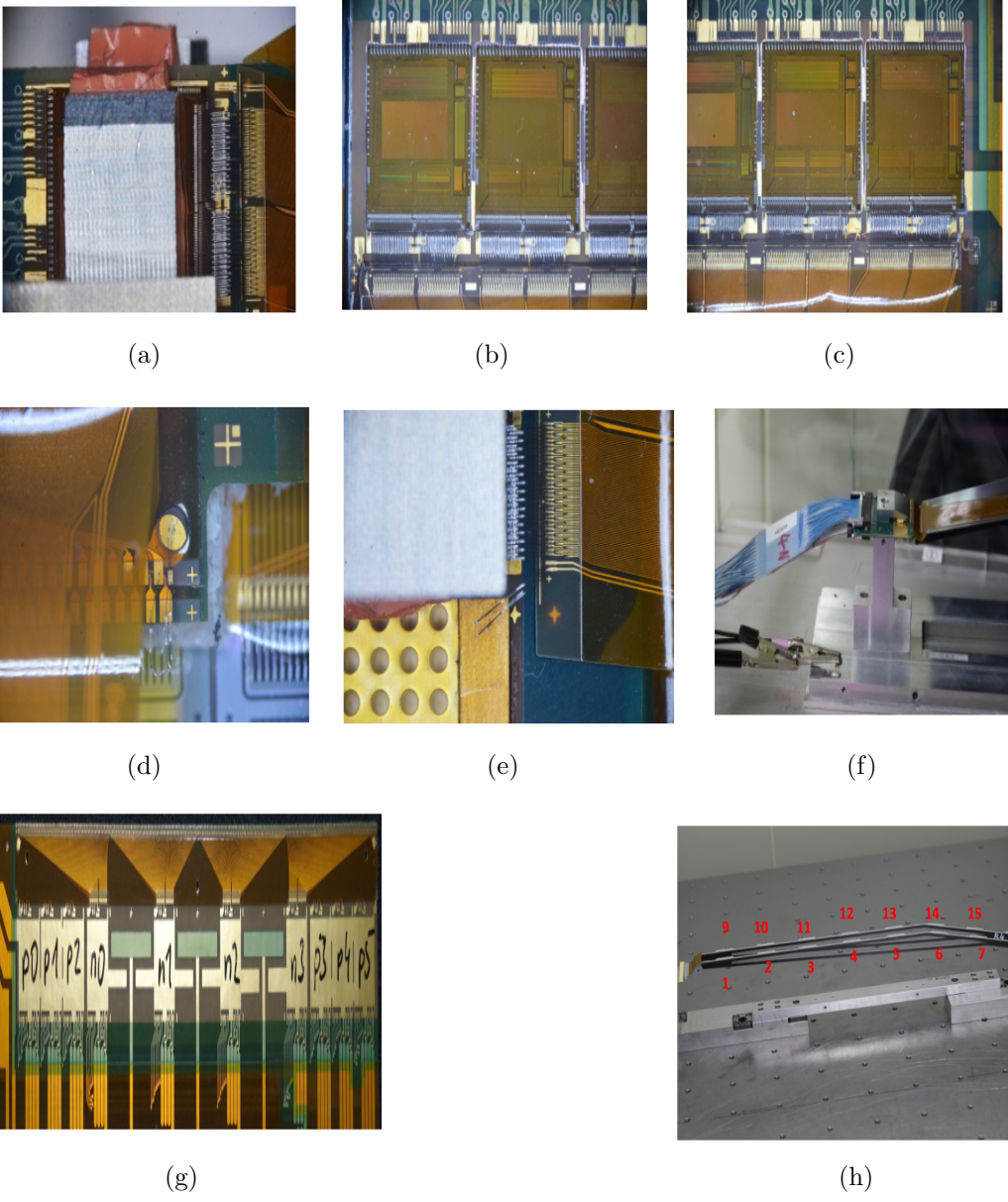


Figure 5.8: (a) APV on FWD hybrid (b) APV on O-Z (c) APV on O-Z (d) n side bias on O-Z (e) APV on FWD hybrid (f) JAE connection to the FWD hybrid (g) APV chip numbering on the origami (h) standoff numbering.

5.3 Visual Inspection of L4

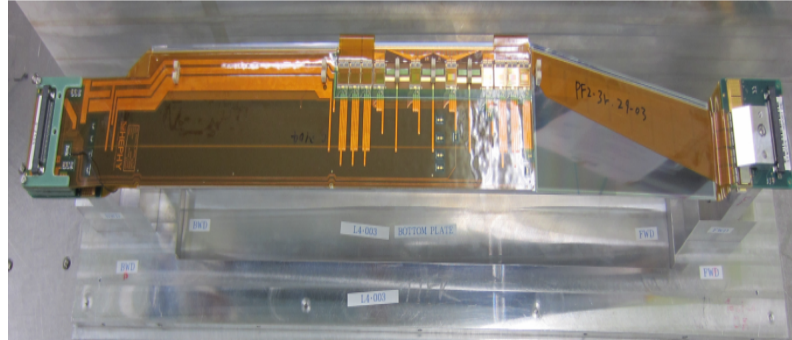


Figure 5.9: L4 ladder.

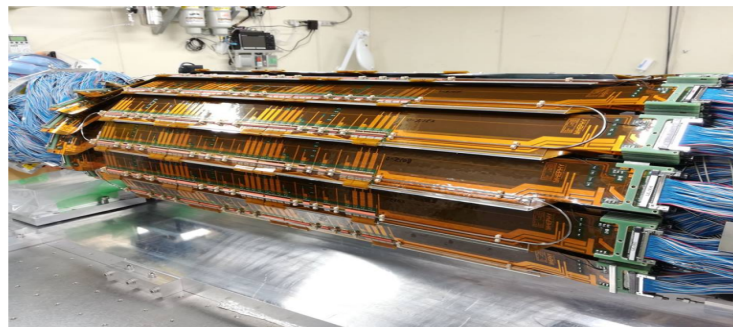


Figure 5.10: Full SVD mounted to the final structure.

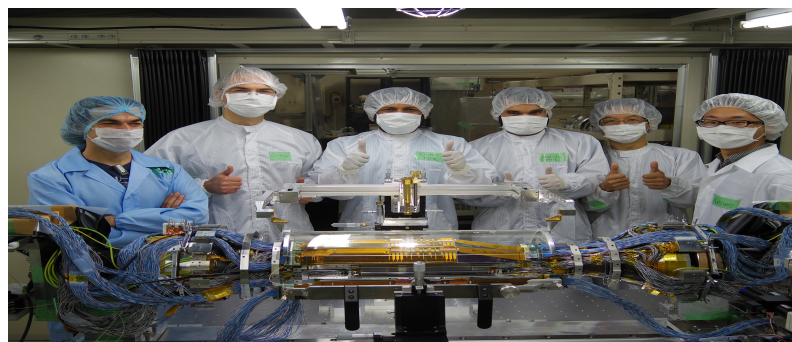


Figure 5.11: Group photo after successfully mounting the ladders.

5.4 Summary

We give the brief introduction of SVD subdetector which is used for precisely determination of vertex position of decay particles. We also put the light on the visual inspection of layer 4. Along with visual inspection, the performance of the Belle II SVD is validated using test beam data as well as first collision data (Phase II). The effect of on the cluster charge is studied in the test beam data and compared with simulations to measure C_{int} for each SVD sensor/side. The S/N ratio with the Phase-II data are in agreement with design expectations.

6

**Rediscovery of $D^{*\pm}$ and $D_s^{*\pm}$ and
measurement of the CKM angle ϕ_3 using
 $B \rightarrow DK$ at Belle II**

6.1 Introduction

This chapter describe the rediscovery of $D_s^{*\pm} \rightarrow D_s^\pm \gamma$ ($D_s^\pm \pi^0$) and $D^{*\pm} \rightarrow D^0 \pi^\pm$ decay modes using Phase III data. The D_s^+ is reconstructed from four decay modes: $K_S^0 K^+$, $K^+ K^- \pi^+$, $\phi \pi^+$, and $\bar{K}^{*0} K^+$, while the D^0 is reconstructed from three decay modes: $K^- \pi^+$, $K^+ K^-$, and $\pi^+ \pi^-$.

We are interested in these decay modes because of their large branching fraction and three charge track at final states. In most of the D_s^\pm decay mode study, we used these modes as control mode for validation the signal mode study. Table 6.1 summarizes the branching fraction of the reconstructed decay modes from PDG and generated sample. We also mention the latest PDG mass and lifetime/width value of non-final state particles in the Table 6.2. We get the clear signature of D_s^+ and D^0 mesons with 3.14 fb^{-1} data sample.

Along with the study of D mesons, we also present the preliminary results of the

Decay mode	Branching Fraction ($\times 10^{-2}$) [5]	
	PDG	generated
$D_s^{*+} \rightarrow D_s^+ \gamma$	93.5 ± 0.7	94.2
$D_s^{*+} \rightarrow D_s^+ \pi^0$	5.8 ± 0.7	5.8
$D_s^+ \rightarrow K^+ K^- \pi^+$	5.39 ± 0.15	0.38
$D_s^+ \rightarrow K_S^0 (\rightarrow \pi^+ \pi^-) K^+$	1.01 ± 0.04	1.03
$D_s^+ \rightarrow \phi (\rightarrow K^+ K^-) \pi^+$	2.24 ± 0.08	2.20
$D_s^+ \rightarrow \bar{K}^{*0} (\rightarrow K^- \pi^+) K^+$	2.58 ± 0.08	2.03
$D^{*+} \rightarrow D^0 \pi^+$	67.7 ± 0.5	67.7
$D^0 \rightarrow K^- \pi^+$	3.946 ± 0.030	3.89
$D^0 \rightarrow K^- K^+$	0.41 ± 0.006	0.39
$D^0 \rightarrow \pi^- \pi^+$	0.14 ± 0.0024	0.14

Table 6.1: Summary of the available measurement of the branching fraction.

physics analysis of $B \rightarrow DK$ for the ϕ_3 measurement at Belle II, are discussed

6.2 Data sample and Selection criteria

in Section 6.4. These results have been published in two conference proceedings [81, 82].

Particle	Mass (MeV/c ²)	Lifetime/Width
D_s^{*+}	2112.2 ± 0.4	$< 1.9 \text{ MeV @ } 90.0\% \text{ C.L.}$
D_s^+	1968.35 ± 0.07	$(5.04 \pm 0.04) \times 10^{-3} \text{ sec}$
ϕ	1019.461 ± 0.016	$4.249 \pm 0.013 \text{ MeV}$
\bar{K}^{*0}	$891.67 \pm 0.26 \text{ MeV}$	$51.4 \pm 0.8 \text{ MeV}$
D^{*+}	2010.26 ± 0.05	$83.4 \pm 1.8 \text{ keV}$
D^0	1864.84 ± 0.05	$(4.101 \pm 0.015) \times 10^{-13} \text{ sec}$

Table 6.2: Summary of the mass and Lifetime/width of non final states particles.

6.2 Data sample and Selection criteria

In order to study the $D_s^{*\pm}$ and $D^{*\pm}$ mesons reconstruction at Belle II, we utilized 3.14 fb⁻¹ of Phase III data.

The selection criteria used to reconstruct the particles of interest is mentioned in Table 6.3.

Variable	Selection criteria
PID	$> 0.6 (K, \pi)$
$M_{K_S^0}, M_\phi, M_{\bar{K}^{*0}}$	$[0.493-0.502], [1.0-1.04], [0.88-0.95] \text{ GeV}/c^2$
$D_s^{*+} \rightarrow D_s^+ \gamma (D_s^+ \pi^0)$ $M_{D_s^+}$ $\Delta M (M_{D_s^{*+}} - M_{D_s^+})$ $p_{D_s^{*+}}^*$	$[1.94-2.0] \text{ GeV}/c^2$ $0.01-0.6 \text{ GeV}/c^2 (0.1-1.0 \text{ GeV}/c^2)$ $> 2.0 \text{ GeV}/c$
$D^{*+} \rightarrow D^0 \pi^+$ d0, z0 M_{D^0} $\Delta M (M_{D^{*+}} - M_{D^0})$ $p_{D^{*+}}^*$	$ d0 < 0.5, z0 < 3 \text{ cm}$ $[1.7-2.1] \text{ GeV}/c^2$ $0.14-0.16 \text{ GeV}/c^2$ $> 2.5 \text{ GeV}/c$
$D_s^+ \rightarrow K_S^0 K^+, K^+ K^- \pi^+, \phi \pi^+, \bar{K}^{*0} K^+$ $M_{D_s^+}$ $p_{D_s^+}^*$	$[1.7-2.1] \text{ GeV}/c^2$ $> 2.0 \text{ GeV}/c$

Table 6.3: Summary of selection criteria.

6.3 Rediscovery of D^{*+} and D_s^{*+} with Phase III data sample

6.3.1 $D_s^{*+} \rightarrow D_s^+ \gamma$, $D_s^+ \rightarrow K^+ K^- \pi^+$, $K_S^0 K^+$, $\phi \pi^+$, $\bar{K}^{*0} K^+$

In this section, we reconstructed the D_s^{*+} from the combination of D_s^+ and gamma. The D_s^+ is reconstructed from $K_S^0 K^+$, $K^+ K^- \pi^+$, $\phi \pi^+$, $\bar{K}^{*0} K^+$ decay modes. Fig. 6.1, 6.2, 6.3, 6.4 show the distributions of ΔM with projection of $M_{D_s^+}$: 1.95–1.975 GeV/ c^2 and distribution of $M_{D_s^+}$ with projection of ΔM : 0.14–0.15 GeV/ c^2 for D_s^+ reconstructed from $K_S^0 K^+$, $K^+ K^- \pi^+$, $\phi \pi^+$, $\bar{K}^{*0} K^+$ decay modes, respectively.

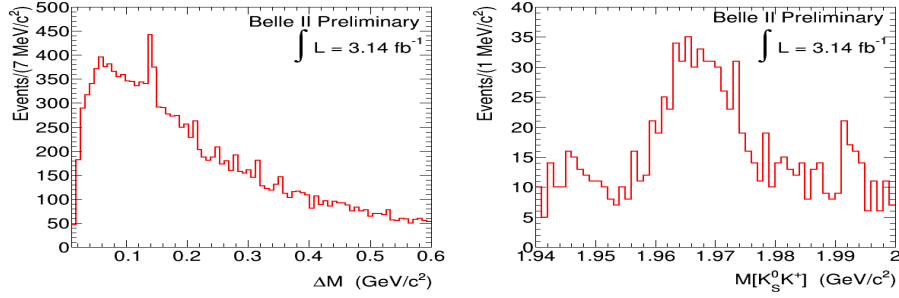


Figure 6.1: Distribution of (a) ΔM (left) and (b) $M(K_S^0 K^+)$ (right) for D_s^+ candidates reconstructed from $D_s^{*+} \rightarrow D_s^+ \gamma$ and $D_s^+ \rightarrow K_S^0 K^+$ decay mode.

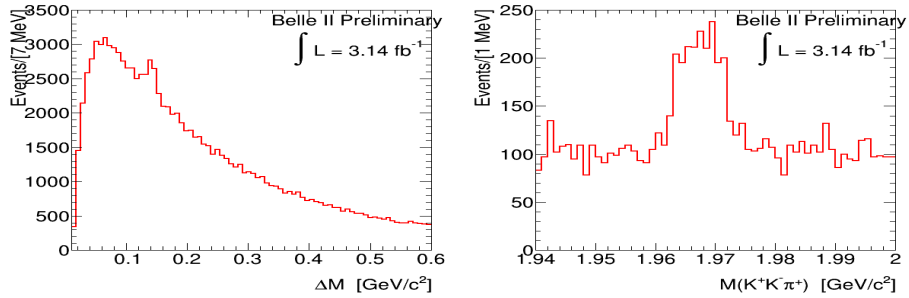


Figure 6.2: Distribution of (a) ΔM (left) and (b) $M(K^+ K^- \pi^+)$ (right) for D_s^+ candidates reconstructed from $D_s^{*+} \rightarrow D_s^+ \gamma$ and $D_s^+ \rightarrow K^+ K^- \pi^+$ decay mode.

6.3 Rediscovery of D^{*+} and D_s^{*+} with Phase III data sample

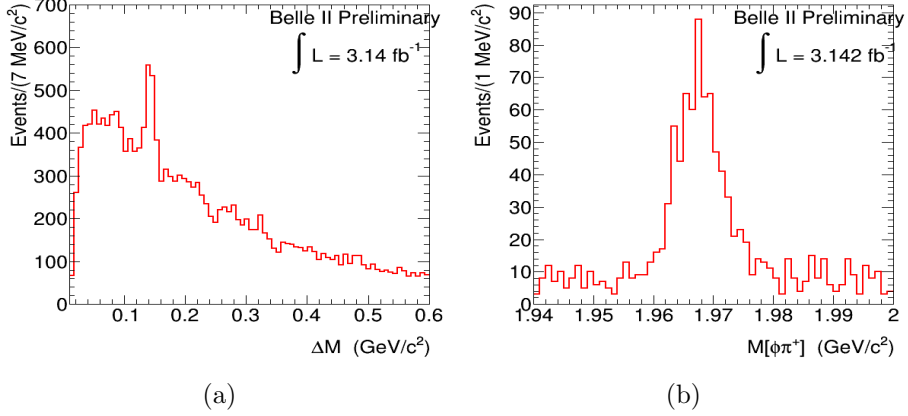


Figure 6.3: Distribution of (a) ΔM and (b) $M(\phi\pi^+)$ for D_s^+ candidates reconstructed from $D_s^{*+} \rightarrow D_s^+\gamma$ and $D_s^+ \rightarrow \phi\pi^+$ decay mode.

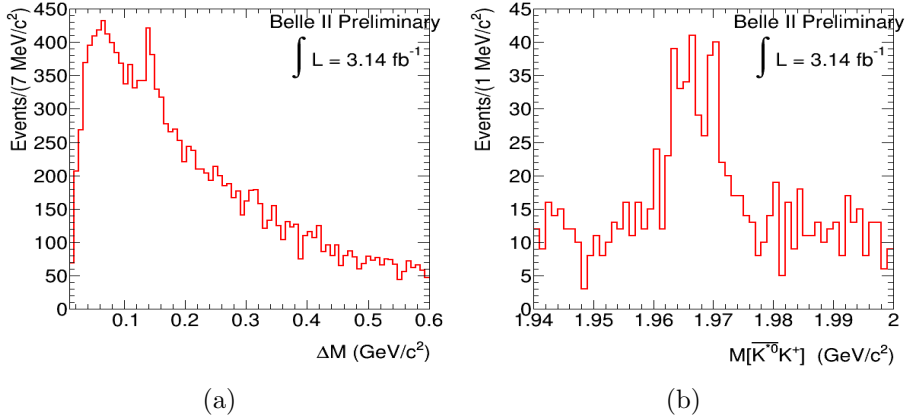


Figure 6.4: Distribution of (a) ΔM and (b) $M(\bar{K}^{*0}K^+)$ for D_s^+ candidates reconstructed from $D_s^{*+} \rightarrow D_s^+\gamma$ and $D_s^+ \rightarrow \bar{K}^{*0}K^+$ decay mode.

We see the clear hint of D_s^+ mesons from $M_{D_s^+}$ distribution and also find the signature of higher resonance in ΔM distribution from $D_s^{*\pm} \rightarrow D_s^\pm\gamma$ decay mode from all D_s^+ sub-decay modes: $K^+K^-\pi^+$, $K_S^0K^+$, $\phi\pi^+$, and $\bar{K}^{*0}K^+$ with 3.14 fb^{-1} data sample which is a good sign for D_s^+ decay mode study.

6.3 Rediscovery of D^{*+} and D_s^{*+} with Phase III data sample

6.3.2 $D_s^{*+} \rightarrow D_s^+ \pi^0$, $D_s^+ \rightarrow K^+ K^- \pi^+$, $K_S^0 K^+$, $\phi \pi^+$, $\bar{K}^{*0} K^+$

In this section, we reconstructed the D_s^{*+} from the combination of D_s^+ and π^0 . The D_s^+ is reconstructed from $K_S^0 K^+$, $K^+ K^- \pi^+$, $\phi \pi^+$, $\bar{K}^{*0} K^+$ decay modes. Fig. 6.5, 6.6, 6.7, 6.8 show the distribution of ΔM with projection of $M_{D_s^+}$: 1.95–1.975 GeV/c^2 and distribution of $M_{D_s^+}$ with projection of ΔM : 0.14–0.15 GeV/c^2 for D_s^+ reconstructed from $K_S^0 K^+$, $K^+ K^- \pi^+$, $\phi \pi^+$, $\bar{K}^{*0} K^+$ decay modes.

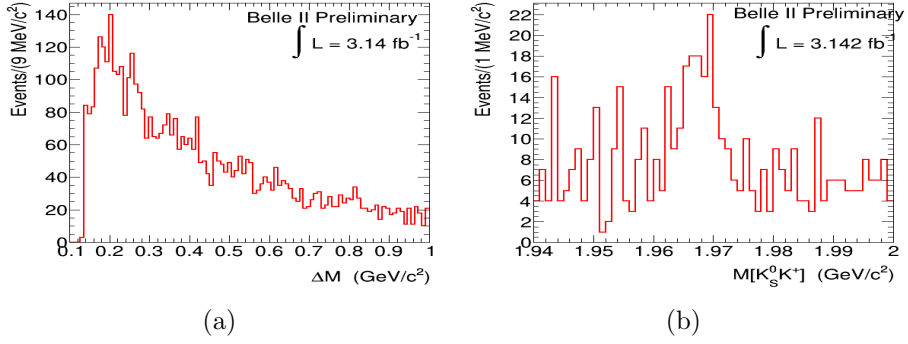


Figure 6.5: Distribution of (a) ΔM and (b) $M(K_S^0 K^+)$ for D_s^+ candidates reconstructed from $D_s^{*\pm} \rightarrow D_s^+ \pi^0$ and $D_s^+ \rightarrow K_S^0 K^+$ decay mode.

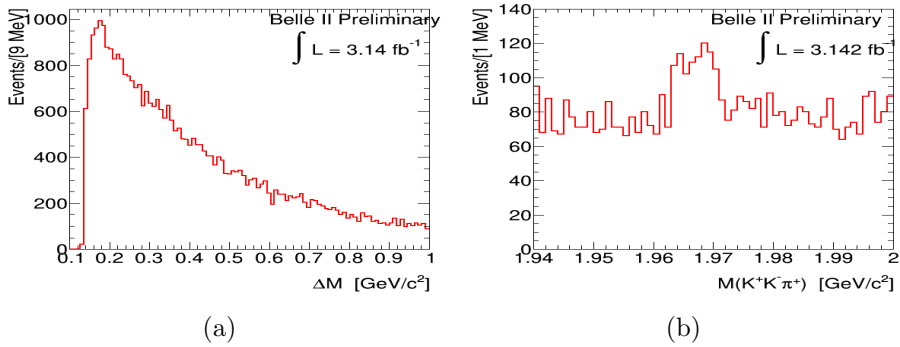


Figure 6.6: Distribution of (a) ΔM and (b) $M(K^+ K^- \pi^+)$ for D_s^+ candidates reconstructed from $D_s^{*+} \rightarrow D_s^+ \pi^0$ and $D_s^+ \rightarrow K^+ K^- \pi^+$ decay mode.

6.3 Rediscovery of D^{*+} and D_s^{*+} with Phase III data sample

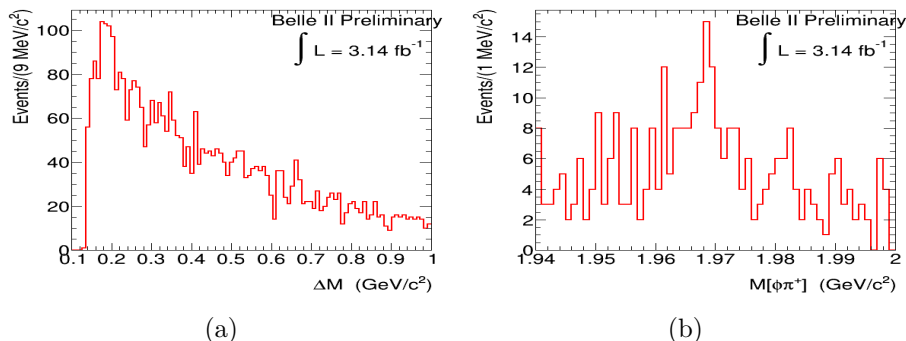


Figure 6.7: Distribution of (a) ΔM and (b) $M(\phi\pi^+)$ for D_s^+ candidates reconstructed from $D_s^{*+} \rightarrow D_s^+\pi^0$ and $D_s^+ \rightarrow \phi\pi^+$ decay mode.

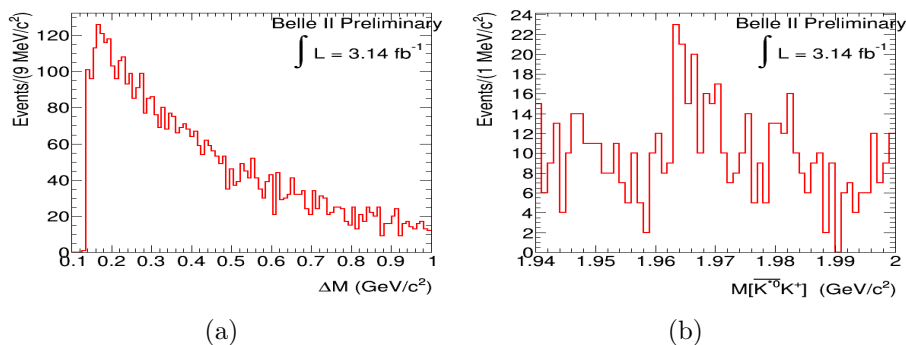


Figure 6.8: Distribution of (a) ΔM and (b) $M(\bar{K}^{*0}K^+)$ for D_s^+ candidates reconstructed from $D_s^{*+} \rightarrow D_s^+\pi^0$ and $D_s^+ \rightarrow \bar{K}^{*0}K^+$ decay mode.

We clearly see the signature of D_s^+ and also find the signature of higher resonance in ΔM distribution from $D_s^{*+} \rightarrow D_s^+\pi^0$ at an integrated luminosity of 3.14 fb^{-1} of collision data for all D_s^+ sub-decay modes: $K^+K^-\pi^+$, $K_S^0K^+$, $\phi\pi^+$ and $\bar{K}^{*0}K^+$.

6.3 Rediscovery of D^{*+} and D_s^{*+} with Phase III data sample

6.3.3 $D^{*+} \rightarrow D^0\pi^+$, $D^0 \rightarrow K^-\pi^+, K^+K^-, \pi^+\pi^-$

In this section, we reconstructed the D^{*+} from the combination of D^0 and π^+ . The D^0 is reconstructed from $K^-\pi^+$, K^+K^- , $\pi^+\pi^-$ decay modes. Fig. 6.9, 6.10, 6.11 show the distribution of ΔM with projection of M_{D^0} : 1.845–1.9 GeV/ c^2 and M_{D^0} with projection of ΔM : 0.144–0.148 GeV/ c^2 for the D^0 meson reconstructed from $K^-\pi^+$, K^+K^- , $\pi^+\pi^-$ decay modes, respectively.

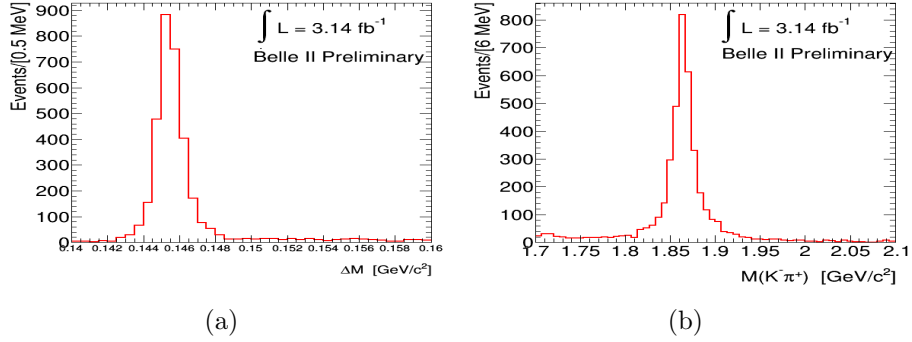


Figure 6.9: Distribution of (a) ΔM and (b) $M(K^-\pi^+)$ for D^0 candidates reconstructed from $D^{*+} \rightarrow D^0\pi^+$ and $D^0 \rightarrow K^-\pi^+$ decay mode.

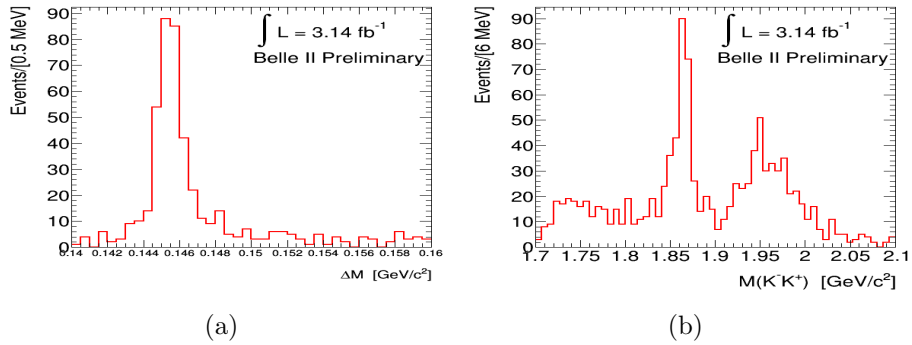


Figure 6.10: Distribution of (a) ΔM and (b) $M(K^+K^-)$ for D^0 candidates reconstructed from $D^{*+} \rightarrow D^0\pi^+$ and $D^0 \rightarrow K^+K^-$ decay mode. The peaking around 1.96 GeV/ c^2 in M_{D^0} coming from $D^0 \rightarrow K^-\pi^+$ decay mode.

6.3 Rediscovery of D^{*+} and D_s^{*+} with Phase III data sample

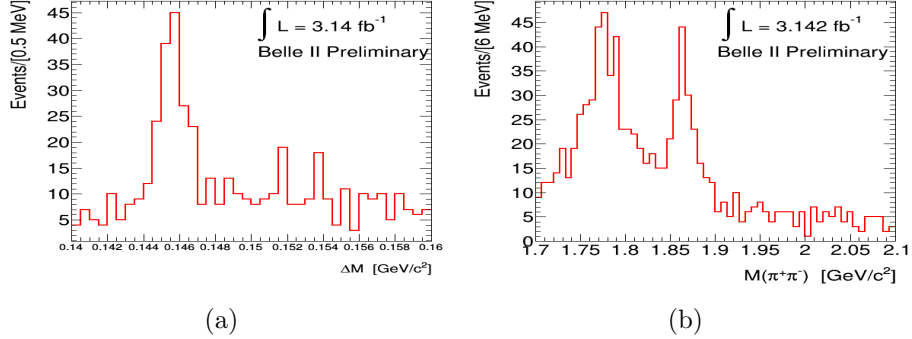


Figure 6.11: Distribution of (a) ΔM and (b) $M(\pi^+\pi^-)$ for D^0 candidates reconstructed from $D^{*+} \rightarrow D^0\pi^+$ and $D^0 \rightarrow \pi^+\pi^-$ decay mode. The peaking around $1.78 \text{ GeV}/c^2$ in M_{D^0} coming from $D^0 \rightarrow K^-\pi^+$ decay mode.

We clearly see the signature of D^0 from $D^{*\pm} \rightarrow D^0\pi^+$, $D^0 \rightarrow K^-\pi^+$, K^+K^- , $\pi^+\pi^-$ decay modes at an integrated luminosity of 3.14 fb^{-1} of collision data. It is good sign for D^0 decay mode study.

6.3.4 Reconstruct D_s^+ and D^+ from $K_S^0K^+$, $K^+K^-\pi^+$, $\phi\pi^+$, and $\bar{K}^{*0}K^+$ decay mode

In this section, we reconstruct D_s^+ mesons from $K_S^0K^+$, $K^+K^-\pi^+$, $\phi\pi^+$, and $\bar{K}^{*0}K^+$ decay mode. Fig. 6.12, 6.13, 6.14, 6.15 show the distribution of $M_{D_s^+}$ from $K_S^0K^+$, $K^+K^-\pi^+$, $\phi\pi^+$, and $\bar{K}^{*0}K^+$ decay mode, respectively. The signal events of D_s^+ is modeled with sum of two Gaussian functions and D^+ is also modeled with the sum of two Gaussian functions. The background events from combinatorial background fitted with 2^{nd} order polynomial. We clearly see the signature of D_s^+ and D^+ mesons from $K_S^0K^+$, $K^+K^-\pi^+$, $\phi\pi^+$, and $\bar{K}^{*0}K^+$ decay modes.

In the Table 6.4, we also compared the ΔM (difference between the mass of D_s^\pm

6.3 Rediscovery of D^{*+} and D_s^{*+} with Phase III data sample

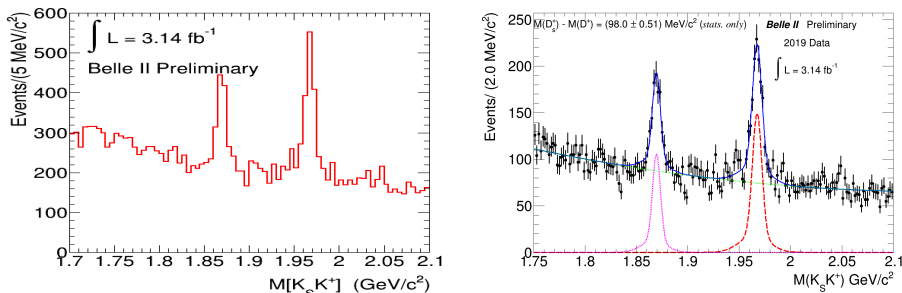


Figure 6.12: Distribution of $M(K_S^0 K^+)$ (a) without fit (b) fitted for D_s^+ candidates reconstructed from $D_s^+ \rightarrow K_S^0 K^+$ decay mode.

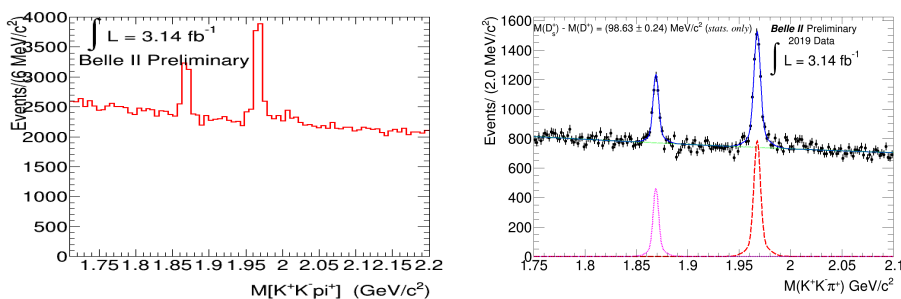


Figure 6.13: Distribution of $M(K^+ K^- \pi^+)$ (a) without fit (b) fitted for D_s^+ candidates reconstructed from $D_s^+ \rightarrow K^+ K^- \pi^+$ decay mode.

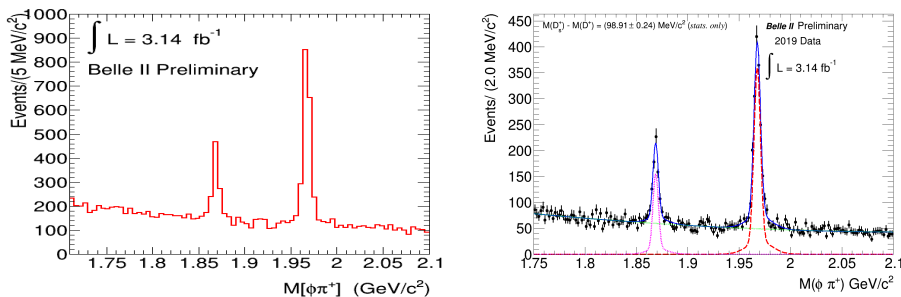


Figure 6.14: Distribution of $M(\phi \pi^+)$ (a) without fit (b) fitted for D_s^+ candidates reconstructed from $D_s^+ \rightarrow \phi \pi^+$ decay mode.

and D^\pm mesons) between the Phase III data and PDG value. The discrepancy between data and PDG value is coming within 1σ for all D_s^\pm sub decay modes.

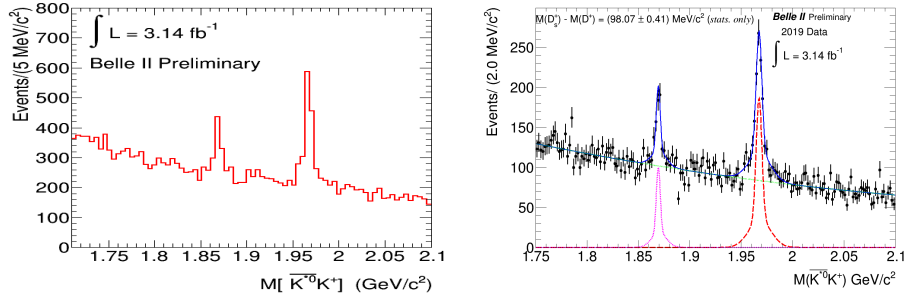


Figure 6.15: Distribution of $M(\bar{K}^{*0}K^+)$ (a) without fit (b) fitted for D_s^+ candidates reconstructed from $D_s^+ \rightarrow \bar{K}^{*0}K^+$ decay mode.

Decay mode	ΔM MeV/c ² (Data)	ΔM MeV/c ² (PDG) [5]
$D_s^+ \rightarrow K_S^0 K^+$	98.0 ± 0.51	98.69 ± 0.05
$D_s^+ \rightarrow K K \pi$	98.63 ± 0.24	98.69 ± 0.05
$D_s^+ \rightarrow \phi \pi^+$	98.91 ± 0.24	98.69 ± 0.05
$D_s^+ \rightarrow \bar{K}^{*0} K^+$	98.07 ± 0.40	98.69 ± 0.05

Table 6.4: Comparison of ΔM between data and PDG live.

6.4 Measurement of the CKM angle ϕ_3

The CKM angle ϕ_3 is one of the least well constrained parameters of the Unitarity Triangle [11, 23]. The precise measurement of ϕ_3 is highly desirable to scrutinise the consistency of the Standard Model and to detect presence of new physics. The measurement that currently dominates sensitivity to ϕ_3 uses $B^\pm \rightarrow D^0 K^\pm$ decays with the neutral D mesons decaying to different final states such as $K^+ K^-$, $K^+ \pi^-$, $K_S^0 \pi^+ \pi^-$ etc. As the sensitivity of ϕ_3 comes from the interference of $b \rightarrow c\bar{u}s$ and $b \rightarrow u\bar{c}s$, therefore, measurement of ϕ_3 is performed by exploiting the difference between $K_S^0 \pi^+ \pi^-$ Dalitz plots for D mesons from B^+ and B^- decay. The measurement of ϕ_3 from $B^\pm \rightarrow D^0 K^\pm$ and $B^\pm \rightarrow \bar{D}^0 K^\pm$ decays is theoretically clean as they occur at the tree level as shown in Figure 6.16.

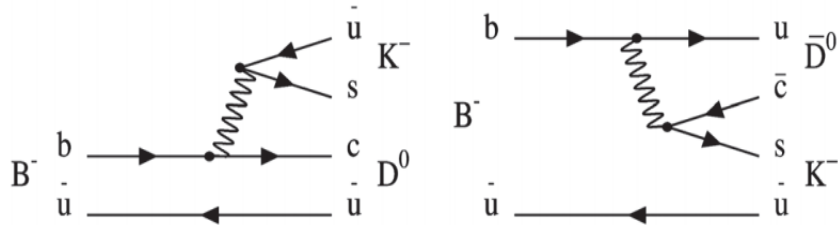


Figure 6.16: Feynman diagram for $B^- \rightarrow D^0 K^-$ (left) and $B^- \rightarrow \bar{D}^0 K^-$ (right) [83].

Various methods [84, 85] for extracting ϕ_3 have been proposed, from which the Dalitz plot analysis method [86] is one of the novel methods. There have been many efforts by BaBar, Belle and LHCb collaborations (Table 6.5) to measure this angle but due to the small data samples produced so far, ϕ_3 is poorly determined. Therefore, an independent measurement with high statistics is required

Sr. No.	Experiment	Measurement of ϕ_3
1	Belle	$(73^{+13}_{-15})^\circ$ [87]
2	BaBar	$(69^{+17}_{-16})^\circ$ [88]
3	LHCb	$(74^{+5.0}_{-5.8})^\circ$ [89]

Table 6.5: Previous measurement results of ϕ_3 .

to measure ϕ_3 . The Belle II [59] experiment at the SuperKEKB asymmetric e^+e^- collider [90], will accumulate the collision data at an unprecedented instantaneous luminosity of $6 \times 10^{35} \text{ cm}^{-2}\text{s}^{-1}$, which is 30 times larger than Belle experiment.

Figure 6.17 shows how the expected uncertainty on ϕ_3 scaled to the luminosity based on toy Monte Carlo studies. It shows that the expected uncertainty with integrated luminosity of 50 ab^{-1} is approximately 3° .

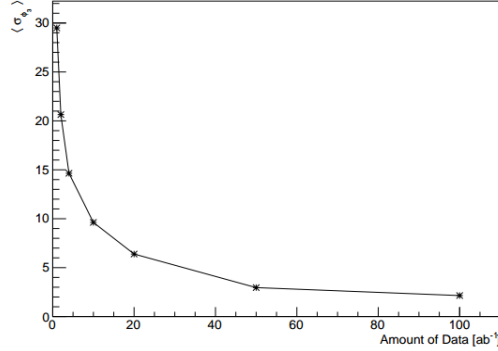


Figure 6.17: The distribution shows the expected uncertainty ($\langle \sigma_{\phi_3} \rangle$) versus luminosity on ϕ_3 [91]. The expected uncertainty on the measurement of ϕ_3 at integrated luminosity of 50 ab^{-1} is 3° . It may also improve by adding more modes, such as $B^\pm \rightarrow D^0(K_S^0 K^+ K^-)K^\pm$.

6.4.1 Physics Analysis for $B^\pm \rightarrow D^0 K^\pm$, $D^0 \rightarrow K_S^0 \pi^+ \pi^-$

The analysis begins with the reconstruction of K_S^0 from the two charged tracks of π^+ and π^- . The invariant mass of K_S^0 is shown in Figure 6.18 (left) with

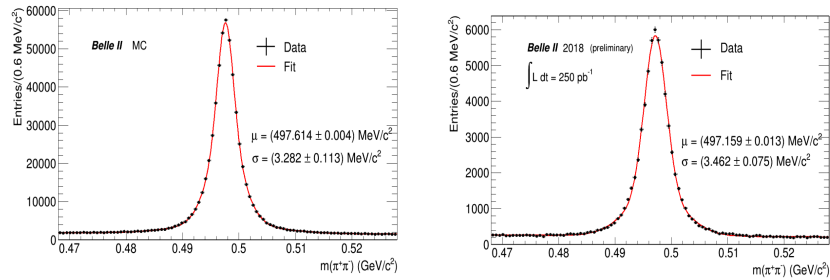


Figure 6.18: Invariant mass of K_S^0 with MC (left) and data (right).

MC samples collected at integrated luminosity 1 fb^{-1} and with Phase II data shown in Figure 6.18 (right). Here, black points are data and red line shows the fit. As it can be seen from the figure, the invariant mass resolution shows good agreement between data and MC. Further, the D^0 is reconstructed from one K_S^0 and two charged tracks of π^+ and π^- followed by the inclusive decay of

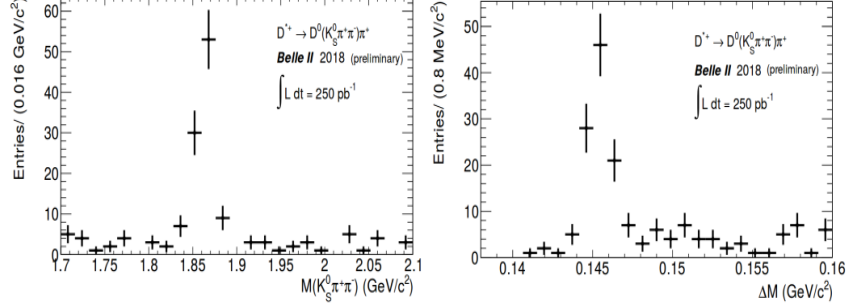


Figure 6.19: Invariant mass (left) and ΔM (right) for D^* tagged mode $D^0 \rightarrow K_S^0 \pi^+ \pi^-$ shown with Phase II data.

$D^{*\pm} \rightarrow D^0(K_S^0 \pi^+ \pi^-) \pi^\pm$. Invariant mass of D^0 is shown in Figure 6.19 (left) and ΔM is shown in Figure 6.19 (right). Here, ΔM is the mass difference between the $D^{*\pm}$ and D^0 candidates.

6.4.2 Physics Analysis for $B^\pm \rightarrow D_{CP} K^\pm$, $D_{CP} \rightarrow K^+ K^-$ and $\pi^+ \pi^-$ decay modes

In this section, we present a study of the decay $B^\pm \rightarrow D_{CP} K^\pm$, where D_{CP} represents a D meson decay to a CP even eigenstate i.e. $K^+ K^-$ and $\pi^+ \pi^-$. We reconstruct the decay of $D^{*\pm} \rightarrow D^0(K^- \pi^+) \pi^\pm$ using Phase II data, corresponding to an integrated luminosity of 472 pb^{-1} . To select $c\bar{c}$ events, the center-of-mass momentum of D^* is required to be greater than $2.5 \text{ GeV}/c$.

The distribution of ΔM is shown in Figure 6.20 (left), where ΔM is the difference between the invariant mass of $D^{*\pm}$ and D^0 meson. The invariant mass distribution of D^0 from $K^- \pi^+$ is shown in Figure 6.20 (right).

Further, the reconstruction of B mesons is carried out with a MC data sample of $2 \times 10^6 B^\pm \rightarrow D^0(K^+ K^-) K^\pm$ events. In order to select B mesons, two important

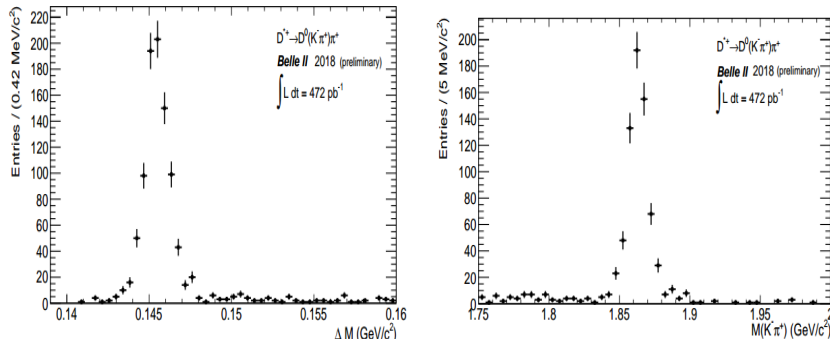


Figure 6.20: ΔM (left) and M_D (right) distribution in Phase II data for $D^0 \rightarrow K^- \pi^+$ final state.

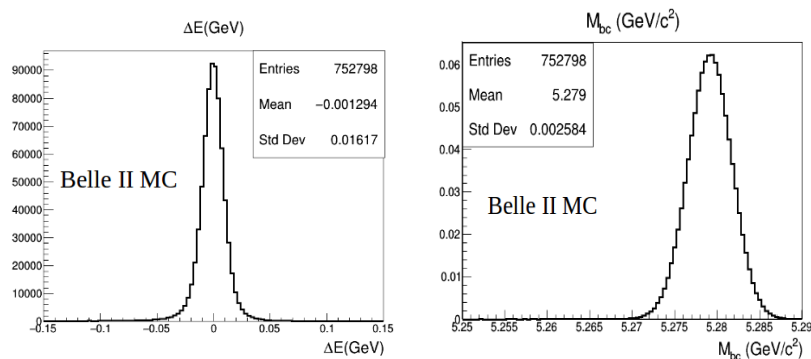


Figure 6.21: ΔE (left) and M_{bc} (right) distribution from MC simulation.

variables, the energy difference, $\Delta E = \sum E_i - E_{\text{beam}}$ and the beam-constrained mass, $M_{bc} = \sqrt{(E_{\text{beam}})^2 - \sum (\vec{p}_i)^2}$, are used. Where E_{beam} is the center-of-mass (CM) beam energy, E_i and p_i are the CM energies and momenta of B candidate's decay product. Figure 6.21 shows the M_{bc} and ΔE distributions reconstructed from the MC sample.

6.5 Summary

We clearly see the signature of D_s^+ and also find the signature of higher resonance in ΔM distribution from $D_s^{*+} \rightarrow D_s^+ \pi^0$ and $D_s^{*+} \rightarrow D_s^+ \gamma$ at an in-

egrated luminosity of 3.14 fb^{-1} of collision data for all D_s^+ sub-decay modes: $K^+K^-\pi^+$, $K_S^0K^+$, $\phi\pi^+$, and $\bar{K}^{*0}K^+$. We also see the signature of D^0 mesons from $D^{*+} \rightarrow D^0\pi^+$ with 3.14 fb^{-1} data sample. The difference between the mass of D_s^+ and D^+ mesons is found to be consistent within the world average.

The results of the first Belle and Belle II combined model-independent measurement of the CKM angle ϕ_3 is determined to be $\phi_3 = (78.4 \pm 11.4 \pm 0.5 \pm 1.0)^\circ$ [92], where the first uncertainty is statistical, the second is the total experimental systematic uncertainty and the third is the systematic uncertainty due to the external c_i and s_i measurements.

7

Summary & Conclusions



This Chapter summarizes the study for $B^+ \rightarrow D_s^+ \eta$, $B^+ \rightarrow D_s^+ K_S^0$, $B^+ \rightarrow D_s^{(*)+} \eta$, $B^+ \rightarrow D_s^{(*)+} K_S^0$, $B^+ \rightarrow D^+ \eta$, and $B^+ \rightarrow D^+ K_S^0$ rare decay modes. We have also reported the improved measurement results of the color-suppressed decay modes: $\bar{B}^0 \rightarrow D^0 \eta$ and $\bar{B}^0 \rightarrow D^0 K^0$. These studies have been performed using the Belle data corresponds to $772 \times 10^6 B\bar{B}$ events. In parallel to analysis, the detector performance studies of the SVD detector has also been performed using data collected with Belle II detector at SuperKEKB factory.

7.1 Search for rare B to charm decays at Belle

The procedure carried out for the study of rare decay modes can be summarized as follows:

- Estimation of the reconstructed efficiency and the background using MC study.
- Most of the background is estimated to come from the continuum events. The FastBDT is used to suppress the continuum suppression.
- No peaking background structure is observed in the signal region. In $B^+ \rightarrow D^+ \eta$ ($B^+ \rightarrow D^+ K_S^0$) decay mode, the peaking background at $\Delta E \sim -0.16$ GeV contributes due to mis-reconstruction from $\bar{B}^0 \rightarrow D^+ \rho^-$ ($\bar{B}^0 \rightarrow D^+ K^{*-}$) decay modes.
- To validate the signal decay modes, we have used $\bar{B}^0 \rightarrow D^0 \eta$ as a control mode for $B^+ \rightarrow D_s^+ \eta$, $D_s^{(*)+} \eta$, $D^+ \eta$ decay modes, and $\bar{B}^0 \rightarrow D^0 K^0$ as a

7.1 Search for rare B to charm decays at Belle

Decay Mode	Yield	Significance (\mathcal{S})	$\mathcal{B}, \times 10^{-5}$
$B^+ \rightarrow D_s^+ \eta$	18.4 ± 7.7	1.2	< 1.4
$B^+ \rightarrow D_s^{*+} \eta$	-1.45 ± 2.3	–	< 1.7
$B^+ \rightarrow D^+ \eta$	34 ± 16	1.4	< 1.2
$B^+ \rightarrow D_s^+ K^0$	-2.71 ± 2.8	–	< 0.3
$B^+ \rightarrow D_s^{*+} K^0$	-2.64 ± 1.6	–	< 0.6
$B^+ \rightarrow D^+ K^0$	-2.99 ± 5.7	–	< 0.2
$\bar{B}^0 \rightarrow D^0 \eta$	1373 ± 63	24.7	$26.6 \pm 1.2 \pm 2.1$
$\bar{B}^0 \rightarrow D^0 K^0$	323 ± 27	14.9	$5.6 \pm 0.5 \pm 0.2$

Table 7.1: Summary of the fitted results.

control mode to study $B^+ \rightarrow D_s^+ K^0$, $D_s^{(*)+} K^0$, $D^+ K^0$ decay modes. The dominant cross-feed contributions comes from the $\bar{B}^0 \rightarrow D^{*0} h$ decay mode. The peaking background at $\Delta E \sim -0.16$ GeV for the $\bar{B}^0 \rightarrow D^0 \eta$ and $\bar{B}^0 \rightarrow D^0 K_S^0$ decay modes are coming from the charged B mesons decays into three final states particle and $B^+ \rightarrow D^0 K^{*+}$ decay modes, respectively.

- The signal extraction procedure is validated on the Monte Carlo and results are found to be reliable.
- After validating selection criteria, reconstruction procedure and signal extraction procedure, the signal events in the data sample has been extracted.

The Table 7.1 summarizes the yield from the fit, signal significance, and branching fraction obtained from the combined D_s^+ , D^+ , and D^0 sub-decay modes from the fitted distributions of ΔE variable.

7.1.1 Conclusions

In the absence of any significant signal in signal decay modes, we provide an upper limit at 90% C.L.. We perform the first search for the $B^+ \rightarrow D^+\eta$ decay mode. The measured U.L. (at 90% C.L.) is a twenty times more stringent than the previously measured limits [28]. We also report the most precise measurement results for the branching fraction of $\bar{B}^0 \rightarrow D^0K^0$ decay, which supersede the previous Belle result [33]. The branching fraction measurement of $\bar{B}^0 \rightarrow D^0\eta$ decay modes is found to consistent with the world average [5] and also supersedes the previous Belle result [31].

7.2 Rediscovery of $D^{*\pm}$ and $D_s^{*\pm}$ at Belle II

This chapter describes the reconstruction of $D_s^{*\pm}$ and $D^{*\pm}$ decay modes from the $D_s^\pm\gamma$ ($D_s^\pm\pi^0$) and $D^0\pi^\pm$ decay modes, respectively with Phase III data sample (included vertex detector). The D_s^+ is reconstructed from four decay modes: $K_S^0K^+$, $K^+K^-\pi^+$, $\phi\pi^+$, and $\bar{K}^{*0}K^+$, while the D^0 is reconstructed from three decay modes: $K^-\pi^+$, K^+K^- , and $\pi^+\pi^-$. This was the first study of D_s^+ at the Belle II.

In the Table 7.2, we have also compared the ΔM (difference between the mass of D_s^\pm and D^\pm mesons) between the data and PDG value.

7.2.1 Conclusions

We clearly see the signature of D_s^+ and D_s^{*+} collected with an integrated luminosity of 3.14 fb^{-1} data. We also see the signature of D^0 mesons from $D^{*+} \rightarrow D^0\pi^+$

7.3 Performance Studies of the SVD

Decay mode	$\Delta M \text{ MeV}/c^2(\text{Data})$	$\Delta M \text{ MeV}/c^2 (\text{PDG})$
$D_s^+ \rightarrow K_S^0 K^+$	98.0 ± 0.51	98.69 ± 0.05
$D_s^+ \rightarrow K K \pi$	98.63 ± 0.24	98.69 ± 0.05
$D_s^+ \rightarrow \phi \pi^+$	98.91 ± 0.24	98.69 ± 0.05
$D_s^+ \rightarrow \bar{K}^{*0} K^+$	98.07 ± 0.40	98.69 ± 0.05

Table 7.2: Comparison of ΔM between data and PDG live.

with 3.14 fb^{-1} data sample. The mass difference between the mass of D_s^+ and D^0 mesons in data comes out to be consistent with the PDG [5].

7.3 Performance Studies of the SVD

The detector performance studies of the SVD is carried out and compared it with the simulation.

In addition, I also participated in the visual inspection and mounted the L4 ladders during the visit at KEK, Japan.

7.3.1 Conclusions

The effect of on the cluster charge is studied in the test beam data and compared with simulations to measure C_{int} for each SVD sensor/side. The S/N ratio with the Phase-II data are in agreement with design expectations.

7.4 Measurement of the CKM angle ϕ_3 using $B \rightarrow DK$ at Belle II

We have discussed the preliminary results of the physics analysis of $B \rightarrow DK$ for the ϕ_3 measurement at Belle II. These results have been published in two conference proceedings [81, 82].

We reconstruct K_S^0 from the two charged tracks of π^+ and π^- with MC samples collected at integrated luminosity of 1 fb^{-1} and with Phase II (one ladder per layer of vertex detector) data. Further, the D^0 is reconstructed from one K_S^0 and two charged tracks of π^+ and π^- followed by the inclusive decay of $D^{*\pm} \rightarrow D^0(K_S^0\pi^+\pi^-)\pi^\pm$.

The study of $B^\pm \rightarrow D_{CP}K^\pm$, where D_{CP} represents a D meson decay to a CP even eigenstate i.e. K^+K^- and $\pi^+\pi^-$ is also carried out. In addition, reconstruction of $D^{*\pm} \rightarrow D^0(K^-\pi^+)\pi^\pm$ using Phase II data, corresponding to an integrated luminosity of 472 pb^{-1} .

7.4.1 Conclusions

With Phase II data sample, the invariant mass resolution of K_S^0 shows good agreement between data and MC. We have obtained the clear signature of D^0 from $K_S^0\pi^+\pi^-$, K^+K^- , and $\pi^+\pi^-$.

BIBLIOGRAPHY

- [1] Gianluca Bianco (ATLAS detector), Ph.D. thesis, 10.13140/RG.2.2.34038.42561 (2020).
- [2] O. W. Greenberg, Phys. Rev. Lett. **13**, 598 (1964).
- [3] T. D. Lee and C. N Yang, Phys. Rev. **104**, 254 (1956).
- [4] C. S. Wu, E. Ambler, R. W. Hayward, D. D. Hoppes, and R. P. Hudson, Phys. Rev. Lett. **105**, 1413 (1957).
- [5] P.A. Zyla *et al.* (Particle Data Group), Prog. Theor. Exp. Phys. **2020**, 083C01 (2020).
- [6] J. H. Christenson, J. W. Cronin, V. L. Fitch, and R. Turlay, Phys. Rev. Lett. **13**, 138 (1964).
- [7] G. L. Glashow, Nucl. Phys. **22**, 579 (1961).
- [8] A. Salam and J. C. Ward, Phys. Lett. **13**, 168 (1964).
- [9] S. Weinberg, Phys. Rev. Lett. **19**, 1264 (1967).
- [10] S. Glashow, J. Iliopoulos, and L. Maiani, Phys. Rev. D **2**, 1285 (1970).
- [11] M. Kobayashi and T. Maskawa, Prog. Theor. Phys. **49**, 652 (1973).

- [12] J. Augustin *et al.* (SLAC-SP-017 Collaboration), Phys. Rev. Lett. **33**, 1406 (1974).
- [13] J. Aubert *et al.* (E598 Collaboration), Phys. Rev. Lett. **33**, 1404 (1974).
- [14] S. Herb *et al.*, Phys. Rev. Lett. **39**, 252 (1977).
- [15] F. Abe *et al.* (CDF Collaboration), Phys. Rev. Lett. **74**, 2626 (1995) [[arXiv:hep-ex/9503002](#)].
- [16] S. Abachi *et al.*, Phys. Rev. Lett. **74**, 2422 (1995) [[arXiv:hepex/9411001](#)].
- [17] V. Fanti *et al.* (NA48 Collaboration), Phys. Lett. B **465**, 335 (1999) [[arXiv:hep-ex/9909022](#)].
- [18] A. Alavi-Harati *et al.* (KTeV Collaboration), Phys. Rev. Lett. **83**, 22 (1999) [[arXiv:hep-ex/9905060](#)].
- [19] B. Aubert *et al.* (BABAR Collaboration), Phys. Rev. Lett. **87**, 091801 (2001) [[arXiv:hep-ex/0107013](#)].
- [20] K. Abe *et al.* (Belle Collaboration), Phys. Rev. Lett. **87**, 091802 (2001) [[arXiv:hepex/0107061](#)].
- [21] B. Aubert *et al.* (BABAR Collaboration), Phys. Rev. Lett. **93**, 131801 (2004) [[arXiv:hepex/0407057](#)].
- [22] B. Aubert *et al.* (BABAR Collaboration), Phys. Rev. Lett. **99**, 021603 (2007) [[arXiv:hepex/0703016](#)].
- [23] N. Cabibbo, Phys. Rev. Lett. **10**, 531 (1963).
- [24] K. Abe *et al.*, (Belle Collaboration), Phys. Rev. Lett. **87**, 091802 (2001).
- [25] B. Aubert *et al.*, (BABAR Collaboration), Phys. Rev. Lett. **87**, 091801 (2001).

- [26] A. J. Buras and L. Silvestrini, Nucl. Phys. B **569**, 3-52 (2000).
- [27] B. Blok, M. Gronau, and J. L. Rosner, Phys. Rev. Lett. **78**, 3999 (1997).
- [28] Alexander *et al.*, Phys. Rev. B **319**, 365 (1993B).
- [29] Aubert *et al.*, Phys. Rev. D **72**, 011102 (2005E).
- [30] J. P. Lees *et al.*, Phys. Rev. D **87**, 039901 (2013).
- [31] S. Blyth *et al.*, Phys. Rev. D **74**, 092002.
- [32] B. Aubert *et al.*, Phys. Rev. D **74**, 031101.
- [33] P. Krokovny *et al.*, Phys. Rev. Lett. **90**, 141802.
- [34] S. Kurokawa and E. Kikutani, Nucl. Instrum. Methods Phys. Res. A **499**, 1 (2003), and other papers included in this volume; T. Abe *et al.*, Prog. Theor. Exp. Phys. 03A001 (2013) and following articles up to 03A011.
- [35] <http://www-acc.kek.jp/KEKB/>.
- [36] <https://upload.wikimedia.org/wikipedia/commons/c/c2/KEKB.png>.
- [37] S. Iwata, TRISTAN experiment (KEK-PROC-93-19).
- [38] H. Kichimi *et al.*, JINST **5**, 03011 (2010).
- [39] <http://cerncourier.com/cws/article/cern/39147>.
- [40] KEKB B-Factory Design Report, KEK Report 95-7, 1995.
- [41] R. B. Palmer, SLAC-PUB 4707, 1988.
- [42] K. Oide, K. Yokoya, Phys. Rev. A **40**, 315 (1989).
- [43] <http://belle.kek.jp/>.
- [44] <https://www.classe.cornell.edu/public/lab-info/upsilon.html>.

- [45] A. Abashian *et al.*, (Belle Collaboration), Nucl. Instrum. Meth. A **479**, 117 (2002), [arXiv:1710.10086].
- [46] J. Brodzicka *et al.*, (Belle Collaboration), Prog. Theor. Exp. Phys. **2012**, 04D001 (2012), [arXiv:1212.5342].
- [47] <https://belle.kek.jp/belle/transparency/slides/BELLE/icondetector.gif>.
- [48] G. Alimonti *et al.* (Belle Collaboration), Nucl. Instrum. Meth. Phys. Res. A **453**, 71 (2000).
- [49] E. Nygard *et al.*, Nucl. Instrum. Meth. A **301**, 506 (1991).
- [50] O. Toker *et al.*, Nucl. Instrum. Meth. A **340**, 572 (1994).
- [51] Y. Horii, PhD thesis, Tohoku University (2010).
- [52] H. Hirano *et al.*, Nucl. Instrum. Meth. A **455**, 294 (2000).
- [53] H. Bethe, Ann. Phys. (Leipzig) **5**, 325 (1930).
- [54] H. Bethe, Z. Phys. **76**, 293 (1932).
- [55] H. Bethe and J. Ashkin, Experimental Nuclear Physics, edited by E. Segre (Wiley, New York, 1953).
- [56] H. Kichimi *et al.*, Nucl. Instrum. Meth. A **453**, 315 (2000).
- [57] <http://sabotin.ung.si/sstanic/belle/nim/total/node65.html>.
- [58] <http://belle.kek.jp/group/trg/>.
- [59] T. Abe *et al.*, Belle II Technical Design Report (2010), [arXiv:1011.0352].
- [60] Y. Ohnishi *et al.*, Prog. Theor. Exp. Phys. **03A011** (2013) 2050.
- [61] <https://docs.belle2.org/>.
- [62] <https://www.belle2.org/e21595/e21770/infoboxContent25431/belle2.pdf>.

- [63] A. Roodman, Blind Analysis in Particle Physics, PHYSTAT2003, SLAC, Stanford, California, September 8-11, 2003.
- [64] Belle Analysis Software Page, <http://belle.kek.jp/>.
- [65] T. Kuhr *et al.* (Belle II Framework Software Group), Comput. Softw. Big Sci. **3**, 1 (2019).
- [66] <https://confluence.desy.de/pages/viewpage.action?pageId=51970172&preview=/3403/B2BIIWorkflow.png>.
- [67] Moritz Gelb *et al.*, arXiv:1810.00019 [hep-ex].
- [68] C. W. Park *et al.*, New corrections of the energies and angles of photons, Internal Belle Note 469.
- [69] https://belle.kek.jp/secured/belle_note/gn1588/BN-Bs1tau-v3.pdf.
- [70] The Fox-Wolfram moments were introduced in G. C. Fox and S. Wolfram, Phys. Rev. Lett. **41**, 1581 (1978). The Fisher discriminant used by Belle, based on modified FoxWolfram moments (SFW), is described in K. Abe *et al.* (Belle Collaboration), Phys. Rev. Lett. **87**, 101801 (2001); Phys. Lett. B **511**, 151 (2001).
- [71] Belle II collaboration, First flavor tagging calibration using 2019 Belle II data, [arXiv:2008.02707](https://arxiv.org/abs/2008.02707) [INSPIRE].
- [72] Giovanni Punzi, Sensitivity of searches for new signals and its optimization, [arXiv:physics/0308063v2](https://arxiv.org/abs/physics/0308063v2).
- [73] S. Nishida, Study of kaon and pion identification using Inclusive D^* sample, Internal Belle Note 779.
- [74] B. Bhuyan, High pT tracking efficiency using partially reconstructed D^* decays, Internal Belle Note 1165.
- [75] N. Dash *et al.* (Belle Collaboration), Phys. Rev. Lett. **119**, 171801 (2017).

- [76] N. J. Joshi *et al.* (Belle Collaboration), Phys. Rev. D **81**, 031101 (2010).
- [77] M. C. Chang *et al.* (Belle Collaboration), Phys. Rev. Lett **98**, 131803 (2007).
- [78] G. J. Feldman and R. D. Cousins, Phys. Rev. D **57**, 3873 (1998).
- [79] G. Rizzo-SVD Ladder Production-BPAC-Feb 13th2017.
- [80] M. Krammer and H. Pernegger, Nucl. Instr. and Methods in Phys. Res, Sect. A **397**, 232-242 (1997).
- [81] Manish Kumar *et al.*, Measurement of the CKM angle ϕ_3 using $B \rightarrow DK$ with Belle II, Springer Proceedings in Physics **261**, 857 (2021).
- [82] Manish Kumar *et al.*, Measurement of the CKM angle ϕ_3 using $B \rightarrow DK$ at Belle II, Springer Proceedings in Physics **234**, 287 (2019).
- [83] J. Brodzicka *et al.*, Physics achievements from the Belle experiment, PTEP 2012, 04D001.
- [84] M. Gronau and D. London, Phys. Lett. **B253**, 483 (1991); M. Gronau and D. Wyler, Phys. Lett. **B265**, 172 (1991).
- [85] D. Atwood, I. Dunietz, and A. Soni, Phys. Rev. Lett. **78**, 3257(1997).
- [86] H. Aihara, K. Arinstein *et al.*, Phys. Rev. D **85**, 112014 (20 12).
- [87] Karim Trabelsi, World average and experimental overview of ϕ_3 , CKM - CONF - 2014.
- [88] J. P. Lees *et al.*, (The BaBar Collaboration), Phys. Rev. D **87** 052015 (2013).
- [89] The LHCb Collaboration, CERN-LHCb-CONF-2018-002.
- [90] Golob B, (The Belle II Collaboration), Super KEKB / Belle II Project, Nuovo Cim. C33 319-326 (2010).

BIBLIOGRAPHY

- [91] Emi Kou *et al.*, (The Belle II Collaboration), The Belle II Physics Book, PTEP 2018.
- [92] F. Abudinen, (Belle, Belle II collaboration), JHEP **2022**, 63 (2022).

List of Publications

1. Measurement of the CKM angle ϕ_3 using $B \rightarrow DK$ at Belle II, Manish Kumar *et al.*, Springer Proceedings in Physics **234**, 287 (2019).
2. Belle II Experiment: Status and Upgrade, Kavita Lalwani, Manish Kumar, Few-Body Systems **59**, 142 (2018).
3. Search for rare decays $B^+ \rightarrow D_s^{(*)+} \eta$, $D_s^{(*)+} \bar{K}^0$, $D^+ \eta$, and $D^+ K^0$, Manish Kumar *et al.*, (submitted to arxiv: <https://arxiv.org/pdf/2208.14218.pdf>).
4. Precise Measurement of the D^0 and D^+ Lifetimes at Belle II, F. Abudinén *et al.* (Belle II collaboration), Phys. Rev. Lett. **127**, 211801 (2021).
5. Search for $B^+ \rightarrow K^+ \nu \bar{\nu}$ Decays Using an Inclusive Tagging Method at Belle II, F. Abudinén *et al.* (Belle II collaboration), Phys. Rev. Lett. **127**, 181802 (2021).
6. Search for Axionlike Particles Produced in e^+e^- Collisions at Belle II, M. De Nuccio and T. Ferber *et al.* (Belle II collaboration), Phys. Rev. Lett. **125**, 161806 (2020).

-
7. Search for an Invisibly Decaying Z' Boson at Belle II in $e^+e^- \rightarrow \mu^+\mu^-(e^\pm \mu^\mp)$ Plus Missing Energy Final States, M. Bertemes, M. Campajola, L. Corona, G. De Pietro, E. Graziani, G. Inguglia, I. Komarov, A. Martini, and L. Zani *et al.* (Belle II collaboration), Phys. Rev. Lett. **124**, 141801 (2020).
 8. Measurement of the integrated luminosity of the Phase 2 data of the Belle II experiment, X. Y. Zhou, S. X. Li, and C. P. Shen *et al.* (Belle II collaboration), Chinese Physics C **44**, 021001 (2020).
 9. Study of $\chi_{bJ}(nP) \rightarrow \omega\Upsilon(1S)$ at Belle, A. Abdesselam *et al.* (Belle collaboration), 2108.03497 [hep-ex](2021).
 10. Measurement of the branching fraction for $B^0 \rightarrow \pi^0\pi^0$ decays reconstructed in 2019-2020 Belle II data, F. Abudinén *et al.* (Belle II collaboration), 2107.02373 [hep-ex](2021).
 11. Rediscovery of $B^0 \rightarrow J/\psi K_L^0$ at Belle II, F. Abudinén *et al.* (Belle II collaboration), 2106.13547 [hep-ex](2021).
 12. Measurements of branching fractions and direct CP asymmetries in $B^0 \rightarrow K^+\pi^-$, $B^+ \rightarrow K_S^0\pi^+$ and $B^0 \rightarrow \pi^+\pi^-$ using 2019 and 2020 data, F. Abudinén *et al.* (Belle II collaboration), 2106.03766 [hep-ex](2021).
 13. Measurement of the time-integrated mixing probability χ_d with a semileptonic double-tagging strategy and 34.6fb^{-1} of Belle II collision data, F. Abudinén *et al.* (Belle II collaboration), 2106.00482 [hep-ex](2021).

-
14. Measurements of branching fractions and direct CP-violating asymmetries in $B^+ \rightarrow K^+\pi^0$ and $\pi^+\pi^0$ decays using 2019 and 2020 Belle II data, F. Abudinén *et al.* (Belle II collaboration), 2105.04111 [hep-ex](2021).
 15. First search for direct CP-violating asymmetry in $B^0 \rightarrow K^0\pi^0$ decays at Belle II, F. Abudinén *et al.* (Belle II collaboration), 2104.14871 [hep-ex](2021).
 16. Measurement of the branching fractions of $B \rightarrow \eta'K$ decays using 2019/2020 Belle II data, F. Abudinén *et al.* (Belle II collaboration), 2104.06224 [hep-ex](2021).
 17. Study of $B \rightarrow D^{(*)}h$ decays using 62.8 fb⁻¹ of Belle II data, F. Abudinén *et al.* (Belle II collaboration), 2104.03628 [hep-ex](2021).
 18. Search for lepton-flavor-violating tau decays to $\ell\gamma$ modes at Belle, A. Abdesselam *et al.* (Belle collaboration), 2103.12994 [hep-ex](2021).
 19. Measurements of branching fractions and CP-violating charge asymmetries in charmless B decays reconstructed in 2019–2020 Belle II data, F. Abudinén *et al.* (Belle II collaboration), 2009.09452 [hep-ex](2020).
 20. Search for the Decay $B_s^0 \rightarrow \eta'\eta$, A. Abdesselam *et al.* (Belle collaboration), 2009.06052 [hep-ex](2020).
 21. Measurement of Hadronic Mass Moments $\langle M_X^n \rangle$ in $B \rightarrow X_c\ell\nu$ Decays at Belle II, F. Abudinén *et al.* (Belle II collaboration), 2009.04493 [hep-ex](2020).

-
22. Measurement of the semileptonic $\bar{B}^0 \rightarrow D^{*+}\ell^-\nu_\ell$ branching fraction with fully reconstructed B meson decays and 34.6 fb^{-1} of Belle II data, F. Abudinén *et al.* (Belle II collaboration), 2008.10299 [hep-ex](2020).
23. Exclusive $B^0 \rightarrow \pi^-\ell^+\nu_\ell$ Decays with Hadronic Full Event Interpretation Tagging in 34.6 fb^{-1} of Belle II Data, F. Abudinén *et al.* (Belle II collaboration), 2008.08819 [hep-ex](2020).
24. Studies of the semileptonic $\bar{B}^0 \rightarrow D^{*+}\ell^-\bar{\nu}_\ell$ and $B^- \rightarrow D^0\ell^-\bar{\nu}_\ell$ decay processes with 34.6 fb^{-1} of Belle II data, F. Abudinén *et al.* (Belle II collaboration), 2008.07198 [hep-ex](2020).
25. A calibration of the Belle II hadronic tag-side reconstruction algorithm with $B \rightarrow X\ell\nu$ decays, F. Abudinén *et al.* (Belle II collaboration), 2008.06096 [hep-ex](2020).
26. τ lepton mass measurement at Belle II, F. Abudinén *et al.* (Belle II collaboration), 2008.04665 [hep-ex](2020).
27. Measurement of two-particle correlations in hadronic e^+e^- collisions at Belle, A. Abdesselam *et al.* (Belle collaboration), 2008.04187 [hep-ex](2020).
28. Rediscovery of $B \rightarrow \phi K^{(*)}$ decays and measurement of the longitudinal polarization fraction f_L in $B \rightarrow \phi K^*$ decays using the Summer 2020 Belle II dataset, F. Abudinén *et al.* (Belle II collaboration), 2008.03873 [hep-ex](2020).

-
29. First flavor tagging calibration using 2019 Belle II data, F. Abudinén *et al.* (Belle II collaboration), 2008.02707 [hep-ex](2020).
30. Charmless B decay reconstruction in 2019 Belle II data, F. Abudinén *et al.* (Belle II collaboration), 2005.13559 [hep-ex](2020).
31. Measurement of the B^0 lifetime using fully reconstructed hadronic decays in the 2019 Belle II dataset, F. Abudinén *et al.* (Belle II collaboration), 2005.07507 [hep-ex](2020).
32. Measurement of the branching fraction $\mathcal{B}(\bar{B}^0 \rightarrow D^{*+}\ell^-\bar{\nu}_\ell)$ with early Belle II data, F. Abudinén *et al.* (Belle II collaboration), 2004.09066 [hep-ex](2020).
33. Run and slow control system of the Belle II silicon vertex detector, C. Irmeler *et al.* (Belle II collaboration), Nucl. Instrum. Meth. A **958**, 162706 (2020).
34. Commissioning of the Belle II Silicon Vertex Detector, G. Casarosa *et al.* (Belle II collaboration), Nucl. Instrum. Meth. A **958**, 162184 (2020).
35. Series production testing and commissioning of the Belle II SVD readout system, R. Thalmeier *et al.* (Belle II collaboration), Nucl. Instrum. Meth. A **958**, 162942 (2020).
36. The Belle II silicon vertex detector: Assembly and initial results , R. Thalmeier *et al.* (Belle II collaboration), Nucl. Instrum. Meth. A **936** , 712-714 (2019).

-
37. Machine learning: hit time finding with a neural network, R. Thalmeier *et al.* (Belle II collaboration), PoS TWEPP2018, 065 (2019).
38. Performance Studies of the Belle II Silicon Vertex Detector, K. Lalwani *et al.* (Belle II collaboration), PoS VERTEX2018, 052 (2019).
39. Spatial Resolution of the Belle II Silicon Vertex Detector, S. Halder *et al.* (Belle II collaboration), PoS VERTEX2018, 054 (2019).
40. The Silicon Vertex Detector of the Belle II Experiment, H. Aihara *et al.* (Belle II collaboration), PoS VERTEX2018, 024 (2019).
41. Construction and quality assurance of the Belle II Silicon Vertex Detector, P.K. Resmi *et al.* (Belle II collaboration), PoS VERTEX2018, 051 (2019).
42. Performance of the Belle II SVD, K. Lalwani *et al.* (Belle II collaboration), Springer Proc. Phys. **234**, 87-92 (2019).
43. Search for a Light Higgs Boson in Single-Photon Decays of $\Upsilon(1S)$ Using $\Upsilon(2S) \rightarrow \pi^+\pi^-\Upsilon(1S)$ Tagging Method, S. Jia, C. P. Shen *et al.* (Belle Collaboration), Phys. Rev. Lett. **128**, 081804 (2022).
44. Measurements of the branching fractions of $\Xi_c^0 \rightarrow \Lambda K_S^0$, $\Xi_c^0 \rightarrow \Sigma^0 K_S^0$, and $\Xi_c^0 \rightarrow \Sigma^+ K^-$ decays at Belle, Y. Li, J. X. Cui, S. Jia, C. P. Shen *et al.* (Belle Collaboration), Phys. Rev. D **105**, L011102 (2022).
45. Study of $\bar{B}^0 \rightarrow D^+ h^- (h = K/\pi)$ decays at Belle, E. Waheed, P. Urquijo *et al.* (Belle Collaboration), Phys. Rev. D **105**, 012003 (2022).

-
46. Measurement of Differential Branching Fractions of Inclusive $B \rightarrow X_u \ell^+ \nu_\ell$ Decays, L. Cao, W. Sutcliffe, R. Van Tonder, F. U. Bernlochner *et al.* (Belle Collaboration), Phys. Rev. Lett. **127**, 261801 (2021).
47. Measurement of the masses and widths of the $\Sigma_c(2455)^+$ and $\Sigma_c(2520)^+$ baryons, J. Yelton *et al.* (Belle Collaboration), Phys. Rev. D **104**, 052003 (2021).
48. Measurement of $\mathcal{B}(B_s \rightarrow D_s X)$ with B_s semileptonic tagging, B. Wang, K. Kinoshita *et al.* (Belle Collaboration), Phys. Rev. D **105**, 012004 (2022).
49. Search for the $\eta_{c2}(1D)$ in $e^+e^- \rightarrow \gamma\eta_{c2}(1D)$ at \sqrt{s} near 10.6 GeV at Belle, S. Jia *et al.* (Belle Collaboration), Phys. Rev. D **104**, 012012 (2021).
50. Measurements of branching fractions and asymmetry parameters of $\Xi_c^0 \rightarrow \Lambda \bar{K}^{*0}$, $\Xi_c^0 \rightarrow \Sigma^0 \bar{K}^{*0}$, and $\Xi_c^0 \rightarrow \Sigma^+ K^{*-}$ decays at Belle, S. Jia, S. S. Tang, and C. P. Shen *et al.* (Belle collaboration), JHEP **2021**, 160 (2021).
51. Measurement of the energy dependence of the $e^+e^- \rightarrow B\bar{B}, B\bar{B}^*$ and $B^*\bar{B}^*$ exclusive cross sections, R. Mizuk and A. Bondar *et al.* (Belle collaboration), JHEP **2021**, 137 (2021).
52. Measurement of branching fractions and CP asymmetries for $D_s^+ \rightarrow K^+(\eta, \pi^0)$ and $D_s^+ \rightarrow \pi^+(\eta, \pi^0)$ decays at Belle, Y. Guan, A. J. Schwartz, and K. Kinoshita *et al.* (Belle collaboration), Phys. Rev. D **103**, 112005 (2021).
53. Search for the decay $B_s^0 \rightarrow \eta' \eta$, N. K. Nisar *et al.* (Belle Collaboration), Phys. Rev. D **104**, L031101 (2021).

-
54. Measurements of the branching fractions of $\Lambda_c^+ \rightarrow p\eta$ and $\Lambda_c^+ \rightarrow p\pi^0$ decays at Belle, S. X. Li and C. P. Shen *et al.* (Belle collaboration), Phys. Rev. D **103**, 072004 (2021).
55. Search for $B_s^0 \rightarrow \eta' X_{s\bar{s}}$ at Belle using a semi-inclusive method, S. Dubey and T. E. Browder *et al.* (Belle collaboration), Phys. Rev. D **104**, 012007 (2021).
56. Measurement of branching fraction and search for CP violation in $B \rightarrow \phi\phi K$, S. Mohanty, A. B. Kaliyar, V. Gaur, and G. B. Mohanty *et al.* (Belle collaboration), Phys. Rev. D **103**, 052013 (2021).
57. Search for lepton-number- and baryon-number-violating tau decays at Belle, D. Sahoo, G. B. Mohanty, and K. Trabelsi *et al.* (Belle collaboration), Phys. Rev. D **102**, 111101(R) (2020).
58. Measurements of partial branching fractions of inclusive $B \rightarrow X_u \ell^+ \nu_\ell$ decays with hadronic tagging, F. Bernlochner, L. Cao, W. Sutcliffe, and R. Van Tonder *et al.* (Belle collaboration), Phys. Rev. D **104**, 012008 (2021).
59. Search for the dark photon in $B^0 \rightarrow A'A'$, $A' \rightarrow e^+e^-$, $\mu^+\mu^-$, and $\pi^+\pi^-$ decays at Belle, S. -H. Park, Y. -J. Kwon *et al.* (Belle collaboration), JHEP **2021**, 191 (2021).
60. Search for a doubly charged DDK bound state in $\Upsilon(1S, 2S)$ inclusive decays and via direct production in e^+e^- collisions at $\sqrt{s} = 10.520, 10.580$,

and 10.867 GeV, Y. Li, S. Jia, and C. P. Shen *et al.* (Belle collaboration),
Phys. Rev. D **102**, 112001 (2020).

Internal Belle II Note

1. $D_s^{*\pm}$ and $D^{*\pm}$ reconstruction in 3.14 fb^{-1} collision data, Manish Kumar, Vishal Bhardwaj, Kavita Lalwani, BELLE2-NOTE-PH-2019-041.
2. Plots for $D^{*\pm} \rightarrow D^0 \pi^\pm$, $D^0 \rightarrow K_S^0 \pi^+ \pi^-$ in 472 pb^{-1} collision data, Prasanth Krishnan, Manish Kumar, Minakshi Nayak, Karim Trabelsi, BELLE2-NOTE-PL-2018-018.
3. Plots for $D^0 \rightarrow K_S^0 \pi^+ \pi^-$ in 250 pb^{-1} collision data, Prasanth Krishnan, Manish Kumar, Minakshi Nayak, Karim Trabelsi, BELLE2-NOTE-PL-2018-017.
4. Plots for $K_S^0 \rightarrow \pi^+ \pi^-$ in 1 fb^{-1} DR2 sample and 250 pb^{-1} collision data after applying goodKs selection, Prasanth Krishnan, Manish Kumar, Minakshi Nayak, Karim Trabelsi, BELLE2-NOTE-PL-2018-016.
5. K_S^0 reconstruction using phase 2 data, Prasanth Krishnan, Manish Kumar, Minakshi Nayak, Karim Trabelsi, BELLE2-NOTE-PH-2018-017.

Bio-Data

Full Name : Manish Kumar
Permanent Address : Vill.+post- Baghru Kalan, Teh.- Safidon, Dist.- Jind,
State - Haryana, Pin-126112.
Mob. No. : +91-9996878760
e-mail : 2016rpy9052@mnit.ac.in

EDUCATION

2016-2022 : Research Scholar, Department of Physics
Malaviya National Institute of Technology Jaipur.
2013-2015 : Master of Science in Physics
(secured 72.6%)
Kurukshetra University, Kurukshetra.
2010-2013 : Bachelor of Science in Physics (Honours)
(secured 71.9%)
S.G.T.B Khalsa College, University of Delhi.

ACHIEVEMENTS AND AWARDS

July 2016 : Research Fellowship from Department of Higher Education
Ministry of Human Resource Development Government of India, MHRD.

2010-2015 : National Scholarship during B.Sc. and M.Sc.

Research Experience

Measurement of the branching fraction of rare decays $B^+ \rightarrow D_s^{(*)+}\eta$, $D_s^{(*)+}\bar{K}^0$, $D^+\eta$, and D^+K^0 ,

- We present the study of rare decay modes $B^+ \rightarrow D_s^{(*)+}h^0$ and $B^+ \rightarrow D^+h^0$, where h^0 denotes the neutral mesons (η , K^0) using a data sample of $(772 \pm 10) \times 10^6$ $B\bar{B}$ events collected at the $\Upsilon(4S)$ resonance using the Belle detector at an asymmetric KEKB collider. In absence of any significant signal events, we provide upper limits at 90% confidence level on the branching fraction of $B^+ \rightarrow D_s^+h^0$, $D_s^{(*)+}h^0$, and D^+h^0 decay modes. We give the first search result for the $B^+ \rightarrow D^+\eta$ decay mode. The measured U.L. (at 90% C.L.) are a twenty times more stringent than the previously measured limits. We report the most precise measurement to date of the branching fraction for $\bar{B}^0 \rightarrow D^0K^0$ decay and also supersede the previous Belle result. The branching fraction measurement of $\bar{B}^0 \rightarrow D^0\eta$ decay modes is consistent with the world average and supersede the previous Belle result.

Rediscovery of $D^{*\pm}$ and $D_s^{*\pm}$ at Belle II

- The reconstruction of $D_s^{*\pm}$ and $D^{*\pm}$ decay modes from the $D_s^\pm\gamma$ ($D_s^\pm\pi^0$) and $D^0\pi^\pm$ decay modes, respectively with early Phase III data sample. The D_s^+ is reconstructed from four decay modes: $K_S^0K^+$, $K^+K^-\pi^+$, $\phi\pi^+$ and $\bar{K}^{*0}K^+$ while the D^0 is reconstructed from three decay modes: $K^-\pi^+$, K^+K^- and $\pi^+\pi^-$.

We are interested in these decay modes because of their large branching fraction and three charge track at final states. In most of the D_s^\pm decay mode study, we used these modes as control mode for validation the signal mode study.

We clearly see the signature of D_s^+ and also find the signature of higher resonance in ΔM distribution from $D_s^{*\pm} \rightarrow D_s^\pm\pi^0$ and $D_s^{*\pm} \rightarrow D_s^\pm\gamma$ at an integrated luminosity of 3.14 fb^{-1} of collision data for all D_s^+ sub-decay modes: $K^+K^-\pi^+$, $K_S^0K^+$, $\phi\pi^+$ and $\bar{K}^{*0}K^+$.

Silicon Vertex Detector (SVD)

- The Belle II experiment at SuperKEKB, an extensive upgrade of Belle, will search for new sources of CP violation and more information find here. At Belle II, the Indian group led the design, prototyping and construction of 4th layer of the silicon strip-based vertex detector (SVD). SVD basically used to precise determination of vertex position of short lived particles. Along vertex position, it also help the tracking reconstruction of low momentum

particles.

Belle II Shift

- I have been actively taking Belle II Monte Carlo production, Control Room (CR), Software Quality (SQ) and SVD Remote Monitoring shifts.

CONFERENCES AND WORKSHOPS ATTENDED

1. 9th International Workshop on the CKM Unitarity Triangle (CKM 2016), held at the Tata Institute of Fundamental Research during November 28 to December 2, 2016.
2. CKM SCHOOL, held at the Tata Institute of Fundamental Research during December 3 to December 7, 2016.
3. Presented analysis updates in the Belle Analysis Workshop (BAW), held at Malaviya National Institute of Technology, Jaipur during November 29 to December 2, 2017.
4. Presented poster in the 16th Conference on Flavor Physics CP Violation (FPCP 2018), held at University of Hyderabad during July 14-18, 2018.
5. Presented analysis update in the Post FPCP SCHOOL, held at IIT Hyderabad during July 19-22, 2018.
6. Presented poster in the XXIII DAE-BRNS HIGH ENERGY PHYSICS SYMPOSIUM, held at IIT Madras during December 10-14, 2018.

-
7. Attended XII SERB School on Experimental High-Energy Physics, held at Tata Institute of Fundamental Research, Mumbai, January 2019.
 8. Presented analysis update in the Belle Analysis Workshop (BAW), held at IISER Mohali during March 1-4, 2019.
 9. Presented poster at XXIV DAE-BRNS HEP Symposium held virtually at NISER, Bhubaneswar, India, December 2020.
 10. Given a tutorial on B2BII framework in virtual Belle Analysis Workshop (BAW), held planned by IISER Mohali, PAU Ludhiana, TIFR Mumbai during July 21-23, 2021.
 11. Presented analysis update on Belle II Physics week, held at TIFR Mumbai, Nov. 29 - Dec 3, 2021.

PUBLICATIONS

1. Search for rare decays $B^+ \rightarrow D_s^{(*)+} \eta$, $D_s^{(*)+} \bar{K}^0$, $D^+ \eta$, and $D^+ K^0$, Manish Kumar *et al.*, (submitted to arxiv: <https://arxiv.org/pdf/2208.14218.pdf>).
2. Measurement of the CKM angle ϕ_3 using $B \rightarrow DK$ with Belle II, Manish Kumar *et al.*, Springer Proceedings in Physics **261**, 857 (2021).
3. Measurement of the CKM angle ϕ_3 using $B \rightarrow DK$ at Belle II, Manish Kumar *et al.*, Springer Proceedings in Physics **234**, 287 (2019).
4. Belle II Experiment: Status and Upgrade, Kavita Lalwani, Manish Kumar, Few-Body Systems **59**, 142 (2018).

Internal Belle II Note

1. $D_s^{*\pm}$ and $D^{*\pm}$ reconstruction in 3.14 fb^{-1} collision data, Manish Kumar, Vishal Bhardwaj, Kavita Lalwani, BELLE2-NOTE-PH-2019-041.
2. Plots for $D^{*+} \rightarrow D^0\pi^+$, $D^0 \rightarrow K_S^0\pi^-\pi^+$ in 472 pb^{-1} collision data, Prasanth Krishnan, Manish Kumar, Minakshi Nayak, Karim Trabelsi, BELLE2-NOTE-PL-2018-018.
3. Plots for $D^0 \rightarrow K_S^0\pi^+\pi^-$ in 250 pb^{-1} collision data, Prasanth Krishnan, Manish Kumar, Minakshi Nayak, Karim Trabelsi, BELLE2-NOTE-PL-2018-017.
4. Plots for $K_S^0 \rightarrow \pi^+\pi^-$ in 1 fb^{-1} DR2 sample and 250 pb^{-1} collision data after applying goodKs selection, Prasanth Krishnan, Manish Kumar, Minakshi Nayak, Karim Trabelsi, BELLE2-NOTE-PL-2018-016.
5. K_S^0 reconstruction using phase 2 data, Prasanth Krishnan, Manish Kumar, Minakshi Nayak, Karim Trabelsi, BELLE2-NOTE-PH-2018-017.

Coauthored more than 80 papers as a member of Belle and Belle II Collaborations.

Date:

Manish Kumar